Egil Vålandsmyr Herland

Theoretical studies of two-component superfluids and superconductors

Thesis for the degree of Philosophiae Doctor

Trondheim, November 2012

Norwegian University of Science and Technology
Faculty of Natural Sciences and Technology
Department of Physics

NTNU – Trondheim
Norwegian University of
Science and Technology

NTNU
Norwegian University of Science and Technology

Thesis for the degree of Philosophiae Doctor

Faculty of Natural Sciences and Technology
Department of Physics

ISBN 978-82-471-4001-7 (printed ver.)
ISBN 978-82-471-4002-4 (electronic ver.)
ISSN 1503-8181

Doctoral theses at NTNU, 2012:338

Printed by NTNU-trykk

Abstract

This thesis presents four research papers in the field of condensed-matter theory. In all four papers, large-scale Monte Carlo simulations are used to investigate phases and phase transitions in two-component models of superconductors and superfluids with multiple broken symmetries. In Article I, a U(1) $\times$ U(1) lattice London superconductor with two different types of intercomponent interactions is investigated with focus on understanding the phases and the phase transitions of the model. Particularly, this model exhibits two different paired phases where proliferation of composite topological defects plays an important role.

In Article II and III, a two-dimensional unconventional two-component Coulomb plasma with two distinct Coulomb interactions is investigated. The plasma relates to inner products of Ising-type quantum Hall states as well as to rotating two-component Bose-Einstein condensates with an intercomponent Andreev-Bashkin drag interaction. We investigate the phases and phase transitions of this plasma. Depending on the strength of the attractive intercomponent interaction, the plasma can undergo a Berezinskii-Kosterlitz-Thouless charge-unbinding transition. It can also undergo a two-dimensional melting transition when there is a strong intracomponent repulsion for one of the components. For the parameter values corresponding to the Ising-type quantum Hall states, the plasma is in a screening phase. This can be used to demonstrate that Ising-type quantum Hall states possess quasiparticles with exotic properties.

In Article IV, the noncompact CP^1 model is investigated. This model is proposed as a critical field theory of the continuous quantum phase transition between the Néel state and the paramagnetic valence bond solid state in a quantum antiferromagnet. The model exhibits a direct transition line between a fully ordered phase with broken SU(2) symmetry and a fully disordered phase. By going to larger systems, we find that the bicritical point, which terminates the direct transition line, has been overestimated in earlier works. This may have important consequences for the determination of the character of the phase transition along the direct transition line.

Preface

This thesis is submitted to the Norwegian University of Science and Technology (NTNU) for partial fulfillment of the requirements for the degree philosphiae doctor.

The study has been performed at the Department of Physics, NTNU, Trondheim, between Autumn 2008 and Autumn 2012, and the supervisor of the thesis has been Prof. Asle Sudbø. The work was funded by the Faculty of Natural Sciences and Technology at NTNU.

All articles involve large-scale Monte Carlo simulations that have required many CPU hours at the supercomputing facilities at the University of Tromsø (`Stallo`) and NTNU (`Vilje`).

Egil Vålandsmyr Herland,
Trondheim, November 2012.

Acknowledgements

During the last four years I have spent at the Physics Department at NTNU occupied with this PhD work, there is a long list of people who have contributed to making this thesis come true.

First of all, I would like to thank my supervisor Professor *Asle Sudbø* for giving me the opportunity to pursue a PhD degree in Physics. Asle has given me the right inspiration by combining hard work with great enthusiasm, and he has enabled me to go forward by providing good advice based on his valuable experience and in-depth knowledge. Especially, I would like to thank him for always having time for us PhD students even in busy times serving as the Head of Department.

Professor *Egor Babaev* has coauthored Articles I-IV [1–4]. I am also very grateful to him for sharing his profound insight into vortex physics, Hopfions and multicomponent Ginzburg-Landau models. Indeed, his critical sense and his ability to spot the interesting and important pieces of our work is highly appreciated.

In August 2010, Egor gave me the opportunity to participate on the workshop *Quantum Solids, Liquids and Gases* at Nordita in Stockholm. Here, I was introduced to the work by Dr *Parsa Bonderson*, Professor *Victor Gurarie* and Professor *Chetan Nayak* related to unconventional Coulomb plasmas. A fruitful collaboration was initiated, that has resulted in Papers II and III [2, 3]. Paper III was also coauthored by Professor *Leo Radzihovsky*.

During the last two years, I have had the pleasure of collaborating closely with fellow PhD student *Troels Arnfred Bojesen*. Together, we have investigated several models, and he has been a valuable discussion partner due to his high level of understanding and good sense of humor. Troels has coauthored Paper IV [4].

Starting together at the same time, my fellow PhD student *Iver Bakken Sperstad* has been an invaluable discussion partner on almost all the physics I have been involved with, during this PhD work. Iver has inspired my by his dedication and hard work, and he always has a good answer to my questions as he considers every problem very carefully. *Iver* and *Troels* are also acknowledged for proofreading this document. I

would also like to thank *Einar Bertin Stiansen* for numerous discussions about physics and methodology, and for his pleasant company at work and when traveling to workshops and conferences.

Also, I would like to mention former and present group members. Back in 2008 when I started this PhD, *Eskil Kulseth Dahl* was about to finish his, and he and former postdoc *Steinar Kragset* gave me a careful introduction to this work by sharing their experience and Monte Carlo programs. I would also like to acknowledge *Jacob Linder*, *Henrik Enoksen* and *Peder Notto Galteland*.

I am very grateful to *Terje Røsten* and my brother *Johan Herland* for helping me out in times of computer problems. *Kari Rummukainen* should also be mentioned for sharing his reweighting software with our group.

I would also like to thank Professor *Anders W. Sandvik*, Dr *Flavio S. Nogueira* and Professor *Jon A. Støvneng* for agreeing to participate on the evaluation committee for this thesis.

My parents *Berit* and *Jan* and my brother *Johan* and sister-in-law *Turid* and also all of my friends and in-laws should be mentioned for moral support and encouragement.

Finally, I wish to thank the most important persons in my life, namely my lovely wife *Maria*, my wonderful daughter *Julia* and my precious son *Joel*. Thank you for loving me!

List of articles

Article I

Egil V. Herland, Egor Babaev, and Asle Sudbø,

Phase transitions in a three dimensional $U(1) \times U(1)$ lattice London superconductor: Metallic superfluid and charge-4e superconducting states

Physical Review B **82**, 134511 (2010) [1]
`arXiv:1006.3311v1 [cond-mat.supr-con]`

We consider a three-dimensional lattice $U(1) \times U(1)$ and $[U(1)]^N$ superconductors in the London limit, with individually conserved condensates. The $U(1) \times U(1)$ problem, generically, has two types of intercomponent interactions of different characters. First, the condensates are interacting via a minimal coupling to the same fluctuating gauge field. A second type of coupling is the direct dissipationless drag represented by a local intercomponent current-current coupling term in the free energy functional. In this work, we present a study of the phase diagram of a $U(1) \times U(1)$ superconductor which includes both of these interactions. We study phase transitions and two types of competing paired phases which occur in this general model: (i) a metallic superfluid phase (where there is order only in the gauge invariant phase difference of the order parameters), (ii) a composite superconducting phase where there is order in the phase sum of the order parameters which has many properties of a single-component superconductor but with a doubled value of electric charge. We investigate the phase diagram with particular focus on what we call "preemptive phase transitions." These are phase transitions *unique to multicomponent condensates with competing topological objects*. A sudden proliferation of one kind of topological defects may come about due to a fluctuating background of topological defects in other sectors of the theory. For $U(1) \times U(1)$ theory with unequal bare stiffnesses where components are coupled by a non-compact gauge field only, we study how this scenario leads to a merger of two $U(1)$ transitions into a single $U(1) \times U(1)$ discontinuous phase transition. We also report a general form of vortex-vortex bare interaction potential and possible

phase transitions in an N-component London superconductor with individually conserved condensates.

Article II

Egil V. Herland, Egor Babaev, Parsa Bonderson, Victor Gurarie, Chetan Nayak, and Asle Sudbø,

Screening properties and phase transitions in unconventional plasmas for Ising-type quantum Hall states

Physical Review B **85**, 024520 (2012) [2]
`arXiv:1111.0135v2 [cond-mat.stat-mech]`

Utilizing large-scale Monte-Carlo simulations, we investigate an unconventional two-component classical plasma in two dimensions which controls the behavior of the norms and overlaps of the quantum-mechanical wave functions of Ising-type quantum Hall states. The plasma differs fundamentally from that which is associated with the two-dimensional XY model and Abelian fractional quantum Hall states. We find that this unconventional plasma undergoes a Berezinskii-Kosterlitz-Thouless phase transition from an insulator to a metal. The parameter values corresponding to Ising-type quantum Hall states lie on the metallic side of this transition. This result verifies the required properties of the unconventional plasma used to demonstrate that Ising-type quantum Hall states possess quasiparticles with non-Abelian braiding statistics.

Article III

Egil V. Herland, Egor Babaev, Parsa Bonderson, Victor Gurarie, Chetan Nayak, Leo Radzihovsky, and Asle Sudbø,

Freezing of unconventional two-dimensional plasmas

Preprint [3]

We study unconventional two-dimensional, two-component classical plasmas on a sphere, with emphasis on detecting signatures of melting transitions. These plasmas, which are relevant to Ising-type quantum Hall states, interact via two different two-dimensional Coulomb interactions. One species of particles in the plasma carries charge of both types (Q_1, Q_2), while the other species carries only charge of the second type $(0, -Q_2)$. We find signatures of a freezing transition at $Q_1^2 \simeq 140$. Here, freezing means that the species with charge of both types will form a Wigner crystal, whereas the species with charge of the second type also shows signatures of being a Wigner crystal, due to the attractive inter-component interaction of the second type. Moreover, there is also a Berezinskii-Kosterlitz-Thouless phase transition at $Q_2^2 \simeq 4$, at which the two species of particles bind to

form molecules that are neutral with respect to the second Coulomb interaction. These two transitions appear to be independent of each other, giving a rectangular phase diagram. As a special case, this sheds new light on the freezing transition of two-dimensional one-component plasmas (for which $Q_2 = 0$).

Article IV

Egil V. Herland, Troels A. Bojesen, Egor Babaev, and Asle Sudbø,

Monte Carlo simulations of the CP^1 two-component superconductor

Preprint [4]

We study the SU(2) symmetric noncompact CP^1 model, with two charged matter fields coupled minimally to a noncompact Abelian gauge field. This model is proposed to exhibit an unusual continuous transition line within the so-called deconfined quantum critical point theory. Earlier Monte Carlo studies of this model have found a weak first-order transition directly between a fully ordered state where the SU(2) is broken, to a fully disordered one. According to earlier studies, the transition line becomes increasingly stronger first-order as a function of coupling up to a bicritical point where the direct transition line splits into two separate transition lines. The intermediate phase is a partially ordered phase in which a global O(3) symmetry is broken, but where the Higgs mass (which is non-zero in the fully ordered state) is zero. The intermediate phase may loosely be described as an SU(2) analogue of a "metallic superfluid". By studying the phase transition at values of the gauge field coupling close to what appears to be a splitting point of the transition line, also considering carefully larger system sizes, we find that the value of the gauge field coupling at which a bicritical point occurs, has been overestimated in previous works. Specifically, we find that the phase transition which in a part of this region can be interpreted as a single first-order line of phase-transitions when studying relatively small system, in actuality reveals itself as two separate phase transitions when studying larger system sizes. This has important ramifications for the determination of the character of the phase-transition line below the bicritical point, describing a direct phase transition from a fully ordered state to a fully disordered state. We also perform a flowgram analysis of the direct transition line with rescaling of the linear system size in order to obtain a data collapse. However, due to large finite-size effects in the data collapse, we are not able to draw firm conclusion on the nature of the transition.

My contribution to the articles

In Article I and III [1,3], I wrote the Monte Carlo program, performed all the simulations, analyzed the results and produced all figures in the paper. I also took part in interpreting the results and writing the paper.

In Article II [2], I wrote the Monte Carlo program, performed all the simulations, analyzed the results and produced all figures in the paper except Fig. 1. I also took part in interpreting the results and writing the paper.

In Article IV [4], I took part in writing the Monte Carlo program, performed most of the simulations, analyzed the simulation results and produced all figures in the paper. I also took part in interpreting the results and writing the paper.

Table of Contents

List of Figures

Chapter 1

Introduction

In very general terms, one may understand physics as the quest for observing and analyzing natural laws. In many cases, profound theoretical understanding can be obtained by applying the language of mathematics to formulate physical quantities and the laws they obey in a precise manner. The perhaps most successful physical theories are those that are able to describe important properties in a wide range of physical system by using simple and general notions. A worthy example of such a theory is the *Landau-Ginzburg-Wilson* theory for phase transitions. This theory has the ability to describe phases and phase transitions in a wide range of completely different and complex systems on the basis of general symmetry arguments.

A specific class of materials for which the Landau-Ginzburg-Wilson theory has been applied with great success, are *strongly correlated materials*. Among such materials are the doped cuprates, which, at low temperatures, display the remarkable property of *high-temperature superconductivity*. Since the discovery of this phenomenon in 1986, these compounds have been studied intensively, and many physicists have been engaged with exploring and understanding these materials. This is perhaps not only because the possible range of applications would be enormous, if one should be able to achieve room-temperature superconductivity, but also because a theoretical understanding of these materials poses exciting and progressive challenges for theorists. Still, after 26 years of tremendous efforts, a theory for the microscopic mechanism responsible for this phenomenon is yet to be established, and it remains one of the major unsolved problems in physics. Despite the lack of scientific consensus regarding the microscopic mechanisms in these materials, the Landau-Ginzburg-Wilson theory has been quite successful in describing important properties regarding the phases and phase transitions exhibited by these materials. For instance, insight into the how these materials respond to an external magnetic field, the role of vortices and understanding the mechanisms for destroying superconductivity, can be obtained by applying Landau-Ginzburg-Wilson theory on these systems.

Another class of materials, that in many ways can be regarded as rather different from the doped cuprates, are *Bose-Einstein condensates*. Although they had been predicted

for many years, a pure experimental realization was not achieved until 1995 when two groups independently were able to create such condensates by using advanced cooling techniques on trapped atomic clouds of alkali atoms. Bose-Einstein condensates are found to exhibit the property of *superfluidity*. Also for these systems, the Ginzburg-Landau-Wilson theory can be used with success.

In this thesis, we investigate three mathematical models that can be used to describe two-component systems of superfluids and superconductors. In Article I, we investigate a model of a two-component London superconductor with two different types of intercomponent interactions. Articles II and III are concerned with an unconventional two-component Coulomb plasma that relates to two-component rotating superfluids as well as to fractional quantum Hall wave functions. In Article IV, a special model of a two-component Ginzburg-Landau superconductor that relates to quantum phase transitions in quantum antiferromagnets, is investigated.

This thesis consists of an introduction followed by four research articles. The introductory part is outlined as follows. Chapter 2 introduces a number of central concepts that play an important role in the scientific work of this thesis. The bulk of the research in this thesis is based on performing large-scale Monte Carlo simulations in order to investigate mathematical models. This method is outlined in Chapter 3. Chapter 4 gives a basic introduction to the models studied in the research articles.

Throughout the thesis, natural units are used when convenient.

Chapter 2

Statistical mechanics and phase transitions

In nature, macroscopic bodies of matter are formed by a large number of what one may regard as elementary building blocks. On the most fundamental level, such building blocks are elementary particles such as quarks, leptons or the gauge bosons. However, for many situations, a more fruitful approach might be to consider larger structures, such as atoms, molecules, cells or even larger particles, as elementary constituents.

In such a system, with a large number of constituents, it is practically impossible to solve the equations of motion and find an exact solution. On the other hand, finding the exact position and momentum of all particles is not interesting when studying a macroscopic body of matter. One would rather like to investigate properties such as heat capacity, pressure, volume or resistivity. Although such observables are ill-defined on the microscopic level, they prove to be unbeatable when it comes to describing macroscopic bulk properties in a precise manner. The framework that enables us to extract such macroscopic quantities on the basis of the underlying microscopic structure, is provided by the tools of *statistical mechanics*. This branch of physics deals with calculating macroscopic observables by treating the microscopic particles in a statistical manner. Hence, the laws that governs such macroscopic systems are fundamentally different from the laws of mechanics in that they are statistical in nature.

When the number of particles is large, such systems exhibit new and, in some sense, unexpected behavior [5]. They will form phases, between which there are *phase transitions* where macroscopic properties change in an abrupt manner. In this context, there are closely related and exiting phenomena such as *spontaneous symmetry breaking*, *universality* and *topological defects*. Understanding these concepts are crucial when it comes to describing macroscopic bodies of matter in a precise and consistent manner.

This chapter is intended to give a reminder of these elementary concepts. My approach will be from a classical point of view, and I will only consider systems in thermal equilibrium. Section 2.1 is a quick reminder of the canonical ensemble in statistical mechanics.

In Sec. 2.2, a short description of first-order and continuous phase transitions is given. A few of the most basic spin models are introduced in Sec. 2.3, and with reference to some of these models a short description of spontaneous symmetry breaking, the Berezinskii-Kosterlitz-Thouless transition and topological defects are given in Sec. 2.4. A short reminder of mean-field theory and renormalization is given in Secs. 2.5 and 2.6 before this chapter ends with the concept of duality and the duality transformation of the XY model in Sec. 2.7. The main references that I have used in this chapter are Refs. [6–11].

2.1 Statistical mechanics

It can be derived from general considerations that for a system in a fixed volume V with N particles and in thermal contact with a heat bath at temperature T,[1] the probability $p[\Psi]$ of being in state Ψ has an exponential dependence,

$$p[\Psi] = \frac{1}{\mathcal{Z}} \mathrm{e}^{-\beta H[\Psi]} . \tag{2.1}$$

Here, $\beta = 1/T$ is the inverse temperature and H is the classical Hamiltonian, which gives the total energy of the system in the actual state. The normalizing factor $\mathcal{Z}$ is called the partition function, and can be found by integrating over all states $\{\Psi\}$,

$$\mathcal{Z} = \int \mathcal{D}\,\Psi \, \mathrm{e}^{-\beta H[\Psi]} . \tag{2.2}$$

The thermal average $\langle O \rangle$ of any physical quantity $O[\Psi]$ is then simply found by calculating the statistical mean value of $O[\Psi]$ for the given probability distribution,

$$\langle O \rangle = \frac{1}{\mathcal{Z}} \int \mathcal{D}\,\Psi O[\Psi] \, \mathrm{e}^{-\beta H[\Psi]} . \tag{2.3}$$

The connection to thermodynamic quantities is made by identifying the Helmholtz free energy F as

$$F = -\frac{1}{\beta} \ln \mathcal{Z}. \tag{2.4}$$

To validate this expression, one may perform a partial differentiation with respect to β on both sides of Eq. (2.4),

$$\frac{\partial F}{\partial \beta} = \frac{1}{\beta^2} \ln \mathcal{Z} - \frac{1}{\beta} \frac{\partial}{\partial \beta} \ln \mathcal{Z} = \frac{1}{\beta} \left(\frac{\partial (\beta F)}{\partial \beta} - F \right) . \tag{2.5}$$

At constant V and N, we have from thermodynamics that the internal energy $U = \partial(\beta F)/\partial\beta$ and the entropy $S = \beta^2 \partial F/\partial\beta$. Hence, Eq. (2.5) reproduces

$$F \equiv U - TS, \tag{2.6}$$

[1] These are the environmental constraints that define the well-known canonical ensemble of statistical mechanics. This is the relevant ensemble for the studies in this thesis. In other situations, other ensembles, such as the microcanonical, the grand canonical or the NPT-ensemble, are used to explore the properties of many-particle systems [12–14].

which is the well-known definition of F from thermodynamics.

Now, essentially all well-known thermodynamic quantities may be expressed in terms of the partition function. For instance, the internal energy is given by

$$U = -\frac{\partial}{\partial\beta}\ln\mathcal{Z} = \langle H\rangle, \tag{2.7}$$

i.e., the internal energy is simply given as the thermal average over the energy of the microstates. The heat capacity $C_V = -\beta^2\partial U/\partial\beta$ is given by

$$C_V = \beta^2\frac{\partial^2}{\partial\beta^2}\ln\mathcal{Z} = \beta^2\left\langle\left(H - \langle H\rangle\right)^2\right\rangle, \tag{2.8}$$

and thus can be recognized as proportional to the thermal variance (or the second central moment) of the microstate energies. In some sense, one may consider calculating the partition function as the ultimate goal in statistical mechanics, as all thermodynamic quantities can be found when the partition function is known.

In Article I [1], this formalism is slightly complicated by the fact that the Hamiltonian of the system has an explicit temperature dependence, $H = H[\beta;\Psi]$. Then, Eq. (2.4) and the leftmost equality of Eqs. (2.7) and (2.8) are still valid, but the rightmost equality in Eqs. (2.7) and (2.8) should be replaced by [1, 15]

$$U = \left\langle\frac{\partial(\beta H)}{\partial\beta}\right\rangle, \tag{2.9}$$

and

$$C_V = \beta^2\left\langle\left(\frac{\partial(\beta H)}{\partial\beta} - \left\langle\frac{\partial(\beta H)}{\partial\beta}\right\rangle\right)^2 - \frac{\partial^2(\beta H)}{\partial\beta^2}\right\rangle. \tag{2.10}$$

In other cases, such as Articles II and III [2, 3], the action $\beta H[\Psi]$ may have a more general form $\beta H[\Psi] \to \sum_\alpha \beta_\alpha H_\alpha[\Psi]$ with multiple couplings β_α, to which the energies $H_\alpha[\Psi]$ are associated. In such cases the generalized free energy in Eq. (2.4), can be used to extract quantities similar to U and C_V by differentiation in higher-dimensional parameter space,

$$U_\alpha = -\frac{\partial}{\partial\beta_\alpha}\ln\mathcal{Z}, \tag{2.11}$$

$$C_{V,\alpha\gamma} = \beta_\alpha\beta_\gamma\frac{\partial^2}{\partial\beta_\alpha\partial\beta_\gamma}\ln\mathcal{Z}. \tag{2.12}$$

2.2 Phase transitions

Loosely speaking, a phase transition should be regarded as some abrupt change in macroscopic properties of a many-particle system when some external parameter is varied. Correspondingly, there is a change in the macroscopic state of the system. For example,

in the case of solidification of H_2O, more commonly known as freezing of water to ice, that external parameter would be the temperature.[2] When $T > 0\,^\circ\mathrm{C}$, H_2O is a liquid, and when $T < 0\,^\circ\mathrm{C}$, H_2O forms a solid. At the point of transition, namely $T = 0\,^\circ\mathrm{C}$, there is an abrupt change in quantities such as the elastic modulus, internal energy and the heat capacity of the system.

Furthermore, most phase transitions may be regarded as a transition between an *ordered* state and a *disordered* state. This may be argued for, by a simple consideration of the Helmholtz free energy F, as defined in Eq. (2.6). At equilibrium, the macroscopic state of the system is determined by minimizing F. This may be done by minimizing the internal energy U or by maximizing the entropy S. However, these two possibilities are in conflict since small U normally corresponds to certain well-arranged microstates and thereby small S. At high T, the TS term will dominate and F is minimized by maximizing S. On the other hand, at low T, the U term will dominate, and F is minimized by reducing U. Hence, in between these two regimes, there must be a transition point where the elementary constituents of the system collectively change from disorder to order or vice versa.

The perhaps most basic formulation of a phase transition, closely related to that above, is that it corresponds to a nonanalytic point in the free energy as a function of external parameters. In the vicinity of a phase transition, the free energy may be written as

$$f(\beta, \dots) = f_{\mathrm{r}}(\beta, \dots) + f_{\mathrm{s}}(\beta, \dots), \tag{2.13}$$

where $f(\beta, \dots) = F(\beta, \dots)/N$ is the intensive free energy, decomposed in its regular part $f_{\mathrm{r}}(\beta, \dots)$ and its singular part $f_{\mathrm{s}}(\beta, \dots)$, and $\beta, \dots$ are the external parameters that the free energy may depend on. The singular part $f_{\mathrm{s}}(\beta, \dots)$ is only truly singular in the *thermodynamic limit*, $N \to \infty$. In fact, the concepts of phases and phase transitions are well-defined only in this limit.

2.2.1 Order parameter

For the purpose of describing phase transitions, the *order parameter* $\mathcal{Q}$ plays an important role. This would be a quantity that incorporates the notion of order and disorder in a quantitative manner. As such, the order parameter is a macroscopic quantity that for most cases is zero in the disordered phase, nonzero in the ordered phase and nonanalytic at the point of the phase transition β_{PT}. A sketch of a typical order parameter in the vicinity of a phase transition is given in Fig. 2.1. There is no general and flawless recipe that can be used to establish which quantity to use as an order parameter, and the most appropriate quantity will depend on the system in question. However, insight into the *symmetries* of the Hamiltonian and knowledge of the order characteristics are needed to identify the order parameter.

For later use, the difference between a *local* and a *global* order parameter should be

[2] To be precise, it is possible to solidify H_2O by changing pressure as well, but here I stick to the most familiar case.

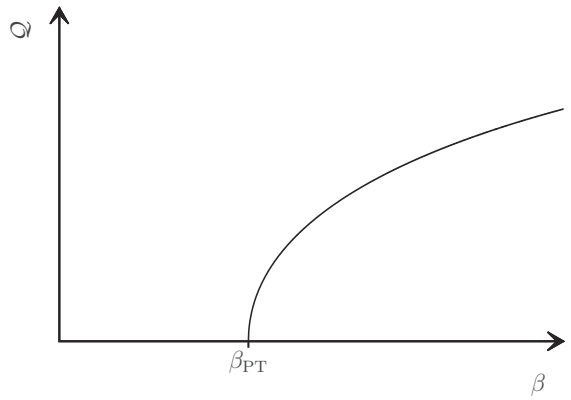

Figure 2.1: A schematic plot of a typical order parameter. The point of the phase transition is denoted β_{PT}. At $\beta < \beta_{\mathrm{PT}}$ (high-T phase), $\mathcal{Q} = 0$ corresponding to the disordered phase. At $\beta > \beta_{\mathrm{PT}}$ (low-T phase), $\mathcal{Q} > 0$ corresponding to the ordered phase. At β_{PT}, $\mathcal{Q}$ is nonanalytic.

mentioned. A local order parameter is an order parameter where thermal averages can be calculated locally in space. Typically, such order parameters can be written as[3]

$$\mathcal{Q} \propto \int \mathrm{d}^d r \, \langle Q(\boldsymbol{r}) \rangle \,, \tag{2.14}$$

where d is the number of spatial dimensions in the system and $Q(\boldsymbol{r})$ is a function of the microscopic degrees of freedom at point $\boldsymbol{r}$ in space. The magnetization in Eq. (2.40) is an example of a local order parameter. A global order parameter typically includes spatial correlations,

$$\mathcal{Q} \sim \int \mathrm{d}^d r \int \mathrm{d}^d r' \left\langle Q(\boldsymbol{r}) Q^*(\boldsymbol{r}') \right\rangle = \int \mathrm{d}^d r \int \mathrm{d}^d r' G(\boldsymbol{r}, \boldsymbol{r}'), \tag{2.15}$$

where

$$G(\boldsymbol{r}, \boldsymbol{r}') = \left\langle Q(\boldsymbol{r}) Q^*(\boldsymbol{r}') \right\rangle , \tag{2.16}$$

is the *two-point correlation function* which measures the spatial correlation of quantity Q between spatial coordinates $\boldsymbol{r}$ and $\boldsymbol{r}'$. Note that thermal averages are not performed locally in Eq. (2.15), and thus, a global order parameter does only make sense when calculated for the whole system. The helicity modulus in Eq. (2.47) and the gauge mass in Eq. (4.12) are examples of global order parameters.

The correlation function in Eq. (2.16) may be used to quantify ordered and disordered phases. Under translational symmetry, we can write $G(\boldsymbol{r}, \boldsymbol{r}') = G(\boldsymbol{r}' - \boldsymbol{r}) \to G(\boldsymbol{r})$, where $\boldsymbol{r}$ now denotes the difference vector between the two spatial coordinates. Typically, when $|\boldsymbol{r}|$ is large, the correlation function decays exponentially,

$$G(\boldsymbol{r}) \sim \mathrm{e}^{-|\boldsymbol{r}|/\xi}, \tag{2.17}$$

[3]For simplicity I write down a scalar order parameter. In some cases, it might be a complex number or a vector quantity.

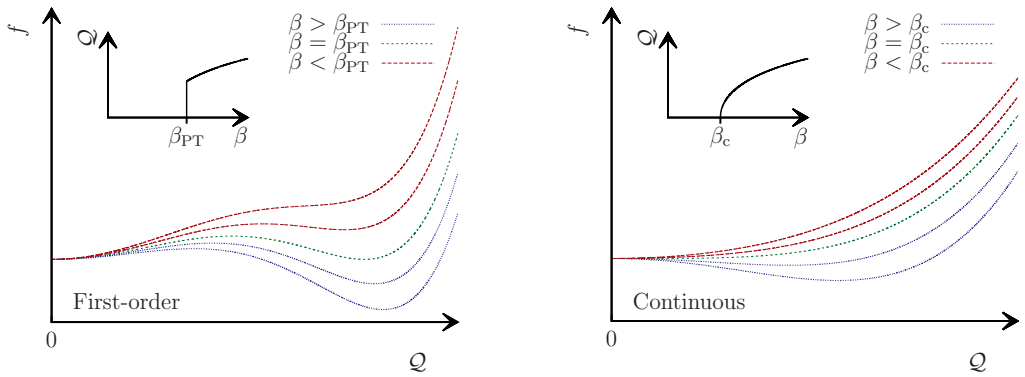

Figure 2.2: Schematic plots of the free energy f as a function of a local order parameter $\mathcal{Q}$ for couplings β in the vicinity of a phase transition. The thermodynamic value of $\mathcal{Q}$ follows the global minimum of f and is given as a function of β in the insets. The leftmost panel shows the case of a first-order phase transition. As a function of β, the global minimum of f has a discontinuous jump at $\beta = \beta_{\mathrm{PT}}$. The rightmost panel shows the case of a continuous phase transition. As a function of β, the global minimum of f is continuous at $\beta = \beta_{\mathrm{c}}$.

where ξ is the *correlation length*. In disordered phases, $G(\boldsymbol{r})$ decays exponentially to zero. However, in the ordered phase the correlation function decays exponentially to a nonzero value. This is so because of the *long-range order* throughout the system in that phase.

2.2.2 First-order phase transitions

Phase transitions are classified according to certain properties related to the free energy. Phase transitions that involve production of latent heat are called *first-order* phase transitions. Such transitions are associated with discontinuous jumps in certain quantities that are first derivatives of the free energy.[4] Examples of such are the internal energy, which is the first derivative with respect to β, and local order parameters, which are first-order derivatives of the free energy with respect to external fields. As such, the ordered and the disordered phase *coexist* at the transition point. A schematic plot of the typical behavior of the free energy and the associated behavior of the local order parameter, in the vicinity of a first-order phase transition, is given in the leftmost panel of Fig. 2.2. At small values of β, the system is in the disordered phase and $\mathcal{Q} = 0$ as given by the global minimum of f. With increasing β, a local minimum develops at a nonzero value of $\mathcal{Q}$, and, at the transition point $\beta = \beta_{\mathrm{PT}}$, it overtakes as the global minimum of f. At β_{PT}, there are two coexisting global minima at different values of $\mathcal{Q}$ corresponding to the two coexisting phases, and consequently, the order parameter is discontinuous. Well-known examples of phase transitions that involve production of latent heat are three-dimensional (3D) melting transitions and vaporization transitions.

[4]The naming stems from the old (and now obsolete) Ehrenfest classification where phase transitions were classified according to the lowest discontinuous derivative of the free energy.

2.2.3 Continuous phase transitions

Transitions that are not first-order are generally classified as *continuous*. They do not involve latent heat, and first derivatives of the free energy are continuous. In some sense, continuous phase transitions may be viewed as a limiting case of first order transitions, in the limit of vanishing difference in the order parameter value between the two coexisting phases at the transition point. Hence, there is only one phase existing at the phase transition and the local order parameter goes to zero continuously. A schematic plot of the typical behavior of the free energy and the associated behavior of the local order parameter, in the vicinity of a continuous phase transition, is given in the rightmost panel of Fig. 2.2. At small values of β the system is in the disordered phase and the global minimum of f is located at $\mathcal{Q} = 0$. With increasing β, the global minimum will start to move away from $\mathcal{Q} = 0$ when $\beta = \beta_c$,[5] in a continuous manner. There are intriguing properties associated with continuous phase transitions in that they exhibit *critical* phenomena and possess *universal* behavior. This will be detailed below.

Critical exponents

At a critical point, the system is found to be in a *critical state*. Here, it is impossible to distinguish between order and disorder. The hallmark of this state is that fluctuations propagate throughout the entire system, i.e., $\xi \to \infty$ at the critical point. This removes the exponential decay in the correlation function, leaving $G(\boldsymbol{r})$ with a long-ranged power law decay,

$$G(\boldsymbol{r}) \propto \frac{1}{|\boldsymbol{r}|^{d-2+\eta}}. \tag{2.18}$$

Here, η is a *critical exponent* and zero external field is assumed. The system will exhibit fluctuations with no intrinsic length scales and becomes *scale-invariant*. That means that the critical state exhibits the same qualitative appearance, even when the system is viewed on different length scales. It follows that the large-scale properties are not sensitive to the microscopic details of the system. Rather, it turns out that such critical properties are determined by the spatial dimension, the symmetry of the order parameter, and the range of the interactions. Hence, the concept of *universality* follows, namely that systems with the same spatial dimension and order parameter symmetry can display the same critical properties, irrespective of the microscopic descriptions. If so, these systems are said to belong to the same *universality class*.

In addition to η, given in Eq. (2.18) above, there are a number of other critical exponents that are associated with power law behavior in the vicinity of a critical point. Let $\tau \equiv (\beta - \beta_c)/\beta$ be the relative deviation from the critical point and let h be the strength of the external field which couples to the local order parameter. The exponent α is then defined by

$$C_V \sim |\tau|^{-\alpha}, \tag{2.19}$$

[5] In the case of a continuous phase transition, it is customary to name the location of the phase transition point as a *critical point* denoted β_c.

when $\tau \to 0^{\pm}$ and $h = 0$. The local order parameter $m = -\partial f/\partial h$ yields the exponent β by

$$m \sim \tau^{\beta}, \tag{2.20}$$

when $\tau \to 0^{+}$ and $h = 0$. The exponent δ is also found from m by

$$m \sim |h|^{1/\delta}\,, \tag{2.21}$$

at $h \to 0^{\pm}$ and $\tau = 0$. Furthermore, the order parameter susceptibility is given by

$$\chi = \frac{\partial m}{\partial h} = -\frac{\partial^2 f}{\partial h^2}, \tag{2.22}$$

and is related to critical exponent γ by

$$\chi \sim |\tau|^{-\gamma}\,, \tag{2.23}$$

when $\tau \to 0^{\pm}$ and $h = 0$. The correlation length also diverges according to a power law with exponent ν,

$$\xi \sim |\tau|^{-\nu}\,, \tag{2.24}$$

when $\tau \to 0^{\pm}$ and $h = 0$.

These six exponents are in fact somewhat interdependent by that they satisfy four scaling relations. These may be deduced on the basis of *Widom's homogeneity postulate* [16],

$$f_{\mathrm{s}}(\lambda^a \tau, \lambda^b h) = \lambda f_{\mathrm{s}}(\tau, h), \tag{2.25}$$

where a and b are constants and λ is an arbitrary scaling factor. Eq. (2.25) is assumed to be valid near the critical point $(\tau, h) = (0, 0)$. The choice $\lambda^a = |\tau|^{-1}$ yields

$$f_{\mathrm{s}}(\tau, h) = |\tau|^{1/a}\, \Phi_{\pm}\left(\frac{h}{|\tau|^{b/a}}\right), \tag{2.26}$$

where $\Phi_{\pm}(x) = f_{\mathrm{s}}(\pm 1, x)$, and the choice $\lambda^b = |h|^{-1}$ yields

$$f_{\mathrm{s}}(\tau, h) = |h|^{1/b}\, \Xi_{\pm}\left(\frac{\tau}{|h|^{a/b}}\right), \tag{2.27}$$

where $\Xi_{\pm}(x) = f_{\mathrm{s}}(x, \pm 1)$. Exponents α, β and γ are now introduced by differentiating Eq. (2.26) to get C_V, m and χ, and compare with Eqs. (2.19), (2.20) and (2.23). Similarly, δ is introduced by differentiating Eq. (2.27) with respect to h to get m, and comparing with Eq. (2.21). Now, a and b can be eliminated in favor of the critical exponents

$$a = \frac{1}{2 - \alpha}, \tag{2.28}$$

$$b = \frac{\delta}{1 + \delta}, \tag{2.29}$$

and two of the scaling relations are obtained,

$$\alpha + 2\beta + \gamma = 2, \tag{2.30}$$
$$\alpha + \beta(\delta + 1) = 2. \tag{2.31}$$

The final two relations, can be derived from Kadanoff's ansatz [17],

$$G\left(|\boldsymbol{r}|, |\tau|\right) = \frac{1}{|\boldsymbol{r}|^{d-2+\eta}} \Omega\left(|\boldsymbol{r}| \, |\tau|^{(2-\alpha)/d}\right), \tag{2.32}$$

for the two-point correlation function close to a critical point. The function $\Omega(z)$ is a function with properties

$$\Omega(x) \sim \begin{cases} C, & x \ll 1, \\ x^{d-2+\eta} \, \mathrm{e}^{-x}, & x \gg 1, \end{cases} \tag{2.33}$$

where C is a constant. Comparing with Eq. (2.24) yields the *hyperscaling* relation,

$$\nu d = 2 - \alpha. \tag{2.34}$$

By linear response theory, the susceptibility is related to the correlation function. Inserting Eq. (2.32) yields

$$\chi \propto \int \mathrm{d}^d r G\left(|\boldsymbol{r}|, |\tau|\right) \propto \int \mathrm{d}r \frac{\Omega\left(r \, |\tau|^{(2-\alpha)/d}\right)}{r^{\eta-1}} = |\tau|^{-(2-\eta)(2-\alpha)/d} \int \mathrm{d}z \frac{\Omega(z)}{z^{\eta-1}}, \tag{2.35}$$

where the substitution $z = r \, |\tau|^{(2-\alpha)/d}$ has been used. Invoking Eq. (2.34) and comparing with Eq. (2.23) yields

$$(2 - \eta)\nu = \gamma. \tag{2.36}$$

These four scaling relations reduce the number of independent critical exponents. Hence, if two exponents are known, the four remaining exponents can be calculated by invoking the scaling relations.[6] In this context, it should also be mentioned that hyperscaling may be violated in certain cases, e.g., when $d > d_{\mathrm{uc}}$, where d_{uc} is the upper critical dimension.[7] Two different system belonging to the same universality class, will exhibit the same critical exponents. Hence, establishing critical exponents is an important task in order to properly characterize a continuous phase transition.

2.3 Basic models

At this point, it will be convenient to introduce a few of the most basic models around. These models are not only introduced here for consistency. In fact, the more complicated

[6] This is not entirely true. If those two exponents happen to be α and ν, then the hyperscaling relation is put out of action.

[7] The upper critical dimension denotes the lowest dimension for that *mean-field theory* predicts correct critical properties. (See Sec. 2.5 for details on mean-field theory.) In most cases $d_{\mathrm{uc}} = 4$.

two-component models in this thesis can, in certain limits, be understood very well by an effective mapping to some of these basic models.

Also, when investigating such a model, it is important to establish the *symmetry* that characterizes the system. By symmetry, I mean a transformation of the microscopic degrees of freedom that leaves the Hamiltonian invariant. More formally, if

$$H[\Lambda\Psi] = H[\Psi], \tag{2.37}$$

where the transformation Λ is a faithful representation of a symmetry group $\mathcal{G}$, then that Hamiltonian is said to have a $\mathcal{G}$ symmetry.

2.3.1 The Ising model

The *Ising model* is a spin model on a lattice that may be used to describe ferromagnetism and antiferromagnetism. The spins s_i, where the index $i \in \{1, \ldots, N\}$ denotes the lattice site and N is the number of spins, can only point in two directions, namely *up* or *down*. In other words, the spins are of unit length $|s_i| = 1 \; \forall \; i$, and are constrained to live in one spin dimension such that the value of the spins must be $+1$ or -1. The Hamiltonian reads[8]

$$H[J, h; \{s_i\}] = -J \sum_{\langle i,j \rangle} s_i s_j - h \sum_{i=1}^{N} s_i, \tag{2.38}$$

where J is the coupling constant, h is the external field, and $\langle i, j \rangle$ means that the sum is over all nearest-neighbor pairs. With $J > 0$, the interactions are ferromagnetic and neighboring spins will tend to point in the same direction, and with $J < 0$, the interactions are antiferromagnetic and neighboring spins will tend to point in opposite directions. In Fig. 2.3 is a typical low-temperature spin configuration in the case of ferromagnetic interaction.

When applying the transformation $s_i \to -s_i \; \forall \; i$, corresponding to a global Z_2 symmetry, Eq. (2.38) yields

$$H[J, h; \{-s_i\}] = H[J, -h; \{s_i\}]. \tag{2.39}$$

Hence, the Ising model in zero external field exhibits a Z_2 symmetry. The Z_2 symmetry is a *discrete symmetry*. When $h \neq 0$, the Z_2 symmetry is *explicitly broken*.[9]

The order parameter for the Ising model in the ferromagnetic case is the magnetization

$$m = \frac{1}{N} \left\langle \sum_{i=1}^{N} s_i \right\rangle. \tag{2.40}$$

[8] For simplicity, I will restrict myself to the nearest-neighbor Ising model with a uniform coupling J. The Ising model often appears in more general forms, with nonuniform coupling $J \to J_{ij}$ (like for spin glasses), and/or with long-ranged interactions, $J_{ij} \neq 0 \; \forall \; i, j \neq i$.

[9] Explicit symmetry breaking means that there is a term in the Hamiltonian (coupling to an external field is a good example) that causes the symmetry to be destroyed.

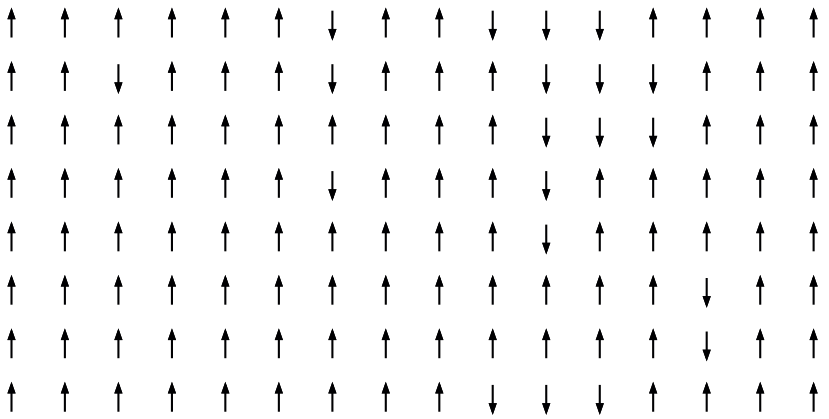

Figure 2.3: A typical zero-field spin configuration for the two-dimensional Ising model. The spins are restricted to point either up or down. In this case the interaction is ferromagnetic, so neighboring spins tend to point in the same direction.

In the antiferromagnetic case, the order parameter is the staggered magnetization $m_{\text{staggered}}$. For the case of a hypercubic lattice,[10] the staggered magnetization is given by

$$m_{\text{staggered}} = \frac{1}{N} \left\langle \sum_{i \in A} s_i - \sum_{i \in B} s_i \right\rangle, \tag{2.41}$$

where the hypercubic lattice is divided into two sublattices A and B, unambiguously defined by that all $i \in A$ have all nearest neighbors in sublattice B and vice versa.

In one spatial dimension, the Ising model was solved analytically by E. Ising in 1925. He found that for $h = 0$, there is no phase transition at finite T.[11] In two dimensions (2D), the Ising model with $h = 0$ was solved by L. Onsager in 1944 [18]. In that case there is a continuous phase transition at $\beta_{\text{c}} = \ln(1 + 2^{1/2})/(2J)$ that separates the disordered phase, characterized by $m = 0$, from the ordered phase, characterized by $|m| > 0$. For three and higher dimension, no exact analytic solution exists, but the Ising model exhibits a continuous phase transition at finite T. The upper critical dimension $d_{\text{uc}} = 4$ for the Ising model, so for $d \geq 4$, mean-field theory is accurate.[12] In addition to the upper critical dimension, it is also customary to set the *lower critical dimension* d_{lc} which denotes the highest dimension for that there is no long-range order at finite temperature. According to the details given above, it should be clear that $d_{\text{lc}} = 1$ for the Ising model.

[10] In the antiferromagnetic case, the ground state order and thus, the most appropriate form of the order parameter, will depend on the lattice structure.

[11] In fact, the Ising model, the XY model in Sec. 2.3.2, and the Heisenberg model in Sec. 2.3.4 are all special cases of the *n-vector model*, and in all such models, with nearest-neighbor interaction and with free boundary conditions, there exists an exact solution for one dimension with no finite-temperature phase transition.

[12] Actually, $d_{\text{uc}} = 4$ for all n-vector models with short-range interactions.

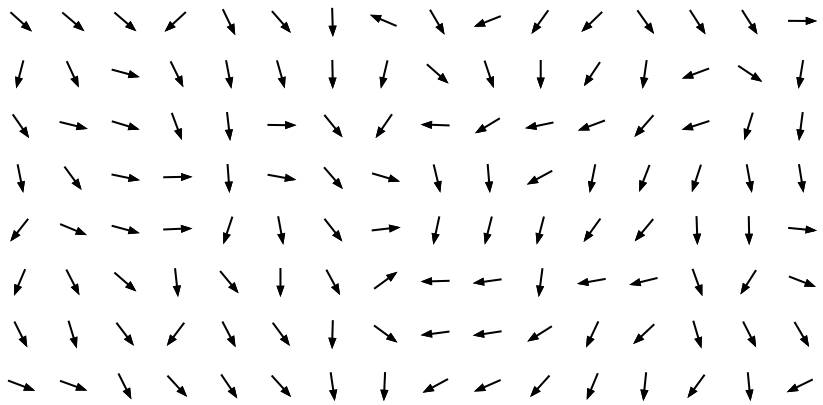

Figure 2.4: A typical zero-field spin configuration for the 2D XY model. The spins can point in any direction in the planar spin space. In this case the interaction is ferromagnetic, so neighboring spins tend to point in the same direction.

2.3.2 The XY model

Increasing the number of spin dimensions to two yields the *XY model*. Now, the spins are promoted to vectors $\boldsymbol{s}_i$ with unit length $|\boldsymbol{s}_i| = 1 \; \forall \; i$. The Hamiltonian is given by

$$H[J, h; \{\boldsymbol{s}_i\}] = -J \sum_{\langle i,j \rangle} \boldsymbol{s}_i \cdot \boldsymbol{s}_j - \boldsymbol{h} \cdot \sum_{i=1}^{N} \boldsymbol{s}_i. \tag{2.42}$$

The spins should be viewed as bound vectors that are capable of pointing from the origin towards any point on the unit circle, and may thus be conveniently parametrized by the angle $\theta_i \in (-\pi, \pi]$ with respect to the x-axis (in spin space), i.e., $\boldsymbol{s}_i = (\cos\theta_i, \sin\theta_i)$. Hence, Eq. (2.42) can be written as

$$H[J, h; \{\theta_i\}] = -J \sum_{\langle i,j \rangle} \cos(\theta_j - \theta_i) - h \sum_{i=1}^{N} \cos\theta_i, \tag{2.43}$$

where coordinate axes are chosen such that $\boldsymbol{h} = (h, 0)$. In Fig. 2.4, a snapshot of a typical spin configuration for the XY model is given. In the case $h = 0$, the Hamiltonian of the XY model is invariant with respect to the transformation $\theta_i \to \theta_i + \varphi \; \forall \; i$, where $\varphi \in \mathbb{R}$. This is a global U(1) symmetry. The U(1) symmetry is a *continuous symmetry*. In an external field, $h \neq 0$, the U(1) symmetry is explicitly broken.

The proper local order parameter for the XY model is the magnetization

$$\boldsymbol{m} = \frac{1}{N} \left\langle \sum_{i=1}^{N} \boldsymbol{s}_i \right\rangle. \tag{2.44}$$

Additionally, in zero external field, the *helicity modulus* $\boldsymbol{\Upsilon}$ is often used as a global order parameter for the XY model and similar models. This quantity is formally defined

as the second derivative of the free energy with respect to an externally imposed and infinitesimal twist $\boldsymbol{\delta}$ of the phases θ_i across the system, [19, 20]

$$\Upsilon_\mu \equiv \left.\frac{\partial^2 f(\boldsymbol{\delta})}{\partial \delta_\mu^2}\right|_{\boldsymbol{\delta}=0} = \frac{1}{N}\left[\left\langle \frac{\partial^2 H[\{\theta_i'\}]}{\partial \delta_\mu^2}\right\rangle - \beta\left\langle\left(\frac{\partial H[\{\theta_i'\}]}{\partial \delta_\mu} - \left\langle\frac{\partial H[\{\theta_i'\}]}{\partial \delta_\mu}\right\rangle\right)^2\right\rangle\right]\Bigg|_{\boldsymbol{\delta}=0}. \tag{2.45}$$

Here, the phase twist corresponds to the transformation

$$\theta_i \to \theta_i' = \theta_i - \boldsymbol{\delta}\cdot\boldsymbol{r}_i \quad \forall \quad i, \tag{2.46}$$

where $\boldsymbol{r}_i$ is the spatial coordinate of lattice site i, and μ denotes spatial direction. Assuming a hypercubic lattice with lattice spacing $a = 1$, inserting Eq. (2.43) with $h = 0$ yields

$$\Upsilon_\mu = \frac{J}{N}\left\{\left\langle\sum_{i=1}^{N}\cos(\Delta_\mu\theta_i)\right\rangle - J\beta\left\langle\left[\sum_{i=1}^{N}\sin(\Delta_\mu\theta_i)\right]^2\right\rangle\right\}, \tag{2.47}$$

for the zero-field XY model. Here, $\Delta_\mu\theta_i = \theta_j - \theta_i$ is a finite lattice difference where j denotes the nearest neighbor to i along the positive μ-axis. Moreover, to obtain Eq. (2.47), I have used that

$$\left.\frac{\partial f(\boldsymbol{\delta})}{\partial \delta_\mu}\right|_{\boldsymbol{\delta}=0} = -\frac{J}{N}\left\langle\sum_{i=1}^{N}\sin(\Delta_\mu\theta_i)\right\rangle = 0, \tag{2.48}$$

due to the even symmetry of the Hamiltonian. The helicity modulus probes the free energy cost associated with twisting the phase. Hence, $\Upsilon_\mu = 0$ in the disordered phase, whereas $\Upsilon_\mu > 0$ in the ordered phase where the spins tend to align over large distances.

In 2D, the XY model exhibits the famous *Berezinskii-Kosterlitz-Thouless transition*. This peculiar phase transition is detailed below in Sec. 2.4.2. In three and higher dimensions a continuous phase transition exists at finite T.

2.3.3 Clock models

Clock models are spin models on a lattice where unit-length spins can take q possible discrete values uniformly distributed on the unit circle. Similar to the XY model, the spins are parametrized by the angles θ_i, but the angles are restricted to only take the values $\theta = 2\pi n/q$ where $n \in \{1, \ldots, q\}$. In Fig. 2.5, the allowed discrete spin directions for $q \in \{3, 4, 5, 8, 16\}$ are shown. Omitting the external field, the Hamiltonian is given by

$$H[J; \{\theta_i\}] = -J\sum_{\langle i,j\rangle}\cos(\theta_j - \theta_i). \tag{2.49}$$

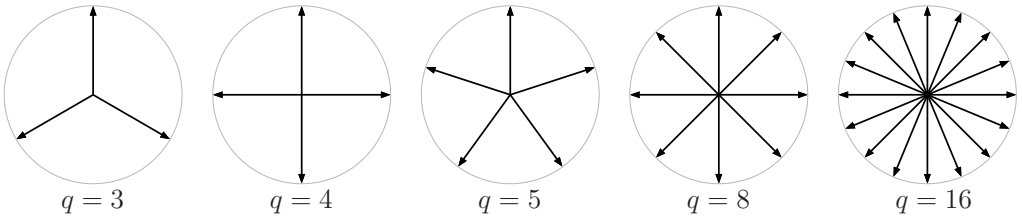

Figure 2.5: Allowed spin directions for clock models with $q \in \{3, 4, 5, 8, 16\}$.

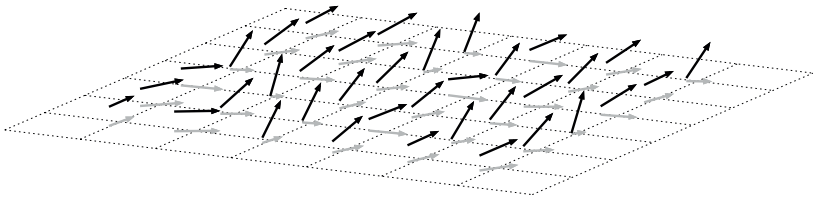

Figure 2.6: A typical zero-field spin configuration for the 2D Heisenberg model. The spins can point in any direction in the 3D spin space. The gray-colored shadows correspond to the spin projections onto the xy-plane. In this case the interaction is ferromagnetic, so neighboring spins tend to point in the same direction.

Hence, the $q = 2$ clock model is identical to the Ising model.[13] In the limit when $q \to \infty$, the clock model becomes the XY model. Actually, clock models with large values of q approximate XY-like models accurately [21–23]. This can be exploited numerically by simulating XY-like models approximately as clock models with many angles q, which is computationally less demanding [12].

2.3.4 The Heisenberg model

For the *Heisenberg model*, the unit spins of the Ising and XY model are promoted to live in three spin dimensions with unit length $|\boldsymbol{s}_i| = 1 \; \forall \; i$. Hence, the spins are bound vectors that can point from the origin towards any point on the surface of the unit sphere. The Hamiltonian reads

$$H[J, h; \{\boldsymbol{s}_i\}] = -J \sum_{\langle i,j \rangle} \boldsymbol{s}_i \cdot \boldsymbol{s}_j - \boldsymbol{h} \cdot \sum_{i=1}^{N} \boldsymbol{s}_i. \tag{2.50}$$

In Fig. 2.6 is a snapshot of a typical spin configuration for the 2D Heisenberg model. When $\boldsymbol{h} = \boldsymbol{0}$, the Hamiltonian is invariant under the transformation $\boldsymbol{s}_i \to \pm G\boldsymbol{s}_i \; \forall \; i$, where

$$G = \begin{pmatrix} \cos\varphi & \sin\varphi & 0 \\ -\sin\varphi\cos\theta & \cos\varphi\cos\theta & \sin\theta \\ \sin\varphi\sin\theta & -\cos\varphi\sin\theta & \cos\theta \end{pmatrix}, \tag{2.51}$$

and where $\varphi, \theta \in \mathbb{R}$. I.e., the Heisenberg model exhibits O(3) symmetry.

[13] It can be shown that also the $q = 4$ clock model is identical to the Ising model with coupling $J/2$.

As for the Ising and XY model, the magnetization, given in Eq. (2.44), is the proper local order parameter. Contrary to the 2D XY model, the 2D Heisenberg model is in the disordered phase with exponentially decaying correlations for all $T > 0$. For three and higher dimensions, a continuous phase transition exists for $T > 0$.

2.4 Phase transitions revisited

2.4.1 Spontaneous symmetry breaking

An important concept that applies to the ordered side of many phase transitions, is *spontaneous symmetry breaking*. That is, the observed thermodynamic averages do not display the same symmetry properties as the Hamiltonian. For example, in the ordered phase of the zero-field Ising model, the long-range order yields a nonzero magnetization, either positive or negative, $m = \pm|m|$, where $|m| > 0$. Hence, by invoking a Z_2 transformation in Eq. (2.40),

$$m[\{-s_i\}] = -m[\{s_i\}] \neq m[\{s_i\}], \tag{2.52}$$

it is clear that the magnetization does not show the Z_2 symmetry of the Hamiltonian [see Eq. (2.39)]. Whether the magnetization is positive or negative can be thought of as randomly determined by fluctuations as the system is cooled below β_c. However, when inside the ordered phase, the fluctuations have a finite correlation length, and consequently, fluctuations are not capable of altering the magnetization globally for a system in the thermodynamic limit.

At first sight, it might seem like there is an inconsistency here. The Z_2 transformation transforms the system into a microstate with exactly opposite magnetization,[14] but at the same time the Z_2 symmetry ensures that the probability in Eq. (2.1) is invariant. Hence, every microstate has a mirror state with equal weight, but opposite magnetization, so the thermal average in Eq. (2.40) should sum up to zero. This is evidently wrong in the ordered phase, and the solution is that the thermodynamic limit must be taken properly. Indeed, for any nonzero h the fraction between the probability of being in some state $P[\Psi]$ and the probability of being in the mirror state $P[\Psi_\mathrm{mirror}]$, is, by Eqs. (2.1) and (2.38),

$$\frac{P[\Psi]}{P[\Psi_\mathrm{mirror}]} = \mathrm{e}^{2\beta h N \bar{s}}, \tag{2.53}$$

where $\bar{s} = (\sum_i s_i)/N$ for the state Ψ. Now, taking the limit $N \to \infty$ yields

$$\frac{P[\Psi]}{P[\Psi_\mathrm{mirror}]} = \begin{cases} \infty, & h > 0, \\ 0, & h < 0, \end{cases} \tag{2.54}$$

[14] To avoid confusion: When magnetization is mentioned in connection with microstates, I simply mean the average spin value for that particular state, i.e., Eq. (2.40) *without* taking the thermal average on the right-hand side.

even when the limit $h \to 0^{\pm}$ is taken afterward. Hence, when the thermodynamic limit is carefully taken *before* $h \to 0^{\pm}$ we find that the probability of state Ψ is *not* equal the probability of state Ψ_{mirror}.[15] In fact, if $P[\Psi]$ is nonzero, then $P[\Psi_{\text{mirror}}]$ is zero. This is called *ergodicity breaking*, namely that the system is prohibited from entering certain regions in phase space. This exclusion is only possible because singularities are introduced when the limit $N \to \infty$ is taken. In contrast, for finite systems there are no exclusions in phase space, and consequently, no spontaneous symmetry breaking. An important lesson to be learned from this is that in the thermodynamic limit, the true probability distribution is not necessarily given by the canonical probability distribution in Eq. (2.1).

Spontaneous symmetry breaking occurs on the ordered side of most phase transitions, but there are important exceptions. The Berezinskii-Kosterlitz-Thouless transition (see Sec. 2.4.2) does not display this behavior. There is also no spontaneous symmetry breaking in systems with a *local* symmetry [24].

2.4.2 The Berezinskii-Kosterlitz-Thouless transition

According to the theorem by Mermin and Wagner [25], continuous symmetries cannot be spontaneously broken at finite temperature when the spatial dimension $d \leq 2$, i.e., the lower critical dimension for systems with continuous symmetry is $d_{\text{lc}} = 2$. This theorem applies to the 2D XY model where no such ordered state is found at low temperatures. However, this does not mean that nothing happens at all. Instead, there is a rather strange and unconventional phase transition occurring which is called the *Berezinskii-Kosterlitz-Thouless phase transition* after its discoverers [26–28].

Since there is no low-temperature ordered phase with long-range order in this case, $\boldsymbol{m} = \mathbf{0}$ for all $\beta < \infty$. However, there is a low-temperature phase which is characterized by a power law decay in the correlation function,

$$G(|\boldsymbol{r}|) \sim |\boldsymbol{r}|^{-\eta(\beta)}\,, \tag{2.55}$$

where $\eta(\beta) = (2\pi J\beta)^{-1}$ is a coupling dependent exponent. Accordingly, the correlation length $\xi = \infty$ throughout the low-temperature phase. Due to these extraordinary properties, the entire low-temperature phase is denoted as a critical phase with *quasi long-range order*. The transition point of the Berezinskii-Kosterlitz-Thouless (BKT) transition β_{BKT} is the lower endpoint of the critical phase, and for $\beta < \beta_{\text{BKT}}$ (high-temperature phase) there are exponentially decaying correlations with a finite ξ. According to the classification scheme the BKT transition is a continuous transition. However, close to the transition point on the disordered side, the correlation length diverges exponentially,

$$\xi \sim \mathrm{e}^{\text{const.}/\sqrt{\beta_{\text{BKT}}-\beta}}, \tag{2.56}$$

and not like the usual power law as for other continuous transitions. Since thermodynamic divergences can be thought of as a consequence of the diverging correlation length,

[15] When $h \to 0^{\pm}$ is taken before $N \to \infty$ in Eq. (2.53), $P[\Psi]/P[\Psi_{\text{mirror}}] = 1$. Hence, the two ways of taking these limits do not *commute*.

the singular part of the free energy should scale as $f_{\mathrm{s}} \sim \xi^{-d}$ close to a continuous phase transition.[16] Hence, the heat capacity exhibits an *essential singularity*,

$$C_V \sim \mathrm{e}^{-\mathrm{const.}/\sqrt{\beta_{\mathrm{BKT}}-\beta}}, \tag{2.57}$$

for a BKT transition.

For obvious reasons, the magnetization does not work very well as an order parameter for the BKT transition. As will be detailed below in Sec. 2.4.3, *vortices* play an essential role in destroying the quasi long-range order at the BKT transition point, and it turns out that this is captured by the helicity modulus Υ_μ. The onset of the critical phase in the BKT transition is signaled by that Υ_μ has a discontinuous jump from zero to a universal value [29,30],

$$\Upsilon_\mu(\beta^+_{\mathrm{BKT}}) = \frac{2}{\pi\beta_{\mathrm{BKT}}}. \tag{2.58}$$

This discontinuity should not be confused with those of a first-order transition as the helicity modulus is a stiffness measure and not a thermodynamic variable.

2.4.3 Topological defects

Topological defects are collective excitations that play an important role in many phase transitions.[17] These objects are nontrivial configurations that typically involve many microscopic degrees of freedom and are stable against small perturbations. Generally, they are found to have a disordered core surrounded by a large ordered or nearly ordered regions. There is a relatively small energy cost associated with them compared to the amount of entropy they produce. Thus, they play an important role in many phase transitions as these objects proliferate and destroy order at long distances when the temperature is such that the entropy they produce wins over the energy cost. Moreover, these defects are nonlocal and depend on large-scale properties, such as symmetries and spatial dimensionality. Well-known examples are domain walls and vortices in spin systems, and dislocations and disclinations in solids.

Domain walls

All possible microstates of the Ising model can be divided into domains. Within a single domain, all spins point in the same direction, and this can be used to identify all domains in that particular state. These domains are separated by the topological defects of the Ising model, namely domain points ($d = 1$), domain lines ($d = 2$), or domain walls ($d = 3$), which separate regions of oppositely aligned spins. In Fig. 2.7, the domain lines

[16] This means that the BKT transition is an infinite order phase transition according to the obsolete Ehrenfest classification scheme, as all orders of derivatives of the free energy are continuous at the phase transition.

[17] Topological defects are also often called *topological objects*, *topological excitations* or *topological solitons*.

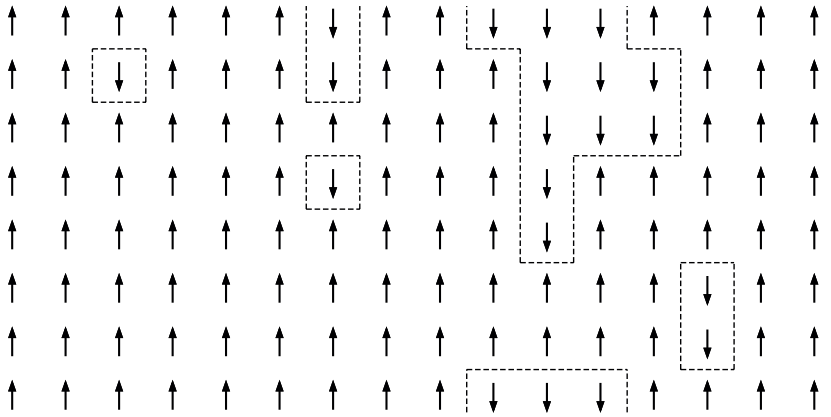

Figure 2.7: Domain lines in the 2D Ising spin configuration, given in Fig. 2.3.

for the spin configuration in Fig. 2.3 are shown explicitly. The phase transitions in the zero-field Ising model are governed by proliferation of such topological defects.

Vortices

The topological defects of the XY model are *vortices* ($d = 2$) or *vortex lines* ($d = 3$). Vortices are recognized by that the phase θ winds an integer number of times when following a closed loop around the vortex. On a lattice this can be formulated as

$$\sum_{\{i,\mu\}\in\mathcal{C}} \Delta_\mu \theta_i = 2\pi n, \tag{2.59}$$

where the phase differences on all links that comprise a closed path $\mathcal{C}$ are summed in the counterclockwise direction. The integer n is the number of times the phase winds when traversing $\mathcal{C}$, and whenever $\Delta_\mu\theta_i$ is outside its primary interval, an integer number of 2π is added such that $\Delta_\mu\theta_i \in [-\pi, \pi)$. By systematically calculating n for all plaquettes in the system, one can map out the location of all vortices in the configuration, as illustrated in Fig. 2.8.

In Fig. 2.8, the vortex excitation is a pair of vortices with opposite winding and not a single vortex. As will be shown in the following, this is the relevant excitation for the 2D XY model. For a single vortex with $n = 1$, the average phase difference between two neighboring spins at average distance $r_{\langle i,j\rangle}$ from the vortex core should approximately be proportional to $r^{-1}_{\langle i,j\rangle}$ since the number of links participating in the closed loop with radius $r_{\langle i,j\rangle}$, is proportional to $r_{\langle i,j\rangle}$. Moreover, when $r_{\langle i,j\rangle}$ is large, the argument of the cosine in Eq. (2.43) is small and well approximated by $\cos x \approx 1 - x^2/2$. Hence, the energy cost of introducing a single vortex into an ordered spin configuration is

$$E_\mathrm{v} \sim \sum_{\langle i,j\rangle} \frac{1}{r^2_{\langle i,j\rangle}} \propto \int_{r_0}^{R} \frac{\mathrm{d}r_{\langle i,j\rangle}}{r_{\langle i,j\rangle}} = \ln\frac{R}{r_0}, \tag{2.60}$$

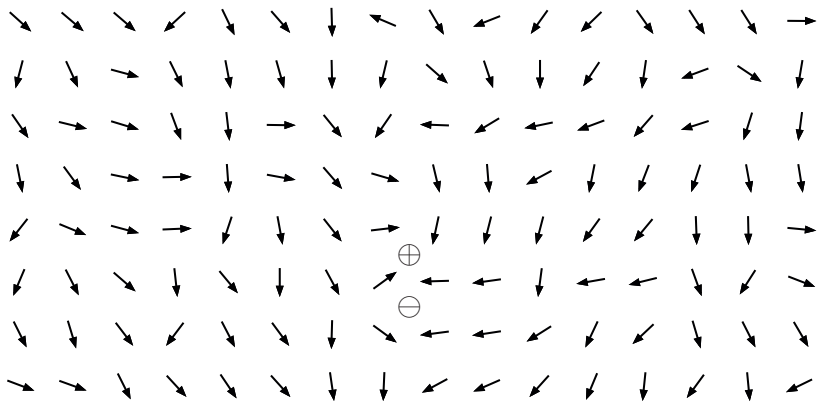

Figure 2.8: Vortices in the 2D XY spin configuration, given in Fig. 2.4. The sign $\oplus$ denotes a vortex with $n = 1$ and the sign $\ominus$ denotes a vortex with $n = -1$.

where the sum is approximated by an integral where the lower cutoff r_0 is on the scale of the lattice spacing a, and the upper cutoff R is on the scale of the system size. Clearly, the cost of introducing a single vortex into the system is by no means small, as it diverges logarithmically with system size. On the other hand, for a pair of vortices with opposite winding, the phase will not wind an integer number of times for a closed path enclosing *both* vortices (see Fig. 2.8). Introducing $r_{\langle i,j\rangle}$ as the average distance from two neighboring spins to the mean vortex position of a vortex pair separated by a distance $2r_{\mathrm{vp}}$, for $r_{\langle i,j\rangle} \gg r_{\mathrm{vp}}$, the phase differences will essentially be unaffected by introducing the vortex pair. Hence, the integral in Eq. (2.60) will have an effective upper cutoff $\sim r_{\mathrm{vp}}$, as the integrand is well approximated by zero above this radius. The energy cost of introducing a vortex pair is thus *finite* with diverging system size,

$$E_{\mathrm{vp}} \sim \ln \frac{r_{\mathrm{vp}}}{r_0}. \tag{2.61}$$

Consequently, vortices that are bound in pairs of opposite windings are a much cheaper excitation than a single vortex in the 2D XY model. Similarly, for the 3D XY model, the relevant excitations are closed vortex loops instead of single vortex lines.

Although a single vortex has a logarithmically divergent energy, it also has a logarithmically divergent entropy $S_{\mathrm{v}} \sim \ln(R/r_0)$. Hence, at large enough temperature, the entropy will start to dominate the change in the free energy, when adding free vortices. This is the point of the BKT transition. When $\beta > \beta_{\mathrm{BKT}}$, the vortices are bound in pairs of opposite winding. At β_{BKT}, the vortices unbind and the quasi long-range order is destroyed. When $\beta < \beta_{\mathrm{BKT}}$, free vortices are abundant throughout the system and spin correlations are short-ranged with an exponential decay. As such, the BKT transition is best understood as a *vortex-pair-unbinding* transition. Correspondingly, in 3D the mechanism for destroying the long-range order is proliferation of vortex loops.

2.5 Mean-field theory

Solving many-body models exactly is in most cases impossible due to the complications that arise with the interaction terms in the Hamiltonian. *Mean-field theory* (MFT) is a scheme for solving such models approximately, by replacing all interactions between a particle and the others with an effective external field. This can be done by approximating all degrees of freedom of the other particles to have a fixed value, namely the thermodynamic average. The benefit is that the complicated many-body problem can be reduced to a simple one-body problem. The drawback is that fluctuations are ignored.

To demonstrate the method, I will calculate the partition function for the zero-field XY model in the mean-field approximation. Eq. (2.42) can be rewritten as

$$H[J;\{\boldsymbol{s}_i\}] = -\sum_{i=1}^{N} \boldsymbol{s}_i \cdot \tilde{\boldsymbol{h}}_i, \tag{2.62}$$

where $\tilde{\boldsymbol{h}}_i$ is an effective external field given by summing over all the nearest neighbors to $\boldsymbol{s}_i$,

$$\tilde{\boldsymbol{h}}_i = \frac{J}{2} \sum_{j \text{ nn. } i} \boldsymbol{s}_j. \tag{2.63}$$

The next step is to replace the neighboring spin fields by the thermal average, $\boldsymbol{s}_j \to \langle \boldsymbol{s}_j \rangle$ in Eq. (2.63). This is the mean-field approximation. In this way, $\tilde{\boldsymbol{h}}_i$ will be a fixed value, and the integrals in the partition function will decouple,

$$\mathcal{Z} = \prod_{i=1}^{N} \mathcal{Z}_i. \tag{2.64}$$

Here, $\mathcal{Z}_i$ will be a single-spin partition function, given by

$$\mathcal{Z}_i = \int_0^{2\pi} \mathrm{d}\theta \, \mathrm{e}^{\beta \boldsymbol{s}_i \cdot \tilde{\boldsymbol{h}}_i} = 2\pi I_0 \left(\beta \left| \tilde{\boldsymbol{h}}_i \right| \right), \tag{2.65}$$

where $I_0(x)$ is the modified Bessel function of the first kind. Assuming uniform magnetization, $\langle \boldsymbol{s}_i \rangle = \boldsymbol{m} \; \forall \; i$, one can obtain the magnetization selfconsistently by differentiation of the partition function.

The strength of MFT is that predictions can be made by a rather straightforward and simple analysis. In particular, in cases when it is safe to approximate all the interactions of a particle by some average value, the MFT predictions are usually good. This is typically outside the critical region and when the number of interactions of a particle is large. The latter would be the case if the number of dimensions is large, or if there are long-range interactions in the Hamiltonian. However, within the critical region when $d < d_{\text{uc}}$, the MFT predictions are often erroneous, and other methods should be used to obtain critical properties.

2.6 Renormalization

The framework that for the last 40 years or so has proven to be tremendously successful in the quest for describing and understanding critical properties in many-particle systems, is given by the *renormalization group theory*. The list of achievements obtained by the renormalization group (RG) theory includes the ability to calculate critical exponents, derivation of Widom's homogeneity postulate [Eq. (2.25)] and Kadanoff's ansatz [Eq. (2.32)], and profound insight into the concept of universality. This is not the place and time for a careful introduction to RG theory, so I will only mention a few of the basic ideas in this respect and recommend Refs. [7–9, 31, 32] for an introduction to the subject.

The basic idea of RG is to study how the Hamiltonian evolves under a RG transformation $\mathcal{R}$ of the system. The RG transformation is a transformation under which the lengths are scaled by a factor $l > 1$, followed by rescaling the microscopic degrees of freedom such that the transformed Hamiltonian is similar to the original one, in terms of the microscopic degrees of freedom. Under this transformation, which basically means to consider the system at a larger scale, the set of couplings $\{K\}$ in the Hamiltonian will transform,

$$\{K'\} = \mathcal{R}\{K\}, \tag{2.66}$$

and by repeating this step, the couplings will constantly change stepwise. The procedure will constitute a *RG flow* of coupling values in coupling space. At a critical point, the system is scale-invariant which means that the Hamiltonian is self-similar under $\mathcal{R}$. I.e., the critical point corresponds to a *fixed point* in the RG flow,

$$\{K^*\} = \mathcal{R}\{K^*\}. \tag{2.67}$$

Moreover, as described in Sec. 2.2.3, the critical exponents are defined by the behavior of certain quantities for couplings in the vicinity of the critical point. As such, the critical exponents as well as other critical properties can be determined by analyzing the RG flow in the vicinity of the corresponding fixed point.

2.7 Duality

An important subject when discussing many of the important models in statistical mechanics, is *duality* [33, 34].[18] The meaning of duality is that a mathematical transformation $\mathfrak{D}$ can be performed, namely the *duality transformation*, such that the model can be expressed by another set of microscopic variables, also called the *dual model*. Even better, the new set of microscopic variables in the dual model are often directly related to the topological excitations of the original model. Generally, for the dual model, the temperature axis is inverted with respect to the original model, $\beta_{\text{dual}} \propto \beta_{\text{org}}^{-1}$. Hence,

[18] The concept of duality is also important in other fields of physics, as well, like field theory and electromagnetism.

the ordered state of the dual model corresponds to the disordered state of the original model, and the order parameter of the dual model may thus be considered as a *disorder parameter* from the point of view of the original model. Also, the dual model has the property that the original model is restored, when subject to the transformation $\mathfrak{D}$,

$$\mathfrak{D}^2 H_{\text{org}} = \mathfrak{D} H_{\text{dual}} = H_{\text{org}}. \tag{2.68}$$

Historically, in the field of statistical mechanics, the duality transformation was first applied by Kramers and Wannier in 1941 [35,36], where they showed that the 2D Ising model is *self-dual*, namely that the dual model of the 2D Ising model also is a 2D Ising model, but with an inverted temperature axis. As such, they were able to calculate the critical temperature *prior* to Onsager's exact solution in 1944 [18]. 30 years or so later, the method was generalized to other lattices and interactions, and applied to other models in the field (see Ref. [33] and references therein).

2.7.1 Duality transformation of the XY model

This derivation mostly follows Refs. [33,37]. The partition function for the zero-field XY model, as given in Eq. (2.43), is written as

$$\mathcal{Z} = \int \mathcal{D}\,\theta \exp\left[\beta \sum_{\boldsymbol{r},\mu} \cos(\Delta_\mu \theta_{\boldsymbol{r}})\right], \tag{2.69}$$

where J is absorbed, $\beta J \to \beta$, and where $\boldsymbol{r}$ (instead of i) denotes the lattice vertices living in two or three spatial dimensions. The cosine is hard to handle analytically, so it is customary to perform the following replacement,

$$\mathrm{e}^{\beta \cos x} \to \sum_{n=-\infty}^{\infty} \mathrm{e}^{-(\beta/2)(x-2\pi n)^2}, \tag{2.70}$$

where $n \in \mathbb{Z}$ is introduced to enforce the periodic behavior of the cosine. This is the so-called Villain approximation [38].[19] Now, the partition function is written as

$$\mathcal{Z} = \int \mathcal{D}\,\theta \prod_{\boldsymbol{r},\mu} \sum_{n_{\boldsymbol{r},\mu}=-\infty}^{\infty} \mathrm{e}^{-(\beta/2)(\Delta_\mu \theta_{\boldsymbol{r}} - 2\pi n_{\boldsymbol{r},\mu})^2}. \tag{2.71}$$

By introducing another auxiliary field $v \in \mathbb{R}$, the fields in the exponent can be decoupled by a Hubbard-Stratonovich transformation [40],

$$\mathrm{e}^{-\beta x^2/2} = \frac{1}{\sqrt{2\pi\beta}} \int_{-\infty}^{\infty} \mathrm{d}v\, \mathrm{e}^{-v^2/(2\beta) + \mathrm{i}vx}, \tag{2.72}$$

[19] Strictly speaking, Eq. (2.70) is not an approximation in a quantitative sense. However, it correctly represents the critical properties of the XY model [39]. Nonuniversal properties, e.g., the critical temperature, are not conserved.

such that

$$\mathcal{Z} = \int \mathcal{D}\,\theta \int \mathcal{D}\,\boldsymbol{v} \prod_{\boldsymbol{r},\mu} \sum_{n_{\boldsymbol{r},\mu}=-\infty}^{\infty} \mathrm{e}^{-v_{\boldsymbol{r},\mu}^2/(2\beta)+\mathrm{i}v_{\boldsymbol{r},\mu}(\Delta_\mu\theta_{\boldsymbol{r}}-2\pi n_{\boldsymbol{r},\mu})}\,. \tag{2.73}$$

Here, and in the following, uninteresting constant factors will be discarded from the partition function. Now, we are able to sum out the integer field n by invoking the Poisson summation formula,

$$\sum_{n=-\infty}^{\infty} \mathrm{e}^{2\pi\mathrm{i}nv} = \sum_{w=-\infty}^{\infty} \delta(v-w), \tag{2.74}$$

where $n, w \in \mathbb{Z}$ and $v \in \mathbb{R}$. The resulting $\mathcal{Z}$ reads

$$\mathcal{Z} = \int \mathcal{D}\,\theta \prod_{\boldsymbol{r},\mu} \sum_{w_{\boldsymbol{r},\mu}=-\infty}^{\infty} \mathrm{e}^{-w_{\boldsymbol{r},\mu}^2/(2\beta)+\mathrm{i}w_{\boldsymbol{r},\mu}\Delta_\mu\theta_{\boldsymbol{r}}}\,. \tag{2.75}$$

By neglecting surface terms, a partial summation yields

$$\sum_{\boldsymbol{r}} w_{\boldsymbol{r},\mu}\Delta_\mu\theta_{\boldsymbol{r}} = -\sum_{\boldsymbol{r}} \theta_{\boldsymbol{r}}\Delta_\mu w_{\boldsymbol{r},\mu}, \tag{2.76}$$

and consequently, the θ field can be integrated over by

$$\int_{-\pi}^{\pi} \mathrm{d}\theta_{\boldsymbol{r}} \exp(-\mathrm{i}\theta_{\boldsymbol{r}} \sum_{\mu} \Delta_\mu w_{\boldsymbol{r},\mu}) = 2\pi\delta_{\boldsymbol{\Delta}\cdot\boldsymbol{w}_{\boldsymbol{r}},0}, \tag{2.77}$$

where $\boldsymbol{\Delta}\cdot\boldsymbol{w}_{\boldsymbol{r}} = \sum_\mu \Delta_\mu w_{\boldsymbol{r},\mu}$. I.e., the θ integration yields the constraint $\sum_\mu \Delta_\mu w_{\boldsymbol{r},\mu} = 0$ on the w field. This constraint is automatically satisfied if we choose $w_{\boldsymbol{r},\mu} = \sum_{\nu,\lambda} \varepsilon_{\mu\nu\lambda}\Delta_\nu g_{\boldsymbol{r},\lambda}$ ($w_{\boldsymbol{r},\mu} = \sum_\nu \varepsilon_{\mu\nu}\Delta_\nu g_{\boldsymbol{r}}$ in 2D),[20] where $g \in \mathbb{Z}$ is another auxiliary gauge field and $\varepsilon_{\mu\nu\lambda}$ is the antisymmetric symbol. Note that by introducing the g field in this way, the g field will live on the *dual lattice*, namely a lattice that is translated half a lattice constant in all directions with respect to the original lattice. The partition function is written as

$$\mathcal{Z} = \sum_{\{g\}} \exp\left[-\frac{1}{2\beta}\sum_{\boldsymbol{r},\mu}\left(\sum_{\nu,\lambda}\varepsilon_{\mu\nu\lambda}\Delta_\nu g_{\boldsymbol{r},\lambda}\right)^2\right]. \tag{2.78}$$

This equation is the dual model of the 3D XY model. (For the 2D XY model, let $\sum_{\nu,\lambda}\varepsilon_{\mu\nu\lambda}\Delta_\nu g_{\boldsymbol{r},\lambda} \to \Delta_\mu g_{\boldsymbol{r}}$.)

As suggested in the beginning of this section, the variables g of the dual model are directly related to the topological defects of the XY model, and we will continue to rewrite Eq. (2.78) to show this explicitly. The vortices $m \in \mathbb{Z}$, are introduced when using the Poisson summation formula [Eq. (2.74)] to replace g by a new field $h \in \mathbb{R}$,

$$\mathcal{Z} = \int \mathcal{D}\,\boldsymbol{h} \sum_{\{m\}} \exp\left\{-\sum_{\boldsymbol{r},\mu}\left[\frac{1}{2\beta}\left(\sum_{\nu,\lambda}\varepsilon_{\mu\nu\lambda}\Delta_\nu h_{\boldsymbol{r},\lambda}\right)^2 - 2\pi\mathrm{i}m_{\boldsymbol{r},\mu}h_{\boldsymbol{r},\mu}\right]\right\}. \tag{2.79}$$

[20] I will proceed with 3D notation.

The next step is to Fourier transform the fields,

$$\mathcal{Z} = \int \mathcal{D}\boldsymbol{h} \sum_{\{m\}} \exp\Bigg[-\sum_{\boldsymbol{q},\mu} \Bigg(\frac{1}{2\beta} \sum_{\nu,\lambda,\rho,\sigma} \varepsilon_{\mu\nu\lambda}\varepsilon_{\mu\rho\sigma} Q_{\boldsymbol{q},\nu} Q_{-\boldsymbol{q},\rho} h_{\boldsymbol{q},\lambda} h_{-\boldsymbol{q},\sigma} - \pi \mathrm{i} m_{\boldsymbol{q},\mu} h_{-\boldsymbol{q},\mu} - \pi \mathrm{i} m_{-\boldsymbol{q},\mu} h_{\boldsymbol{q},\mu} \Bigg) \Bigg], \tag{2.80}$$

where $Q_{\boldsymbol{q},\mu} = 2\mathrm{i}\sin(q_\mu/2)\exp(\mathrm{i}q_\mu/2)$ is the Fourier space representation of the lattice difference operator. We are free to *choose* gauge, $\sum_\mu \Delta_\mu h_{\boldsymbol{r},\mu} = 0$, such that the first term in the exponent is written as

$$\sum_{\mu,\nu,\lambda,\rho,\sigma} \varepsilon_{\mu\nu\lambda}\varepsilon_{\mu\rho\sigma} Q_{\boldsymbol{q},\nu} Q_{-\boldsymbol{q},\rho} h_{\boldsymbol{q},\lambda} h_{-\boldsymbol{q},\sigma} = \sum_{\nu,\lambda} Q_{\boldsymbol{q},\nu} Q_{-\boldsymbol{q},\nu} h_{\boldsymbol{q},\lambda} h_{-\boldsymbol{q},\lambda}, \tag{2.81}$$

when the relation $\sum_\mu \varepsilon_{\mu\nu\lambda}\varepsilon_{\mu\rho\sigma} = \delta_{\nu\rho}\delta_{\lambda\sigma} - \delta_{\nu\sigma}\delta_{\lambda\rho}$ has been invoked. Moreover, we complete the squares, such that the partition function reads

$$\mathcal{Z} = \int \mathcal{D}\boldsymbol{h} \sum_{\{m\}} \exp\Bigg[-\sum_{\boldsymbol{q},\mu} \Bigg(\tilde{h}_{\boldsymbol{q},\mu} \frac{\sum_\nu Q_{\boldsymbol{q},\nu} Q_{-\boldsymbol{q},\nu}}{2\beta} \tilde{h}_{-\boldsymbol{q},\mu} + m_{\boldsymbol{q},\mu} \frac{2\pi^2\beta}{\sum_\nu Q_{\boldsymbol{q},\nu} Q_{-\boldsymbol{q},\nu}} m_{-\boldsymbol{q},\mu} \Bigg) \Bigg], \tag{2.82}$$

where

$$\tilde{h}_{\boldsymbol{q},\mu} = h_{\boldsymbol{q},\mu} - 2\pi\mathrm{i} \frac{\beta}{\sum_\nu Q_{\boldsymbol{q},\nu} Q_{-\boldsymbol{q},\nu}} m_{\boldsymbol{q},\mu}, \tag{2.83}$$

is the shifted h field. The integration over the h field is Gaussian and the model finally reads

$$\mathcal{Z} = \sum_{\{m\}} \exp\left(-2\pi^2\beta \sum_{\boldsymbol{q},\mu} m_{\boldsymbol{q},\mu} V_{\boldsymbol{q}} m_{-\boldsymbol{q},\mu} \right), \tag{2.84}$$

where

$$V_{\boldsymbol{q}} = \frac{1}{\sum_\nu Q_{\boldsymbol{q},\nu} Q_{-\boldsymbol{q},\nu}}. \tag{2.85}$$

In 2D, the derivation from Eq. (2.78) and onwards, is similar to 3D but with only one μ component for the g, h and m fields. Hence, the final model is similar as for 3D, but with $m_{\boldsymbol{q},\mu} \to m_{\boldsymbol{q}}$ and no μ sum. Also, remember that the number of terms for the ν sum is d dependent,

$$\sum_\nu Q_{\boldsymbol{q},\nu} Q_{-\boldsymbol{q},\nu} = 4 \sum_{\nu=1}^{d} \sin^2\left(\frac{q_v}{2}\right). \tag{2.86}$$

Transforming back to real space, the partition function in Eq. (2.84) reads

$$\mathcal{Z} = \sum_{\{m\}} \exp\left(-2\pi^2\beta \sum_{\boldsymbol{r},\boldsymbol{r}'\neq\boldsymbol{r},\mu} m_{\boldsymbol{r},\mu} V'_{\boldsymbol{r}-\boldsymbol{r}'} m_{\boldsymbol{r}',\mu} \right), \tag{2.87}$$

where

$$V'_{\boldsymbol{r}-\boldsymbol{r}'} = V_{\boldsymbol{r}-\boldsymbol{r}'} - V_{\boldsymbol{0}} = \frac{1}{N}\sum_{\boldsymbol{q}} \frac{\mathrm{e}^{-\mathrm{i}\boldsymbol{q}(\boldsymbol{r}-\boldsymbol{r}')}-1}{4\sum_{\nu=1}^{d}\sin^2(q_v/2)}. \tag{2.88}$$

Here, the infrared divergence in the sum of Eq. (2.84) has been regularized by subtracting the divergent $V_{\boldsymbol{0}}$ from the potential [41, 42]. Since

$$\sum_{\boldsymbol{r},\boldsymbol{r}',\mu} m_{\boldsymbol{r},\mu} V_{\boldsymbol{r}-\boldsymbol{r}'} m_{\boldsymbol{r}',\mu} = \sum_{\boldsymbol{r},\boldsymbol{r}'\neq\boldsymbol{r},\mu} m_{\boldsymbol{r},\mu} V'_{\boldsymbol{r}-\boldsymbol{r}'} m_{\boldsymbol{r}',\mu} + V_{\boldsymbol{0}} \sum_{\mu} \left(\sum_{\boldsymbol{r}} m_{\boldsymbol{r},\mu} \right)^2, \tag{2.89}$$

this enforces the constraint $\sum_{\boldsymbol{r}} m_{\boldsymbol{r},\mu} = 0$, as configurations with $\sum_{\boldsymbol{r}} m_{\boldsymbol{r},\mu} \neq 0$ will have zero weight in the partition function.

The partition function in Eq. (2.87) describes a system of integer-valued vortex segments (vortices in 2D) interacting with the long-range potential given in Eq. (2.88). This potential is in fact a lattice Coulomb potential which decays $\sim 1/r$ in 3D and $\sim -\ln r$ in 2D. Note that the constraint $\sum_{\boldsymbol{r}} m_{\boldsymbol{r},\mu} = 0$ corresponds to closed vortex loops in 3D and to overall charge neutrality in 2D. For the 2D case, this mapping to the 2D neutral Coulomb gas played an essential role to understand the role of vortices and to derive the properties of the BKT transition [26–29].

Chapter 3

Monte Carlo simulations

Using the framework of statistical mechanics, the macroscopic properties of the models we are investigating can be found by calculating the partition function in Eq. (2.2), or, more precisely, the thermal averages in Eq. (2.3). Calculating a sum of terms does not sound too difficult, but after a moment of consideration one would soon realize that the number of constituents do not have to be very large before the number of terms will be impossible to handle. Of course, there are analytical methods that can handle series with many terms, but due to the complexity of the interactions, analytic solutions are rare and have only been obtained in a few simple cases, for instance for the 2D zero-field Ising model [18]. Also, approximation schemes such as mean-field theory or perturbation series often fail to produce accurate predictions, especially in the interesting region close to a phase transition. We thus have to rely on numerical computations. In the context of statistical mechanics and phase transitions, a very successful method, and the tool of our choice, is *Monte Carlo simulation*.

Monte Carlo[1] may loosely refer to a class of methods that utilizes repeated random sampling to calculate a mathematical or statistical problem. Such methods differ from many other numerical methods in that they are *stochastic* and not *deterministic*. This means that two or more repeated calculations will not yield the same result, but rather differ in a stochastic manner. The stochastic nature of the calculation introduces random errors in the results, but these errors can, in principle, be reduced by increasing the number of samples obtained.

This chapter is intended to outline details of the Monte Carlo method that have been used in this work. Sec. 3.1 will introduce the elementary building blocks leading up to the Metropolis-Hastings algorithm. In Section 3.2, I will discuss a few important issues that must be considered in order to produce a reliable and accurate outcome. Sec. 3.3 is mainly devoted to the parallel tempering algorithm. Sec. 3.4 discusses the reweighting technique, and the Secs. 3.5, 3.6 and 3.7 are devoted to how the output from the simulations can be used to detect critical phenomena and phase transitions. For

[1] The method is named after the famous casino in Monaco.

literature on Monte Carlo simulations in statistical mechanics, I would like to recommend Refs. [12, 43, 44].

3.1 Simulating statistical mechanics

3.1.1 Monte Carlo integration

The main task in statistical mechanics is to calculate integrals as in Eq. (2.3). When this is done by repeated random sampling, it is called *Monte Carlo integration*. The basic theorem of Monte Carlo integration is that the integral I of a function $f(\boldsymbol{x})$ over a volume V can be well approximated by [45]

$$I = \int \mathrm{d}V f(\boldsymbol{x}) \approx V\bar{f}, \tag{3.1}$$

where $\bar{f}$ is the arithmetic mean obtained by sampling $f(\boldsymbol{x})$ in M randomly chosen points $\boldsymbol{x}_i, i \in \{1, \ldots, M\}$,

$$\bar{f} = \frac{1}{M}\sum_{i=1}^{M} f(\boldsymbol{x}_i). \tag{3.2}$$

The points $\boldsymbol{x}_i$ must be chosen from a uniform probability distribution within V. Given that these points are statistically independent, the one standard deviation error estimate is

$$\sigma_I = V\sqrt{\frac{\sum_{i=1}^{M}\left[f(\boldsymbol{x}_i) - \bar{f}\right]^2}{M(M-1)}}. \tag{3.3}$$

So, why should we bother to choose the points $\boldsymbol{x}_i$ randomly instead of choosing $\boldsymbol{x}_i$ in a regular manner? The main reason for this is the *curse of dimensionality*. It can be shown that the standard methods for numerical evaluation of integrals in a deterministic fashion, produces systematic errors that typically scale $\sim M^{-s/d}$, where M is the number of evaluations of $f(\boldsymbol{x})$, d is the number of dimensions to integrate over, and s is a number ~ 1 that depends on the specific method at hand [44, 46]. In any case, it should be clear that d does not have to be very large before the Monte Carlo error scaling $\sim M^{-1/2}$ in Eq. (3.3) clearly outperforms deterministic methods. Indeed, this would be the case for the models of statistical mechanics where the number of degrees of freedom (i.e., d) is very large.

3.1.2 Importance sampling

In many cases, the integrand $f(\boldsymbol{x})$ may vary significantly within the volume that we would like to integrate over. Clearly, one should expect the total estimate of I to improve if the space where $f(\boldsymbol{x})$ is large is allowed to be sampled more frequently compared with the space where $f(\boldsymbol{x})$ is small. This is the idea of *importance sampling*. A simple example

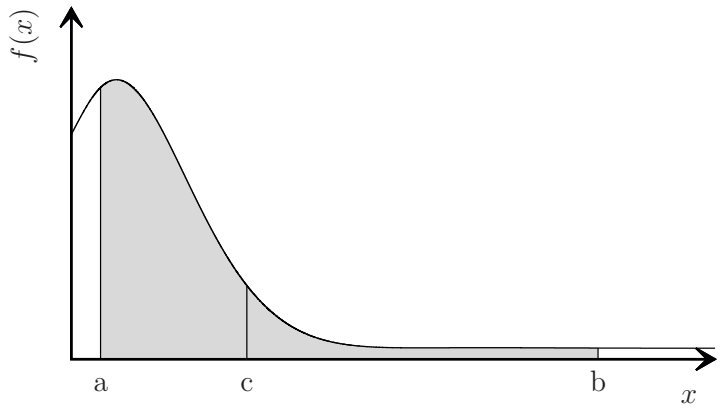

Figure 3.1: Simple utilization of importance sampling for a one dimensional integral $I = \int_a^b \mathrm{d}x f(x)$. By dividing the total interval $[a, b)$ into subintervals $[a, c)$ and $[c, b)$, one can improve the total estimate of I by sampling the interval $[a, c)$ where $f(x)$ is large more frequently than the interval $[c, b)$ where $f(x)$ is small.

is given in Fig. 3.1. In this case, the total estimate of I can be improved by dividing the total interval $[a, b)$ into two subintervals, $I = \int_a^b \mathrm{d}x f(x) = \int_a^c \mathrm{d}x f(x) + \int_c^b \mathrm{d}x f(x)$. The corresponding Monte Carlo estimate is

$$I \approx \frac{c-a}{M_1} \sum_{i=1}^{M_1} f(x_i) + \frac{b-c}{M_2} \sum_{i=1}^{M_2} f(y_i), \tag{3.4}$$

where samples $x_i, i \in \{1, \ldots, M_1\}$ are taken from the interval $[a, b)$ and samples $y_i, i \in \{1, \ldots, M_2\}$ are taken from the interval $[c, b)$. By selecting M_1 and M_2 such that $M_1/(c-a) > M_2/(b-c)$, the estimate for I will improve, since the part where $f(x)$ is large, is sampled more frequently.

More formally, the integral I may be rewritten

$$I = \int \mathrm{d}V f(\boldsymbol{x}) = \int \mathrm{d}p(\boldsymbol{x}) \frac{f(\boldsymbol{x})}{p(\boldsymbol{x})}, \tag{3.5}$$

where $\mathrm{d}p(\boldsymbol{x}) = p(\boldsymbol{x})\mathrm{d}V$. If we choose the points $\boldsymbol{x}_i$ according to the probability distribution $p(\boldsymbol{x})$, the Monte Carlo estimate for I is given by

$$I \approx \frac{V}{M} \sum_{i=1}^{M} \frac{f(\boldsymbol{x}_i)}{p(\boldsymbol{x}_i)}, \tag{3.6}$$

and the error estimate is found by substituting $f(\boldsymbol{x}_i) \to f(\boldsymbol{x}_i)/p(\boldsymbol{x}_i)$ in Eq. (3.3). By a proper choice of $p(\boldsymbol{x}_i)$, this error estimate can be significantly smaller than the original error estimate.

In statistical mechanics, we are interested in calculating the expectation values given by Eq. (2.3). If the states Ψ_i are selected randomly from a uniform probability distribution,

the Monte Carlo estimate of $\langle O \rangle$ is

$$\langle O \rangle \approx \frac{\sum_{i=1}^{M} O[\Psi_i] \, \mathrm{e}^{-\beta H[\Psi_i]}}{\sum_{i=1}^{M} \mathrm{e}^{-\beta H[\Psi_i]}}. \tag{3.7}$$

However, in the spirit of importance sampling, a much better choice would be to randomly select Ψ_i according to the canonical probability distribution [Eq. (2.1)]. Then, the most probable states will be sampled more frequently, and the Monte Carlo estimate for $\langle O \rangle$ will take the convenient form

$$\langle O \rangle \approx \frac{1}{M} \sum_{i=1}^{M} O[\Psi_i]. \tag{3.8}$$

3.1.3 Markov chains

What strategy should we use to find the states Ψ_i? We could try to generate states from scratch by assigning values to all the degrees of freedom in a random fashion. However, when the number of degrees of freedom is very large, it is practically impossible to generate states from scratch, according to a nontrivial probability distribution. The solution to this problem is to generate a *Markov chain*. This is a stochastic sequence of states obtained by letting the microscopic degrees of freedom evolve dynamically according to a prescribed set of rules. Such a sequence can be written

$$X_1 \to X_2 \to \cdots \to X_{t-1} \to X_t \to X_{t+1} \to \cdots \to X_{T-1} \to X_T, \tag{3.9}$$

where X_t is the state at time step t and T is the total number of steps in the sequence. To avoid confusion, it is important to clarify that in this context, the time t, which usually is called Monte Carlo time, bears no physical meaning. It is merely a convenient way to describe the dynamics of the stochastic sequence. In order for this stochastic sequence to be a proper Markov chain, it must obey the *Markov property*, namely that the transition probability of moving from state Ψ_i at t to state Ψ_j at $t+1$, $\mathcal{P}(X_t = \Psi_i \to X_{t+1} = \Psi_j)$, is independent of the history leading to state Ψ_i at t,

$$\mathcal{P}(X_t = \Psi_i \to X_{t+1} = \Psi_j) = \mathcal{P}(X_{t+1} = \Psi_j | X_t = \Psi_i). \tag{3.10}$$

Furthermore, it is convenient to choose the transition probabilities to be time independent, i.e.,

$$\mathcal{P}(X_t = \Psi_i \to X_{t+1} = \Psi_j) = \mathcal{P}(X_{t+n} = \Psi_i \to X_{t+n+1} = \Psi_j) = \mathcal{P}(\Psi_i \to \Psi_j), \tag{3.11}$$

where $n \in \mathbb{Z}$. Also, the sequence must naturally obey the *sum rule* which is a mathematical way of saying that the sequence must go somewhere,

$$\sum_j \mathcal{P}(\Psi_i \to \Psi_j) = 1. \tag{3.12}$$

Based on these three simple criteria, the probability of being in state Ψ_i at time $t+1$, $p(X_{t+1} = \Psi_i)$, clearly must be given by the so-called master equation,

$$\begin{aligned} p(X_{t+1} = \Psi_i) &= \sum_j p(X_t = \Psi_j)\mathcal{P}(\Psi_j \to \Psi_i) \\ &= p(X_t = \Psi_i)\left[1 - \sum_{j\neq i} \mathcal{P}(\Psi_i \to \Psi_j)\right] + \sum_{j\neq i} p(X_t = \Psi_j)\mathcal{P}(\Psi_j \to \Psi_i). \end{aligned} \tag{3.13}$$

Now, for the Markov chain to be useful for our purposes, we would like to evolve the Markov chain into some state of equilibrium where the sequence traverses phase space according to the requested probability distribution, $p(X_t = \Psi_i) = p(X_{t+n} = \Psi_i) = p(\Psi_i)$ for all $n \in \mathbb{Z}$. Inserting this in Eq. (3.13) yields the *balance condition*,

$$\sum_i p(\Psi_i)\mathcal{P}(\Psi_i \to \Psi_j) = \sum_i \mathcal{P}(\Psi_j \to \Psi_i)p(\Psi_j) = p(\Psi_j). \tag{3.14}$$

In other words, the balance condition ensures that if the stochastic process reaches the state of equilibrium, it will stay there. The Markov chain must also obey the *ergodicity condition*, namely that it must be possible for the system to go from a state Ψ_i into any other state Ψ_j within a finite number of time steps.[2]

It is possible to show that the stochastic process will evolve into the state of equilibrium as a consequence of the conditions given above. The deviation from the equilibrium probability distribution at time t can be calculated by

$$D_t = \sum_i \left| p(X_t = \Psi_i) - p(\Psi_i) \right|. \tag{3.15}$$

By invoking Eqs. (3.13) and (3.14), this deviation at time $t+1$ is given by

$$\begin{aligned} D_{t+1} &= \sum_i \left| \sum_j p(X_t = \Psi_j)\mathcal{P}(\Psi_j \to \Psi_i) - p(\Psi_i) \right| \\ &= \sum_i \left| \sum_j \left[p(X_t = \Psi_j) - p(\Psi_j) \right] \mathcal{P}(\Psi_j \to \Psi_i) \right|. \end{aligned} \tag{3.16}$$

Clearly, the absolute value of a sum must be smaller than or equal to summing the absolute value of each term, and since the probability $\mathcal{P}(\Psi_j \to \Psi_i) \geq 0$, we find that

$$D_{t+1} \leq \sum_{i,j} \left| p(X_t = \Psi_j) - p(\Psi_j) \right| \mathcal{P}(\Psi_j \to \Psi_i) = D_t, \tag{3.17}$$

where Eq. (3.12) has been used. This means that after some initial time, the random walk of the Markov chain in phase space will visit states according to the requested probability distribution.

[2] This must be considered when the trial moves, taking the Markov chain from one state to the next, are determined. In some cases (e.g., Article II and III [2, 3]), nonergodic trial moves may speed up calculations. Such moves must be mixed with ergodic trial moves to make sure that the full Markov chain obeys the ergodicity condition [47, 48].

3.1.4 The Metropolis-Hastings algorithm

The celebrated *Metropolis-Hastings algorithm* is simply a convenient choice of the transition probability $\mathcal{P}(\Psi_i \to \Psi_j)$ that obeys the conditions given above [49, 50]. It turns out that it is convenient to construct transition probabilities that obey *detailed balance*,

$$p(\Psi_j)\mathcal{P}(\Psi_j \to \Psi_i) = p(\Psi_i)\mathcal{P}(\Psi_i \to \Psi_j). \tag{3.18}$$

This condition ensures that the balance condition [Eq. (3.14)] is met termwise.[3] The transition probability is given by $\mathcal{P}(\Psi_i \to \Psi_j) = \mathcal{P}_{\text{sel}}(\Psi_i \to \Psi_j)\mathcal{P}_{\text{acc}}(\Psi_i \to \Psi_j)$, where $\mathcal{P}_{\text{sel}}(\Psi_i \to \Psi_j)$ is the probability of proposing the update to Ψ_j, given state Ψ_i, and where $\mathcal{P}_{\text{acc}}(\Psi_i \to \Psi_j)$ is the probability of accepting that update. Here, the selection probability is chosen such that $\mathcal{P}_{\text{sel}}(\Psi_i \to \Psi_j) = \mathcal{P}_{\text{sel}}(\Psi_j \to \Psi_i)$. Moreover, the acceptance probability for the Metropolis-Hastings algorithm is chosen to be

$$\mathcal{P}_{\text{acc}}(\Psi_i \to \Psi_j) = \min\left\{1, \frac{p(\Psi_j)}{p(\Psi_i)}\right\}, \tag{3.19}$$

where

$$\frac{p(\Psi_j)}{p(\Psi_i)} = \mathrm{e}^{-\beta(H[\Psi_j]-H[\Psi_i])}, \tag{3.20}$$

in the case of the canonical probability distribution. By inspection, the choice in Eq. (3.19) satisfies Eq. (3.18). The Metropolis algorithm can be described as follows:

1. Generate an initial state Ψ_i.
2. Propose a new state Ψ_j.
3. Calculate $w = p(\Psi_j)/p(\Psi_i) = \mathrm{e}^{-\beta(H[\Psi_j]-H[\Psi_i])}$.
4. Generate a uniform random number $r \in [0, 1]$.
5. If $r \leq w$, assign Ψ_i to be the new state, $\Psi_i = \Psi_j$. Else, keep the old state, $\Psi_i = \Psi_i$.
6. Perform measurements on Ψ_i.
7. Repeat 1. $\to$ 6. until results have converged.

Step 2. involves a move that generates the new trial state. For the Metropolis-Hastings algorithm, this is typically a *local update* that only involves a local transformation on a single degree of freedom in the existing state. In the case of the Ising model, this would be to flip a single spin, $s_{\boldsymbol{r}} \to -s_{\boldsymbol{r}}$. For the XY model, one would typically rotate a single spin to a random new direction, $\theta_{\boldsymbol{r}} \to \theta_{\boldsymbol{r},\text{new}}$, where $\theta_{\boldsymbol{r},\text{new}} \in (-\pi, \pi]$. A *Monte Carlo sweep* is then to sequentially (or randomly) traverse the system, proposing one

[3] Note that detailed balance puts stricter conditions on the transition probabilities than required by the balance condition. Hence, it is possible to construct algorithms that obey the balance condition without detailed balance [51, 52].

local update for all (or a number of) degrees of freedom in the system.[4] Usually, the measurements are performed after an integer number of Monte Carlo sweeps. Hence, in the scheme given above, it is common to repeat steps 1. $\rightarrow$ 5. a number of times before proceeding to step 6.

3.2 Issues

3.2.1 Pseudorandom number generators

Random numbers play an essential role in Monte Carlo simulations. For the Metropolis-Hastings algorithm detailed above, random numbers are used to determine if the proposed state should be accepted (step 4. and 5.), and they are also often used in the process of selecting the proposal (step 2.). In this context, the random numbers are not *truly* random. They are generated by mathematical sequences and are completely deterministic and reproducible. However, they may be used for our purposes because the sequences produce numbers that are uncorrelated and with a distribution similar to what one should expect for a sequence of true random numbers. In addition, since they are deterministic, they are reproducible, given the same set of input, called *seed*. The algorithm for constructing such a sequence is called a *pseudorandom number generator* (PRNG).

Different PRNGs may differ in terms of how well and how long they reproduce the properties of true random numbers. Over the years, there are examples of established PRNGs that turned out to misbehave when carefully tested [53, 54]. In this work, we have used the Mersenne Twister algorithm [55], which is considered to be a state-of-the-art PRNG for Monte Carlo simulations. In parallel applications, the PRNG on each CPU is seeded separately.

3.2.2 Boundary conditions

Due to inevitable limitations in computer resources, Monte Carlo simulations are always restricted to be performed on finite systems. Hence, there is a $(d-1)$-dimensional boundary that must be accounted for. *Boundary conditions* (BCs) should be thought of as restraints that applies to the degrees of freedom that are located on the boundary. Since the relative importance of the boundary decreases when system size increases, one should expect bulk properties calculated using different BCs to converge in the thermodynamic limit. However, for finite systems, it is clear that the numerical results can depend on the BCs, and in some cases, certain BCs can be more appropriate than

[4] Strictly speaking, a sequential updating scheme does *not* satisfy detailed balance. This can be understood by noticing that the selection probabilities $\mathcal{P}_{\text{sel}}(\Psi_i \rightarrow \Psi_j)$ will vary within the sequence, such that $\mathcal{P}_{\text{sel}}(\Psi_i \rightarrow \Psi_j) \neq \mathcal{P}_{\text{sel}}(\Psi_j \rightarrow \Psi_i)$. However, the balance condition will be satisfied every sweep. See Refs. [51, 52].

others [12]. Here, I will mention the BCs that applies to this work, namely *periodic boundary conditions* (PBCs) and *spherical boundary conditions*.

Periodic boundary conditions

PBCs can most simply be thought of as wrapping the edges around such that the edge with normal in the positive μ-direction will be in contact with the edge in the negative μ-direction. In this way, particles along this edge will be neighbors to the particles along the opposite edge. For example, in the 2D XY model with vertices $\boldsymbol{r} = (x, y)$ where coordinates $x, y \in \{1, \ldots, L\}$, the boundary conditions can be expressed $\theta_{(L+1,y)} = \theta_{(1,y)}$, $\theta_{(0,y)} = \theta_{(L,y)}$, $\theta_{(x,L+1)} = \theta_{(x,1)}$ and $\theta_{(x,0)} = \theta_{(x,L)}$. Hence, a system with PBCs in d dimensions is topologically equivalent to a $(d+1)$-dimensional torus. PBCs are useful in order to simulate bulk properties, since all particles are surrounded as for bulk particles, and this will effectively eliminate spurious boundary effects. PBCs are, by far, the most commonly used BCs for Monte Carlo simulations in statistical mechanics. However, there are issues with PBCs. A system with PBCs is not rotationally symmetric. Also, treating long-range interactions imposes additional complications [12, 56–58]. PBCs are used in Articles I and IV [1, 4].

Spherical boundary conditions

In Articles II and III [2,3], the Monte Carlo simulations are performed with particles that live on a 2D surface and that in principle are not constrained to live on the vertices of a lattice.[5] In addition, the particles interact with logarithmically decaying long-ranged interactions. For such systems, a viable alternative is spherical boundary conditions (SBCs), namely to let the particles live on the surface of a sphere [12, 14, 63–66]. Similar to PBCs, this is a clever way of avoiding boundary effects, but contrary to PBCs, this is done without introducing the complications that are associated with long-range interactions in systems with PBCs. Also, rotational symmetry is conserved.

There are also a few issues with SBCs. Although the SBCs are rather simple to implement, the computational cost for long-range interactions scales as $\sim N^2$, where N is the number of particles. Secondly, the curvature of the spherical surface will introduce lattice defects. Specifically, in the case of finding the ground state of Coulomb charges on the spherical surface (Thompson's problem), there must be at least 12 disclination defects in the triangular lattice, due to Euler's theorem. In addition, numerical works suggest that there are additional defects, in terms of dislocations and disclinations [66,67]. Compared with a plane where the ground state would be a triangular Wigner crystal with no defects [68], the defects on the spherical surface will hamper calculations of translational and orientational order in phases where such should be expected.

[5] Of course, such particles can be constrained to live on a lattice, but this can introduce numerical artifacts, e.g., pinning [59–62].

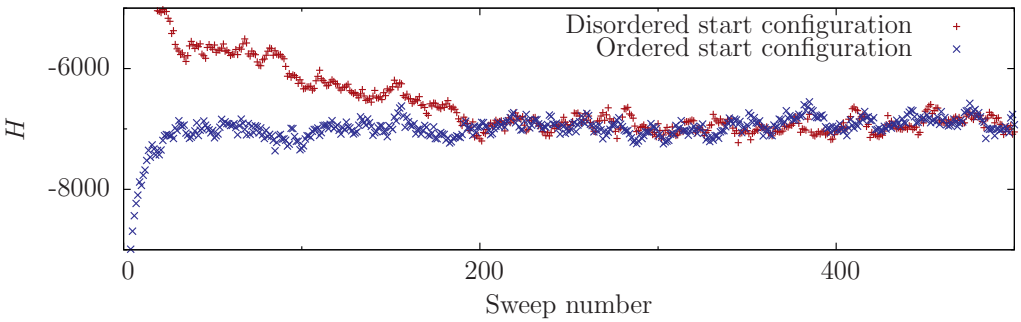

Figure 3.2: Time series of the energy H for the 500 initial Monte Carlo sweeps of a zero-field 3D XY model at $\beta J = 0.55$ with $L = 16$. Results are presented for both ordered and disorder start configurations in order to compare equilibration.

3.2.3 Equilibration

Initially, one must choose a start configuration that will constitute the initial step in the Markov chain. Typically, this is a state where all degrees of freedom are set to a random value, or oppositely, a state that is completely ordered. As outlined in Sec. 3.1.3, the Markov chain must then perform a number of steps before the sequence converges to the equilibrium probability distribution. This part of the simulation is called *equilibration* or *thermalization*, and it is important to ensure that the system is equilibrated before computing thermal averages.[6] This can be done by observing how all the quantities evolve with Monte Carlo time, ensuring that all observables have converged to fluctuating around a constant mean value. In Fig. 3.2, a plot of the initial measurements of a quantity under equilibration is given. As suggested in the figure, in cases when it may be difficult to determine when the system is well equilibrated, comparing the convergence of both disordered (hot) and ordered (cold) starts is useful. Other approaches may be to compute temporal averages over a limited number of samples to look for convergence, or to calculate averages over larger parts of the time series, systematically removing the initial samples until total average converges. Typically, the time it takes to equilibrate the system increases with system size and near phase transitions.

3.2.4 Error estimates

Unfortunately, generating samples by the means of a Markov chain has a major drawback. Consecutive measurements in Monte Carlo time tend to be highly correlated. Although the random walk in the configuration space obeys the Markov property, that walk projected down on the space of a given observable will generally not obey the Markov property and may thus have a memory that goes far beyond the previous step. For Monte Carlo estimates as given in Eq. (3.8), the proper error estimate that takes

[6] Actually, under certain conditions, this early dynamic evolution of the system towards equilibrium, can be used to investigate critical phenomena and phase transitions. This is called *short-time critical dynamics* [69, 70].

correlations into account is given by

$$\sigma_{\langle O\rangle} = \sqrt{\frac{1+2\tau_{\text{auto}}}{M(M-1)}\sum_{i=1}^{M}\left(O[\Psi_i]-\langle O\rangle\right)^2}, \tag{3.21}$$

where τ_{auto} is the autocorrelation time measured in units of Monte Carlo time between consecutive measurements. The autocorrelation time can be found by considering the normalized autocorrelation function,

$$\phi_t = \frac{1}{\langle O^2\rangle - \langle O\rangle^2}\left(\frac{1}{M-t}\sum_{i=1}^{M-t} O_i O_{i+t} - \langle O\rangle^2\right), \tag{3.22}$$

where $O_i = O[\Psi_i]$, given that the samples are ordered in Monte Carlo time. For large t, an exponential decay with τ_{auto} as the characteristic time scale is expected for ϕ_t,

$$\phi_t \sim \mathrm{e}^{-t/\tau_{\text{auto}}}. \tag{3.23}$$

Hence, an estimate of τ_{auto} can be found by summing over ϕ_t,

$$\tau_{\text{auto}} \approx \sum_t \phi_t. \tag{3.24}$$

Jackknife error estimates

A very practical way to estimate errors is given by the *Jackknife method* [71,72]. Consider a dataset of M time-ordered measurements, and divide it into K bins such that there are M/K samples in every bin. I.e., $O_i, i \in \{1,\ldots,M\} \to O_{b,j}, b \in \{1,\ldots,K\}, j \in \{1,\ldots,M/K\}$. The number of bins should not be too large. This is to make sure that the number of samples in every bin is much larger than τ_{auto}, such that the bins can be treated as statistically independent of each other. From these bins, the Jackknife variables $\mathfrak{O}_b, b \in \{1,\ldots,K\}$ are calculated by

$$\mathfrak{O}_b = \frac{K}{M(K-1)}\sum_{\substack{b'=1\\ b'\neq b}}^{K}\sum_{j=1}^{M/K} O_{b',j}. \tag{3.25}$$

Note that $\mathfrak{O}_b$ is *not* the average over all samples in bin b. Rather, it is the average over all samples *except* those in bin b. This is illustrated in Fig. 3.3. The Jackknife variables can be used to estimate the average and error of function $f(\langle O\rangle)$. The Jackknife estimator for the average is given by

$$f(\langle O\rangle) \approx \frac{1}{K}\sum_{b=1}^{K} f\left(\mathfrak{O}_b\right), \tag{3.26}$$

and the Jackknife estimator for the error is given by

$$\sigma_{f(\langle O\rangle)} \approx \sqrt{\frac{K-1}{K}\sum_{b=1}^{K}\left(f\left(\mathfrak{O}_b\right) - \frac{1}{K}\sum_{b'=1}^{K} f\left(\mathfrak{O}_{b'}\right)\right)^2}. \tag{3.27}$$

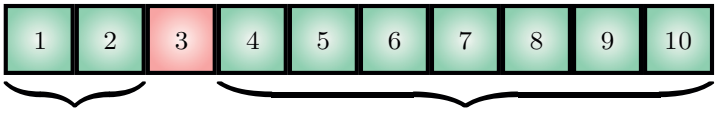

Figure 3.3: Example of the Jackknife method. The timeseries has been divided into $K = 10$ bins that are considered to be statistically independent. The Jackknife variable $\mathfrak{O}_3$ is calculated as the average over all bins except for bin number 3.

A major advantage by using the Jackknife method is that it can be used to estimate averages and errors in cases where $f(\langle O \rangle)$ may be a brutally nonlinear function, or in cases with multiple, possibly correlated, observables, $f = f(\langle O_1 \rangle, \langle O_2 \rangle, \dots)$.

3.2.5 Critical slowing down

Close to the critical point, the autocorrelation time can be very large. Specifically,

$$\tau_{\text{auto}} \sim \xi^z \sim |\tau|^{-\nu z}, \tag{3.28}$$

where z is the dynamic critical exponent. The autocorrelation time will therefore diverge in the critical limit, when $\tau \to 0$. This is called *critical slowing down* and it poses a major challenge that must be dealt with, in order to obtain reliable results near the critical point of continuous phase transitions. In certain spin models, *cluster algorithms* which make use of global updates in an efficient way, are capable of dealing with this problem [73, 74].

3.2.6 Exponential tunneling time

First-order transitions are characterized by coexisting phases that are separated by a region with a higher free energy (see Fig. 2.2). At the phase transition, it can be shown that this barrier will lead to an exponentially increased tunneling and autocorrelation time [75],

$$\tau_{\text{auto}} \sim \mathrm{e}^{L^{d-1}}, \tag{3.29}$$

as a function of linear system size L given that the samples are obtained by local updates according to the canonical probability distribution. In such cases, the system size does not have to be very large before true equilibrium sampling is very difficult. This problem can be alleviated by certain extended ensemble methods (see Sec. 3.3).

3.3 Generalized ensemble simulations

From a naive point of view, the canonical probability distribution may be seen as the ultimate choice of distribution to obtain configurations from, as it guarantees that all states that are sampled have equal weights and thus contribute on an equal footing

when thermodynamic averages are calculated [see Eq. (3.8)]. However, since subsequent samples are correlated, this may be a too simple-minded attitude. If the autocorrelation time is large, every new sample will essentially be a copy of the previous sample and only limited new information is gained per update. Hence, numerous steps are needed in order to obtain a good estimate of thermodynamic averages by Eq. (3.8). This is typically the case when states with a high probability, according to the canonical probability distribution, have very different configurations such that numerous local updates are needed to obtain an accurate sampling of the actual states in phase space. For instance, this is the problem in the case of scale-invariant fluctuations, i.e., critical slowing down. We may also have the case when the high-probability states are separated by energy barriers in phase space, as illustrated in Fig. 3.4. In this case, the random walk from a region of high-probability states to the next, is highly unlikely as it involves local updates with a very small probability to be accepted. This is the case for first-order transitions and for systems with rough energy landscapes.

In certain cases these problems can be dealt with by cluster algorithms [73, 74]. Shortly speaking, cluster algorithms can be viewed as an efficient way of proposing nonlocal updates that effectively allow the Markov chain to traverse phase space in a rapid manner. However, there are a lot of models where efficient implementations of cluster algorithms are missing. Also, there may be technical issues that may be in disfavor for the cluster algorithms.

Another option is the *generalized ensemble methods*. These methods allow for a rapid movement in phase space by accessing states that are highly improbable according to the canonical probability distribution. This is done either by going to different couplings or by sampling states from a different probability distribution. In Fig. 3.4, a schematic figure is given, that in a qualitative manner illustrates the random walks generated by the ordinary Metropolis-Hastings algorithm, the cluster algorithms and the generalized ensemble methods. Among the generalized ensemble methods are the multicanonical algorithm [75, 76], simulated tempering [77, 78], parallel tempering [79–81], the Wang-Landau algorithm [82, 83] and the optimized ensemble technique [84]. Here, we will pay particular attention to the parallel tempering algorithm since that algorithm is extensively used in this work.[7]

3.3.1 Parallel tempering

The basic idea of the parallel tempering algorithm[8] [79–81] is to simulate multiple replicas of the same system simultaneously at equally many values of the coupling. The replicas are allowed to perform a random walk in coupling space by occasionally proposing updates where replicas at different couplings are allowed to exchange.[9] Consequently,

[7] It should be mentioned that for Article IV [4], the Wang-Landau algorithm was implemented and carefully tested. However, the results in that paper were obtained with the parallel tempering algorithm, as it was found to outperform Wang-Landau for large calculations running on many CPUs.

[8] Also called the replica-exchange method.

[9] Typically, one performs an integer number of Monte Carlo sweeps with the ordinary Metropolis-Hastings algorithm before a parallel tempering move is proposed.

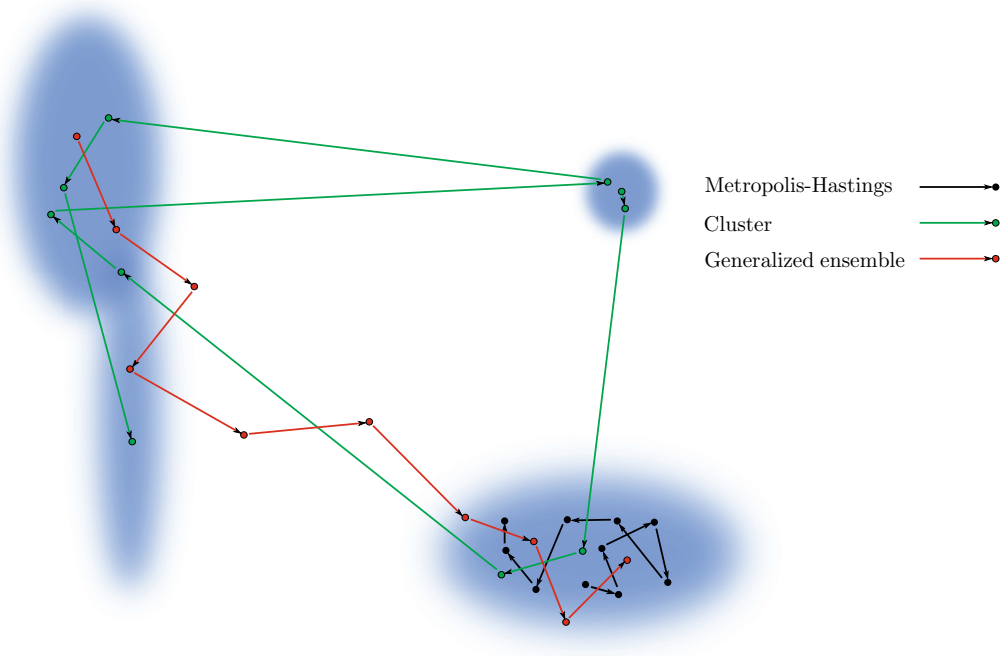

Figure 3.4: Schematic figure of random walks in phase space performed by a Metropolis-Hastings algorithm with local updates, a cluster algorithm and a generalized ensemble method. Blue-shaded regions correspond to regions with high-probability states according to the canonical probability distribution. The random walk of the Metropolis-Hastings algorithm is easily trapped within a single region. The random walk of the cluster algorithms may jump between regions by nonlocal updates. The random walk of the generalized ensemble methods can traverse barriers in phase space by accessing states that are improbable from the point of view of the canonical probability distribution.

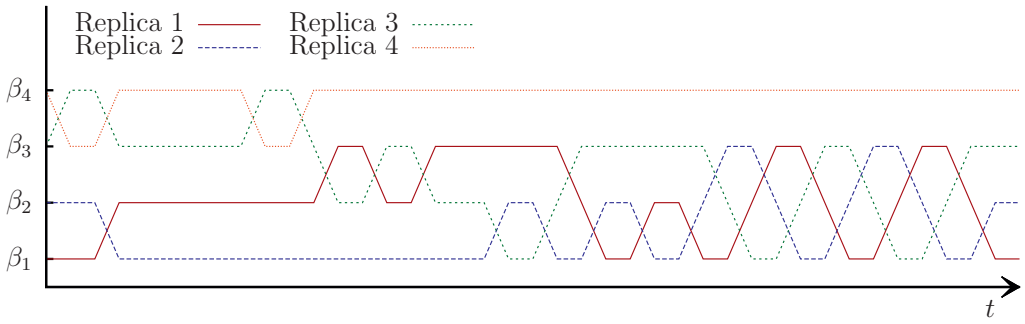

Figure 3.5: Plot of the random walk of replicas for couplings $\beta_i, i \in 1, 2, 3, 4$ as a function of Monte Carlo time t for a Monte Carlo simulation with the parallel tempering algorithm.

they will occasionally visit higher temperatures where disordered states are more easily accessible. This will improve the mobility in phase space such that a representative selection of states can be obtained, also at lower temperatures. An example of the random walk of replicas in coupling space, is given in Fig. 3.5. Typical applications for this algorithm are systems that have rough energy landscapes.

Consider a system with an extended ensemble of C replicas Ψ_m of the same system associated with C different couplings β_m. The probability distribution for this extended ensemble is given by

$$p\left(\Psi_1, \beta_1; \ldots; \Psi_m, \beta_m; \ldots; \Psi_C, \beta_C\right) = \prod_{m=1}^{C} p\left(\Psi_m, \beta_m\right), \tag{3.30}$$

where $p\left(\Psi_m, \beta_m\right)$ is the probability distribution for state Ψ_m at coupling β_m. We now define $\mathcal{P}(\Psi_a, \beta_a; \Psi_b, \beta_b)$ as the transition probability of exchanging the configuration at β_a with the configuration at β_b. The detailed balance condition reads

$$\begin{aligned} &p\left(\ldots; \Psi_a, \beta_a; \ldots; \Psi_b, \beta_b; \ldots\right) \mathcal{P}(\Psi_a, \beta_a; \Psi_b, \beta_b) \\ &= p\left(\ldots; \Psi_b, \beta_a; \ldots; \Psi_a, \beta_b; \ldots\right) \mathcal{P}(\Psi_b, \beta_a; \Psi_a, \beta_b). \end{aligned} \tag{3.31}$$

We can choose selection probabilities such that $\mathcal{P}_{\text{sel}}(\Psi_a, \beta_a; \Psi_b, \beta_b) = \mathcal{P}_{\text{sel}}(\Psi_b, \beta_a; \Psi_a, \beta_b)$. Then, inserting Eq. (3.30) in Eq. (3.31) yields

$$\frac{\mathcal{P}_{\text{acc}}(\Psi_a, \beta_a; \Psi_b, \beta_b)}{\mathcal{P}_{\text{acc}}(\Psi_b, \beta_a; \Psi_a, \beta_b)} = \frac{p\left(\Psi_b, \beta_a\right) p\left(\Psi_a, \beta_b\right)}{p\left(\Psi_a, \beta_a\right) p\left(\Psi_b, \beta_b\right)} = \mathrm{e}^{\Delta}, \tag{3.32}$$

where

$$\Delta = \beta_a \left(H[\beta_a; \Psi_a] - H[\beta_a; \Psi_b]\right) - \beta_b \left(H[\beta_b; \Psi_a] - H[\beta_b; \Psi_b]\right). \tag{3.33}$$

We have assumed the canonical probability distribution in the rightmost equality of Eq. (3.32) and we allow for an explicit coupling dependence in the Hamiltonian, as in Article I [1]. With no explicit coupling dependence, $\Delta = (\beta_a - \beta_b)(H[\Psi_a] - H[\Psi_b])$. The acceptance probability for the parallel tempering move is chosen to be

$$\mathcal{P}_{\text{acc}}(\Psi_a, \beta_a; \Psi_b, \beta_b) = \min\left\{1, \frac{p\left(\Psi_b, \beta_a\right) p\left(\Psi_a, \beta_b\right)}{p\left(\Psi_a, \beta_a\right) p\left(\Psi_b, \beta_b\right)}\right\} = \min\left\{1, \mathrm{e}^{\Delta}\right\}. \tag{3.34}$$

Optimal choice of couplings

It turns out that the performance of the parallel tempering algorithm is sensitive to the distribution of couplings and the number of replicas in the simulation. First of all, in order to enjoy the benefits of parallel tempering, one must ensure that the lowest coupling value β_1 is properly within the disordered phase such that the random walk can traverse energy barriers in phase space. The acceptance rate for the parallel tempering update is essentially given by the amount of overlap in the distribution of visited energies (energy histograms). Hence, the distance between couplings should not be too large. On the other hand, the couplings should not be too closely spaced either, because that means a lot more moves must be performed in order to traverse the coupling range.

In this work, I have used two different schemes for determining the couplings, given that the two ends of the coupling range are set. In Ref. [85], Hukushima presents an iterative procedure to determine the couplings that is based on the criterion that acceptance rates for the parallel tempering move to the nearest neighbor coupling should be equal for all couplings. This iterative procedure requires knowledge of the internal energy $U(\beta)$, and thus, an initial and short Monte Carlo simulation must be performed to obtain $U(\beta)$ approximately. The other scheme, presented in Ref. [86], is based on an assumption that the optimal distribution of couplings is obtained by minimizing the round-trip times that the replicas use to traverse the range of couplings. For this approach, initial simulations are performed to measure the diffusion of replicas in coupling space such that the couplings can be reallocated towards the bottlenecks by an iterative feedback procedure. Compared with the method above (Ref. [85]), this iterative feedback procedure will allocate more resources at the bottlenecks and thus yields a temperature dependent acceptance rate that peaks in regions with small diffusivity. The drawback of this method is that the initial runs to collect round-trip data may require such a large computational effort that it sometimes is practically impossible to use this method. Hence, in this work, I have used a method that collects round-trip data by measuring first-passage-times [87]. This method will, similar to Ref. [86], minimize the round-trip times, but at a lower initialization cost.

In Article I [1], the method by Hukushima was used, whereas in Articles III and IV [3,4], I mostly found the couplings by measuring first-passage-times. In cases with very narrow bottlenecks, one should find couplings by minimizing round-trip-times. Otherwise, both methods work fine.

It should be mentioned that, compared with the ordinary Metropolis-Hastings algorithm, there are not many drawbacks by adding the parallel tempering algorithm. It is relatively easy to implement, it can easily be applied for parallel computations, and the extra computational cost of the parallel tempering update is in most cases negligible. However, in cases when parallel tempering means simulations over a much larger number of couplings than necessary, parallel tempering may be a waste of computational resources. Also, as described above, parallel tempering may add a nonnegligible amount of extra Monte Carlo sweeps in order to initialize the couplings. In addition, one should be aware that with parallel tempering, results obtained at different couplings will be

somewhat correlated.

3.4 Reweighting

A Monte Carlo simulation can be said to provide information on which states that are probable for a specific value of the coupling β. Normally, we do not store all the information of all degrees of freedom in every state, but certain important observables, like the internal energy, magnetization or information on topological defects are stored in organized time series where each row corresponds to a sampled state and each column corresponds to a given observable. However, this information is not restricted to that specific coupling alone. Clearly, according to the probability distribution [Eq. (2.1)], the probability for a given state should not change too much if we only change the coupling by a small amount. *Reweighting* is a set of techniques that enables us to make use of the samples obtained at one coupling in order to calculate observables at nearby couplings, simply by changing the Boltzmann weight according to the change in the coupling value [88, 89].

3.4.1 Single-histogram reweighting

Consider a Monte Carlo simulation at coupling value β_1 where measurement of energy $H[\Psi_i], i \in \{1, \ldots, M\}$, and the observable $O[\Psi_i], i \in \{1, \ldots, M\}$, are stored in time series during the simulations.[10] The thermal average of observable $O[\Psi]$ at a nearby coupling β_2 can be rewritten as

$$\begin{aligned}\langle O \rangle_{\beta_2} &= \frac{\int \mathcal{D}\,\Psi O[\Psi]\,\mathrm{e}^{-\beta_2 H[\Psi]}}{\mathcal{Z}_{\beta_2}} = \frac{\int \mathcal{D}\,\Psi O[\Psi]\,\mathrm{e}^{-(\beta_2-\beta_1)H[\Psi]}\,\mathrm{e}^{-\beta_1 H[\Psi]}}{\int \mathcal{D}\,\Psi\,\mathrm{e}^{-(\beta_2-\beta_1)H[\Psi]}\,\mathrm{e}^{-\beta_1 H[\Psi]}} \\ &= \frac{\langle O[\Psi]\,\mathrm{e}^{-(\beta_2-\beta_1)H[\Psi]}\rangle_{\beta_1}}{\langle \mathrm{e}^{-(\beta_2-\beta_1)H[\Psi]}\rangle_{\beta_1}}. \end{aligned} \tag{3.35}$$

I.e., the thermal average of $O[\Psi]$ at β_2 can be found, simply by calculating the thermal average of the two observables, $O[\Psi]\exp\{-(\beta_2-\beta_1)\,H[\Psi]\}$ and $\exp\{-(\beta_2-\beta_1)\,H[\Psi]\}$ at β_1. Hence, by Eq. (3.8), the Monte Carlo estimate of $O[\Psi]$ at β_2 is given by

$$\langle O \rangle_{\beta_2} \approx \frac{\sum_i O[\Psi_i]\,\mathrm{e}^{-(\beta_2-\beta_1)H[\Psi_i]}}{\sum_i \mathrm{e}^{-(\beta_2-\beta_1)H[\Psi_i]}}. \tag{3.36}$$

In Fig. 3.6, an example of the heat capacity obtained by single-histogram reweighting is given. Notice that errors increase at couplings far away from the simulated coupling. When $\beta_2 - \beta_1$ is large, significant contributions to the thermal average at β_2 will come from states that are insufficiently sampled at β_1, and consequently, the reweighting technique breaks down. Reweighting is only reliable for couplings that have a large overlap in the energy histograms with the simulated coupling.

[10] Here, we assume that the states are found by drawing from the canonical probability distribution and that the action is on the usual and simple form, $\beta H[\Psi]$.

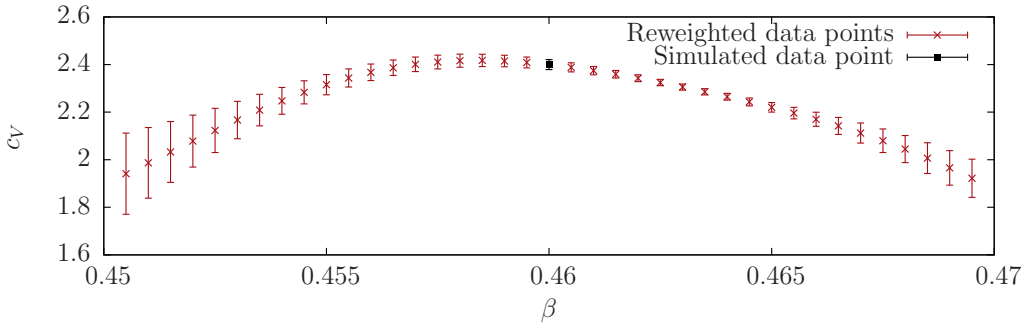

Figure 3.6: Results for the specific heat c_V as a function of coupling β. All data points, except the one at $\beta = 0.46$, are obtained by reweighting of data from the Monte Carlo simulation at $\beta = 0.46$.

3.4.2 Multi-histogram reweighting

The reweighting method outlined above can be improved by combining time series of data obtained from simulations at multiple different couplings. Consider a number of R simulations that have been performed at couplings $\beta_j, j \in \{1, \ldots, R\}$, and that each of these simulations measure energy $H_j[\Psi_i], i \in \{1, \ldots, M_j\}$, and observable $O_j[\Psi_i], i \in \{1, \ldots, M_j\}$. It can be showed [89,90] that the Monte Carlo estimate of observable $O[\Psi]$ at reweighted temperature β is given by

$$\langle O \rangle_\beta \approx \sum_{j=1}^{R} \sum_{i=1}^{M_j} \frac{O_j[\Psi_i] g_j^{-1} \, \mathrm{e}^{-\beta H_j[\Psi_i] - F_\beta}}{\sum_{k=1}^{R} M_k g_k^{-1} \, \mathrm{e}^{-\beta_k H_j[\Psi_i] + F_{\beta_k}}}, \tag{3.37}$$

where $g_j = 1 + 2\tau_{\mathrm{auto},j}$ and F_β is a free-energy-like parameter given by

$$\mathrm{e}^{-F_\beta} = \sum_{j=1}^{R} \sum_{i=1}^{M_j} \frac{g_j^{-1} \, \mathrm{e}^{-\beta H_j[\Psi_i]}}{\sum_{k=1}^{R} M_k g_k^{-1} \, \mathrm{e}^{-\beta_k H_j[\Psi_i] + F_{\beta_k}}}. \tag{3.38}$$

All the values $F_{\beta_j}, j \in \{1, \ldots, R\}$ can be found selfconsistently by solving the set of nonlinear equations found by $F_\beta \to F_{\beta_j} \; \forall \; j$ in Eq. (3.38). This set of equations can be solved numerically. In Fig. 3.7, an example of results obtained by multi-histogram reweighting is presented. Taking advantage of statistics obtained through multiple simulations has significant impact on the final result, as seen by smoother curves and smaller error bars. However, one must ensure that there is a large overlap between neighboring energy histograms. Also, in the case of parallel tempering, there is not so much to be gained from multi-histogram reweighting since the states sampled at a given coupling are correlated with those that are sampled at neighboring couplings.

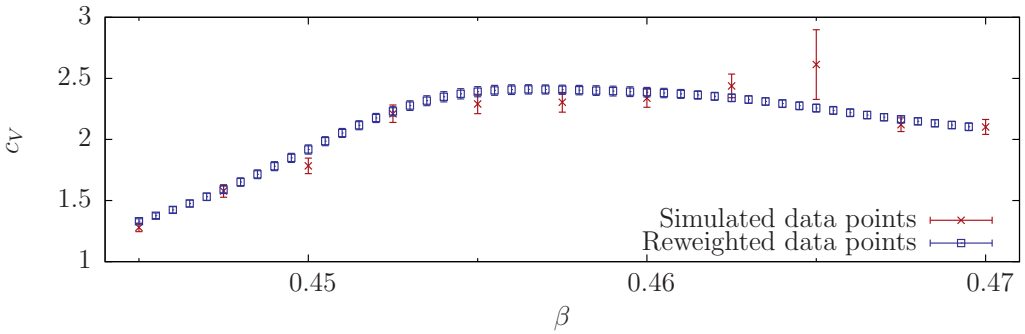

Figure 3.7: Results for the specific heat c_V as a function of coupling β. Results obtained by multi-histogram reweighting and results obtained directly from the simulations are compared.

3.5 Finite-size scaling

Although we most often are interested in the thermodynamic limit, we are restricted to finite system sizes for the numerical calculations. In many cases this is not a problem. Specifically, when the correlation length ξ is small compared to the linear system size L, the system can be considered to contain many similar and uncorrelated regions that essentially produce the same physics. Increasing the system size will only increase the number of these regions, but intensive quantities will approximately stay constant, and hence, the physics in the thermodynamic limit can easily be extracted.[11] However, when the condition $\xi \ll L$ is not valid, there may be large finite-size effects. Typically, intensive quantities that are expected to be singular or discontinuous, are often rather smooth but may change significantly with increasing system size. At first sight, this may seem like a confusing mess, but one should rather be joyful. Most often such behavior means that there is an interesting phase transition around. Also, by treating these effects in a systematic manner, one can investigate many important properties of the actual phase transition. This is the art of *finite-size scaling*.

These finite-size effects are understood as a consequence of the limit imposed on the correlation length by the finite system size. When approaching a critical phase transition, the correlation length ξ should diverge as $|\tau|^{-\nu}$, but for a finite system it will eventually stop growing when $\xi \sim L$. Hence, quantities that should be singular for a continuous phase transition will not diverge but rather saturate within a critical region of size $|\tau| \sim L^{-1/\nu}$. Returning to Widom's homogeneity postulate in Eq. (2.25) with $h = 0$ and $\lambda = L^{(2-\alpha)/\nu}$ as the arbitrary scaling factor, the scaling of the singular part of the free energy with respect to L is given by

$$f_{\mathrm{s}}(\tau) = L^{-(2-\alpha)/\nu} f_{\mathrm{s}}(L^{1/\nu}\tau). \tag{3.39}$$

Taking the second derivative of $f_{\mathrm{s}}(\tau)$ with respect to the coupling yields

$$c_V \sim L^{\alpha/\nu}\mathcal{C}(L^{1/\nu}\tau), \tag{3.40}$$

[11] These considerations are neglecting surface effects that may not be negligible for small systems.

where $\mathcal{C}(x)$ is a scaling function that is analytic in x. Relations as in Eq. (3.40) highlight the possibilities given by finite-size scaling. Simply by calculating c_V at the critical point for different values of L by Monte Carlo simulations, one can extract information on the values of the critical exponents. Finite-size relations for other thermodynamic quantities are derived in a similar fashion to that above. The magnetization has the scaling form given by

$$m \sim L^{-\beta/\nu}\mathcal{M}(L^{1/\nu}\tau), \tag{3.41}$$

where $\mathcal{M}(x)$ is the scaling function, and the susceptibility scales according to

$$\chi \sim L^{\gamma/\nu}\mathcal{K}(L^{1/\nu}\tau), \tag{3.42}$$

where $\mathcal{K}(x)$ is the scaling function.

It should be noted that in general, there are subdominant corrections to the finite-size scaling forms [47, 91–93]. In some cases, and in particular for small systems, such corrections may complicate the scaling analysis. Also, for finite sizes, the true critical point is generally *not* located at the peaks of thermodynamic quantities. The coupling corresponding to such a peak is called the *pseudocritical coupling* and scales as

$$\beta_{\mathrm{c}}(L) \approx \beta_{\mathrm{c}} + CL^{-1/\nu}, \tag{3.43}$$

where C is a constant. In principle, calculating the thermodynamic quantities at $\beta_{\mathrm{c}}(L)$ or at β_{c} should approximately yield the same scaling results, but in some cases the finite-size corrections to scaling may differ. Also, to calculate quantities at β_{c} requires that one is able to find β_{c} with high precision.

In certain cases, it might be difficult to extract exponents by Eq. (3.40), particularly when α is small or negative. In Refs. [94, 95] it was found that the third central moment of the microstate energies,

$$M_3 = \frac{\beta^3}{L^3}\left\langle (H - \langle H\rangle)^3 \right\rangle, \tag{3.44}$$

can be used to extract α and ν rather precisely. The scaling of M_3, which is the third derivative of $f_{\mathrm{s}}(\tau)$ with respect to the coupling, is given by

$$M_3 \sim L^{(1+\alpha)/\nu}\mathcal{C}'(L^{1/\nu}\tau), \tag{3.45}$$

where $\mathcal{C}'(x)$ is the scaling function. This quantity typically exhibits an antisymmetric curve with respect to the pseudocritical point. It has a negative peak for $\beta < \beta_{\mathrm{c}}(L)$ and a positive peak for $\beta > \beta_{\mathrm{c}}(L)$. The peak-to-peak difference in the M_3 value scales as

$$(\Delta M_3)_{\mathrm{height}} \sim L^{(1+\alpha)/\nu}, \tag{3.46}$$

and, by Eq. (3.43), the difference in the coupling values scales as

$$(\Delta M_3)_{\mathrm{width}} \sim L^{-1/\nu}. \tag{3.47}$$

Note that M_3 provides independent measurements of both α and ν, and may thus serve as a check of hyperscaling. Also, the corrections to finite-size scaling for M_3 are small compared with c_V.

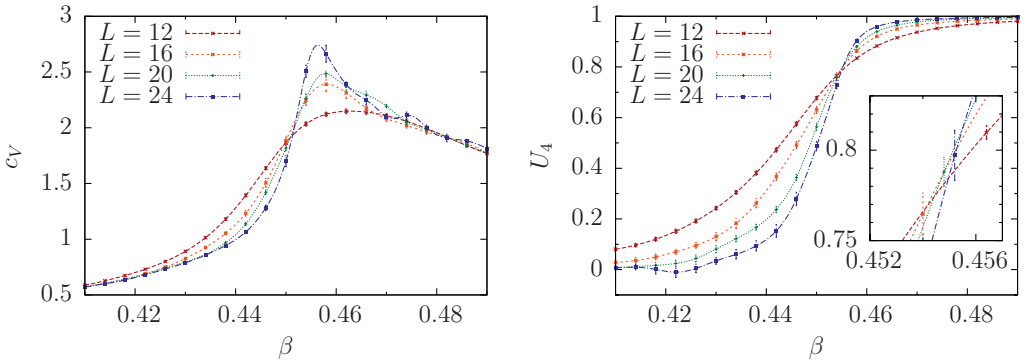

Figure 3.8: Results of the specific heat c_V and the Binder cumulant U_4 as functions of coupling β for the 3D XY model. The system sizes used are $L \in \{12, 16, 20, 24\}$. The inset in the right panel zooms in on the crossings of the Binder cumulants. Note that the crossings of the Binder cumulants yield a more precise determination of β_c than the pseudocritical coupling of the specific heat. High-precision calculations for the 3D XY model find the critical coupling to be $\beta_c = 0.454\,16(1)$ [98, 99].

A quantity that often is capable of finding the critical coupling with high precision is the *Binder cumulant* [96, 97],

$$U_4 = \frac{D+2}{2}\left(1 - \frac{D}{D+2}\frac{\langle \bar{m}^4 \rangle}{\langle \bar{m}^2 \rangle^2}\right), \tag{3.48}$$

where $\bar{\boldsymbol{m}} = (1/N)\sum_{\boldsymbol{r}} \boldsymbol{s}_{\boldsymbol{r}}$ is the magnetization of a given microstate,[12] and D is the number of components in $\bar{\boldsymbol{m}}$. At the critical point, the leading order L dependence of the ratio $\langle \bar{m}^4 \rangle / \langle \bar{m}^2 \rangle^2$ factors out and consequently, U_4 will, to the leading order, have a size-independent universal value at the critical point [93]. This means that U_4 curves obtained for different system sizes will intersect close to the critical point and a finite-size analysis of these crossings will in most cases converge very rapidly to β_{c}. This is exemplified in Fig. 3.8. The crossings of the Binder cumulants in the right panel converge more rapidly to β_c compared with the peak of the specific heat in the left panel.

Besides using M_3, an alternative way to determine ν is to calculate the logarithmic derivative of the second power of the magnetization [91],

$$\frac{\partial}{\partial \beta} \ln \langle \bar{m}^2 \rangle = \frac{\langle \bar{m}^2 H \rangle}{\langle \bar{m}^2 \rangle} - \langle H \rangle. \tag{3.49}$$

This quantity scales $\sim L^{1/\nu}$. Since the logarithmic derivative exhibits a peak similar to the specific heat, it is possible to find ν by measuring the logarithmic derivative at the pseudocritical coupling without having to determine β_{c} by an analysis of the Binder crossings.

[12] I.e., the thermal averaged magnetization m in Eq. (3.41), is related to $\bar{\boldsymbol{m}}$ by $m = \langle |\bar{\boldsymbol{m}}| \rangle$.

3.6 Detecting first-order transitions

The method outlined above aims at detecting and describing continuous phase transitions. If the phase transition under investigation exhibits true power law scaling with critical exponents that are mutually consistent and that can be related to a specific universality class, it is usually taken as evidence for a continuous phase transition. For a first-order transition, there is no diverging correlation length at the transition point. Indeed, in the case of a weak first-order transition, the correlation length may be large close to the phase transition, and consequently, the physical quantities that we can extract from the simulation may look very similar to what one would expect for a continuous transition. However, the true nature of the first-order transition will eventually be revealed if systems with $L \gg \xi$, where ξ is the correlation length at the transition point, are within reach numerically.

3.6.1 Lee-Kosterlitz method

The method suggested by Lee and Kosterlitz [100, 101] aims at verifying first-order transitions by looking for the existence of a free energy barrier and latent heat. Close to a first-order transition, the energy histograms obtained from a Monte Carlo simulation will exhibit a bimodal shape given that L is large enough. These two peaks correspond to the two coexisting phases of a first-order transition. The exact point of the phase transition can be located under the condition that the two peaks must be of equal height. One can easily get there by the reweighting methods described in Sec. 3.4. This will produce histograms qualitatively similar to that in Fig. 3.9. Following Lee and Kosterlitz, any histogram of the energies H obtained at coupling β by measuring M samples, is given by

$$\mathcal{N}(H;\beta) = M\frac{\Omega(H)\,\mathrm{e}^{-\beta H}}{\mathcal{Z}(\beta)}, \tag{3.50}$$

where $\Omega(H)$ is the number of states with energy H and $\mathcal{Z}(\beta)$ is the partition function. If we now define the quantity $A(H;\beta) = -\ln\left[\mathcal{N}(H;\beta)\right]/\beta$, we find that this must be a free-energy-like quantity since

$$A(H;\beta) = \frac{1}{\beta}\ln\left[\frac{Z(\beta)}{M}\right] + H - \frac{1}{\beta}\ln\left[\Omega(H)\right] = F(H) + \text{const.} \tag{3.51}$$

At the point of a first-order phase transition β_{PT}, the free energy barrier separating the two phases is given by considering the free energy difference between the local minimum and the two peaks in the energy histogram,

$$\Delta F = \frac{1}{\beta}\ln\left[\frac{\mathcal{N}_{\max}(H)}{\mathcal{N}_{\min}(H)}\right] = \frac{1}{\beta}\ln\left[\frac{P_{\max}(H/L^3)}{P_{\min}(H/L^3)}\right], \tag{3.52}$$

where $P(H/L^3) \propto \mathcal{N}(H)$ is the normalized energy histogram measured exactly at β_{PT}. For a first-order transition, ΔF corresponds to the tension associated with the domain walls separating the two coexisting phases at the transition point. Hence, the finite-size

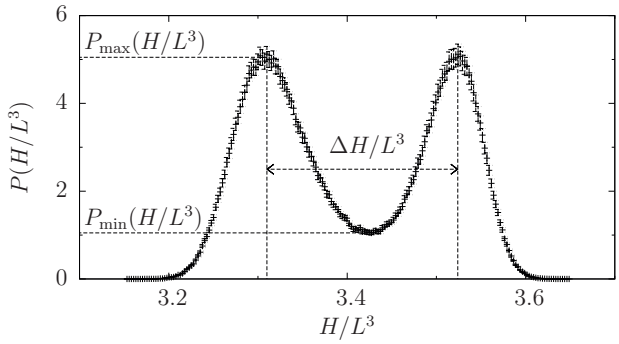

Figure 3.9: Example of an energy histogram with a bimodal distribution. $P(H/L^3)$ is the normalized energy histogram, and H/L^3 in the intensive internal energy. The free energy barrier ΔF is given by the peak value $P_{\max}(H/L^3)$ and the value of intermediate minimum $P_{\min}(H/L^3)$. The difference in energy between the two peaks equals the latent heat ΔH. This histogram is taken from Fig. 5 in Article I [1].

scaling of the free energy barrier is $\Delta F \sim L^{d-1}$. In addition, one should also measure the intensive energy difference between the two peaks in the energy histogram, denoted by $\Delta H/L^3$ in Fig. 3.9. This difference is the latent heat released when going from the ordered to the disordered phase, and should scale $\sim$ const. with increasing L to ensure that it does not vanish in the thermodynamic limit.

As a final remark, note that observing a bimodal energy distribution is *not* sufficient evidence for a first-order transition. In the literature, there are examples of such in cases where the transition is not first-order [13, 102–104]. For a first-order transition, one must also ensure that proper first-order scaling is obeyed over a sufficiently large range of sizes.

3.6.2 Other methods

For a first-order transition there is no true critical behavior with scale invariance and critical exponents. However, finite-size scaling can still be used to verify the existence of a first-order transition, as thermodynamic quantities at the transition point will have a characteristic size-dependence that can easily be deduced. For a heuristic derivation of the scaling of the specific heat, one can approximate the probability distribution of the energy to be a sum of two Gaussians that are centered at H_1 and H_2, respectively. In that case, $\langle H \rangle = (H_1 + H_2)/2$ and $\langle (H - \langle H \rangle)^2 \rangle = (H_1 - H_2)^2/4 + \text{const.}$ The specific heat is given by

$$c_V = \frac{\beta^2}{L^d} \left\langle (H - \langle H \rangle)^2 \right\rangle \sim \frac{\beta^2 L^d}{4} \left(\frac{H_1}{L^d} - \frac{H_2}{L^d} \right)^2 . \tag{3.53}$$

I.e., the leading order size-dependence of the specific heat is $c_V \sim L^d$ for a first-order transition. This can be shown in a more rigorous manner [12, 105]. In fact, first-order transitions exhibit finite-size scaling with *effective* exponents $\alpha = 1$ and $\nu = 1/d$ [106,

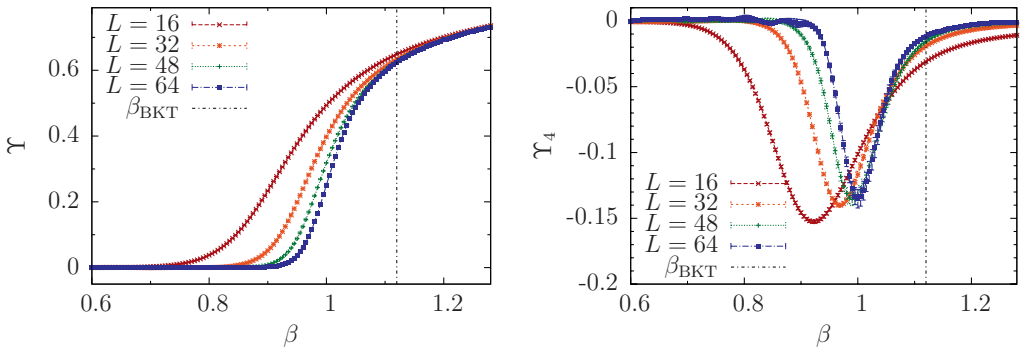

Figure 3.10: Results for the helicity modulus and the fourth-order modulus around the BKT transition in the zero-field 2D XY model. Left panel: The helicity modulus $\Upsilon = (\Upsilon_x + \Upsilon_y)/2$ as a function of coupling β. The helicity modulus converges slowly towards a discontinuous jump at β_{BKT} in the thermodynamic limit. Right panel: The fourth-order modulus $\Upsilon_4 = (\Upsilon_{4,x} + \Upsilon_{4,y})/2$ as a function of coupling β. The negative dip converges towards a finite value at β_{BKT} in the thermodynamic limit. The value of the BKT transition point is $\beta_{\mathrm{BKT}} = 1.120(1)$ [109, 110].

107]. It is thus feasible to perform finite-size scaling also in the case of first-order transitions to check if the effective exponents of first-order transitions are obtained.

Another method that can be used to check if a transition is first-order, is to study the Binder cumulant. For a first-order transition, this quantity exhibits a diverging negative dip, when the transition point is approached from the disordered side [97, 104, 108].

3.7 Detecting the Berezinskii-Kosterlitz-Thouless transition

As described in Sec. 2.4.2, the BKT transition can be recognized by the universal jump in the helicity modulus Υ_μ at the lower endpoint of the critical phase [Eq. (2.58)]. However, the discontinuous jump may not be easily recognized from simulations due to large finite-size effects. In the left panel of Fig. 3.10, a plot of the helicity modulus for the 2D XY model is given. The convergence towards a discontinuous jump at β_{BKT} is very slow. In this work, we have essentially used two different methods to verify the existence and determining the critical point of BKT transitions. A short description is given below.

3.7.1 Weber-Minnhagen method

Since Υ_μ is defined as the second derivative of the free energy density with respect to a phase twist with scaling $\sim L^{-1}$, the scaling of Υ_μ with system size is given by $\Upsilon_\mu \propto L^{2-d}$. In two dimensions, when $2 - d = 0$, one must include logarithmic corrections in order to get an accurate description of the finite-size scaling. Weber and Minnhagen found that

the finite-size scaling given by [111]

$$\Upsilon_\mu(L) \approx \Upsilon_\mu(\infty)\left(1+\frac{1}{2\ln L + C}\right), \tag{3.54}$$

is obeyed very well as β_{BKT} is approached from above. Here, $\Upsilon_\mu(\infty)$ is the value of the helicity modulus in the thermodynamic limit and C is a constant. Hence, a good fit to Eq. (3.54) should be obtained at β_{BKT} for a BKT transition. This can be used to verify the BKT nature of a phase transition. A more detailed description of this method is given in Appendix C of Article II [2].

3.7.2 Fourth-order modulus

Another method, suggested by Minnhagen and Kim in Ref. [112], can verify the existence of the discontinuous jump in the helicity modulus. This can be done by calculating the fourth-order derivative of the free energy, namely the *fourth-order modulus*,

$$\begin{aligned}\Upsilon_{4,\mu} \equiv & \frac{1}{L^4}\frac{\partial^4 F(\boldsymbol{\delta})}{\partial \delta_\mu^4}\bigg|_{\boldsymbol{\delta}=0} = \frac{1}{L^4}\Bigg[\left\langle \partial^4 H\right\rangle - 4\beta\left\langle\left(\partial^3 H - \left\langle\partial^3 H\right\rangle\right)\left(\partial H - \langle\partial H\rangle\right)\right\rangle \\ & - 3\beta L^4\left\langle\left(\tilde{\Upsilon}_\mu - \left\langle\tilde{\Upsilon}_\mu\right\rangle\right)^2\right\rangle + 2\beta^3\left\langle\left(\partial H - \langle\partial H\rangle\right)^4\right\rangle\Bigg]\Bigg|_{\boldsymbol{\delta}=0},\end{aligned} \tag{3.55}$$

where

$$\partial^p H = \frac{\partial^p H[\{\theta_i'\}]}{\partial \delta_\mu^p}, \tag{3.56}$$

is short-hand notation, and

$$\tilde{\Upsilon}_\mu = \frac{1}{L^2}\left[\partial^2 H - \beta\left(\partial H - \langle\partial H\rangle\right)^2\right], \tag{3.57}$$

is the thermally fluctuating helicity modulus in two dimensions.[13] In the right panel of Fig. 3.10, a plot of the fourth-order modulus for the 2D XY model is given.

In order to show how $\Upsilon_{4,\mu}$ can be used as evidence of the discontinuous jump in the helicity modulus, one must consider the stability of the free energy with respect to the dimensionless (or global) phase twist $\tilde{\Delta}_\mu = L\delta_\mu$. A Taylor expansion of the free energy in low orders of $\tilde{\Delta}_\mu$ yields

$$F(\tilde{\Delta}_\mu) - F(0) = \Upsilon_\mu\frac{\tilde{\Delta}_\mu^2}{2} + \Upsilon_{4,\mu}\frac{\tilde{\Delta}_\mu^4}{4!} + \mathcal{O}(\tilde{\Delta}_\mu^6), \tag{3.58}$$

where odd-order derivatives vanish under the condition that the change in the free energy must be invariant under the transformation $\tilde{\Delta}_\mu \to -\tilde{\Delta}_\mu$ [113]. In order to maintain the stability of the system, the change in the free energy must be greater or equal to zero. For small $\tilde{\Delta}_\mu$, the second-order term will always dominate the higher-order terms

[13] I.e., $\Upsilon_\mu = \langle\tilde{\Upsilon}_\mu\rangle|_{\boldsymbol{\delta}=0}$

and consequently, Υ_μ must also be greater or equal to zero. But if Υ_μ is zero, then the fourth-order term may play a role. Specifically, if $\Upsilon_{4,\mu}$ turns out to be *finite* and *negative* at β_{BKT} in the thermodynamic limit, then Υ_μ cannot go continuously to zero. Hence, investigations of the fourth-order modulus can be used to verify the discontinuous jump of the helicity modulus for a BKT-transition. In the right panel of Fig. 3.10, the fourth-order modulus is found to exhibit a negative dip that can be associated with the transition point. To ensure that this dip does not vanish with increasing system size, one can simulate different system sizes and extrapolate the results to the thermodynamic limit.

Chapter 4

Effective models of superfluids and superconductors

Superconductivity and superfluidity are phenomena that occur in certain materials at low temperatures. Superconductivity means that there is exactly zero electrical resistance in the material and that magnetic fields are expelled from the bulk of the material. Superfluidity means that the material is a fluid with zero viscosity.

All the models that have been investigated in this work may be considered to be *effective* models that can describe *two-component* superfluids and superconductors under certain conditions. This chapter intends to outline these models from a phenomenological point of view. In Sec. 4.1, the famous Ginzburg-Landau theory for superconductors is introduced. In Sec. 4.2, the London model for strong type-II superconductors is presented and Sec. 4.3 is devoted to a short description of superfluids. Before proceeding to discuss the two-component models that constitute the bulk of this work, in Sec. 4.4, the realization of continuum models on a lattice is explained. Sec. 4.5 introduces two-component superfluids interacting via an Andreev-Bashkin drag interaction. The next section (Sec. 4.6) is devoted to the *Moore-Read plasma*, which is an unconventional Coulomb plasma that is related to two-component rotating superfluids as well as certain fractional quantum Hall states. In Sec. 4.7, we discuss the two-component London superconductor where the components interact via a minimal coupling to the same noncompact gauge field. Then, in Sec. 4.8, a two-component London superconductor model with both Andreev-Bashkin and gauge field interaction is discussed, before this chapter ends in Sec. 4.9 with a specific model of a two-component superconductor, which is related to the concept of *deconfined quantum criticality*.

4.1 Ginzburg-Landau theory

4.1.1 Landau theory

In 1937, L. Landau presented a mathematical description of a phase transition from an ordered to a disordered phase [6]. This description is *phenomenological* in the sense that it is based on symmetry considerations and pays no respect to microscopic details. Landau postulated that in the neighborhood of a phase transition, the free energy can be expanded in powers of a small order parameter M,[1]

$$F(\beta, M) = F(\beta, 0) + \frac{\alpha t}{2} M^2 + \frac{u}{4!} M^4 + \dots, \tag{4.1}$$

where $\alpha, u > 0$ are free parameters and $t = (\beta_{\mathrm{MFT}} - \beta)/\beta$, where β_{MFT} is the critical coupling as predicted by mean-field theory. The expansion in Eq. (4.1) should only include terms allowed by symmetry. For instance, in this example, we have assumed that $F(\beta, M) = F(\beta, -M)$ and hence, odd-order terms are not allowed by symmetry. In an external field h, this symmetry is explicitly broken, and a linear term $-hM$ must be included.

4.1.2 Ginzburg-Landau theory

Landau theory is a mean-field theory and its predictions are often incorrect within the critical region. As described in Sec. 2.5, the reason for this is that the fluctuations are ignored. Hence, a natural improvement is *Ginzburg-Landau theory* which allow fluctuations by introducing a spatially varying order parameter $m(\boldsymbol{r})$,

$$H[m] = \int \mathrm{d}^d r \left\{ \frac{g}{2} \left[\nabla m(\boldsymbol{r})\right]^2 + \frac{\alpha t}{2} m^2(\boldsymbol{r}) + \frac{u}{4!} m^4(\boldsymbol{r}) + \dots \right\}, \tag{4.2}$$

where g is a free parameter. The spatial fluctuations cost free energy and this is accounted for by including the simplest possible gradient term that is consistent with the symmetries of the system.

4.1.3 Ginzburg-Landau theory for superconductors

The Ginzburg-Landau theory for superconductors was put forward by V. L. Ginzburg and L. Landau in 1950 [114]. This is a Ginzburg-Landau theory that describes a charged condensate with a local complex order parameter $\psi(\boldsymbol{r}) = |\psi(\boldsymbol{r})|\, \mathrm{e}^{\mathrm{i}\theta(\boldsymbol{r})}$ that couples minimally with strength e to the electromagnetic gauge field $\boldsymbol{A}(\boldsymbol{r})$. The effective Hamiltonian

[1] For simplicity, here I use a scalar order parameter.

reads

$$H[\psi, \boldsymbol{A}] = \int \mathrm{d}^d r \Big\{ \frac{g}{2} \left| [\nabla - \mathrm{i}e\boldsymbol{A}(\boldsymbol{r})]\psi(\boldsymbol{r}) \right|^2 + \frac{\alpha t}{2} \left|\psi(\boldsymbol{r})\right|^2 + \frac{u}{4!} \left|\psi(\boldsymbol{r})\right|^4 + \frac{1}{2}[\nabla \times \boldsymbol{A}(\boldsymbol{r})]^2 \Big\}. \tag{4.3}$$

The amplitude of the order parameter represents the local density of superconducting electrons, $|\psi(\boldsymbol{r})|^2 = n_\mathrm{s}(\boldsymbol{r})$. After the microscopic BCS theory in 1957 [115], and subsequently, Gorkov's derivation of the Ginzburg-Landau model from the BCS theory [116], it was understood that $n_\mathrm{s}(\boldsymbol{r})$ should be interpreted as the local density of Cooper pairs.

The model in Eq. (4.3) is invariant under the transformation,

$$\begin{aligned} \psi(\boldsymbol{r}) &\to \psi(\boldsymbol{r})\, \mathrm{e}^{\mathrm{i}\varphi(\boldsymbol{r})}, \\ \boldsymbol{A}(\boldsymbol{r}) &\to \boldsymbol{A}(\boldsymbol{r}) + \frac{1}{e}\nabla\varphi(\boldsymbol{r}), \end{aligned} \tag{4.4}$$

where $\varphi(\boldsymbol{r})$ is an arbitrary real-valued function. This is called a local U(1) symmetry or a U(1) gauge symmetry. According to Elitzur's theorem [24], there is no spontaneous symmetry breaking of local symmetries. Hence, there is no local order parameter associated with the phase transition in this model. Rather, in gauge theories like Eq. (4.3), the onset of the superconducting phase is associated with dynamic generation of *effective* gauge field mass $m_{\boldsymbol{A}}$ and screening of the magnetic field $\boldsymbol{B}(\boldsymbol{r}) = \nabla \times \boldsymbol{A}(\boldsymbol{r})$. This is the Anderson-Higgs mechanism in superconductors [117, 118]. The gauge field mass $m_{\boldsymbol{A}}$ is zero in the normal phase and nonzero in the Meissner (Higgs) phase, and it can be used as a global order parameter for the superconducting phase transition.

It can be shown [37, 119] that there are two important length scales in this model. The magnetic penetration depth, given by

$$\lambda = \sqrt{\frac{u}{3! g e^2 \alpha |t|}}, \tag{4.5}$$

is the characteristic length for screening a magnetic field, and the coherence length, given by

$$\xi = \sqrt{\frac{g}{\alpha |t|}}, \tag{4.6}$$

is the correlation length of the variation of $|\psi(\boldsymbol{r})|$. Both Eqs. (4.5) and (4.6) are given at the mean-field level. The ratio $\kappa = \lambda/\xi$ is called the *Ginzburg-Landau parameter*. For small values of the Ginzburg-Landau parameter $\kappa < \kappa_\mathrm{tri}$,[2] the phase transition in the Ginzburg-Landau model is first-order [120]. For $\kappa > \kappa_\mathrm{tri}$, the transition is continuous [121]. By mean-field theory, one can calculate that $\kappa_\mathrm{tri} = 1/\sqrt{2}$. However, in Ref. [122], the value of this point was found to be $\kappa_\mathrm{tri} = 0.76(4)/\sqrt{2}$. In that work, it was also argued that the exact same point separates type-I and type-II superconductors.[3]

[2] The point where a continuous phase transition changes to a first-order phase transition is called a *tricritical point*.

[3] Superconductors can be classified as *type I* or *type II* according to how they respond to an applied magnetic field. Type I superconductors cannot be penetrated by a weak magnetic field (this is the Meissner effect), whereas for type II superconductors, magnetic flux can penetrate the bulk of the superconductor in terms of vortices.

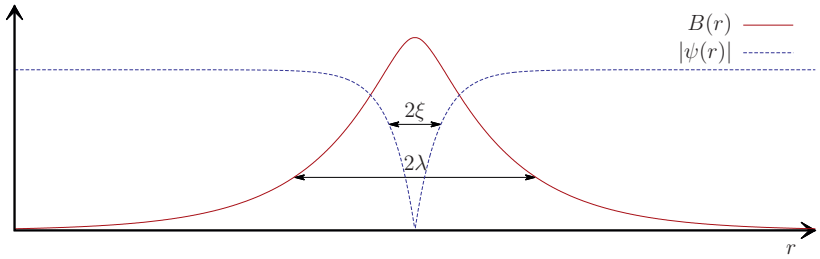

Figure 4.1: Schematic illustration of an Abrikosov vortex core cross section. The decay of the magnetic field $B(r)$ and the decay of the order parameter amplitude $|\psi(r)|$ are determined by the characteristic lengths λ and ξ, respectively.

Vortices of the Ginzburg-Landau model

The Ginzburg-Landau model for superconductors exhibits vortices, or more precisely, Abrikosov flux tubes as topological defects [123].[4] In Fig. 4.1, a schematic illustration of the core of an Abrikosov vortex is given. At the core of the vortex, the amplitude $|\psi(\boldsymbol{r})|$ decays to zero with characteristic length ξ. In this way the gradient term of Eq. (4.3) will not diverge with $\nabla\theta(\boldsymbol{r})$ at the core of the vortex. Moreover, the circulating current around the vortex core will allow a magnetic field $\boldsymbol{B}(\boldsymbol{r})$, that decays with characteristic length λ, to penetrate the bulk of the superconductor. Because of the nonzero magnetic flux associated with the vortex, we can think of the vortex as a region in the normal phase surrounded by bulk in the superconducting phase. It can be shown [37] that the magnetic flux Φ carried by a vortex is quantized,

$$\Phi = \oint_{\mathcal{C}} \mathrm{d}\boldsymbol{l} \cdot \boldsymbol{A}(\boldsymbol{r}) = \frac{2\pi n}{e}. \tag{4.7}$$

Here, $\mathcal{C}$ is a closed contour within the superconducting bulk and $n \in \mathbb{Z}$.

Gauge mass

The gauge mass $m_{\boldsymbol{A}}$ can be extracted from correlators that are associated with the gauge field [126–128]. Consider the correlator of the magnetic field,

$$G_{\boldsymbol{B}}(\boldsymbol{r}' - \boldsymbol{r}) = \left\langle \boldsymbol{B}(\boldsymbol{r}) \cdot \boldsymbol{B}(\boldsymbol{r}') \right\rangle . \tag{4.8}$$

The Fourier transform is given by

$$G_{\boldsymbol{B}}(\boldsymbol{q}) = \left\langle \boldsymbol{B}(-\boldsymbol{q}) \cdot \boldsymbol{B}(\boldsymbol{q}) \right\rangle . \tag{4.9}$$

In the Meissner phase, the magnetic flux will not fluctuate on large scales and consequently, $G_{\boldsymbol{B}}(q \to 0) = 0$. In the normal phase, the magnetic flux will proliferate such

[4] In the particle physics community, these magnetic flux tubes are called *Nielsen-Olesen vortices* [124]. They may also be called *Abrikosov-Nielsen-Olesen vortices* [125].

that $G_{\boldsymbol{B}}(q \to 0) > 0$. Hence, $G_{\boldsymbol{B}}(\boldsymbol{q})$ can be used as an order parameter[5] of the superconducting phase transition [4,125,126]. This correlator will have the general form given by

$$G_{\boldsymbol{B}}(\boldsymbol{q}) \propto \frac{\boldsymbol{q}^2}{\boldsymbol{q}^2 + \Sigma(\boldsymbol{q})}, \tag{4.10}$$

where the self-energy $\Sigma(\boldsymbol{q})$ can be written as [127]

$$\Sigma(\boldsymbol{q}) = m_{\boldsymbol{A}}^2 + C|\boldsymbol{q}|^{2-\eta} + \mathcal{O}(|\boldsymbol{q}|^{\delta}). \tag{4.11}$$

Here, C is a constant, η is a critical exponent and $\delta > 2 - \eta$. By Eqs. (4.10) and (4.11), it is easy to see that the gauge mass can be determined by

$$m_{\boldsymbol{A}}^2 \propto \lim_{q \to 0} \frac{\boldsymbol{q}^2}{G_{\boldsymbol{B}}(\boldsymbol{q})}. \tag{4.12}$$

4.2 The London approximation

In the London approximation, the amplitude of the superconducting order parameter field is assumed to be uniform and constant,

$$\psi(\boldsymbol{r}) = |\psi(\boldsymbol{r})| \, \mathrm{e}^{\mathrm{i}\theta(\boldsymbol{r})} \approx |\psi_0| \, \mathrm{e}^{\mathrm{i}\theta(\boldsymbol{r})} \, . \tag{4.13}$$

When inserted in Eq. (4.3), the effective model for superconductors in the London approximation reads

$$H[\theta, \boldsymbol{A}] = \int \mathrm{d}^d r \left\{ \frac{g|\psi_0|^2}{2} \left[\nabla\theta(\boldsymbol{r}) - e\boldsymbol{A}(\boldsymbol{r})\right]^2 + \frac{1}{2}[\nabla \times \boldsymbol{A}(\boldsymbol{r})]^2 \right\}, \tag{4.14}$$

where uninteresting constant terms have been discarded.[6] Eq. (4.14) exhibits a U(1) gauge symmetry [Eq. (4.4)]. The energy cost of introducing a single vortex in the London superconductor can be shown to be given by [37]

$$E_{\mathrm{v}} \sim \ln \frac{\lambda}{\xi}. \tag{4.15}$$

I.e., the energy cost of introducing a single vortex in a London superconductor is *finite* with diverging system size.

The London approximation is regarded to be a good approximation when κ is large, that is, for strong type-II superconductors. In Fig. 4.1, this would correspond to the case where λ is much larger than ξ. Hence, it should be clear that $|\psi(\boldsymbol{r})|$ can be well approximated to be spatially constant except for a cutoff near the vortex core. Although the London model here is presented as an approximation of the Ginzburg-Landau model,

[5] To be more precise, I should have called it a *disorder parameter* as it is zero in the ordered phase and nonzero in the normal phase.

[6] For continuum models, one must introduce an ultraviolet cutoff at vortex cores in order to avoid an infinite energy cost associated with vortices.

it is an adequate approximation for many properties of type-II superconductors and is in fact valid for a broader temperature range than the Ginzburg-Landau model.

In a classic paper by Dasgupta and Halperin, the London superconductor was found to undergo a continuous transition of the inverted 3D XY universality class [129]. This superconductor to normal phase transition is governed by proliferation of vortex loops with quantized flux [130, 131]. I.e., on the superconducting side of the transition (when $\beta > \beta_c$), vortex loops are confined and unable to destroy the superconductivity, whereas at β_c, the line tension of the vortex loops vanishes such that the vortex loops unbind and destroy superconductivity.

4.2.1 Effective Hamiltonian in terms of vortices

The London superconductor model in Eq. (4.14) can be written in terms of interacting vortex loops.[7] The partition function of the London superconductor is written

$$\mathcal{Z} = \int \mathcal{D}\,\theta \int \mathcal{D}\,\boldsymbol{A}\,\mathrm{e}^{-S}, \tag{4.16}$$

where

$$S = \frac{\beta}{2}\int \mathrm{d}^3 r \left\{ g|\psi_0|^2 \left[\nabla\theta(\boldsymbol{r}) - e\boldsymbol{A}(\boldsymbol{r})\right]^2 + \left[\nabla \times \boldsymbol{A}(\boldsymbol{r})\right]^2 \right\}. \tag{4.17}$$

We choose the gauge $\nabla \cdot \boldsymbol{A}(\boldsymbol{r}) = 0$ and Fourier transform Eq. (4.17) to find

$$S = \frac{\beta}{2}\int \mathrm{d}^3 q \Big\{ g|\psi_0|^2 \boldsymbol{U}(\boldsymbol{q})\boldsymbol{U}(-\boldsymbol{q}) - \frac{m_0^2}{e}\left[\boldsymbol{U}(\boldsymbol{q})\boldsymbol{A}(-\boldsymbol{q}) + \boldsymbol{U}(-\boldsymbol{q})\boldsymbol{A}(\boldsymbol{q})\right] + (q^2 + m_0^2)\boldsymbol{A}(\boldsymbol{q})\boldsymbol{A}(-\boldsymbol{q}) \Big\}, \tag{4.18}$$

where $\boldsymbol{U}(\boldsymbol{q})$ is the Fourier transform of $\boldsymbol{U}(\boldsymbol{r}) = \nabla\theta(\boldsymbol{r})$ and $m_0^2 \equiv g|\psi_0|^2 e^2$. By completing the squares of the gauge field with $\tilde{\boldsymbol{A}}(\boldsymbol{q}) = \boldsymbol{A}(\boldsymbol{q}) - [(m_0^2/e)/(q^2 + m_0^2)]\boldsymbol{U}(\boldsymbol{q})$ as the shifted gauge field, the integration over the gauge field can be performed. The resulting partition function is written

$$\mathcal{Z} = \int \mathcal{D}\,\theta\ \exp\left[-\frac{\beta g|\psi_0|^2}{2}\int \mathrm{d}^3 q \frac{q^2}{q^2 + m_0^2}\boldsymbol{U}(\boldsymbol{q})\boldsymbol{U}(-\boldsymbol{q}) \right]. \tag{4.19}$$

The phase gradient $\boldsymbol{U}(\boldsymbol{r})$ can be decomposed into a longitudinal and a transverse part, $\boldsymbol{U}(\boldsymbol{r}) = [\boldsymbol{U}(\boldsymbol{r})]_L + [\boldsymbol{U}(\boldsymbol{r})]_T$. The longitudinal component corresponds to the curl-free spin waves, i.e., $\nabla \times [\boldsymbol{U}(\boldsymbol{r})]_L = \boldsymbol{0}$. The transverse component corresponds to the divergence-free vortex defects, i.e., $\nabla \cdot [\boldsymbol{U}(\boldsymbol{r})]_T = 0$. It is well known that it is the vortices and not the spin waves that play an important role at the critical point, and for this purpose, we can disregard the longitudinal part of the phase gradient [37]. The vortices are found by taking the curl of the phase gradient,

$$\nabla \times \boldsymbol{U}(\boldsymbol{r}) = \nabla \times [\boldsymbol{U}(\boldsymbol{r})]_T = 2\pi \boldsymbol{m}(\boldsymbol{r}), \tag{4.20}$$

[7] Here, we assume three spatial dimensions, $d = 3$.

where $\boldsymbol{m}(\boldsymbol{r})$ is the integer-valued vortex field. Also, note that $\nabla\cdot\boldsymbol{m}(\boldsymbol{r}) = 0$ by Eq. (4.20). Taking the curl on both sides of Eq. (4.20) followed by a Fourier transformation yields

$$[\boldsymbol{U}(\boldsymbol{q})]_T = 2\pi\mathrm{i}\frac{\boldsymbol{q}\times\boldsymbol{m}(\boldsymbol{q})}{q^2}. \tag{4.21}$$

Finally, by inserting Eq. (4.21) in Eq. (4.19), we arrive at the vortex formulation of the London superconductor,

$$\mathcal{Z} = \int \mathcal{D}\,\boldsymbol{m}\ \exp\left[-2\pi^2\beta g|\psi_0|^2\int \mathrm{d}^3q\frac{1}{q^2+m_0^2}\boldsymbol{m}(\boldsymbol{q})\boldsymbol{m}(-\boldsymbol{q})\right]. \tag{4.22}$$

Note that the potential $V(q) = g|\psi_0|^2/(q^2+m_0^2)$ is the screened Yukawa potential. I.e., the bare interaction of the charged vortices in the London superconductor is screened by the gauge field. The quantity m_0 can be interpreted as the bare mass and m_0^{-1} is the bare screening length of the vortex interactions. The Yukawa potential decays exponentially, $V(r) \sim \mathrm{e}^{-m_0 r}/r$. In the limit $e = 0$, the potential decays with a power law, $V(r) \sim 1/r$. This means that the charged vortex interactions are short-ranged with an exponential decay, whereas neutral vortex interactions are long-ranged with a $1/r$ decay (cf. Sec. 2.7.1).

In this context, it should also be mentioned that in the case of a London superconductor, the gauge mass $m_{\boldsymbol{A}}$ can be found by calculating vortex correlators [1, 128, 132, 133]. In Article I [1], the normal to superconductor phase transition was monitored by finding $m_{\boldsymbol{A}}$ in this way.

4.3 Superfluids

The property of superfluidity can be found to occur in Bose-Einstein condensates (BECs). A BEC is a state of matter where a macroscopic fraction of bosons occupy the ground state of the system. For a thorough introduction to BECs and superfluidity, Refs. [134, 135] can be recommended. These are also the main references for this section.

The BEC is usually described by the Gross-Pitaevskii energy expression,

$$H[\psi] = \int \mathrm{d}^d r\left[\frac{1}{2m}\left|\nabla\psi(\boldsymbol{r})\right|^2 + V(\boldsymbol{r})\left|\psi(\boldsymbol{r})\right|^2 + \frac{U_0}{2}\left|\psi(\boldsymbol{r})\right|^4\right], \tag{4.23}$$

where m is the boson mass, $V(\boldsymbol{r})$ is the external trapping potential, U_0 is the effective interaction parameter and $\psi(\boldsymbol{r}) = |\psi(\boldsymbol{r})|\,\mathrm{e}^{\mathrm{i}\theta(\boldsymbol{r})}$ is the complex condensate wave function. The velocity of the condensate is given by

$$\boldsymbol{v}(\boldsymbol{r}) = \frac{\psi^*(\boldsymbol{r})\nabla\psi(\boldsymbol{r}) - \psi(\boldsymbol{r})\nabla\psi^*(\boldsymbol{r})}{2m\mathrm{i}|\psi(\boldsymbol{r})|^2} = \frac{\nabla\theta(\boldsymbol{r})}{m}. \tag{4.24}$$

It can be showed that the BEC is a superfluid if the condensate velocity is smaller than some limit $v_\mathrm{c} = \min_{\boldsymbol{p}}\epsilon(\boldsymbol{p})/p$, where $\epsilon(\boldsymbol{p})$ is the excitation energy of the fluid and $\boldsymbol{p}$ is the momentum. The limit v_c is referred to as the *Landau critical velocity*.

The condensate can accommodate topological defects in terms of vortices. Vortices are located at singular points in the phase field $\theta(\boldsymbol{r})$. According to Eq. (4.24), $\nabla \times \boldsymbol{v}(\boldsymbol{r}) = 0$ for all regular points of $\theta(\boldsymbol{r})$, and hence, the superfluid is irrotational. However at points where $\theta(\boldsymbol{r})$ is singular, the curl of the velocity field is nonzero and the circulation is given by

$$\oint_{\mathcal{C}} \mathrm{d}\boldsymbol{l} \cdot \boldsymbol{v}(\boldsymbol{r}) = \frac{2\pi q}{m}, \tag{4.25}$$

where $q \in \mathbb{Z}$ denotes the total vortex charge within the contour $\mathcal{C}$. This is the *Onsager-Feynman quantization theorem*, and it expresses that the circulation in the superfluid is quantized. Eq. (4.25) is the superfluid counterpart of the magnetic flux quantization in superconductors [Eq. (4.7)].

In the London limit, $|\psi(\boldsymbol{r})| = n^{1/2}$, where n is the density of the condensate, the Hamiltonian of the superfluid condensate in Eq. (4.23) is given by the continuum XY model,

$$H[\theta] = \frac{n}{2m} \int \mathrm{d}^d r \, [\nabla\theta(\boldsymbol{r})]^2 \,, \tag{4.26}$$

where uninteresting constant terms have been discarded. Vortices in superfluid ^{4}He are considered to be adequately described by this model [39]. The London limit is also called the *hydrodynamic limit*.

4.3.1 Rotating superfluids

When a superfluid is subject to rotation, the response is rather remarkable. Quantized vortices will form, and they will be arranged in a pattern similar to the triangular Abrikosov lattice of strong type-II superconductors [136, 137]. Such vortex arrays are widely studied, and they appear in different contexts such as the interior of neutron stars [138], trapped Bose-Einstein condensates [137] and rotating superfluid ^{4}He [139].

In a rotating frame, the Gross-Pitaevskii energy expression is written as

$$H[\psi] = \int \mathrm{d}^d r \Big\{ \frac{1}{2m} \left| [\nabla - \mathrm{i}m(\boldsymbol{\Omega} \times \boldsymbol{r})] \, \psi(\boldsymbol{r}) \right|^2 + \Big[V(\boldsymbol{r}) - \frac{m}{2} (\boldsymbol{\Omega} \times \boldsymbol{r})^2 \Big] \, |\psi(\boldsymbol{r})|^2 + \frac{U_0}{2} \, |\psi(\boldsymbol{r})|^4 \Big\}, \tag{4.27}$$

where $\boldsymbol{\Omega}$ is the angular velocity. Invoking the London approximation $|\psi(\boldsymbol{r})| = n^{1/2}$ and disregarding constant terms in the Hamiltonian, the model reads

$$H[\theta] = \frac{n}{2m} \int \mathrm{d}^d r \, [\nabla\theta(\boldsymbol{r}) - m(\boldsymbol{\Omega} \times \boldsymbol{r})]^2 \,. \tag{4.28}$$

This is the frustrated XY model. The frustration is given by the rotation term $m(\boldsymbol{\Omega} \times \boldsymbol{r})$, which essentially makes certain nonzero variations of the phase field energetically favorable. This leads to a number of rotationally induced vortices in the condensate,

$$n_{\mathrm{v}} = \frac{2m\Omega}{2\pi}, \tag{4.29}$$

where n_v is the number of vortices per unit area in the plane perpendicular to $\boldsymbol{\Omega}$. The model [Eq. (4.28)] is considered to be valid when the purpose is to study the vortices of a slowly rotating superfluid. In this case the average vortex separation is much larger than the *healing length* ξ, which is the coherence length associated with depletion of $|\psi(\boldsymbol{r})|$ near the vortex core. In Refs. [140, 141], the frustrated XY model with an inhomogeneous density was used to model vortex matter in trapped Bose-Einstein condensates. For rapidly rotating vortices, the density of vortices will increase and the vortices will eventually start to overlap. In this case, the London approximation is not longer valid and other models must be used [142, 143].

Notice the similarity between Eq. (4.28) and the London superconductor in Eq. (4.14). When gauge field fluctuations in the London superconductor can be neglected such that the Maxwell term can be disregarded, the model in Eq. (4.28) describes a superconductor in an external magnetic field with $e\boldsymbol{A}(\boldsymbol{r}) = m(\boldsymbol{\Omega} \times \boldsymbol{r})$. I.e., the angular velocity $\boldsymbol{\Omega}$ plays the same role in a superfluid as an external magnetic field $\boldsymbol{B}_\mathrm{ext}$ in a type-II superconductor. In extreme type-II superconductors, gauge field fluctuations can, in many cases, be ignored, and hence, the model in Eq. (4.28) has been widely used to describe vortex matter in extreme type-II superconductors [144–148]. At low temperatures, the vortices of this model are arranged in a triangular Abrikosov lattice. Upon heating, there is a first-order melting transition of the vortex lattice into an incoherent vortex liquid. Note that this in clearly different from the nonfrustrated case where there is a continuous transition with proliferation of vortex loops.

4.4 Lattice regularization

The models that were introduced in Chapter 2 were naturally defined on a lattice, but the models in this chapter have been formulated as continuum models. In order to perform numerical simulations, continuum models must be converted to a lattice formulation that is suitable for computational purposes. Additionally, lattice formulations are convenient in that they naturally provide the ultraviolet cutoff needed for introducing vortices in certain models.

In general, there is no unique way to discretize a continuum model. However, it is required that the continuum model must be recovered in the limit of zero lattice spacing. Also, symmetries must be preserved. Here, we will restrict ourselves to 3D cubic lattices with size L^3 and with uniform lattice constants $a_\mu = a \; \forall \; \mu \in \{x, y, z\}$. Scalar fields are then defined on the vertices $\boldsymbol{r} \in \{ai\hat{\boldsymbol{x}} + aj\hat{\boldsymbol{y}} + ak\hat{\boldsymbol{z}} \mid i, j, k \in \{1, \ldots, L\}\}$ of the lattice,

$$\psi(\boldsymbol{r}) \to \psi_{\boldsymbol{r}}. \tag{4.30}$$

Derivatives are replaced by lattice differences,

$$\frac{\partial \psi(\boldsymbol{r})}{\partial r_\mu} \to \frac{\psi_{\boldsymbol{r}+a\hat{\boldsymbol{\mu}}} - \psi_{\boldsymbol{r}}}{a} = \frac{\Delta_\mu \psi_{\boldsymbol{r}}}{a}, \tag{4.31}$$

The gauge-invariant gradients that appear in the Ginzburg-Landau model and the Gross-Pitaevskii in a rotating frame are replaced by the gauge-invariant lattice difference,

$$\left[\frac{\partial}{\partial r_\mu} - \mathrm{i}eA_\mu(\boldsymbol{r})\right]\psi(\boldsymbol{r}) \to \frac{1}{a}\left(\psi_{\boldsymbol{r}+a\hat{\boldsymbol{\mu}}}\,\mathrm{e}^{-\mathrm{i}eaA_{\mu,\boldsymbol{r}}} - \psi_{\boldsymbol{r}}\right), \tag{4.32}$$

where the gauge field $A_{\mu,\boldsymbol{r}}$ lives on the link $(\boldsymbol{r}, \boldsymbol{r}+a\hat{\boldsymbol{\mu}})$ and is given by the line integral

$$A_{\mu,\boldsymbol{r}} = \int_{\boldsymbol{r}}^{\boldsymbol{r}+a\hat{\boldsymbol{\mu}}} \mathrm{d}\boldsymbol{l} A_\mu(\boldsymbol{r}). \tag{4.33}$$

The Maxwell term is replaced by a plaquette sum,

$$[\nabla \times \boldsymbol{A}(\boldsymbol{r})]_\mu \to \frac{1}{a}\sum_{\nu,\lambda}\varepsilon_{\mu\nu\lambda}\Delta_\nu A_{\lambda,\boldsymbol{r}}. \tag{4.34}$$

Finally, the integral is replaced by a lattice sum,

$$\int \mathrm{d}^3 r \to a^3 \sum_{\boldsymbol{r}}. \tag{4.35}$$

With the abovementioned discretization scheme, the lattice Ginzburg-Landau model reads

$$H[\psi, \boldsymbol{A}] = a^3 \sum_{\boldsymbol{r}}\Bigg[-\frac{g}{a^2}\sum_{\mu}|\psi_{\boldsymbol{r}+a\hat{\boldsymbol{\mu}}}||\psi_{\boldsymbol{r}}|\cos\left(\Delta_\mu\theta_{\boldsymbol{r}} - eaA_{\mu,\boldsymbol{r}}\right) + \left(\frac{3g}{a^2} + \frac{\alpha t}{2}\right)|\psi_{\boldsymbol{r}}|^2 + \frac{u}{4!}|\psi_{\boldsymbol{r}}|^4 + \frac{1}{2a^2}\sum_{\mu}\left(\sum_{\nu,\lambda}\varepsilon_{\mu\nu\lambda}\Delta_\nu A_{\lambda,\boldsymbol{r}}\right)^2\Bigg]. \tag{4.36}$$

The lattice London superconductor model is found by taking the London limit in Eq. (4.36),[8]

$$H[\theta, \boldsymbol{A}] = \sum_{\mu,\boldsymbol{r}}\left[-g|\psi_0|^2\cos\left(\Delta_\mu\theta_{\boldsymbol{r}} - eA_{\mu,\boldsymbol{r}}\right) + \frac{1}{2}\left(\sum_{\nu,\lambda}\varepsilon_{\mu\nu\lambda}\Delta_\nu A_{\lambda,\boldsymbol{r}}\right)^2\right], \tag{4.37}$$

and the lattice version of the rotating superfluid model in the London limit [Eq. (4.28)] reads

$$H[\theta] = -\frac{n}{m}\sum_{\mu,\boldsymbol{r}}\cos\left[\Delta_\mu\theta_{\boldsymbol{r}} - m(\boldsymbol{\Omega}\times\boldsymbol{r})_\mu\right]. \tag{4.38}$$

Naively, it looks like the vortices have disappeared in Eqs. (4.36), (4.37) and (4.38), as summing a closed loop of lattice differences trivially is zero due to the single-valuedness of θ. However, the vortices are reintroduced by demanding that the gauge-invariant phase difference is within its primary interval, $\Delta_\mu\theta_{\boldsymbol{r}} - eaA_{\mu,\boldsymbol{r}} \in [-\pi, \pi)$ (see also Sec. 2.4.3) [149].

[8] We discard uninteresting constant terms in the Hamiltonian, and the lattice constant is set to $a = 1$.

4.5 Two-component superfluids with an Andreev-Bashkin interaction

Quite generally, one can have multicomponent systems, i.e., mixtures with several distinguishable species of particles. Here, we consider a mixture of two independently conserved components that are in the superfluid state. The two components can interact via a nondissipative drag term, in certain contexts also called the Andreev-Bashkin effect. In the hydrodynamic limit, the effective Hamiltonian of such a mixture can be written as

$$H[\theta_1,\theta_2] = \frac{1}{2}\int \mathrm{d}^d r \Bigg\{ \sum_{j=1,2} m_j n_j \left[\frac{\nabla\theta_j(\boldsymbol{r})}{m_j}\right]^2 - \sqrt{m_1 m_2}\, n_d \left[\frac{\nabla\theta_1(\boldsymbol{r})}{m_1} - \frac{\nabla\theta_2(\boldsymbol{r})}{m_2}\right]^2 \Bigg\}, \tag{4.39}$$

where m_j, n_j and $\theta_j(\boldsymbol{r})$ is the mass, density and phase field of component $j \in \{1,2\}$ and n_d is the effective density of one component that is being dragged by the superfluid velocity of the other component. Note that in order to maintain stability of the system described by Eq. (4.39), the drag density must satisfy the relation

$$n_d < \frac{n_1 n_2}{n_1\sqrt{\frac{m_1}{m_2}} + n_2\sqrt{\frac{m_2}{m_1}}}. \tag{4.40}$$

The model in Eq. (4.39) is invariant under the transformation $\theta_j(\boldsymbol{r}) \to \theta_j(\boldsymbol{r}) + \varphi_j \;\forall\; j \in \{1,2\}$ where $\varphi_j \in \mathbb{R}$. I.e., the model exhibits a $\mathrm{U}(1) \times \mathrm{U}(1)$ symmetry.

The Andreev-Bashkin interaction first appeared in the context of ^{4}He-^{3}He mixtures [150, 151]. It also appears in the context of neutron stars [152–154], spatially separated electronic superconductors [155] and in mixtures of BECs on optical lattices [156–158]. The Andreev-Bashkin term has been derived from a microscopic model in Ref. [159].

4.5.1 Paired phases and composite vortices

The model in Eq. (4.39) can be rewritten as

$$H[\theta_1,\theta_2] = \frac{1}{2}\int \mathrm{d}^d r \Bigg\{ \sum_{j=1,2} (m_j n_j - \sqrt{m_1 m_2}\, n_d) \left[\frac{\nabla\theta_j(\boldsymbol{r})}{m_j}\right]^2 + 2\sqrt{m_1 m_2}\, n_d \left[\frac{\nabla\theta_1(\boldsymbol{r})}{m_1}\right] \cdot \left[\frac{\nabla\theta_2(\boldsymbol{r})}{m_2}\right] \Bigg\}. \tag{4.41}$$

Due to the last term, it will be energetically favorable for the two components to flow in opposite directions (counter-flow) if n_d is positive. If n_d is negative,[9] it will be

[9] To avoid confusion, a negative n_d does not mean that there is a negative density. It only means that the effects of the drag change direction.

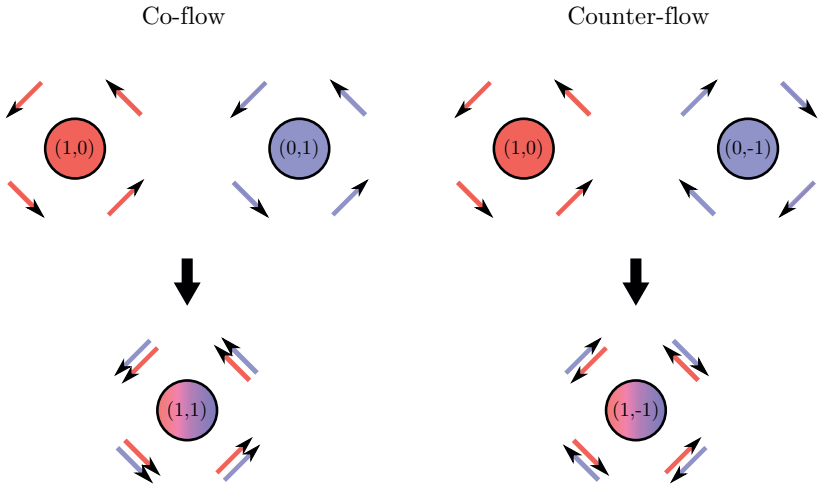

Figure 4.2: Schematic illustration of the formation of composite vortices. The arrows indicate the direction of the superfluid flow (and not the phase angle). Individual vortices and the superfluid flow of component 1 and component 2 are given by red and blue colors, respectively. The topological charge of the vortices is given by (q_1, q_2).

energetically favorable to flow in the same direction (co-flow). Consequently, it will be energetically favorable for vortices to appear in composite structures, and when the cores of two vortices of different species overlap, we call that structure a *composite vortex*. In Fig. 4.2, a schematic illustration of the formation of a co-directed and a counter-directed composite vortex is given. For a general two-component composite vortex, we may denote the topological charge by (q_1, q_2) where $q_j \in \mathbb{Z} \; \forall \; j \in \{1, 2\}$ denotes the number of phase windings around the vortex core when following the phase angle of component j. Individual vortices in each of the two components are then denoted by $(1, 0)$ and $(0, 1)$. In most cases, the relevant composite vortices to consider will be co-directed vortices $(1, 1)$ or counter-directed vortices $(1, -1)$. However, in certain cases [158, 160], composite vortices with even higher topological charge may be relevant.

Given that the strength of the Andreev-Bashkin interaction is large enough, systems governed by Eq. (4.41) can have so-called *paired phases* [156–158, 160]. These are phases where the order is associated with a certain linear combination of the phases and with a background of proliferated composite vortices [160]. For instance, in the case when $m_1 = m_2 = m$, it will be energetically cheaper to proliferate composite counter-directed vortices $(1, -1)$ instead of individual ones, given that n_d is large enough. The system then undergoes a phase transition from the ordered state, with fully broken $\mathrm{U}(1) \times \mathrm{U}(1)$ symmetry, into a paired phase with a broken $\mathrm{U}(1)$ symmetry associated with the phase sum.

4.5.2 Preemptive vortex loop proliferation

As described above, in an interacting two-component superfluid, there are different kinds of vortices, both individual and composite, that can destroy order in the system. From the point of view of the ordered phase, these can be thought of as *competing* to proliferate and disorder the system. The kind of vortex that is associated with the smallest phase stiffness will proliferate first. Now, when this kind of vortex has proliferated, the effective model for the remaining order in the system must account for the nontrivial background of proliferated vortex loops that will renormalize the phase stiffness of the remaining kinds of confined vortices. This can be done by *separation of variables* [160,161]. In this context, separation of variables is to rewrite the original model in order to separate out the linear phase combination that is unaffected by the proliferated vortex tangle.[10] The remaining phase stiffness associated with the kinds of vortices that compete to destroy the remaining order of the system, can be found by considering the prefactor of this term. If the initial vortex loop proliferation renormalizes the remaining phase stiffness such that proliferation of another kind of vortex promptly follows to destroy the remaining order in the system, we say that the phase transition is *preemptive* [160]. In other words, the preemptive transition should be understood as a direct transition from the ordered phase to the normal phase occurring due to interactions between competing vortices that renormalize the phase stiffness. Numerical results show that phase transitions governed by preemptive vortex loop proliferation may have a first-order character [160,162,163].

4.5.3 Generalized helicity modulus

With two components in the system, one must generalize the helicity modulus [Eq. (2.45)] to account for the stiffness associated with twisting linear combinations of phases. The phase twist in Eq. (2.46) can be generalized to [1,160]

$$\theta_j(\boldsymbol{r}) \to \theta_j'(\boldsymbol{r}) = \theta_j(\boldsymbol{r}) - a_j \boldsymbol{\delta} \cdot \boldsymbol{r}, \tag{4.42}$$

where $j \in \{1,2\}$ denotes the component and a_j is a real number associated with the phase twist in component j. For instance, choosing $a_2 = -a_1$ will correspond to the phase twist that measure the stiffness associated with $(1,-1)$ vortices. In Article I [1], the lattice Hamiltonian can be written on the general form

$$H[\theta_1,\theta_2] = \sum_{\mu,\boldsymbol{r}} \mathcal{H}\left(\Delta_\mu \theta_{1,\boldsymbol{r}}, \Delta_\mu \theta_{2,\boldsymbol{r}}\right). \tag{4.43}$$

By calculating the right hand side of Eq. (2.45) with the twist given in Eq. (4.42) (see also Ref. [160]), the generalized helicity modulus can be written on the compact form

$$\Upsilon_{\mu,(a_1,a_2)} = a_1^2 \Upsilon_{\mu,11} + 2a_1 a_2 \Upsilon_{\mu,12} + a_2^2 \Upsilon_{\mu,22}, \tag{4.44}$$

[10] In the example above, when $(1,-1)$ vortices proliferate, the phase gradient combination $\nabla\theta_1 + \nabla\theta_2$ is unaffected.

where

$$\Upsilon_{\mu,jk} = \frac{1}{L^d}\Bigg[\left\langle \sum_{\boldsymbol{r}} \partial_j\partial_k\mathcal{H}\right\rangle - \beta\left\langle\left(\sum_{\boldsymbol{r}}\partial_j\mathcal{H} - \left\langle\sum_{\boldsymbol{r}}\partial_j\mathcal{H}\right\rangle\right)\left(\sum_{\boldsymbol{r}}\partial_k\mathcal{H} - \left\langle\sum_{\boldsymbol{r}}\partial_k\mathcal{H}\right\rangle\right)\right\rangle\Bigg], \tag{4.45}$$

and where

$$\partial_j\mathcal{H} = \frac{\partial\mathcal{H}\left(\Delta_\mu\theta_{1,\boldsymbol{r}}, \Delta_\mu\theta_{2,\boldsymbol{r}}\right)}{\partial\Delta_\mu\theta_{j,\boldsymbol{r}}}, \tag{4.46}$$

is short-hand notation. The quantities $\Upsilon_{\mu,11}$ and $\Upsilon_{\mu,22}$ correspond to the helicity modulus of the two single components and $\Upsilon_{\mu,12}$ can be interpreted as a renormalized drag coefficient [160].

4.6 Unconventional Coulomb plasmas

In Articles II and III [2,3], we study a 2D two-component classical Coulomb plasma that is related to rotating two-component superfluids with an Andreev-Bashkin interaction (see Sec. 4.6.1). This plasma also relates to fractional quantum Hall wave functions [164]. We call this plasma *unconventional* as the particles interact through two *different* Coulomb interactions. For reasons to be discussed in Sec. 4.6.2, we also call it the *Moore-Read plasma*. The canonical partition function of this plasma can be written as

$$\mathcal{Z} = \int\left(\prod_{i=1}^{N}\mathrm{d}^2 z_i\right)\left(\prod_{a=1}^{N}\mathrm{d}^2 w_a\right)\mathrm{e}^{-S[\boldsymbol{z},\boldsymbol{w}]},$$

$$\begin{aligned} S[\boldsymbol{z},\boldsymbol{w}] = &- Q_2^2\sum_{a<b=1}^{N}\ln|\boldsymbol{w}_a-\boldsymbol{w}_b| - (Q_1^2+Q_2^2)\sum_{i<j=1}^{N}\ln|\boldsymbol{z}_i-\boldsymbol{z}_j| \\ &+ Q_2^2\sum_{a,i=1}^{N}\ln|\boldsymbol{w}_a-\boldsymbol{z}_i| + V_{\mathrm{BG}}[\boldsymbol{z}], \end{aligned} \tag{4.47}$$

where $\boldsymbol{w}_a$ are the position vectors of the particles of the first component and $\boldsymbol{z}_i$ are the position vectors of the particles of the second component. There are N particles of each component. The particles can be thought of as carrying two charges each that interact logarithmically by two different channels. The w particles carry zero charge in the first channel and charge $-Q_2$ in the second channel, whereas the z particles carry charge Q_1 in the first channel and charge Q_2 in the second channel. Moreover, charges in the first channel do not interact with charges in the second channel. From this, it should be clear that two z particles will interact repulsively with strength $Q_1^2+Q_2^2$, where the Q_1^2 term comes from the charges interacting in channel 1 and the Q_2^2 term comes from the charges interacting in channel 2. Two w particles will interact repulsively with

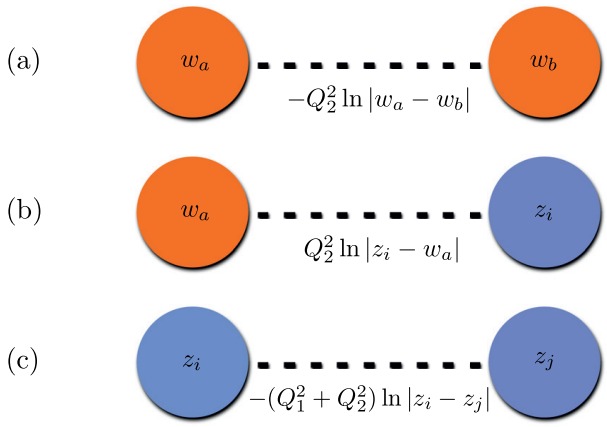

Figure 4.3: Graphical overview of the intracomponent and the intercomponent interactions in the Moore-Read plasma. The interaction between w particles is repulsive with strength Q_2^2, as shown in (a). The interaction between w and z particles is attractive with strength Q_2^2, as shown in (b). The interaction between z particles, shown in (c), is repulsive with strength $Q_1^2 + Q_2^2$.

strength Q_2^2 coming from the charges interacting in channel 2. There is no contribution from channel 1 as the value of the charge in this channel is zero. A w particle and a z particle will interact attractively with strength Q_2^2 as the two particles carry charges with opposite signs but with same strength in channel 2. Here, there is also no contribution from channel 1 as the w particle carry zero charge in this channel. We must also add a short-range hard-core repulsion to regularize the attractive interactions between w and z particles [2]. The intracomponent and intercomponent interactions are summarized in Fig. 4.3. The term $V_{\mathrm{BG}}[\boldsymbol{z}]$ in Eq. (4.47) accounts for the interactions with the neutralizing background that must be included to ensure neutrality in channel 1.

4.6.1 Mapping to a Coulomb plasma

As detailed in Sec. 2.7.1, the 2D XY model can be written in terms of vortices (or charges) interacting logaritmically with distance. Here, we will show that a two-component rotating Bose-Einstein condensate with an Andreev-Bashkin interaction can be mapped onto the unconventional Coulomb plasma described above. Generalizing Eq. (4.28) for two components, and including the Andreev-Bashkin interaction yields a model that can be written as

$$\mathcal{Z} = \int \mathcal{D}\,\theta_1 \int \mathcal{D}\,\theta_2\, \mathrm{e}^{-\beta H[\theta_1,\theta_2]}, \tag{4.48}$$

$$H[\theta_1,\theta_2]=\frac{1}{2}\int \mathrm{d}^2r\Bigg\{\sum_{j=1,2} m_j n_j\left[\frac{\nabla\theta_j(\boldsymbol{r})}{m_j}-\boldsymbol{\Theta}(\boldsymbol{r})\right]^2 - \sqrt{m_1m_2}n_d\left[\frac{\nabla\theta_1(\boldsymbol{r})}{m_1}-\frac{\nabla\theta_2(\boldsymbol{r})}{m_2}\right]^2\Bigg\}, \tag{4.49}$$

where $\boldsymbol{\Theta}(\boldsymbol{r})=\boldsymbol{\Omega}\times\boldsymbol{r}$ with $\boldsymbol{\Omega}=\Omega\hat{\boldsymbol{z}}$. In 3D, this model has been investigated in Refs. [165, 166]. The Hamiltonian in Eq. (4.49) can be rewritten on the form

$$H[\theta_1,\theta_2]=\frac{1}{2}\int \mathrm{d}^2r\sum_{j,k=1,2}\left[\nabla\theta_j(\boldsymbol{r})-m_j\boldsymbol{\Theta}(\boldsymbol{r})\right]R_{jk}\left[\nabla\theta_k(\boldsymbol{r})-m_k\boldsymbol{\Theta}(\boldsymbol{r})\right], \tag{4.50}$$

where

$$R=\begin{pmatrix}\frac{n_1}{m_1}-\frac{1}{m_1}\sqrt{\frac{m_2}{m_1}}n_d & \frac{n_d}{\sqrt{m_1m_2}}\\ \frac{n_d}{\sqrt{m_1m_2}} & \frac{n_2}{m_2}-\frac{1}{m_2}\sqrt{\frac{m_1}{m_2}}n_d\end{pmatrix}. \tag{4.51}$$

Similar to that described in Sec. 4.2.1, the phase gradient can be decomposed into a longitudinal and a transverse part, and we disregard the longitudinal spin wave part of the phase gradient. Moreover, the vortices are found by taking the curl of the phase gradient such that

$$\nabla\times\left[\nabla\theta_j(\boldsymbol{r})-m_j\boldsymbol{\Theta}(\boldsymbol{r})\right]=2\pi\left[l_j(\boldsymbol{r})-\frac{m_j}{\pi}\Omega\right]\hat{\boldsymbol{z}}, \tag{4.52}$$

where $l_j(\boldsymbol{r})$ is the integer-valued vortex field of component j. Taking the curl on both sides of Eq. (4.52) followed by a Fourier transformation yields

$$\boldsymbol{U}_j(\boldsymbol{q})=2\pi\mathrm{i}\frac{\boldsymbol{q}\times\left[l_j(\boldsymbol{q})-(2\pi)^2f_j\delta(\boldsymbol{q})\right]\hat{\boldsymbol{z}}}{q^2}, \tag{4.53}$$

where $\boldsymbol{U}_j(\boldsymbol{q})$ is the Fourier transform of $\boldsymbol{U}_j(\boldsymbol{r})=[\nabla\theta_j(\boldsymbol{r})]_T-m_j\boldsymbol{\Theta}(\boldsymbol{r})$ and $f_j=m_j\Omega/\pi$ is the number density of rotationally induced vortices in component j [see Eq. (4.29)]. By Fourier transforming the Hamiltonian in Eq. (4.50) and inserting Eq. (4.53), the model is written

$$\mathcal{Z}=\int\mathcal{D}\,l_1\int\mathcal{D}\,l_2\,\mathrm{e}^{-\beta H[l_1,l_2]},$$
$$H[l_1,l_2]=\frac{1}{2}\int\mathrm{d}^2q\sum_{j,k=1,2}\left[l_j(\boldsymbol{q})-(2\pi)^2f_j\delta(\boldsymbol{q})\right]\frac{R_{jk}}{q^2}\left[l_k(-\boldsymbol{q})-(2\pi)^2f_k\delta(-\boldsymbol{q})\right]. \tag{4.54}$$

Transforming the Hamiltonian back to real space yields

$$H[l_1,l_2]=\frac{1}{2}\int\mathrm{d}^2r\int\mathrm{d}^2r'\sum_{j,k=1,2}\left[l_j(\boldsymbol{r})-f_j\right]R_{jk}\left[l_k(\boldsymbol{r}')-f_k\right]V(\boldsymbol{r}'-\boldsymbol{r}), \tag{4.55}$$

where

$$V(\boldsymbol{r}'-\boldsymbol{r})=\int\mathrm{d}^2q\frac{1}{q^2}\,\mathrm{e}^{\mathrm{i}\boldsymbol{q}\cdot(\boldsymbol{r}'-\boldsymbol{r})}=-2\pi\ln\left|\boldsymbol{r}'-\boldsymbol{r}\right|. \tag{4.56}$$

In order to obtain a model with a fixed number of vortices, similar to Eq. (4.47), one must neglect the effect of thermally induced vortex pairs by using

$$l_j(\boldsymbol{r}) = \sum_{a=1}^{N_j} \delta(\boldsymbol{r} - \boldsymbol{r}_{j,a}), \tag{4.57}$$

where N_j is the number of rotationally induced vortices of component j. By inserting Eq. (4.57) in Eq. (4.55) and writing out the component sums, the Hamiltonian is written

$$\begin{aligned} H[\boldsymbol{r}_1, \boldsymbol{r}_2] = -2\pi \Bigg[& R_{11} \sum_{a<b=1}^{N_1} \ln|\boldsymbol{r}_{1,a} - \boldsymbol{r}_{1,b}| + R_{12} \sum_{a=1}^{N_1} \sum_{b=1}^{N_2} \ln|\boldsymbol{r}_{1,a} - \boldsymbol{r}_{2,b}| \\ & + R_{22} \sum_{a<b=1}^{N_2} \ln|\boldsymbol{r}_{2,a} - \boldsymbol{r}_{2,b}| - (R_{11} f_1 + R_{12} f_2) \sum_{a=1}^{N_1} I(\boldsymbol{r}_{1,a}) \\ & - (R_{12} f_1 + R_{22} f_2) \sum_{a=1}^{N_2} I(\boldsymbol{r}_{2,a}) \Bigg], \end{aligned} \tag{4.58}$$

where

$$I(\boldsymbol{r}_{j,a}) = \int \mathrm{d}^2 r \ln|\boldsymbol{r} - \boldsymbol{r}_{j,a}| \,. \tag{4.59}$$

The Moore-Read plasma in Eq. (4.47) is a special case of Eq. (4.58) for specific values of m_1, m_2, n_1, n_2 and n_d. To obtain equally many rotationally induced vortices, we must choose $m_1 = m_2 = m$ such that $f_1 = f_2 = f$. Moreover, by absorbing the factor $2\pi\beta/m$ in the density coefficients (n_1, n_2 and n_d), the Moore-Read plasma is recovered by $R_{11} = Q_2^2$, $R_{12} = -Q_2^2$ and $R_{22} = Q_1^2 + Q_2^2$ (i.e., $\boldsymbol{r}_1 = \boldsymbol{w}$ and $\boldsymbol{r}_2 = \boldsymbol{z}$). This means that the Moore-Read plasma corresponds to a two-component rotating BEC with coefficients

$$\begin{aligned} n_1 &= 0, \\ n_2 &= Q_1^2, \\ n_d &= -Q_2^2. \end{aligned} \tag{4.60}$$

We also identify the term $V_{\mathrm{BG}}[\boldsymbol{z}] = fQ_1^2 \sum_{a=1}^{N} I(\boldsymbol{z}_a)$ as the interaction between the z particles and a negative uniform background with charge density fQ_1 in channel 1 and zero charge density in channel 2.

4.6.2 Relation to fractional quantum Hall states

In effective 2D electron systems subjected to low temperatures and strong magnetic fields, the Hall conductivity σ shows quantized plateaus, $\sigma = \nu e^2/h$, where e is the elementary charge and h is Planck's constant. For the fractional quantum Hall effect, the filling factor ν takes on quantized values, $\nu = p/q$, where $p, q \in \mathbb{Z}$ with no common factors.

Theoretical understanding of the fractional quantum Hall effect can be achieved by proposing trial wave functions with fractionally charged quasiparticles. This was first

done by Robert B. Laughlin in 1983 [167, 168], proposing the so-called Laughlin trial wave functions, which explains the $\nu = 1/q$ fractional quantum Hall states.[11] The squared norm of these trial wave functions maps to the partition function of a 2D one-component Coulomb plasma. This is a plasma of N identical particles with charge Q, and is a special case of the Moore-Read plasma presented in Eq. (4.47) above, in the limit $Q_2^2 = 0$. Recently, Bonderson, Gurarie and Nayak showed that the so-called Ising-type quantum Hall states can be mapped to classical Coulomb plasmas [164]. In particular, the squared norm of the Moore-Read trial wave functions maps to the unconventional plasma, given in Eq. (4.47). By referring to screening properties of the classical plasmas, one can verify the existence of quasiparticles in the actual quantum Hall states [164].

4.6.3 Two-dimensional melting

In Article III [3], the Moore-Read plasma is studied under conditions where the particles crystallize into a solid structure. This section is a brief reminder of solids and melting in two dimensions.

In opposition to the familiar case of three dimensional solids, a solid in two dimensions does not exhibit long-range translational order. At finite temperatures, the long-range translational order is destroyed by long-wavelength fluctuations as stated by the Mermin-Wagner theorem [25, 169]. Instead there is quasi long-range translational order with a power law decay in the translational correlation function. Although the 2D solid does not exhibit long-range translational order, it does exhibit long-range *orientational* order [170]. The orientational correlations decay exponentially to a nonzero value.[12]

Upon heating, a solid undergoes a melting transition into an incoherent liquid with exponentially decaying correlations for both translational and orientational order. The melting of 2D solids is theoretically considered by the so-called Kosterlitz-Thouless-Halperin-Nelson-Young (KTHNY) theory [173–176]. According to the KTHNY theory, the 2D solid first melts into a hexatic liquid with short-range translational order and quasi long-range orientational order. The transition is a BKT-like transition where the quasi long-range translational order is destroyed by unbinding of dislocation defects. The hexatic liquid will display the quasi long-range orientational order until a higher transition temperature is reached. At this point the quasi long-range orientational order is destroyed by unbinding of disclinations in a BKT phase transition, and the system will turn into an isotropic vortex liquid with short-range orientational order.

However, in opposition to the KTHNY theory, the 2D solid may melt directly into a liquid by a premature unbinding of disclinations. This was pointed out already from the very beginning by Halperin and Nelson [173]. It has turned out to be a difficult task to investigate the nature of 2D melting. The KTHNY scenario has been confirmed in some

[11] In 1998, Laughlin was jointly awarded the Nobel prize in physics for this work.

[12] It should also be mentioned that there are studies that argue for the absence of a finite-temperature solid phase in the 2D one-component plasma [65, 66, 171, 172]. This issue has been addressed in Article III [3], and we find that these claims are false.

cases [177–182], whereas other works find that the transition is first-order [63, 183, 184]. This has lead to an understanding that the nature of 2D melting is not universal, but dependent on specific properties in the system.

4.6.4 Brief summary of Article II and III

The Moore-Read plasma has two well-known limiting cases. In the case when $Q_2^2 = 0$, only the interactions in channel 1 are retained, and we have the 2D one-component plasma. Early Monte Carlo simulations of this model found that it undergoes a weak first-order melting transition at $Q_1^2 \approx 140$ [63,183–185]. In the other case, when $Q_1^2 = 0$, only the interactions in channel 2 are retained, and we have the 2D two-component neutral Coulomb plasma. This plasma played a very important role for the understanding of the BKT-transition, and is well-studied, both theoretically and numerically [14, 27, 28, 41, 42, 186–188]. At low density, this plasma undergoes a BKT charge-unbinding transition at $Q_2^2 = 4$.

For reasons given in Sec. 3.2.2 and in the spirit of Refs. [14, 63], the simulations in both Articles II and III are performed with spherical boundary conditions. Due to the hard-core repulsion associated with the particles, there is a finite density of particles, given by the packing fraction $\eta \propto Ns/A$, where s is the area occupied by a single particle and A is the surface area of the entire system. The physics of plasmas that undergo a charge-unbinding transition is dependent on the density [14, 42, 186].[13] In this work we studied the plasma for a few different values of small density. The screening properties were investigated by measuring a generalized inverse dielectric constant that accounts for charges interacting in two different channels. The inverse dielectric constant is analogous to the helicity modulus in 2D XY-like models [30, 189, 190], and the methods outlined in Sec. 3.7 can be used to investigate the charge-unbinding transition in the Moore-Read plasma.

In Article II [2], we investigate the Moore-Read plasma in the case when the value of Q_1 is 0 and 2. When $Q_1 = 0$, the simulations can be thought of as a reference for the $Q_1 = 2$ case, as the Moore-Read plasma is reduced to the 2D two-component neutral Coulomb plasma in this case. When $Q_1 = 2$, we find that the Moore-Read plasma undergoes a BKT charge-unbinding transition. The critical coupling of this transition is $Q_{2,\mathrm{c}}^2 \approx 4$ in the low-density limit. For the densities that were investigated, the critical coupling increased with higher density in accordance with the $Q_1 = 0$ case. When $Q_2^2 < Q_{2,\mathrm{c}}^2$ the w and z particles should be considered as free and capable of screening test particles. When $Q_2^2 > Q_{2,\mathrm{c}}^2$ the w and z particles are bounded in pairs due to the attractive interaction in channel 2, and consequently, they are incapable of screening test charges interacting in channel 2. This means that in the case of $Q_2^2 = 3$, that is, the important parameter value for the Ising-type quantum Hall states, the plasma is screening. This result verifies that Ising-type quantum Hall states can possess quasiparticles with exotic

[13] Results from simulations of the 2D two-component neutral Coulomb plasma show that the critical coupling increases with higher density. When density is large, the phase transition changes from a BKT transition to a first-order transition.

properties.

In Article III [2], the focus is on large values of Q_1^2. In order to detect the 2D solid phase, an azimuthally averaged structure factor that is appropriate for the spherical geometry is measured. The results show that there is a solid phase in the Moore-Read plasma for large values of Q_1^2. Here, this means that the z particles freeze due to the strong interactions in channel 1. In addition, we observe that the w particles also exhibit signatures of being in a solid state. This can be attributed to the attractive interactions between w and z particles in channel 2, which means that the w particles tend to be co-centered with the z particles. This phenomenon is also observed for values of $Q_2^2 < 4$ when the w and z particles are considered to be on the metallic side of the charge-unbinding transition. We find this phenomenon to be analogous to the *modulated vortex liquid* in a two-component rotating Bose-Einstein condensate, reported in Ref. [166].

4.7 Two-component London superconductors

The London superconductor model of a two-component charged condensate with independently conserved components is given by

$$H[\theta_1, \theta_2, \boldsymbol{A}] = \int \mathrm{d}^d r \left\{ \sum_{j=1,2} \frac{\rho_j}{2} \left[\nabla\theta_j(\boldsymbol{r}) - e_j \boldsymbol{A}(\boldsymbol{r})\right]^2 + \frac{1}{2}[\nabla \times \boldsymbol{A}(\boldsymbol{r})]^2 \right\}, \tag{4.61}$$

where $\rho_j \equiv g|\psi_{j,0}|^2$ is the *bare stiffness* and e_j is the charge coupling of component j. The two components interact in an indirect manner as they both are coupled to the same fluctuating gauge field.

4.7.1 Charged and neutral modes

By separation of variables, it is possible to rewrite the model in Eq. (4.61) as [128,191,192]

$$\begin{aligned} H[\theta_1, \theta_2, \boldsymbol{A}] = \frac{1}{2} \int \mathrm{d}^d r \Bigg\{ & \frac{\rho_1\rho_2}{m_0^2} \left[e_2\nabla\theta_1(\boldsymbol{r}) - e_1\nabla\theta_2(\boldsymbol{r})\right]^2 + [\nabla \times \boldsymbol{A}(\boldsymbol{r})]^2 \\ & + \frac{1}{m_0^2} \left[e_1\rho_1\nabla\theta_1(\boldsymbol{r}) + e_2\rho_2\nabla\theta_2(\boldsymbol{r}) - m_0^2\boldsymbol{A}(\boldsymbol{r})\right]^2 \Bigg\}, \end{aligned} \tag{4.62}$$

where $m_0^2 \equiv \rho_1 e_1^2 + \rho_2 e_2^2$. The first term identifies the neutral mode, which does not couple to the gauge field, whereas the last term identifies the charged mode, characterized by its coupling to the gauge field. Note that the neutral mode identifies a linear combination of the phases that is gauge-invariant. Eq. (4.62) is invariant under the global transformation

$$e_2\theta_1(\boldsymbol{r}) - e_1\theta_2(\boldsymbol{r}) \to e_2\theta_1(\boldsymbol{r}) - e_1\theta_2(\boldsymbol{r}) + \varphi, \tag{4.63}$$

where $\varphi \in \mathbb{R}$. It is also invariant under the local gauge transformation

$$\begin{aligned} e_1\rho_1\theta_1(\boldsymbol{r}) + e_2\rho_2\theta_2(\boldsymbol{r}) &\to e_1\rho_1\theta_1(\boldsymbol{r}) + e_2\rho_2\theta_2(\boldsymbol{r}) + \chi(\boldsymbol{r}), \\ \boldsymbol{A}(\boldsymbol{r}) &\to \boldsymbol{A}(\boldsymbol{r}) + \frac{1}{m_0^2}\nabla\chi(\boldsymbol{r}), \end{aligned} \tag{4.64}$$

where $\chi(\boldsymbol{r})$ is an arbitrary real-valued function. I.e., the symmetries of the two-component London superconductor are a global U(1) symmetry associated with the phase combination of the neutral mode and a local U(1) gauge symmetry associated with the phase combination of the charged mode.

As for the one-component London superconductor, we can investigate the vortex interactions by rewriting the model in terms of vortex elements [1, 128]. In 3D, the result is

$$\mathcal{Z} = \int \mathcal{D}\,\boldsymbol{m}_1 \int \mathcal{D}\,\boldsymbol{m}_2 \, \exp\left[-2\pi^2\beta \int \mathrm{d}^3q \sum_{j,k=1,2} \boldsymbol{m}_j(\boldsymbol{q}) V_{jk}(q^2) \boldsymbol{m}_k(-\boldsymbol{q})\right], \tag{4.65}$$

where $\boldsymbol{m}_j(\boldsymbol{q})$ is the Fourier transform of the integer-valued vortex field of component j and $V_{jk}(q^2)$ is the vortex interaction potential, given by

$$V_{jk}(q^2) = \frac{\rho_j\delta_{jk} - e_j\rho_j e_k\rho_k/m_0^2}{q^2} + \frac{e_j\rho_j e_k\rho_k/m_0^2}{q^2 + m_0^2}. \tag{4.66}$$

The first term is a long-ranged Coulomb potential, while the second term is a screened Yukawa potential with m_0 as the inverse bare screening length. This means that the magnetic flux tubes of the two-component London superconductor have a rather complex interaction with both long-ranged and short-ranged contributions. Compared with the one-component London superconductor in Eq. (4.22), the gauge field is no longer fully capable of screening the vortex interactions such that there is a nonzero Coulomb term left in the potential. Note that at short distances compared with the bare screening length ($q^2 \gg m_0^2$), the contributions from the gauge field in Eq. (4.66) effectively cancel out. I.e., vortices separated by a distance much shorter than the bare screening length will interact similar to a decoupled two-component neutral condensate. However, for vortices outside the bare screening length, the effects of the gauge field will modify the interactions and, in particular, mediate intercomponent vortex interactions.

Similar to the two-component superfluid with Andreev-Bashkin interactions, the two-component London superconductor may exhibit composite vortices and paired phases [163]. Specifically, in the case when the charge coupling $e_1 = e_2 = e$ is large, the composite $(1, 1)$ vortices can be mapped to an ordinary flux tube of a one-component London superconductor with finite energy per unit length. Starting in the ordered phase, the system will undergo a phase transition with proliferation of $(1, 1)$ vortices that will disorder the charged sector of the model. However, since these vortices are incapable of disordering the neutral sector, the order associated with the first term of Eq. (4.62) is retained. The resulting phase is a superfluid paired phase where the global U(1) symmetry associated with the neutral mode is broken. This phase is often called

a *metallic superfluid* [128, 193]. With an external magnetic field, this model has been extensively studied in the context of liquid metallic hydrogen [128, 191, 193–196]. Also, it appears as an effective model of easy-plane quantum antiferromagnets [163, 197–199].

4.7.2 Brief summary of main results

In Sec. IV of Article I [1],[14] the two-component London superconductor was investigated in the case where $e_1 = e_2 = e$. In particular, we focused on the case with stiffness disparity, $\rho_1 \neq \rho_2$. When disparity is large, there are two clearly separated phase transitions that can be understood by proliferation of individual topological defects [$(1,0)$ and $(0,1)$] (see also Refs. [128, 133]). When disparity is small we find a region of competing topological defects that is characterized by a merger of transition lines. Hence, there is a direct transition from the ordered state to the normal state, and we find clear signatures of a first-order transition along this line also in the case when $\rho_1 \neq \rho_2$. When the charge e increases, the region with a direct transition line extends into the region with larger and larger disparity. I.e., for fixed stiffnesses that are not too different, there will be a merger of transition lines with increasing charge. However, at even higher charges, the direct transition line will eventually split into two transition lines with a metallic superfluid phase sandwiched in between. The transition from the ordered phase into the metallic superfluid phase, can be understood in terms of proliferation of composite $(1,1)$ vortices that effectively can be mapped onto a one-component superconductor with effective stiffness $\rho' = \rho_1 + \rho_2$. The metallic superfluid state is destroyed by proliferation of individual $(1,0)$ and $(0,1)$ vortices that effectively can be mapped onto a one-component superfluid with effective stiffness $\rho' = \rho_1\rho_2/(\rho_1 + \rho_2)$.

4.8 Two-component London superconductors with an Andreev-Bashkin interaction

The main objective of Article I [1], is to study a two-component London superconductor with an additional Andreev-Bashkin drag term in three dimensions. The model can be written as

$$H[\theta_1, \theta_2, \boldsymbol{A}] = \frac{1}{2}\int \mathrm{d}^3 r \Bigg\{ \sum_{j=1,2} \rho_j \left[\nabla\theta_j(\boldsymbol{r}) - e_j \boldsymbol{A}(\boldsymbol{r})\right]^2 + \left[\nabla \times \boldsymbol{A}(\boldsymbol{r})\right]^2 - \rho_d \left[\nabla\theta_1(\boldsymbol{r}) - e_1\boldsymbol{A}(\boldsymbol{r}) - \nabla\theta_2(\boldsymbol{r}) + e_2\boldsymbol{A}(\boldsymbol{r})\right]^2 \Bigg\}, \tag{4.67}$$

where ρ_j is the bare stiffness of component j and ρ_d is the strength of the Andreev-Bashkin interaction. In this system, the two components can interact both via the gauge field and via the dissipationless drag term. As for the two-component London

[14] In the context of Article I, the results of the two-component London superconductor appear as a special case of the more involved model discussed below in Sec. 4.8.

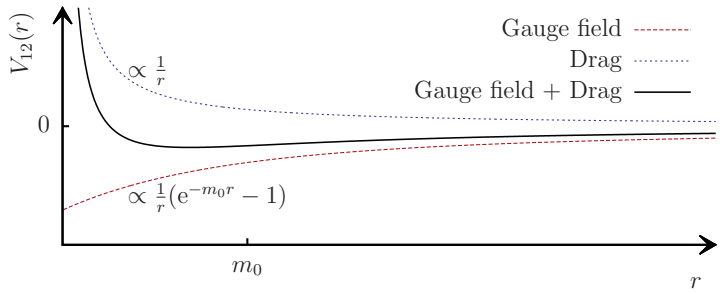

Figure 4.4: Schematic illustration of the intercomponent interaction $V_{12}(r)$ of the Andreev-Bashkin coupled two-component London superconductor. For this example, the coefficients $\rho_1 = \rho_2 = 1.0$, $e_1 = e_2 = 1.0$ and $\rho_d = 0.2$ were used.

superconductor, this model can be rewritten in a form that explicitly identifies the charged and neutral modes,

$$H[\theta_1, \theta_2, \boldsymbol{A}] = \frac{1}{2} \int \mathrm{d}^d r \Big\{ \frac{\rho_1\rho_2 - \rho_2(\rho_1 + \rho_2)}{m_0^2} \left[e_2 \nabla\theta_1(\boldsymbol{r}) - e_1 \nabla\theta_2(\boldsymbol{r}) \right]^2 + \left[\nabla \times \boldsymbol{A}(\boldsymbol{r}) \right]^2 + \frac{1}{m_0^2} \left[e_j R_{j1} \nabla\theta_1(\boldsymbol{r}) + e_j R_{j2} \nabla\theta_2(\boldsymbol{r}) - m_0^2 \boldsymbol{A}(\boldsymbol{r}) \right]^2 \Big\}, \quad (4.68)$$

where

$$R = \begin{pmatrix} \rho_1 - \rho_d & \rho_d \\ \rho_d & \rho_2 - \rho_d \end{pmatrix}, \quad (4.69)$$

and

$$m_0^2 \equiv (\rho_1 - \rho_d) e_1^2 + (\rho_2 - \rho_d) e_2^2 + 2\rho_d e_1 e_2. \quad (4.70)$$

In Eq. (4.68), sum over repeated component indices is assumed. This model exhibits a global U(1) symmetry associated with the phase combination of the neutral mode and a local U(1) gauge symmetry associated with the phase combination of the charged mode. In terms of vortex elements, the model can be written as given in Eq. (4.65) with interaction potential

$$V_{jk}(q^2) = \frac{R_{jk} - e_l e_m R_{lj} R_{mk}/m_0^2}{q^2} + \frac{e_l e_m R_{lj} R_{mk}/m_0^2}{q^2 + m_0^2}, \quad (4.71)$$

The intercomponent interaction, given by $V_{12}(q^2)$, will include a Coulomb contribution from the Andreev-Bashkin drag, and both a Coulomb and a Yukawa term from the gauge field mediated interactions. At short vortex separations, the contribution from the drag will dominate. However, at large separations, the gauge field and drag will compete on an equal footing. In Fig. 4.4, a schematic plot that illustrates this competition is given. Observe that the drag and the gauge field interactions individually yield a monotonically decaying interaction potential. However, their combined efforts can lead to an interesting nonmonotonic decay.

It is not straightforward to convert the continuum formulation of the current-current interaction into a discrete formulation appropriate for numerical simulations. However,

as pointed out in Ref. [160], the continuum physics is adequately reproduced by using the Villain model [see Eq. (2.70)] [38, 39]. The lattice formulation of Eq. (4.67) thus reads

$$H[\theta_1, \theta_2, \boldsymbol{A}; \beta] = -\frac{1}{\beta} \sum_{\mu, \boldsymbol{r}} \ln \left(\sum_{n_{1,\mu,\boldsymbol{r}}} \sum_{n_{2,\mu,\boldsymbol{r}}} \mathrm{e}^{-S} \right), \tag{4.72}$$

where

$$S = \frac{\beta}{2} \left[\rho_1 u_{1,\mu,\boldsymbol{r}}^2 + \rho_2 u_{2,\mu,\boldsymbol{r}}^2 - \rho_d (u_{1,\mu,\boldsymbol{r}} - u_{2,\boldsymbol{r},\mu})^2 + \left(\sum_{\nu,\lambda} \varepsilon_{\mu\nu\lambda} \Delta_\nu A_{\lambda,\boldsymbol{r}} \right)^2 \right], \tag{4.73}$$

$$u_{j,\mu,\boldsymbol{r}} = \Delta_\mu \theta_{j,\boldsymbol{r}} - e_j A_{\mu,\boldsymbol{r}} - 2\pi n_{j,\mu,\boldsymbol{r}}, \tag{4.74}$$

and $n_{j,\mu,\boldsymbol{r}} \in \mathbb{Z} \; \forall \; j, \mu, \boldsymbol{r}$.

4.8.1 Brief summary of main results

In Sec. V A of Article I [1], we investigate the model in Eq. (4.73) in the case of equal stiffnesses $\rho_1 = \rho_2 = \rho = 1$ and with equal charges $e_1 = e_2 = e$. We also restrict ourselves to positive ρ_d. In this case, the contributions to the intercomponent interactions from the gauge field and the drag term are of opposite signs, see Fig. 4.4. In particular, we map out the phase diagram as a function of ρ_d and e, and find that the model exhibits two competing paired phases. When e is large and ρ_d is small, we find a metallic superfluid phase associated with order in the neutral sector of Eq. (4.68). This phase can be entered from the ordered phase by proliferation of $(1, 1)$ vortices that will destroy the superconductivity in the system. The transition is similar to the phase transition of an ordinary one-component superconductor with effective stiffness $\rho' = 2\rho$. The metallic superfluid phase is destroyed by proliferation of individual $(1, 0)$ and $(0, 1)$ vortices that effectively can be mapped onto a one-component superfluid with effective stiffness $\rho' = (\rho - 2\rho_d)/2$. For high values of ρ_d, we find a paired superconducting phase that can be associated with order in the charged sector of Eq. (4.68). The phase can be reached by proliferation of composite $(1, -1)$ vortices that will destroy the order associated with the neutral sector of the model. These vortex excitations can effectively be mapped onto a one-component superfluid with renormalized stiffness $\rho' = 2(\rho - 2\rho_d)$. The paired superconducting phase is destroyed by proliferation of individual $(1, 0)$ and $(0, 1)$ vortices that effectively can be mapped onto a one-component superconductor with doubled electric charge $e' = 2e$ and effective stiffness $\rho' = \rho/2$. The effective doubling of the electric charge occurs because the order of the paired phase is associated with the phase sum, i.e., only co-directed electrical current is dissipationless in this phase. In accordance with previous works [160, 163], we find a first-order transition of the direct transition line in regions that can be associated with strong competition between different topological defects.

4.9 Two-component Ginzburg-Landau superconductors

The Ginzburg-Landau theory for superconductors, described in Sec. 4.1.3 for a one-component superconductor, can be generalized to two components. For a two-component charged condensate that is minimally coupled to the same electromagnetic gauge field, the Ginzburg-Landau model can be written as[15]

$$H[\psi_1,\psi_2,\boldsymbol{A}] = \int \mathrm{d}^d r \Bigg(\sum_{j=1,2} \left\{ \frac{g_j}{2} \left|[\nabla - \mathrm{i}e_j \boldsymbol{A}(\boldsymbol{r})]\psi_j(\boldsymbol{r})\right|^2 + \frac{\alpha_j}{2}\left|\psi_j(\boldsymbol{r})\right|^2 + \frac{u_j}{4!}\left|\psi_j(\boldsymbol{r})\right|^4 \right\} + \frac{2u_{12}}{4!}\left|\psi_1(\boldsymbol{r})\right|^2\left|\psi_2(\boldsymbol{r})\right|^2 + \frac{\gamma}{2}\left[\psi_1^*(\boldsymbol{r})\psi_2(\boldsymbol{r}) + \psi_1(\boldsymbol{r})\psi_2^*(\boldsymbol{r})\right] + \frac{1}{2}[\nabla\times\boldsymbol{A}(\boldsymbol{r})]^2 \Bigg). \tag{4.75}$$

In the following, we will investigate the special case of Eq. (4.75) that exhibits an SU(2) symmetry. By appropriate choices of the free parameters, Eq. (4.75) can be written as

$$H[\boldsymbol{\Psi},\boldsymbol{A}] = \int \mathrm{d}^d r \Bigg\{ \frac{1}{2}\left|[\nabla - \mathrm{i}e\boldsymbol{A}(\boldsymbol{r})]\,\boldsymbol{\Psi}(\boldsymbol{r})\right|^2 + \frac{\alpha}{2}\left|\boldsymbol{\Psi}(\boldsymbol{r})\right|^2 + \frac{u}{4!}\left|\boldsymbol{\Psi}(\boldsymbol{r})\right|^4 + \frac{1}{2}[\nabla\times\boldsymbol{A}(\boldsymbol{r})]^2 \Bigg\}, \tag{4.76}$$

where $\boldsymbol{\Psi}^\dagger(\boldsymbol{r}) = (\psi_1^*(\boldsymbol{r}), \psi_2^*(\boldsymbol{r}))$. Eq. (4.76) is invariant under the SU(2) transformation,

$$\boldsymbol{\Psi}(\boldsymbol{r}) \to U\boldsymbol{\Psi}(\boldsymbol{r}), \tag{4.77}$$

where U is a 2×2 unitary matrix with $|U| = 1$.

4.9.1 Relation to deconfined quantum criticality

There has been considerable interest in models similar to Eq. (4.76), particularly since they appear as effective models of quantum antiferromagnets and are related to the concept of *deconfined quantum criticality* (DQC). The quantum Hamiltonian of Heisenberg spin $S = 1/2$ operators $\hat{\boldsymbol{S}}_i$ on a 2D square lattice is given by

$$H = J\sum_{\langle i,j\rangle} \hat{\boldsymbol{S}}_i \cdot \hat{\boldsymbol{S}}_j + \ldots, \tag{4.78}$$

where the sum is over all nearest-neighbor pairs and $J > 0$ is the antiferromagnetic nearest-neighbor coupling. Here, ... describes additional terms that can be added and possibly change the ground state of the system. In the case when no additional terms

[15] Additional terms, e.g., an Andreev-Bashkin term [200], can be added under appropriate circumstances.

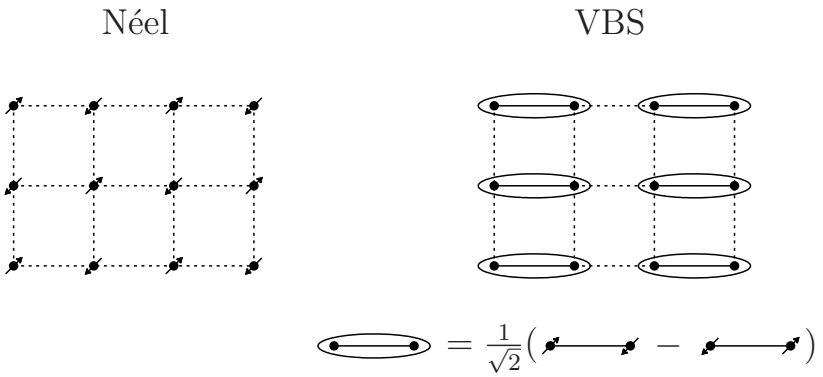

Figure 4.5: Schematic figure of two possible ground states for the Heisenberg quantum antiferromagnet. To the left is the Néel ground state with long-range antiferromagnetic order. To the right is the paramagnetic VBS ground state with broken discrete translational symmetry.

are added, the ground state is the Néel state with long-range antiferromagnetic order. However, when additional terms are added, the system can undergo a quantum phase transition into other states such as the paramagnetic valence bond solid (VBS). In Fig. 4.5, a schematic illustration of these two different ground states is presented. The Néel ground state breaks spin rotation symmetry whereas the VBS ground state breaks discrete translational symmetry.

According to the usual Landau-Ginzburg-Wilson (LGW) theory of phase transitions, it is not possible to have a generic continuous phase transition between two phases with different broken symmetries. The phase transition must either be first-order, or there should be a region of coexistence. Thus, a continuous transition can only be obtained by fine tuning to a multicritical point. However, numerical and experimental studies suggested that LGW predictions were wrong in certain cases [201–203]. In 2004, the DQC scenario was introduced by Senthil and coworkers [197, 198, 204]. They showed that near continuous quantum phase transitions, the LGW theory is invalidated by subtle quantum interference effects, and that certain quantum phase transitions, such as the Néel-VBS transition above, are continuous.

In Refs. [197–199, 204], it was proposed that the effective field theory of the Néel-VBS transition at the critical point is the so-called noncompact CP^1 (NCCP^1) model. This is a model with two complex matter fields with SU(2) symmetry that are minimally coupled to the same noncompact U(1) gauge field. The model can be written as

$$\mathcal{Z} = \int \mathcal{D}\,\boldsymbol{\Psi} \int \mathcal{D}\,\boldsymbol{A}\, \mathrm{e}^{-\beta H[\boldsymbol{\Psi},\boldsymbol{A}]},$$

$$H[\boldsymbol{\Psi},\boldsymbol{A}] = \frac{1}{2}\sum_{\mu,\boldsymbol{r}} \left[-\left(\boldsymbol{\Psi}^{\dagger}_{\boldsymbol{r}} \boldsymbol{\Psi}_{\boldsymbol{r}+\hat{\boldsymbol{\mu}}}\, \mathrm{e}^{-\mathrm{i}eA_{\mu,\boldsymbol{r}}} + \mathrm{c.c.} \right) + \left(\sum_{\nu,\lambda} \varepsilon_{\mu\nu\lambda} \Delta_{\nu} A_{\lambda,\boldsymbol{r}} \right)^2 \right], \qquad (4.79)$$

where matter fields must obey the CP^1 constraint, $|\boldsymbol{\Psi}_{\boldsymbol{r}}| = 1$. Note that this model pre-

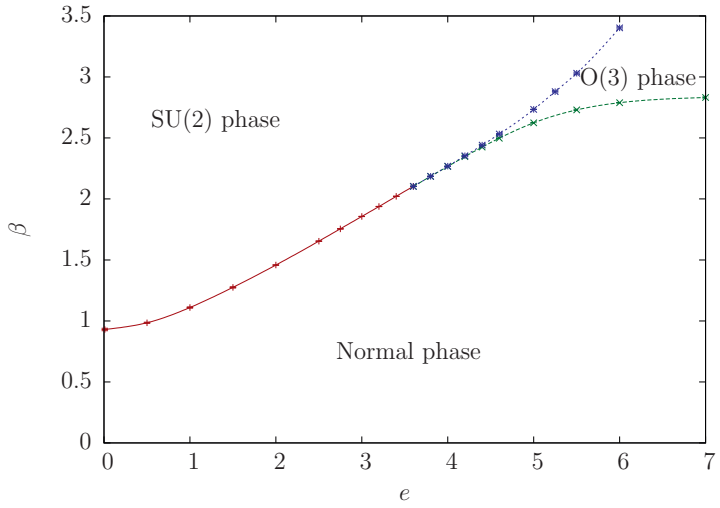

Figure 4.6: Phase diagram of the NCCP^1 model from the simulations in Ref. [4]. SU(2) phase: Fully ordered phase with spontaneously broken O(3) symmetry and massive gauge field (superconductor). O(3) phase: Spontaneously broken O(3) and massless gauge field. Normal phase: Restored O(3) symmetry and massless gauge field.

cisely is the lattice realization of the two-component SU(2) superconductor in Eq. (4.76), when subject to the CP^1 constraint. This model has been studied by Motrunich and Vishwanath in Ref. [125] and by Kuklov *et al.* in Ref. [205]. In this model, there is a local U(1) gauge symmetry and a global O(3) symmetry that is associated with the gauge neutral vector field given by $\boldsymbol{n_r} = \boldsymbol{\Psi}_{\boldsymbol{r}}^{\dagger}\boldsymbol{\sigma}\boldsymbol{\Psi}_{\boldsymbol{r}}$. Here, $\boldsymbol{\sigma} = (\sigma_x, \sigma_y, \sigma_z)$ is a vector where the components are the Pauli matrices. The phase diagram of the model is found to exhibit three distinct phases, see Fig. 4.6. In particular, there is a paired phase when e is large, analogous to the metallic superfluid phase in the two-component London superconductor. The Néel-VBS transition corresponds to a direct transition from the SU(2) phase to the normal phase in Fig. 4.6.

Initially, this model was studied in the case where the SU(2) symmetry is broken down to a U(1) $\times$ U(1) symmetry [140,163,199].[16] However, contrary to what the DQC theory predicts, it was established that the phase transition along the entire direct transition line is first-order [140, 163]. In the studies of the full NCCP^1 model, Motrunich and Vishwanath find a continuous transition along the direct transition line for small values of e, in accordance with the DQC scenario [125]. On the other hand, in the work by Kuklov *et al.*, it was found that the direct transition line is a first-order transition [205]. In Article IV [4], we perform an additional investigation of the NCCP^1 model accessing larger system sizes than what has been done previously.

[16] This corresponds to the two-component London superconductor in Eq. (4.61) in the case $\rho_1 = \rho_2$.

4.9.2 Brief summary of main results

In this work, we pay particular attention to the region in the vicinity of the bicritical point, which is the point where the direct transition line between the SU(2) phase and the normal phase splits. By simulating larger systems, we find that the bicritical point has been overestimated in earlier works. In particular, we estimate the bicritical point $e_{\rm bc}$ to be below $e = 3.8$ (Ref. [125] estimate $e_{\rm bc} \approx 4.0$ and Ref. [205] estimate $e_{\rm bc} \approx 4.4$). This means that a significant portion of the direct transition line that in Refs. [125, 205] was found to be a first-order transition, really is two separate transitions. In addition, we find that for sizes smaller than what is required to resolve two separate transitions, there are strong thermal signatures similar to what one would expect for a weak first-order transition. This means that one may mistakenly conclude to have a first-order transition in cases where the direct transition line is splitted. This could also be the case for $e < 3.8$ where no direct evidence of splitting are found for the system sizes that was simulated in this work. In this region, we find clear signatures of a weak first-order transition with a bimodal structure developing in the energy histograms. However, the signatures are too weak to confirm that proper first-order scaling is obeyed (see Sec. 3.6).

Similar to Refs. [125, 205], we have also measured flowgrams in order to investigate the character of the phase transition along the direct transition line. For a tricritical point one should expect to see a clear separatrix in the flowgrams, but this was not obtained. Still, for $e < 3.0$, the flowgrams seem to saturate for the system sizes available, which is consistent with interpreting the transition as continuous. However, the convergence is very slow, such that one cannot exclude divergent behavior at larger system sizes. We thus perform a curve collapse analysis [163, 205, 206]. By rescaling system sizes with a coupling dependent scaling function, an adequate collapse is obtained for all values of $e \in [0.5, 3.6]$. This means that we are able to collapse flowgrams for all couplings along the direct transition line up the region where we find signatures of a first-order transition. This is consistent with Refs. [205, 206]. However, with an adequate good collapse, we mean that we are able to collapse the flowgrams such that the curves are collapsing on the master curve for *large* systems. We note that for $e > 1.5$, there are many datapoints, corresponding to sizes $L \lesssim 20$, that systematically falls *below* the master curve. This can be interpreted as finite-size effects associated with small system sizes, but since these effects are not seen for $e < 2.0$, we are not certain that these are finite-size effects. Consequently, we cannot draw firm conclusions regarding the nature of the phase transition along the direct transition line as we find that larger systems must be studied to confirm that a good collapse can be obtained.

Bibliography

[1] E. V. Herland, E. Babaev, and A. Sudbø, Phys. Rev. B **82**, 134511 (2010).

[2] E. V. Herland *et al.*, Phys. Rev. B **85**, 024520 (2012).

[3] E. V. Herland *et al.*, Two-dimensional freezing of an unconventional two-component plasma, preprint, 2012.

[4] E. V. Herland, T. A. Bojesen, E. Babaev, and A. Sudbø, Monte Carlo simulations of the CP^1 two-component superconductor, preprint, 2012.

[5] P. W. Anderson, Science **177**, 393 (1972).

[6] L. D. Landau and E. M. Lifshitz, *Statistical Physics*, Second ed. (Pergamon Press, Oxford, 1969).

[7] J. J. Binney, N. J. Dowrick, A. J. Fisher, and M. E. J. Newman, *The Theory of Critical Phenomena. An Introduction to the Renormalization Group* (Oxford University Press, Oxford, 1992).

[8] N. Goldenfeld, *Lectures on Phase Transitions and the Renormalization Group* (Addison-Wesley Publishing Company, 1992).

[9] P. M. Chaikin and T. C. Lubensky, *Principles of condensed matter physics* (Cambridge University Press, 1995).

[10] H. E. Stanley, Rev. Mod. Phys. **71**, S358 (1999).

[11] E. H. Hauge, Go critical!, Lecture notes, NTNU, 2001.

[12] D. P. Landau and K. Binder, *A Guide to Monte-Carlo Simulations in Statistical Physics*, Third ed. (Cambridge University Press, Cambridge, 2009).

[13] H. Behringer and M. Pleimling, Phys. Rev. E **74**, 011108 (2006).

[14] J. M. Caillol and D. Levesque, Phys. Rev. B **33**, 499 (1986).

[15] A. K. Nguyen and A. Sudbø, Phys. Rev. B **58**, 2802 (1998).

[16] B. Widom, J. Chem. Phys. **43**, 3892 (1965).

[17] L. P. Kadanoff, Physics **2**, 263 (1966).

[18] L. Onsager, Phys. Rev. **65**, 117 (1944).

[19] M. E. Fisher, M. N. Barber, and D. Jasnow, Phys. Rev. A **8**, 1111 (1973).

[20] Y.-H. Li and S. Teitel, Phys. Rev. B **47**, 359 (1993).

[21] S. Elitzur, R. B. Pearson, and J. Shigemitsu, Phys. Rev. D **19**, 3698 (1979).

[22] C. M. Lapilli, P. Pfeifer, and C. Wexler, Phys. Rev. Lett. **96**, 140603 (2006).

[23] J. Hove and A. Sudbø, Phys. Rev. E **68**, 046107 (2003).

[24] S. Elitzur, Phys. Rev. D **12**, 3978 (1975).

[25] N. D. Mermin and H. Wagner, Phys. Rev. Lett. **17**, 1133 (1966).

[26] V. Berezinskii, Sov. Phys. JETP **32**, 493 (1970).

[27] J. M. Kosterlitz and D. J. Thouless, J. Phys. C **6**, 1181 (1973).

[28] J. M. Kosterlitz, J. Phys. C **7**, 1046 (1974).

[29] D. R. Nelson and J. M. Kosterlitz, Phys. Rev. Lett. **39**, 1201 (1977).

[30] P. Minnhagen and G. G. Warren, Phys. Rev. B **24**, 2526 (1981).

[31] K. G. Wilson, Rev. Mod. Phys. **55**, 583 (1983).

[32] M. E. Fisher, Rev. Mod. Phys. **70**, 653 (1998).

[33] R. Savit, Rev. Mod. Phys. **52**, 453 (1980).

[34] L. P. Kadanoff, *Statistical Physics: Statics, Dynamics and Renormalization* (World Scientific, Singapore, 2000).

[35] H. A. Kramers and G. H. Wannier, Phys. Rev. **60**, 252 (1941).

[36] H. A. Kramers and G. H. Wannier, Phys. Rev. **60**, 263 (1941).

[37] K. Fossheim and A. Sudbø, *Superconductivity: Physics and Applications* (John Wiley & Sons, London, 2004).

[38] Villain, J., J. Phys. (Paris) **36**, 581 (1975).

[39] H. Kleinert, *Gauge fields in condensed matter physics, Vol. 1* (World Scientific, Singapore, 1989).

[40] J. Hubbard, Phys. Rev. Lett. **3**, 77 (1959).

[41] J.-R. Lee and S. Teitel, Phys. Rev. B **46**, 3247 (1992).

[42] J. Lidmar and M. Wallin, Phys. Rev. B **55**, 522 (1997).

[43] K. Binder and D. W. Heermann, *Monte Carlo Simulation in Statistical Physics. An Introduction*, Fourth ed. (Springer-Verlag, Berlin/Heidelberg/New York, 2002).

[44] H. G. Katzgraber, Introduction to Monte Carlo Methods, arXiv:0905.1629v3 [cond-mat.stat-mech], 2011.

[45] W. H. Press, S. A. Teukolsky, W. T. Vetterling, and B. P. Flannery, *Numerical Recipes in C++. The Art of Scientific Computing*, Second ed. (Cambridge University Press, 2002).

[46] S. Weinzierl, Introduction to Monte Carlo methods, arXiv:hep-ph/0006269v1 (unpublished), 2000.

[47] M. Hasenbusch, K. Pinn, and S. Vinti, Phys. Rev. B **59**, 11471 (1999).

[48] S. Wenzel, W. Janke, and A. M. Läuchli, Phys. Rev. E **81**, 066702 (2010).

[49] N. Metropolis, A. W. Rosenbluth, M. N. Rosenbluth, A. H. Teller, and E. Teller, J. Chem. Phys. **21**, 1087 (1953).

[50] W. K. Hastings, Biometrika **57**, 97 (1970).

[51] V. I. Manousiouthakis and M. W. Deem, J. Chem. Phys. **110**, 2753 (1999).

[52] H. Suwa and S. Todo, Phys. Rev. Lett. **105**, 120603 (2010).

[53] G. Marsaglia, Proc. Natl. Acad. Sci. **61**, 25 (1968).

[54] A. M. Ferrenberg, D. P. Landau, and Y. J. Wong, Phys. Rev. Lett. **69**, 3382 (1992).

[55] M. Matsumoto and T. Nishimura, ACM Trans. Model. Comput. Simul. **8**, 3 (1998).

[56] J. W. Perram and S. W. de Leeuw, Physica A **109**, 237 (1981).

[57] L. Greengard and V. Rokhlin, J. Comput. Phys. **73**, 325 (1987).

[58] A. C. Maggs and V. Rossetto, Phys. Rev. Lett. **88**, 196402 (2002).

[59] S. Hattel and J. Wheatley, Phys. Rev. B **50**, 16590 (1994).

[60] S. A. Hattel and J. M. Wheatley, Phys. Rev. B **51**, 11951 (1995).

[61] M. Franz and S. Teitel, Phys. Rev. B **51**, 6551 (1995).

[62] A. K. Nguyen and A. Sudbø, Phys. Rev. B **57**, 3123 (1998).

[63] J. M. Caillol, D. Levesque, J. J. Weis, and J. P. Hansen, J. Stat. Phys. **28**, 325 (1982).

[64] J. M. Caillol and D. Levesque, J. Chem. Phys. **94**, 597 (1991).

[65] J. A. O'Neill and M. A. Moore, Phys. Rev. B **48**, 374 (1993).

[66] M. J. W. Dodgson and M. A. Moore, Phys. Rev. B **55**, 3816 (1997).

[67] D. J. Wales, H. McKay, and E. L. Altschuler, Phys. Rev. B **79**, 224115 (2009).

[68] E. Wigner, Phys. Rev. **46**, 1002 (1934).

[69] B. Zheng, Int. J. Mod. Phys. B **12**, 1419 (1998).

[70] E. V. Albano *et al.*, Rep. Prog. Phys. **74**, 026501 (2011).

[71] B. Efron, Ann. Statist. **7**, 1 (1979).

[72] B. Efron, SIAM Review **21**, 460 (1979).

[73] R. H. Swendsen and J.-S. Wang, Phys. Rev. Lett. **58**, 86 (1987).

[74] U. Wolff, Phys. Rev. Lett. **62**, 361 (1989).

[75] B. A. Berg and T. Neuhaus, Phys. Rev. Lett. **68**, 9 (1992).

[76] B. A. Berg and T. Neuhaus, Phys. Lett. B **267**, 249 (1991).

[77] A. P. Lyubartsev, A. A. Martsinovski, S. V. Shevkunov, and P. N. Vorontsov-Velyaminov, J. Chem. Phys. **96**, 1776 (1992).

[78] E. Marinari and G. Parisi, Eur. Phys. Lett. **19**, 451 (1992).

[79] R. H. Swendsen and J.-S. Wang, Phys. Rev. Lett. **57**, 2607 (1986).

[80] K. Hukushima and K. Nemoto, J. Phys. Soc. Jpn. **65**, 1604 (1996).

[81] D. J. Earl and M. W. Deem, Phys. Chem. Chem. Phys. **7**, 3910 (2005).

[82] F. Wang and D. P. Landau, Phys. Rev. Lett. **86**, 2050 (2001).

[83] R. E. Belardinelli, S. Manzi, and V. D. Pereyra, Phys. Rev. E **78**, 067701 (2008).

[84] S. Trebst, D. A. Huse, and M. Troyer, Phys. Rev. E **70**, 046701 (2004).

[85] K. Hukushima, Phys. Rev. E **60**, 3606 (1999).

[86] H. G. Katzgraber, S. Trebst, D. A. Huse, and M. Troyer, J. Stat. Mech. **2006**, P03018 (2006).

[87] W. Nadler, J. H. Meinke, and U. H. E. Hansmann, Phys. Rev. E **78**, 061905 (2008).

[88] A. M. Ferrenberg and R. H. Swendsen, Phys. Rev. Lett. **61**, 2635 (1988).

[89] A. M. Ferrenberg and R. H. Swendsen, Phys. Rev. Lett. **63**, 1195 (1989).

[90] E. P. Münger and M. A. Novotny, Phys. Rev. B **44**, 4314 (1991).

[91] A. M. Ferrenberg and D. P. Landau, Phys. Rev. B **44**, 5081 (1991).

[92] M. Campostrini, M. Hasenbusch, A. Pelissetto, P. Rossi, and E. Vicari, Phys. Rev. B **63**, 214503 (2001).

[93] K. S. D. Beach, L. Wang, and A. W. Sandvik, Data collapse in the critical region using finite-size scaling with subleading corrections, arXiv:cond-mat/0505194v1 [cond-mat.stat-mech], 2005.

[94] A. Sudbø, E. Smørgrav, J. Smiseth, F. S. Nogueira, and J. Hove, Phys. Rev. Lett. **89**, 226403 (2002).

[95] J. Smiseth, E. Smørgrav, F. S. Nogueira, J. Hove, and A. Sudbø, Phys. Rev. B **67**, 205104 (2003).

[96] K. Binder, Z. Phys. B **43**, 119 (1981).

[97] A. W. Sandvik, AIP Conf. Proc. **1297**, 135 (2010).

[98] M. Campostrini, M. Hasenbusch, A. Pelissetto, and E. Vicari, Phys. Rev. B **74**, 144506 (2006).

[99] I.-H. Jeon, J.-G. Shin, and M.-C. Cha, J. Korean Phys. Soc. **60**, 581 (2012).

[100] J. Lee and J. M. Kosterlitz, Phys. Rev. Lett. **65**, 137 (1990).

[101] J. Lee and J. M. Kosterlitz, Phys. Rev. B **43**, 3265 (1991).

[102] N. Schreiber and J. Adler, J. Phys. A **38**, 7253 (2005).

[103] N. G. Fytas, A. Malakis, and K. Eftaxias, J. Stat. Mech. **2008**, P03015 (2008).

[104] S. Jin, A. Sen, and A. W. Sandvik, Phys. Rev. Lett. **108**, 045702 (2012).

[105] M. S. S. Challa, D. P. Landau, and K. Binder, Phys. Rev. B **34**, 1841 (1986).

[106] M. E. Fisher and A. N. Berker, Phys. Rev. B **26**, 2507 (1982).

[107] J. L. Cardy and P. Nightingale, Phys. Rev. B **27**, 4256 (1983).

[108] K. Vollmayr, J. D. Reger, M. Scheucher, and K. Binder, Z. Phys. B **91**, 113 (1993).

[109] P. Olsson, Phys. Rev. B **52**, 4526 (1995).

[110] M. Hasenbusch, J. Phys. A **38**, 5869 (2005).

[111] H. Weber and P. Minnhagen, Phys. Rev. B **37**, 5986 (1988).

[112] P. Minnhagen and B. J. Kim, Phys. Rev. B **67**, 172509 (2003).

[113] K. Børkje, S. Kragset, and A. Sudbø, Phys. Rev. B **71**, 085112 (2005).

[114] V. L. Ginzburg and L. D. Landau, Sov. Phys. JETP **20**, 1064 (1950).

[115] J. Bardeen, L. N. Cooper, and J. R. Schrieffer, Phys. Rev. **108**, 1175 (1957).

[116] L. P. Gor'kov, Sov. Phys. JETP. **9**, 1364 (1959).

[117] P. W. Anderson, Phys. Rev. **130**, 439 (1963).

[118] P. W. Higgs, Phys. Rev. Lett. **13**, 508 (1964).

[119] M. Tinkham, *Introduction to Superconductivity* (McGraw-Hill, 1975).

[120] B. I. Halperin, T. C. Lubensky, and S.-k. Ma, Phys. Rev. Lett. **32**, 292 (1974).

[121] H. Kleinert, Lett. Nuovo Cim. **35**, 405 (1982).

[122] S. Mo, J. Hove, and A. Sudbø, Phys. Rev. B **65**, 104501 (2002).

[123] A. A. Abrikosov, Sov. Phys. JETP **5**, 1174 (1957).

[124] H. Nielsen and P. Olesen, Nucl. Phys. B **61**, 45 (1973).

[125] O. I. Motrunich and A. Vishwanath, Comparative study of Higgs transition in one-component and two-component lattice superconductor models, arXiv:0805.1494v1 [cond-mat.stat-mech], 2004.

[126] P. Olsson and S. Teitel, Phys. Rev. Lett. **80**, 1964 (1998).

[127] K. Kajantie, M. Laine, T. Neuhaus, A. Rajantie, and K. Rummukainen, Nucl. Phys. B **699**, 632 (2004).

[128] J. Smiseth, E. Smørgrav, E. Babaev, and A. Sudbø, Phys. Rev. B **71**, 214509 (2005).

[129] C. Dasgupta and B. I. Halperin, Phys. Rev. Lett. **47**, 1556 (1981).

[130] Z. Tešanović, Phys. Rev. B **59**, 6449 (1999).

[131] A. K. Nguyen and A. Sudbø, Phys. Rev. B **60**, 15307 (1999).

[132] J. Hove and A. Sudbø, Phys. Rev. Lett. **84**, 3426 (2000).

[133] J. Smiseth, E. Smørgrav, and A. Sudbø, Phys. Rev. Lett. **93**, 077002 (2004).

[134] L. Pitaevskii and S. Stringari, *Bose–Einstein Condensation* (Oxford University Press, 2003).

[135] C. Pethick and H. Smith, *Bose–Einstein Condensation in Dilute Gases*, Second ed. (Cambridge University Press, 2008).

[136] S. Stock, B. Battelier, V. Bretin, Z. Hadzibabic, and J. Dalibard, Laser Phys. Lett. **2**, 275 (2005).

[137] A. L. Fetter, Rev. Mod. Phys. **81**, 647 (2009).

[138] G. Baym, C. Pethick, and D. Pines, Nature **224**, 673 (1969).

[139] E. J. Yarmchuk, M. J. V. Gordon, and R. E. Packard, Phys. Rev. Lett. **43**, 214 (1979).

[140] S. Kragset, E. Babaev, and A. Sudbø, Phys. Rev. Lett. **97**, 170403 (2006).

[141] S. Kragset, E. Babaev, and A. Sudbø, Phys. Rev. A **77**, 043605 (2008).

[142] G. Watanabe, G. Baym, and C. J. Pethick, Phys. Rev. Lett. **93**, 190401 (2004).

[143] N. R. Cooper, S. Komineas, and N. Read, Phys. Rev. A **70**, 033604 (2004).

[144] Y.-H. Li and S. Teitel, Phys. Rev. Lett. **66**, 3301 (1991).

[145] R. E. Hetzel, A. Sudbø, and D. A. Huse, Phys. Rev. Lett. **69**, 518 (1992).

[146] X. Hu, S. Miyashita, and M. Tachiki, Phys. Rev. Lett. **79**, 3498 (1997).

[147] A. K. Nguyen and A. Sudbø, Eur. Phys. Lett. **46**, 780 (1999).

[148] A. K. Nguyen and A. Sudbø, Phys. Rev. B **60**, 15307 (1999).

[149] A. Polyakov, Phys. Lett. B **59**, 82 (1975).

[150] A. F. Andreev and E. P. Bashkin, Sov. Phys. JETP **42**, 164 (1975).

[151] G. E. Volovik, V. P. Mineev, and I. M. Khalatnikov, Sov. Phys. JETP **42**, 342 (1975).

[152] M. A. Alpar, S. A. Langer, and J. A. Sauls, Astrophys. J. **282**, 533 (1984).

[153] E. Babaev, Phys. Rev. D **70**, 043001 (2004).

[154] E. Babaev, Phys. Rev. Lett. **103**, 231101 (2009).

[155] J.-M. Duan and S. Yip, Phys. Rev. Lett. **70**, 3647 (1993).

[156] A. B. Kuklov and B. V. Svistunov, Phys. Rev. Lett. **90**, 100401 (2003).

[157] A. Kuklov, N. Prokof'ev, and B. Svistunov, Phys. Rev. Lett. **92**, 030403 (2004).

[158] V. M. Kaurov, A. B. Kuklov, and A. E. Meyerovich, Phys. Rev. Lett. **95**, 090403 (2005).

[159] D. V. Fil and S. I. Shevchenko, Phys. Rev. A **72**, 013616 (2005).

[160] E. K. Dahl, E. Babaev, S. Kragset, and A. Sudbø, Phys. Rev. B **77**, 144519 (2008).

[161] E. K. Dahl, *Theoretical Studies of Condensed Matter Systems with Multiple Broken Symmetries*, PhD thesis, NTNU, 2008.

[162] A. Kuklov, N. Prokof'ev, and B. Svistunov, Phys. Rev. Lett. **93**, 230402 (2004).

[163] A. Kuklov, N. Prokof'ev, B. Svistunov, and M. Troyer, Ann. Phys. **321**, 1602 (2006).

[164] P. Bonderson, V. Gurarie, and C. Nayak, Phys. Rev. B **83**, 075303 (2011).

[165] E. K. Dahl, E. Babaev, and A. Sudbø, Phys. Rev. B **78**, 144510 (2008).

[166] E. K. Dahl, E. Babaev, and A. Sudbø, Phys. Rev. Lett. **101**, 255301 (2008).

[167] R. B. Laughlin, Phys. Rev. Lett. **50**, 1395 (1983).

[168] R. B. Laughlin, Rev. Mod. Phys. **71**, 863 (1999).

[169] N. D. Mermin, J. Math. Phys. **8**, 1061 (1967).

[170] N. D. Mermin, Phys. Rev. **176**, 250 (1968).

[171] M. A. Moore and A. Pérez-Garrido, Phys. Rev. Lett. **82**, 4078 (1999).

[172] P. A. McClarty and M. A. Moore, Phys. Rev. B **75**, 172507 (2007).

[173] B. I. Halperin and D. R. Nelson, Phys. Rev. Lett. **41**, 121 (1978).

[174] D. R. Nelson and B. I. Halperin, Phys. Rev. B **19**, 2457 (1979).

[175] A. P. Young, Phys. Rev. B **19**, 1855 (1979).

[176] K. J. Strandburg, Rev. Mod. Phys. **60**, 161 (1988).

[177] K. Chen, T. Kaplan, and M. Mostoller, Phys. Rev. Lett. **74**, 4019 (1995).

[178] K. Zahn, R. Lenke, and G. Maret, Phys. Rev. Lett. **82**, 2721 (1999).

[179] M. A. Bates and D. Frenkel, Phys. Rev. E **61**, 5223 (2000).

[180] J. Dietel and H. Kleinert, Phys. Rev. B **73**, 024113 (2006).

[181] S. I. Lee and S. J. Lee, Phys. Rev. E **78**, 041504 (2008).

[182] Guillamon I. *et al.*, Nat. Phys. **5**, 651 (2009).

[183] P. Choquard and J. Clerouin, Phys. Rev. Lett. **50**, 2086 (1983).

[184] M. Franz and S. Teitel, Phys. Rev. Lett. **73**, 480 (1994).

[185] S. de Leeuw and J. Perram, Physica A **113**, 546 (1982).

[186] G. Orkoulas and A. Z. Panagiotopoulos, J. Chem. Phys. **104**, 7205 (1996).

[187] P. Minnhagen, Rev. Mod. Phys. **59**, 1001 (1987).

[188] P. Gupta and S. Teitel, Phys. Rev. B **55**, 2756 (1997).

[189] P. Olsson, Phys. Rev. B **46**, 14598 (1992).

[190] P. Olsson, Phys. Rev. B **52**, 4511 (1995).

[191] E. Babaev, Phys. Rev. Lett. **89**, 067001 (2002).

[192] E. Babaev, L. D. Faddeev, and A. J. Niemi, Phys. Rev. B **65**, 100512 (2002).

[193] Babaev Egor, Sudbo Asle, and Ashcroft N. W., Nature **431**, 666 (2004).

[194] E. Smørgrav, J. Smiseth, E. Babaev, and A. Sudbø, Phys. Rev. Lett. **94**, 096401 (2005).

[195] E. Smørgrav, E. Babaev, J. Smiseth, and A. Sudbø, Phys. Rev. Lett. **95**, 135301 (2005).

[196] E. Babaev and N. W. Ashcroft, Nat. Phys. **3**, 530 (2007).

[197] T. Senthil, A. Vishwanath, L. Balents, S. Sachdev, and M. P. A. Fisher, Science **303**, 1490 (2004).

[198] T. Senthil, L. Balents, S. Sachdev, A. Vishwanath, and M. P. A. Fisher, Phys. Rev. B **70**, 144407 (2004).

[199] O. I. Motrunich and A. Vishwanath, Phys. Rev. B **70**, 075104 (2004).

[200] E. Babaev, Phys. Rev. B **79**, 104506 (2009).

[201] P. Coleman, C. Pépin, Q. Si, and R. Ramazashvili, J. Phys.: Condens. Matter **13**, R723 (2001).

[202] G. R. Stewart, Rev. Mod. Phys. **73**, 797 (2001).

[203] A. W. Sandvik, S. Daul, R. R. P. Singh, and D. J. Scalapino, Phys. Rev. Lett. **89**, 247201 (2002).

[204] S. Sachdev, Quantum phases and phase transitions of Mott insulators, in *Lecture Notes in Physics: Quantum magnetism*, edited by U. Schollwock, J. Richter, D. J. J. Farnell, and R. A. Bishop, Springer, Berlin, 2004.

[205] A. B. Kuklov, M. Matsumoto, N. V. Prokof'ev, B. V. Svistunov, and M. Troyer, Phys. Rev. Lett. **101**, 050405 (2008).

[206] A. B. Kuklov, M. Matsumoto, N. V. Prokof'ev, B. V. Svistunov, and M. Troyer, Comment on "Comparative study of Higgs transition in one-component and two-component lattice superconductor models", arXiv:0805.2578v1 [cond-mat.stat-mech], 2008.

Article I

Phase transitions in a three dimensional $U(1) \times U(1)$ lattice London superconductor: Metallic superfluid and charge-4e superconducting states

Physical Review B **82**, 134511 (2010)

Phase transitions in a three dimensional $U(1)\times U(1)$ lattice London superconductor: Metallic superfluid and charge-4*e* superconducting states

Egil V. Herland,[1] Egor Babaev,[2,3] and Asle Sudbø[1]
[1]*Department of Physics, Norwegian University of Science and Technology, N-7491 Trondheim, Norway*
[2]*Department of Theoretical Physics, The Royal Institute of Technology, 10691 Stockholm, Sweden*
[3]*Physics Department, University of Massachusetts, Amherst, Massachusetts 01003, USA*
(Received 14 June 2010; published 8 October 2010)

We consider a three dimensional lattice $U(1)\times U(1)$ and $[U(1)]^N$ superconductors in the London limit with individually conserved condensates. The $U(1)\times U(1)$ problem, generically, has two types of intercomponent interactions of different characters. First, the condensates are interacting via a minimal coupling to the same fluctuating gauge field. A second type of coupling is the direct dissipationless drag represented by a local intercomponent current-current coupling term in the free-energy functional. In this work, we present a study of the phase diagram of a $U(1)\times U(1)$ superconductor which includes both of these interactions. We study phase transitions and two types of competing paired phases which occur in this general model: (i) a metallic superfluid phase (where there is order only in the gauge-invariant phase difference of the order parameters), (ii) a composite superconducting phase where there is order in the phase sum of the order parameters which has many properties of a single-component superconductor but with a doubled value of electric charge. We investigate the phase diagram with particular focus on what we call "preemptive phase transitions." These are phase transitions *unique to multicomponent condensates with competing topological objects*. A sudden proliferation of one kind of topological defects may come about due to a fluctuating background of topological defects in other sectors of the theory. For $U(1)\times U(1)$ theory with unequal bare stiffnesses where components are coupled by a noncompact gauge field only, we study how this scenario leads to a merger of two $U(1)$ transitions into a single $U(1)\times U(1)$ discontinuous phase transition. We also report a general form of vortex-vortex bare interaction potential and possible phase transitions in an N-component London superconductor with individually conserved condensates.

DOI: 10.1103/PhysRevB.82.134511 PACS number(s): 67.85.De, 67.85.Fg, 67.90.+z, 74.20.De

I. INTRODUCTION

Phase diagrams and critical phenomena in superfluids and superconductors with $U(1)$ symmetry are well understood theoretically and well investigated numerically. The understanding is largely based on identifying and describing the behavior of proliferating topological defects. In two dimensions, a transition from a superfluid to a normal state can be described as unbinding of vortex-antivortex pairs, which disorders the superfluid phase yielding a Berezinskii-Kosterlitz-Thouless transition into a normal state.[1] In three dimensions, the topological defects of $U(1)$ theory are vortex loops, proliferation of which yields a continuous phase transition in the three dimensional (3D) xy universality class in the case of superfluids [with global $U(1)$ symmetry], or inverted 3Dxy in the case of superconductors [with local $U(1)$ symmetry].[2–4] However, it was recently found that in interacting mixtures of $U(1)$ symmetric condensates the situation changes principally, yielding much more complex physics, different phase diagrams and transitions. Many aspects of the phase transitions in systems with several interacting components are still poorly understood and debated.

The main important new aspect arising in an interacting mixture is connected with the fact that, as reviewed below, under certain quite generic conditions the vortices with high topological charge (or *bound states of vortices*) acquire crucial importance for various aspects in the physics of these systems. This is in contrast to single-component systems where only the lowest-topological-charge defects (i.e., only vortices with 2π phase winding) are important. The complexity arising from the relevance of topological defects with high topological charge include formation of what is called "metallic superfluid phases," in context of electrically charged systems, or "paired phases," in context of electrically neutral systems. In these states no conventional real-space pairing takes places. However, there is order only in the sum or difference of the phases of the condensate with phases being individually disordered.[5–10] Moreover, it also results in a complicated and still poorly understood nature of the phase transitions from a fully symmetric state to a state with all symmetries broken,[10–13] when there is a competition between proliferating low- and high-order topological defects. This is again a phenomenon which has no counterpart in single-component systems. Various aspects of related effects were also studied in different models with a compact gauge field and with SU(2) symmetry.[14]

Recently, it has been found that two kinds of intercomponent interactions lead to the distinct mixture-specific phenomena mentioned above. Namely, in a mixture of charged condensates, the intercomponent interaction is represented by the coupling between the charged complex scalar matter fields mediated by a fluctuating gauge field.[5,7–10,15] On the other hand, in the case of an electrically neutral condensate mixture, some related (but at the same time principally different) effects can be produced by a strong dissipationless drag (current-current interaction[6,13,16] which in some physical situations is also called Andreev-Bashkin interaction).[17] The intercomponent couplings by gauge field and the dissi-

pationless drag have so far only been studied separately, while in a generic $U(1)\times U(1)$ system, terms leading to both of these effects are allowed by symmetry. Thus, generically the phase diagram and critical phenomena in a $U(1)\times U(1)$ system is a problem with two coupling constants. The interplay between them has, to our knowledge, not been investigated so far.

In this work, we report a quantitative study of a generic $U(1)\times U(1)$ London superconductor which has both kinds of intercomponent coupling (gauge field and current-current drag). This includes, in particular, the situations where these two different kinds of intercomponent couplings compete with each other.

This paper is organized as follows. In Sec. II, the general model we consider is introduced, and the neutral and charged modes and the vortex representation of the general model, obtained by a duality transformation, are identified. Section III is devoted to the numerical methods we employ in this study. The results obtained in the special case with no intercomponent dissipationless drag, is presented in Sec. IV, followed by the results of the general model with competing gauge field and Andreev-Bashkin interactions in Sec. V. In Sec. VI, we discuss the general N-component case, before we arrive to the conclusions in Sec. VII. We also present analytical details presenting the duality transform for a general N-component model in Appendix A and a derivation of the expression for the gauge-field correlator in Appendix B.

II. MODEL

We study a generic two-component London superconductor. In the London limit, one neglects the fluctuations of the density fields $|\psi_{1,2}|$ of the complex scalar functions $\psi_j = |\psi_j| e^{i\theta_j}$ describing two superconducting components (i.e., setting $|\psi_{1,2}| \approx \text{const}$). Fluctuations of the phases θ_j, and the gauge field $\mathbf{A}$ are allowed. The compact support of the phase variables $\theta_i \in [0, 2\pi\rangle$ implies that phase fluctuations lead to vortex excitations, capable of destroying superconductivity/superfluidity, in this system. The London limit is an adequate approximation for many properties of strongly type-II superconductors, and in fact transcends the validity of the Ginzburg-Landau theory. The free-energy density of this system can be written as

$$F = \sum_{j=1,2} \frac{\rho_j}{2}(\nabla\theta_j - e_j\mathbf{A})^2 + \frac{(\nabla\times\mathbf{A})^2}{2} - \frac{\rho_d}{2}(\nabla\theta_1 - e_1\mathbf{A} - \nabla\theta_2 + e_2\mathbf{A})^2, \quad (1)$$

where ρ_j physically represent the bare phase stiffnesses of the problem. In addition to the intercomponent coupling between the two charged condensates via a fluctuating gauge field $\mathbf{A}$, we include a direct intercomponent dissipationless current-current interaction with strength ρ_d, which has the form[17]

$$F_{drag} = \rho_d(\nabla\theta_1 - e_1\mathbf{A})\cdot(\nabla\theta_2 - e_2\mathbf{A}). \quad (2)$$

It is a part of the last term in Eq. (1). The particle currents of both species then depend on the common vector potential and superfluid velocities of both condensates (i.e., particles belonging to one condensate can be carried by superfluid velocity of the other),

$$\mathbf{j}_1 = (\rho_1 - \rho_d)(\nabla\theta_1 - e_1\mathbf{A}) + \rho_d(\nabla\theta_2 - e_2\mathbf{A}), \quad (3)$$

$$\mathbf{j}_2 = (\rho_2 - \rho_d)(\nabla\theta_2 - e_2\mathbf{A}) + \rho_d(\nabla\theta_1 - e_1\mathbf{A}). \quad (4)$$

For generality, we allow for unequal charges e_j in the two components of the system, examples of the systems with oppositely charged condensates are given below. Note that the drag term implies that there is a stability criterion that must be applied to the system. If ρ_d exceeds a critical limit, to be determined below, the spectrum of the system will be unbounded from below and hence the theory will be ill defined. The bare stiffness coefficients ρ_j must be positive, $\rho_j \geq 0$, on simple physical grounds.

The physical model in Eq. (1) is discussed in the context of the projected quantum ordered states of hydrogen or its isotopes at high compression[7–9,15,18,19] where the different fields correspond to condensates formed by electrons, protons, or deuterons. A similar model appears in some models of neutron stars interior where the two fields represent protonic and Σ^- hyperon Cooper pairs.[20] Moreover, the model with equal phase stiffnesses $\rho_1 = \rho_2$ and charges $e_1 = e_2$, appears as an effective model in the theories of easy-plane quantum antiferromagnets.[21,22] Related models were also studied in various contexts in low dimensions.[5,23]

The model has topological excitations which are vortices with $2\pi n_j$, $n_j = \pm 1, \pm 2, \ldots$ phase winding in the phase of component j. We denote vortices by the pair of integers (n_1, n_2) characterizing phase windings of the vortex in question. Thus, vortices with phase winding in only one component are denoted (1,0) or (0,1). The model also possesses composite vortices where both integers associated with the phase windings (around or nearly around the same core) in the two species are nonzero. In this paper, we will only consider the composite vortices (1,1) and (1,−1) which have codirected and counterdirected phase windings in the two components, respectively. However, composite vortices with higher topological charges, such as $(1, n_2)$ or $(n_1, 1)$, may be relevant under certain conditions.[13,24]

A. Charged and neutral modes

By separation of variables,[9,19,25] we may rewrite the model in Eq. (1) in a form where the composite charged and neutral modes are explicitly identified,

$$F = \frac{1}{2}\left[\frac{\rho_1\rho_2 - \rho_d(\rho_1+\rho_2)}{m_0^2}(e_2\nabla\theta_1 - e_1\nabla\theta_2)^2 + \frac{1}{m_0^2}(e_jR_{j1}\nabla\theta_1 + e_jR_{j2}\nabla\theta_2 - m_0^2\mathbf{A})^2 + (\nabla\times\mathbf{A})^2\right], \quad (5)$$

where the coefficients are given by

$$R = \begin{pmatrix} \rho_1 - \rho_d & \rho_d \\ \rho_d & \rho_2 - \rho_d \end{pmatrix} \quad (6)$$

and

$$m_0^2 = (\rho_1 - \rho_d)e_1^2 + (\rho_2 - \rho_d)e_2^2 + 2\rho_d e_1 e_2. \quad (7)$$

Throughout the paper, there is an implicit sum over repeated component indices. The coefficient m_0 should not be confused with the mass of the components. These are included in ρ_j, whereas m_0 determines the inverse bare screening length of the screened interactions in the system, details will be given in Sec. II C. The first term of Eq. (5) is identified as the neutral mode that does not couple to the vector potential. The second term is the charged mode, characterized by its coupling to the vector potential.

From Eq. (5), it is seen that for stability of the system (in the sense that the free-energy functional should be bounded from below) the coefficient of the first term should be positive. It is readily shown that the criterion for this is that

$$\rho_d < \frac{\rho_1 \rho_2}{\rho_1 + \rho_2}. \quad (8)$$

Note that this criterion is identical to the one derived in Ref. 13 and does not depend on charge. Actually, there are no restrictions on the value of the electric charge e to obtain a well-defined theory.

Note that in Eq. (1), the phases of the two components do not represent gauge-invariant quantities. However, when the model is rewritten on the form in Eq. (5), observe that the neutral mode identifies a linear combination of the phase gradients that is a gauge-invariant quantity decoupled from the vector potential $\mathbf{A}$, $\nabla(e_2\theta_1 - e_1\theta_2)$. Thus, the $U(1) \times U(1)$ symmetry of the model may be interpreted as possessing a "composite" electrically neutral (or "global") $U(1)$ symmetry associated with the phase combination of the neutral mode, and a composite $U(1)$ gauge symmetry which is coupled to vector potential $\mathbf{A}$ and thus is associated with the charged mode. Importantly, the identification of the charged and a neutral mode does not imply that the modes are decoupled because both modes depend on phases θ_i which are constrained to have $2\pi \times$ integer phase windings.

B. Case $\rho_d = 0$, $e_1 = e_2 = e$

We briefly review the physics of a two-component $U(1) \times U(1)$ superconductor with individually conserved condensates, coupled only by the gauge field, i.e., in the absence of Andreev-Bashkin (i.e., mixed-gradient) terms. In the London limit the free energy may be read off from Eq. (5),

$$F = \frac{1}{2}\frac{\rho_1\rho_2}{\rho_1 + \rho_2}[\nabla(\theta_1 - \theta_2)]^2 + \frac{1}{2}\frac{[\rho_1 \nabla \theta_1 + \rho_2 \nabla \theta_2 - e(\rho_1 + \rho_2)\mathbf{A}]^2}{\rho_1 + \rho_2} + \frac{1}{2}(\nabla \times \mathbf{A})^2. \quad (9)$$

The important new physics arising in the model, Eq. (9), compared to single-component GL model is that the lowest-order topological defects with a 2π phase winding only in one phase θ_i have a logarithmically diverging energy per unit length due to a neutral supercurrent while vortices where both phases have 2π winding have finite energy per unit length.[19,26] Under certain conditions vortices where both phases wind, i.e., (1,1), can proliferate without triggering a proliferation of the simplest vortices (1,0) and (0,1).

Consider now a composite (1,1) vortex. Such an excitation, if vortices in two components share the same core, has nontrivial contribution to the following terms in the free energy, Eq. (9):

$$F^{\text{eff}}_{(1,1)} = \frac{1}{2}\frac{[\rho_1 \nabla \theta_1 + \rho_2 \nabla \theta_2 - e(\rho_1 + \rho_2)\mathbf{A}]^2}{\rho_1 + \rho_2} + \frac{1}{2}(\nabla \times \mathbf{A})^2. \quad (10)$$

If the (1,1) vortex has phase windings around a common core, it can be mapped onto a vortex in a single-component superconductor. Then, by increasing electric charge one can make the energy cost of a vortex per unit length in a lattice London superconductor arbitrarily small (because the vortex energy depends logarithmically on the penetration depth which is in turn a function of electric charge). Thus, in a lattice London superconductor the critical temperature of proliferation of the vortices can be arbitrary small if the value of the electric charge is sufficiently large. Therefore, in the two-component model, Eq. (9), one may, by increasing the value of electric charge, proliferate (1,1) vortices without proliferating individual vortices (1,0) or (0,1). The latter two produce a phase gradient in the gauge-invariant phase difference $\theta_1 - \theta_2$. This features a stiffness which is not renormalized by the proliferation of the (1,1) vortices.

Since the (1,1) vortices do not have a topological charge in the phase difference, they cannot disorder the first term in Eq. (9), but they disorder the charged sector represented by the second term. The resulting state therefore features long-range ordering in the phase difference and can be characterized by $\langle e^{i(\theta_1 - \theta_2)} \rangle \neq 0$ while $\langle e^{i\theta_1} \rangle = 0$, $\langle e^{i\theta_2} \rangle = 0$, and there is no Meissner effect. The free energy for the resulting phase is given by the following term [i.e., it has only broken global $U(1)$ symmetry] while the stiffness of the charged $U(1)$ mode is renormalized to zero by proliferated composite vortices,

$$F^{\text{eff}}_{(1,-1)} = \frac{1}{2}\frac{\rho_1\rho_2}{\rho_1 + \rho_2}[\nabla(\theta_1 - \theta_2)]^2. \quad (11)$$

The proliferation of composite defects resulting into this state was shown to arise in two-dimensional (2D) systems at any finite temperatures.[5] In three dimensions, this phase can be induced by a magnetic field via melting of a composite vortex lattice.[7,8] An analogous phase was also found in a three dimensional lattice superconductor arising without applied external field from fluctuations if the value of the electric charge is very large.[10] Since there is no Meissner effect in the resulting phase, but at the same time there is a broken neutral $U(1)$ symmetry, the term metallic superfluid (MSF) was coined for it.[7] Also related phases are sometimes called "paired phases."[10] The latter term is motivated by the fact that in such situations the (quasi) long-range order is retained only in some linear combination of phases while individual phases are disordered. Importantly it should not be confused with the conventional "real-space" pairing of bosons.

Case $\rho_1=\rho_2$

Consider the case where $\rho_1=\rho_2$. At high values of the electric charge e, the model was shown to feature a MSF phase without applied field.[10] This implies that at large e the system undergoes two phase transitions when the temperature is increased. The first transition is from a state with broken $U(1)\times U(1)$ symmetry into the MSF with broken $U(1)$ symmetry, driven by a proliferation of composite (1,1) vortices. The second transition is one where the remaining broken $U(1)$ symmetry is restored by proliferation of individual vortices, resulting in a normal state. At low values of e, one cannot separate characteristic temperatures of the proliferation of composite and individual vortices and thus, the model should have only one phase transition from broken $U(1)\times U(1)$ to a normal state. In the case $\rho_1=\rho_2$, the latter phase transition was conjectured to be a continuous phase transition in a novel universality class in the work of Ref. 12. However, subsequent works show that the phase transition is first order,[10,11] see also Ref. 14. Moreover, the analysis performed in Ref. 10 indicates that the $U(1)\times U(1)$ to a normal-state transition is first order for any values of electric charge in the $\rho_1=\rho_2$ model. Note that the standard theories of vortex loop proliferation yield a second-order transition.[2,3] An analysis of a simpler two-component model (with no gauge-field coupling but with direct current-current coupling) which, like the model, Eq. (9), also features low-energy composite vortices, provides some evidence that the first-order transition takes place whenever a restoration of the $U(1)\times U(1)$ broken symmetry is driven by proliferation of *competing tangles of different kinds of vortices*,[13] e.g., tangles of (1,0), (0,1) vortices and a tangle of (1,1) vortices. The term "preemptive vortex-loop proliferation transition" was coined for this scenario.[13] Note that in a charged $U(1)\times U(1)$ theory for arbitrary values of electric charge one cannot rule out in a simple way that composite vortices participate in a competition with the individual vortices in the symmetry-restoration transition since composite vortices have finite energy per unit length.

C. Dual model

We will now perform a duality transformation that reduces the model in Eq. (1) to a theory of interacting vortex loops of two species. These are the topological objects which drive the phase transition between the normal state and a state with broken symmetries in the systems we consider. When the phases and gauge field are fluctuating the statistical sum of the London two-component superconductor with intercomponent drag can be represented as follows:

$$Z=\int \mathcal{D}\theta_1 \int \mathcal{D}\theta_2 \int \mathcal{D}\mathbf{A} e^{-S},$$

$$S=\frac{\beta}{2}\int d^3r\{[\nabla\times\mathbf{A}(\mathbf{r})]^2 + [\nabla\theta_j(\mathbf{r})-e_j\mathbf{A}(\mathbf{r})]R_{jk}[\nabla\theta_k(\mathbf{r})-e_k\mathbf{A}(\mathbf{r})]\}, \quad (12)$$

where β is the inverse temperature.

We now choose the gauge $\nabla\cdot\mathbf{A}(\mathbf{r})=0$ and Fourier transform the action. The action is then written as

$$S=\frac{\beta}{2}\int d^3q\left[\tilde{\mathbf{A}}(\mathbf{q})(q^2+m_0^2)\tilde{\mathbf{A}}(-\mathbf{q})+\mathbf{U}_j(\mathbf{q})\times\left(R_{jk}-\frac{e_l e_m R_{lj}R_{mk}}{q^2+m_0^2}\right)\mathbf{U}_k(-\mathbf{q})\right], \quad (13)$$

where the Fourier transform of $\nabla\theta_j(\mathbf{r})$ is denoted by $\mathbf{U}_j(\mathbf{q})$. Moreover we have completed the squares of the gauge field with $\tilde{\mathbf{A}}(\mathbf{q})=\mathbf{A}(\mathbf{q})-e_jR_{jk}\mathbf{U}_k(\mathbf{q})/(q^2+m_0^2)$ as the shifted gauge field. By integration of the shifted gauge field, the model is written as

$$Z=\int \mathcal{D}\theta_1\int \mathcal{D}\theta_2 e^{-S},$$

$$S=\frac{\beta}{2}\int d^3q\mathbf{U}_j(\mathbf{q})\left(R_{jk}-\frac{e_l e_m R_{lj}R_{mk}}{q^2+m_0^2}\right)\mathbf{U}_k(-\mathbf{q}) \quad (14)$$

with the phases as the only remaining fluctuating quantities. The phase gradient can be decomposed into a longitudinal and a transverse part, $\mathbf{U}_j(\mathbf{q})=[\mathbf{U}_j(\mathbf{q})]_L+[\mathbf{U}_j(\mathbf{q})]_T$, where the longitudinal component corresponds to regular smooth phase fluctuations with zero curl, i.e., "spin waves." Hence, the longitudinal part is curl free, $\mathbf{q}\times[\mathbf{U}_j(\mathbf{q})]_L=\mathbf{0}$ and the transverse part is divergence free, $\mathbf{q}\cdot[\mathbf{U}_j(\mathbf{q})]_T=0$ and thus it is associated with quantized vortices. One can introduce the field $\mathbf{m}_j(\mathbf{q})$ which is the Fourier transform of the integer-valued vortex field for component j,

$$i\mathbf{q}\times[\mathbf{U}_j(\mathbf{q})]_T=2\pi\mathbf{m}_j(\mathbf{q}), \quad j=1,2. \quad (15)$$

Note that this relation yields the constraint $\mathbf{q}\cdot\mathbf{m}_j(\mathbf{q})=0$, i.e., the thermal vortex excitations in the theory are closed loops as required by the single valuedness of the order parameter in an infinite system. In the following, we will disregard the longitudinal phase fluctuations since the physics at the critical points in this system is governed by the vortex excitations and not the spin waves. The latter are known to be innocuous and incapable of destroying long-range order in three dimensional systems. By Eq. (15), the transverse phase gradient is explicitly written as

$$[\mathbf{U}_j(\mathbf{q})]_T=2\pi i\frac{\mathbf{q}\times\mathbf{m}_j(\mathbf{q})}{q^2}, \quad j=1,2, \quad (16)$$

and thus, we finally express the statistical sum via vortex fields,

$$Z=\sum_{\mathbf{m}_1}\sum_{\mathbf{m}_2} e^{-S},$$

$$S=2\beta\pi^2\int d^3q\mathbf{m}_j(\mathbf{q})V_{jk}(q^2)\mathbf{m}_k(-\mathbf{q}). \quad (17)$$

Here, the summation over the vortex fields $\mathbf{m}_j(\mathbf{q})$ is constrained by $\mathbf{q}\cdot\mathbf{m}_j(\mathbf{q})=0$, such that the integer-valued real-space vortex fields $\mathbf{m}_j(\mathbf{r})$ form closed loops only. The vortex-vortex interactions are given by

$$V_{jk}(q^2)=\frac{1}{q^2}\left(R_{jk}-\frac{e_l e_m R_{lj}R_{mk}}{q^2+m_0^2}\right)\Leftrightarrow V(q^2)=\begin{pmatrix}\dfrac{\rho_1-\rho_d-\dfrac{(e_jR_{j1})^2}{m_0^2}}{q^2}+\dfrac{\dfrac{(e_jR_{j1})^2}{m_0^2}}{q^2+m_0^2} & \dfrac{\rho_d-\dfrac{e_je_kR_{j1}R_{k2}}{m_0^2}}{q^2}+\dfrac{\dfrac{e_je_kR_{j1}R_{k2}}{m_0^2}}{q^2+m_0^2}\\ \dfrac{\rho_d-\dfrac{e_je_kR_{j1}R_{k2}}{m_0^2}}{q^2}+\dfrac{\dfrac{e_je_kR_{j1}R_{k2}}{m_0^2}}{q^2+m_0^2} & \dfrac{\rho_2-\rho_d-\dfrac{(e_jR_{j2})^2}{m_0^2}}{q^2}+\dfrac{\dfrac{(e_jR_{j2})^2}{m_0^2}}{q^2+m_0^2}\end{pmatrix}. \tag{18}$$

Here, we have used the identity

$$[\mathbf{U}_j(\mathbf{q})]_T\cdot[\mathbf{U}_k(-\mathbf{q})]_T=\frac{(2\pi)^2}{q^2}\mathbf{m}_j(\mathbf{q})\cdot\mathbf{m}_k(-\mathbf{q}), \tag{19}$$

found by Eq. (16). We may now interpret m_0, given by Eq. (7), as the inverse bare screening length that sets the scale of the Yukawa interactions in the system.

We remind the reader briefly of what is known for the one-component case, i.e., $\rho_2=0$, $\rho_d=0$, $e_2=0$, $\rho_1=\rho\neq 0$, $e_1=e\neq 0$ in Eq. (18). Then, we have $V_{11}=[\rho-e^2\rho^2/(q^2+m_0^2)]/q^2$ with $m_0^2=\rho e^2$. Thus, $V_{11}=\rho/(q^2+m_0^2)$ is a screened interaction between the vortices, mediated by the fluctuating gauge field. This is drastically different from the multicomponent case, where one fluctuating gauge field is incapable of fully screening interactions between vortex excitations in all condensate fields.[5,8,9]

The interactions between vortex elements in the system are generally seen to include two parts: A long-range Coulomb interaction with no intrinsic length scale that decays as $1/r$ and a short-range Yukawa interaction with an exponential decay. Note that in the index representation of Eq. (18), the first term, R_{jk}/q^2 will dominate the second term, $e_l e_m R_{lj}R_{mk}/[q^2(q^2+m_0^2)]\sim q^{-4}$, at short distances when q^2 is large, because the Yukawa and Coulomb part of the second term will cancel each other. Effectively, at short distances, the vortices will interact as if the gauge field does not fluctuate. On the other hand, at large distances, when q^2 is small, the Coulomb part of the second term will dominate its Yukawa counterpart and the second term will be of the same order as the first term $\sim q^{-2}$. Thus, the $1/r$ contributions from the gauge-field mediated interactions between vortices sets in when intervortex separation becomes larger than the characteristic distance m_0^{-1}. Also note that by decreasing the gauge-field coupling constant e, m_0^{-1} grows and so does the distance where the effects of the gauge field are negligible. In particular, when $\rho_d=0$ in Eq. (18) (this corresponds to the work in Refs. 5 and 9), we have the case that the interactions between elementary vortices of different species tend to cancel out at short intervortex separations, whereas there will be interactions at large intervortex separations that are mediated by the gauge field.

In the general model with the mixed-gradient terms considered here (i.e., with $\rho_d\neq 0$), there is in addition unscreened $1/r$ interaction between vortices belonging to different condensates which is mediated by the direct Andreev-Bashkin drag. Thus, contrary to the $\rho_d=0$ case, there will be unscreened Coulomb interactions at all length scales.

Observe that in the limit, $e_1=e_2=0$, Eq. (18) eliminates Yukawa-type interaction potential and resulting to only long-range interactions $V(q^2)=R/q^2$ like in a two-component superfluid with Andreev-Bashkin effect, see Ref. 13. Observe also that in contrast to the neutral model in Ref. 13, in the above case when $e_{1,2}\neq 0$ one always has a bound state of vortices which has finite energy per unit length, as discussed in Sec. II B.

Thus, the vortex-vortex interaction matrix shows that adding the mixed-gradient Andreev-Bashkin-type drag term to a superconductor, where components interact only via a fluctuating gauge field, might significantly alter the physics of fluctuations as a consequence of a substantial change in the interactions between topological excitations.

Finally, in the spirit of Sec. II A, we may rewrite the action in Eq. (17) in a form where the charged and the neutral modes are explicitly identified,

$$S=2\beta\pi^2\int d^3q\left\{\frac{\rho_1\rho_2-\rho_d(\rho_1+\rho_2)}{m_0^2}[e_2\mathbf{m}_1(\mathbf{q})-e_1\mathbf{m}_2(\mathbf{q})]\times\frac{1}{q^2}[e_2\mathbf{m}_1(-\mathbf{q})-e_1\mathbf{m}_2(-\mathbf{q})]+\frac{1}{m_0^2}[e_jR_{j1}\mathbf{m}_1(\mathbf{q})+e_jR_{j2}\mathbf{m}_2(\mathbf{q})]\frac{1}{q^2+m_0^2}[e_kR_{k1}\mathbf{m}_1(-\mathbf{q})+e_kR_{k2}\mathbf{m}_2(-\mathbf{q})]\right\}. \tag{20}$$

Note that the vortex fields in the neutral sector interacts by an unscreened Coulomb interaction only while the vortex fields in the charged sector interacts by a screened Coulomb (Yukawa) interaction. From this it follows that the corresponding propagators are given by $\langle[e_2\mathbf{m}_1(\mathbf{q})-e_1\mathbf{m}_2(\mathbf{q})]\cdot[e_2\mathbf{m}_1(-\mathbf{q})-e_1\mathbf{m}_2(-\mathbf{q})]\rangle\sim q^2$ and $\langle[e_jR_{j1}\mathbf{m}_1(\mathbf{q})+e_jR_{j2}\mathbf{m}_2(\mathbf{q})]\cdot[e_jR_{j1}\mathbf{m}_1(-\mathbf{q})+e_jR_{j2}\mathbf{m}_2(-\mathbf{q})]\rangle\sim q^2+\tilde{m}_0^2$. Here, $\tilde{m}_0$ is the *effective* dynamically generated gauge mass that is nonzero in the low-temperature phase and vanishes at the charged critical point. Moreover, there is also a neutral critical point associated with ordering the neutral sector of Eq. (20) with a corresponding nonanalytic variation in the temperature dependence of the coefficient of the q^2 term.

Note that for any value of ρ_d, the interactions of the vortex fields in the neutral sector are independent of any variation in the charges e_1 and e_2 provided that the ratio e_2/e_1 is kept fixed, as readily seen by inspection of Eq. (20). On the other hand, the interactions in the charged sector depends on

the value of the charge in the Yukawa factor $1/(q^2+m_0^2)$.

Given the very different form of intervortex interactions produced by the gauge-field coupling and by the Andreev-Bashkin drag, the interesting case when these interactions compete with each other cannot be mapped onto the previously studied regimes of systems interacting only by gauge field or only by intercomponent drag. Investigating the physics arising from this competition is the main objective in this paper.

III. DETAILS OF THE MONTE CARLO SIMULATIONS

Large-scale Monte Carlo (MC) simulations were performed in order to explore the phases and phase transitions of the model, Eq. (1). We discretize space into a three dimensional cubic lattice of size $L\times L\times L$ with lattice spacing $a=1$. The phases are defined on the vertices of the lattice, $\theta_j(\mathbf{r})\to\theta_{\mathbf{r},j}$ and the phase gradient is a finite difference of the phase at two neighboring lattice points, $\partial_\mu\theta_j(\mathbf{r})\to\Delta_\mu\theta_{\mathbf{r},j}=\theta_{\mathbf{r}+\hat{\boldsymbol{\mu}},j}-\theta_{\mathbf{r},j}$. The gauge field is associated with the links between the lattice points, $A_\mu(\mathbf{r})\to A_{\mathbf{r},\mu}$. Moreover, the curl of the gauge field yields a plaquette sum $[\nabla\times\mathbf{A}(\mathbf{r})]_\mu\to\Sigma_{\nu\eta}\varepsilon_{\mu\nu\eta}\Delta_\nu A_{\mathbf{r},\eta}$. Here, $\varepsilon_{\mu\nu\eta}$ is the Levi-Civita symbol. The compact phases $\theta_{\mathbf{r},j}$ have to be 2π periodic. This is accommodated by the Villain approximation of the effective Hamiltonian,[27] which also yields a faithful lattice representation of the direct current-current interaction (i.e., drag) term.[13] Our effective lattice model thus reads

$$Z=\int_0^{2\pi}\mathcal{D}\theta_1\int_0^{2\pi}\mathcal{D}\theta_2\int_{-\infty}^{\infty}\mathcal{D}\mathbf{A}e^{-\beta H[\theta_1,\theta_2,\mathbf{A};\beta]},$$

$$H[\theta_1,\theta_2,\mathbf{A};\beta]=\sum_{\mathbf{r},\mu}-\beta^{-1}\ln\left\{\sum_{n_{\mathbf{r},\mu,1}}\sum_{n_{\mathbf{r},\mu,2}}e^{-S}\right\},\qquad(21)$$

where the local Villain action is

$$S=\frac{\beta}{2}\Bigg[\rho_1u_{\mathbf{r},\mu,1}^2+\rho_2u_{\mathbf{r},\mu,2}^2-\rho_d(u_{\mathbf{r},\mu,1}-u_{\mathbf{r},\mu,2})^2+\left(\sum_{\nu\eta}\varepsilon_{\mu\nu\eta}\Delta_\nu A_{\mathbf{r},\eta}\right)^2\Bigg].\qquad(22)$$

Here, $u_{\mathbf{r},\mu,j}=\Delta_\mu\theta_{\mathbf{r},j}-e_jA_{\mathbf{r},\mu}-2\pi n_{\mathbf{r},\mu,j}$ is a one-component Villain argument. The sum over the integer-valued fields, $n_{\mathbf{r},\mu,j}$, is from $-\infty$ to ∞ ensures 2π periodicity of the Hamiltonian with respect to the gauge-invariant phase difference.

All Monte Carlo simulations start with an initialization of the system, either disordered, when all phases and gauge fields are chosen at random, or ordered, when phases and gauge fields are chosen constant throughout the system. Subsequently, a sufficiently large number of sweeps is performed in order to thermalize the system. As a valuable check on the simulations, the calculated quantities should be invariant with respect to the initialization procedure. A Monte Carlo sweep includes local updating of all five fluctuating field variables (compact phases $\theta_{\mathbf{r},j}\in[0,2\pi\rangle$ and the noncompact gauge field $A_{\mathbf{r},\mu}$) at all lattice sites in the system, according to the Metropolis-Hastings algorithm.[28] There is no gauge fixing involved, as summation over gauge equivalent configurations will cancel out when calculating thermal averages of gauge-invariant quantities. Moreover, periodic boundary conditions are applied in all simulations.

In most cases, we also apply the so-called parallel tempering algorithm,[29] allowing a global swap of configurations between neighboring couplings, after the local updating is finished. The explicit temperature dependence in the Hamiltonian of the Villain model[30] must be considered when calculating the probability of exchanging configurations between two coupling values β, β', which is

$$W_{PT}=\begin{cases}1, & \text{if } \Delta<0,\\ e^{-\Delta}, & \text{if } \Delta\geq 0,\end{cases}\qquad(23)$$

where $\Delta=\beta'(H[X;\beta']-H[X';\beta'])-\beta(H[X;\beta]-H[X';\beta])$, and X, X' are the configurations at β, β' initially. To increase the performance of the parallel tempering algorithm, the set of coupling values was selected according to the initialization procedure in Ref. 31, to yield approximately the same acceptance rate for the parallel tempering move throughout the entire range of coupling values in the simulation. By introducing the parallel tempering algorithm, the quality of the statistical output was substantially improved by reducing the autocorrelation time at critical points by 1–2 orders of magnitude compared with conventional Monte Carlo simulations with local updates only. Even in regions of the phase diagram where coupling intervals were too large for configurations to access all coupling values within a reasonable amount of MC sweeps, which is required to take full advantage of the parallel tempering method,[29] an improvement of the statistical output was achieved.

A. Specific heat

We measure the specific heat per site C_v by the energy fluctuations,

$$\frac{C_vL^3}{\beta^2}=\langle(H-\langle H\rangle)^2\rangle,\qquad(24)$$

where the brackets denote thermal average with respect to the partition function in Eq. (21). In fact, this expression is not quite right for the Villain model because of the explicit temperature dependence in the Hamiltonian.[30] Generally, the specific heat is given by $L^3C_v=-\beta^2\partial U/(\partial\beta)$, where the internal energy is given by $U=-\partial\ln Z/(\partial\beta)$.[32] Thus, the specific heat is written as

$$\frac{C_vL^3}{\beta^2}=\left\langle\left(\frac{\partial(\beta H)}{\partial\beta}-\left\langle\frac{\partial(\beta H)}{\partial\beta}\right\rangle\right)^2-\frac{\partial^2(\beta H)}{\partial\beta^2}\right\rangle.\qquad(25)$$

We expect no extra singular behavior due to the temperature dependence in the Villain Hamiltonian, so the singular behavior in Eq. (25) should also be captured in the energy fluctuations of Eq. (24). Thus, we expect Eq. (24) to reproduce the correct critical behavior of the heat capacity, as was the case in Ref. 33. In practice, both equations were used, and the results were identical with respect to critical behavior. In the analysis of the Monte Carlo simulations, the critical temperature of the phase transitions was determined by locating the anomaly of the heat capacity, and the same criti-

cal temperature was found with both equations.

B. Helicity modulus

The helicity modulus is a global measure of phase coherence in a superfluid (i.e., decoupled from gauge field) order parameter. It measures the energy cost associated with an infinitesimal twist $\boldsymbol{\delta}$ in the phase of an order parameter across the system. In order to obtain the correct energy cost with respect to composite phase combinations such as, e.g., phase difference, we must perform a general twist in a linear combination of the order parameter phases,

$$\theta_{\mathbf{r},j} \to \theta'_{\mathbf{r},j} = \theta_{\mathbf{r},j} - a_j \boldsymbol{\delta} \cdot \mathbf{r}, \tag{26}$$

where a_j now is a real number associated with the phase twist in component j. By selecting a_1, a_2, we may measure the phase coherence of any linear combination, $a_1\theta_1 + a_2\theta_2$, in order parameter space. That is, if we want to measure the helicity modulus of the neutral mode associated with the phase difference we must impose a twist in the phase difference, i.e., $a_1 = 1$, $a_2 = -1$. In general, the helicity modulus is given by the second derivative of the free energy with respect to the infinitesimal twist,

$$\Upsilon_{\mu,(a_1,a_2)} = \frac{1}{L^3} \frac{\partial^2 F[\theta']}{\partial \delta_\mu^2}\bigg|_{\boldsymbol{\delta}=0} = \frac{1}{L^3}\left[\left\langle \frac{\partial^2 H[\theta']}{\partial \delta_\mu^2}\right\rangle - \beta\left\langle \left(\frac{\partial H[\theta']}{\partial \delta_\mu} - \left\langle \frac{\partial H[\theta']}{\partial \delta_\mu}\right\rangle\right)^2\right\rangle\right]\Bigg|_{\boldsymbol{\delta}=0}, \tag{27}$$

where the notation θ' simply means that all phase variables are replaced according to Eq. (26). In our case, with an isotropic system, we expect the helicity modulus to yield directionally independent results within statistical errors. For more details on the helicity modulus in the special case of the Villain model, we refer to Refs. 13 and 33.

C. Gauge mass

To capture the properties of the gauge field $\mathbf{A}$, we study the gauge-field correlator $\langle \mathbf{A}_\mathbf{q}\mathbf{A}_{-\mathbf{q}}\rangle$, explicitly given for the lattice model,

$$\langle \mathbf{A}_\mathbf{q}\mathbf{A}_{-\mathbf{q}}\rangle = \frac{2}{\beta(|\mathbf{Q}_\mathbf{q}|^2 + m_0^2)}\left[1 + \frac{2\beta\pi^2 \mathcal{G}_{c,\mathbf{q}}}{|\mathbf{Q}_\mathbf{q}|^2(|\mathbf{Q}_\mathbf{q}|^2 + m_0^2)}\right], \tag{28}$$

where $|\mathbf{Q}_\mathbf{q}|^2$ is the Fourier representation of the discrete Laplace operator, given by $|\mathbf{Q}_\mathbf{q}|^2 = \Sigma_\mu [2\sin(q_\mu/2)]^2$, with $q_\mu = 2\pi n_\mu / L$, $n_\mu \in [1, \ldots, L]$ and

$$\mathcal{G}_{c,\mathbf{q}} = \langle e_j e_l R_{jk} R_{lm} \mathbf{m}_{\mathbf{q},k} \cdot \mathbf{m}_{-\mathbf{q},m}\rangle, \tag{29}$$

is the correlation function of the linear combination of vortex fields that corresponds to the charged sector of Eq. (20). Here $\mathbf{m}_{\mathbf{q},j}$ is the lattice model vortex field of component j in Fourier space. The details of the derivation are given in Appendix B. In particular, we will use this quantity to extract the order parameter for the normal fluid-superconductor phase transition, i.e., the dynamically generated gauge-field mass or Higgs mass. The effective gauge mass $m_\mathbf{A}$ is extracted from the gauge-field correlator by[8,9,34]

$$m_\mathbf{A}^2 = \lim_{\mathbf{q}=0} \frac{2}{\beta\langle \mathbf{A}_\mathbf{q}\mathbf{A}_{-\mathbf{q}}\rangle}. \tag{30}$$

This quantity is employed as order parameter of the superconducting phase. Note that the dynamic creation of mass at T_c and the onset of the Meissner phase, the manifestation of the Higgs mechanism in London superconductors, is governed entirely by the long-distance behavior of the vortex correlator of the charged mode, cf. Eqs. (28) and (29). In the ordered phase, where vortex loops are confined, $\lim_{\mathbf{q}\to 0}\langle \mathbf{m}_k(\mathbf{q})\mathbf{m}_m(-\mathbf{q})\rangle \sim q^2$, such that $\lim_{\mathbf{q}\to 0}\langle \mathbf{A}(\mathbf{q})\mathbf{A}(-\mathbf{q})\rangle \sim$ const, rendering the gauge field massive. When vortex loops proliferate, $\lim_{\mathbf{q}\to 0}\langle \mathbf{m}_k(\mathbf{q})\mathbf{m}_m(-\mathbf{q})\rangle = \text{const} \neq 0$, such that $\lim_{\mathbf{q}\to 0}\langle \mathbf{A}(\mathbf{q})\mathbf{A}(-\mathbf{q})\rangle \sim 1/q^2$, rendering the gauge field massless.

In the Monte Carlo simulations, the vortex fields of both species are extracted from the phase and gauge-field distributions by considering the plaquette sum of the gauge-invariant phase difference,

$$\sum_{\nu\eta} \varepsilon_{\mu\nu\eta}\Delta_\nu(\Delta_\eta \theta_{\mathbf{r},j} - e_j A_{\mathbf{r},\eta}) = 2\pi m_{\mathbf{r},\mu,j}, \tag{31}$$

where the left-hand side is the plaquette sum of the gauge-invariant phase difference, $\Delta_\mu \theta_{\mathbf{r},j} - e_j A_{\mathbf{r},\mu}$ and $m_{\mathbf{r},\mu,j}$ is the real-space vortex field. The gauge-invariant phase difference must be kept in the primary interval for each link in the plaquette sum in order to accommodate vortices in the lattice model. Now, by Fourier transformation of the vortex field, $\mathcal{G}_{c,\mathbf{q}}$ is calculated, and to find the gauge mass, curve fitting of the quantity $2/(\beta\langle \mathbf{A}_\mathbf{q}\mathbf{A}_{-\mathbf{q}}\rangle)$ is performed for small q values in order to extract the $q \to 0$ limit.

IV. MONTE CARLO RESULTS, $\rho_d = 0$, $e_1 = e_2 = e$

Here we present the simulation results for the case discussed in Sec. II B. In this section we consider in general unequal stiffnesses $\rho_1 \neq \rho_2$ in the regime where $\rho_d = 0$.

Figure 1 shows the simulation results varying the stiffness ρ_2, when the other stiffness ρ_1 is set to unity. Results are obtained for six different values of the electric charge, and we focus on the regimes where there is a strong competition between proliferating topological defects. We locate the critical inverse temperature of the charged and the neutral critical point by locating the anomaly of the heat capacity associated with the phase transition. The charged critical point is associated with the point where the Meissner effect sets in, evident by onset of the effective gauge mass $m_\mathbf{A}$, whereas the neutral critical point is associated with the onset of the order in the gauge-invariant phase difference with a corresponding nonzero value of the associated helicity modulus $\Upsilon_{\mu,(1,-1)}$.

A. Topological excitations

Consider now the case when the neutral critical line is situated above the charged critical line, that is, when going from phase I $[U(1) \times U(1)$ broken symmetry] to phase III

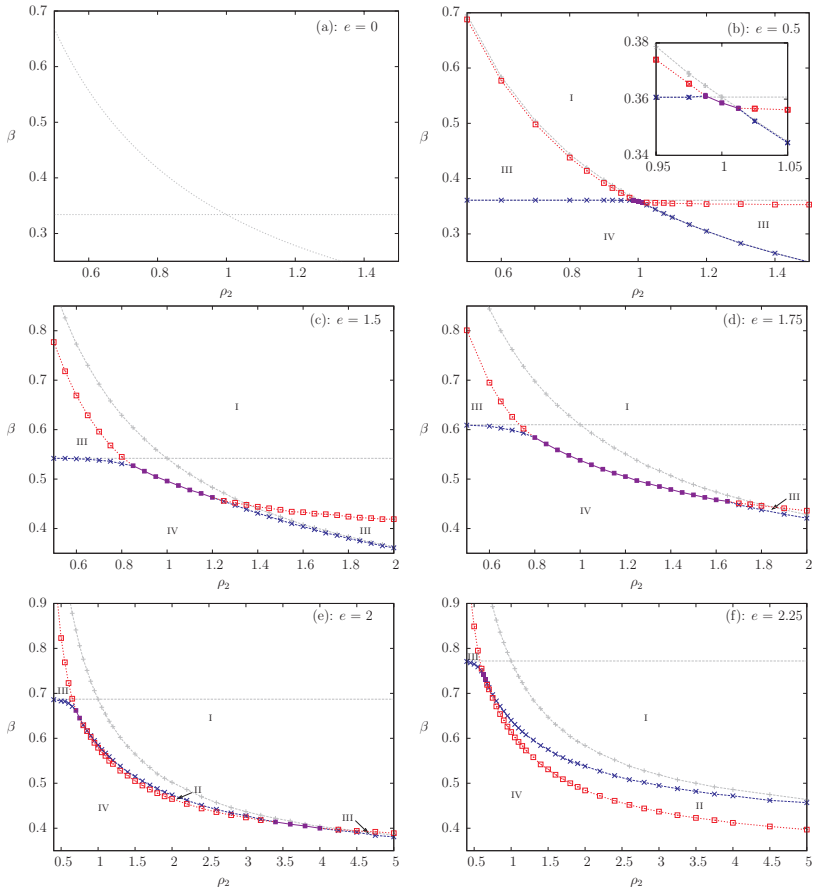

FIG. 1. (Color online) The phase diagram in the (ρ_2, β) plane for the model in Eq. (9) at six increasing values of the electric charge e when $\rho_1 = 1$. Blue x markers ($\times$) connected with dashed lines are charged critical points and red squares ($\square$) connected with dotted lines are the neutral critical points. When these critical points are merged, it is shown by filled squares ($\blacksquare$) in violet connected with solid lines. Moreover, with lines in silver color, we present critical points of one-component superconductors with e as denoted in panel. The horizontal line is the critical line when $\rho = \rho_1 = 1$, and the plus markers (+) are the critical points when $\rho = \rho_2$. For these reference lines, the dashed and dotted line type correspond to charged and neutral critical points, as above. The inset in panel (b) is a magnification of the region where the lines merge. Phases are denoted by roman numbers. I. Ordered phase with spontaneously broken $U(1) \times U(1)$ symmetry, $m_{\mathbf{A}} \neq 0$, $\Upsilon_{\mu,(1,-1)} \neq 0$. II. Spontaneously broken global $U(1)$ symmetry, with restored $U(1)$ gauge symmetry, $m_{\mathbf{A}} = 0$, $\Upsilon_{\mu,(1,-1)} \neq 0$. III. Spontaneously broken $U(1)$ gauge symmetry, with restored global $U(1)$ symmetry, $m_{\mathbf{A}} \neq 0$, $\Upsilon_{\mu,(1,-1)} = 0$. IV. Normal phase with fully restored $U(1) \times U(1)$ symmetry, $m_{\mathbf{A}} = 0$, $\Upsilon_{\mu,(1,-1)} = 0$. The system size considered is 32^3. Except for inset, error bars are smaller than marker size and thus omitted from diagram.

[broken $U(1)$ charged symmetry] across the neutral phase transition line in Fig. 1. This phase transition is driven either by proliferation of (0,1) or (1,0) vortices. The composite (1,1) vortices do not couple to the neutral sector of Eq. (9) and can thus never be responsible for destroying the order in the neutral sector. The other composite topological excitation $(1,-1)$ is, by inspection of Eq. (9), seen to have neither energetic nor entropic advantage over individual vortices. Because the vortices (1,0), (0,1) cost the same amount of energy in the neutral sector, but the vortex with lowest stiffness ρ_j costs less energy in the charged sector, the neutral critical line must be associated with proliferation of individual vortices of the component with the smallest value of the bare stiffness ρ_j, when going from phase I to phase III. Outside the region where there is a strong competition between different kinds of vortex excitations, this phase transition is found to be of second order in the 3Dxy universality class.[9] When the individual vortices proliferate, the corresponding stiffness is renormalized to zero and the remaining condensate will be a charged condensate with order in the remaining component. Thus, the remaining condensate will, at a higher temperature, have a phase transition similar to that of the following one-component superconductor,

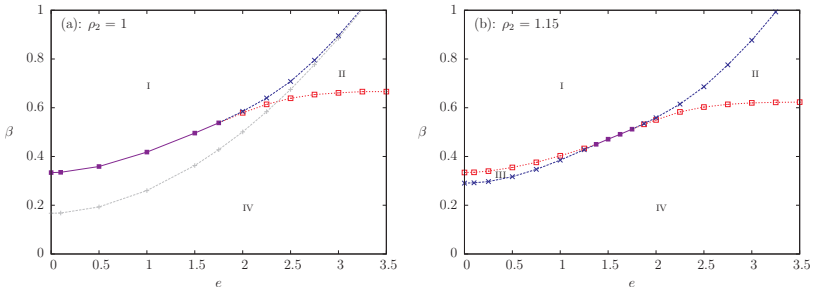

FIG. 2. (Color online) The phase diagram in the (β, e) plane for the two-component 3D London model, Eq. (9), with $\rho_1=1$ and for two different values of ρ_2. In the left diagram $\rho_2=\rho_1=\rho=1$ whereas $\rho_2=1.15$ in the right diagram, i.e., there is a moderate disparity. Markers and line types are the same as in Fig. 1, i.e., blue x markers ($\times$) connected with dashed lines are charged critical points, red squares ($\square$) connected with dotted lines are neutral critical points, filled squares ($\blacksquare$) in violet connected with solid lines are merged transitions. The silvered plus markers (+) in the left diagram is a one-component reference line of a superconductor with bare stiffness 2ρ and charge e. Roman numbers denote the different phases as given in the caption of Fig. 1. Note that these diagrams are 2D cross sections of a 3D phase diagram in (β, ρ_2, e) space perpendicular to the cross sections in Fig. 1. The lattice size is 32^3. Errors are smaller than marker size and thus omitted from diagram.

$$F^{\text{eff}}_{\text{III}\to\text{IV}} = \frac{\rho_j}{2}(\nabla\theta_j - e\mathbf{A})^2 + \frac{(\nabla\times\mathbf{A})^2}{2}, \tag{32}$$

where j now is the index of the component with largest stiffness ρ_j.

This is verified in Fig. 1 by observing that the charged critical line between III and IV asymptotically approaches the one-component reference lines away from the region of competition between different kinds of topological excitations. This phase transition is second order and in the universality class of the inverted 3Dxy transition.[9]

When there is a transition from phase I $[U(1)\times U(1)$ broken symmetry] to phase II [broken $U(1)$ neutral symmetry] in panels (e) and (f) of Fig. 1, the charged critical point is situated at a lower temperature than the neutral critical point. In this case the topological defects responsible for the phase transition are (1,1) vortices, because the other possible vortices will destroy order in the neutral sector of Eq. (9), and thus are not proliferating at this transition line. As discussed in Sec. II B, the (1,1) vortices proliferating from an ordered background may be mapped onto a single-component superconductor with effective stiffness (neglecting the internal structure of the vortices) $\rho' = \rho_1 + \rho_2$,

$$F^{\text{eff}}_{\text{I}\to\text{II}} = \frac{\rho_1+\rho_2}{2}(\nabla\theta - e\mathbf{A})^2 + \frac{(\nabla\times\mathbf{A})^2}{2}. \tag{33}$$

In Fig. 2 we show results when bare component stiffnesses ρ_j are kept fixed and electric charge e is varied. In panel (a), we also present a one-component reference line corresponding to the phase transition of the superconductor in Eq. (33). Indeed, away from the splitting point, the transition from I to II approaches this reference line. Note that the mapping in Eq. (33) yields a one-component superconductor with stiffness $\rho_1+\rho_2$ that always is stiffer than the two reference lines in Fig. 1 (which are one-component superconductors with stiffness ρ_1 and ρ_2). Thus, the charged transition line between phase I and phase II is always lower than the reference lines in Fig. 1. Phase II in Figs. 1 and 2 is the metallic superfluid phase (i.e., exhibiting order only in the gauge-invariant phase difference) discussed in Sec. II B and the effective free energy in the remaining superfluid condensate is given in Eq. (11). The cheapest topological defects that proliferate at higher temperatures and destroy the remaining composite order in this phase, are individual vortices. Hence, away from the region of competing topological defects (i.e., away from the splitting point), the transition line from phase II to phase IV should be similar to a one-component superfluid with effective stiffness $\rho' = \rho_1\rho_2/(\rho_1+\rho_2)$,

$$F^{\text{eff}}_{\text{II}\to\text{IV}} = \frac{\rho_1\rho_2}{2(\rho_1+\rho_2)}(\nabla\theta)^2. \tag{34}$$

Note that in both panels of Fig. 2, the neutral transition line between II and IV is found to be asymptotically independent of e, thus approaching a constant value asymptotically far away from the region of competition with different vortices, as Eq. (34) suggests. Moreover, Eq. (34) predicts the value $\beta = \beta_c(\rho_1+\rho_2)/(\rho_1\rho_2)$ of the actual line, which corresponds well with the results in the figure. Here, $\beta_c \approx 0.334$ is the critical point of the one-component superfluid ($e=0$) when $\rho=1$.

Note that vortices on the form (n_1, n_2) with $n_j \geq 1$, $n_{k\neq j} > 1$ can, by inspection of Eq. (9), be shown to always be energetically unfavorable compared with other topological excitations in this model. Such higher-order vortices are thus not relevant when $\rho_d=0$ and $e_1=e_2=e$.

B. Gauge-field fluctuation driven merger of the phase transitions in case of unequal bare stiffnesses

We next discuss the evolution of the phase diagrams in Figs. 1 and 2 when e is varied. When charge increases, the energy of the composite (1,1) vortices (which have no topological charge in the neutral sector), as well as the energy associated with charged currents of individual vortices decrease. This leads to a formation of a region in the phase

diagram which is characterized by a *merger of the two* $U(1)$ transitions in the case of unequal bare stiffnesses of the two condensates. Thus, even in the case of unequal stiffnesses, when the coupling to a fluctuating noncompact gauge field is sufficiently strong, there appears a phase transition directly from the ordered phase with spontaneously broken $U(1) \times U(1)$ symmetry to the fully disordered normal phase. See also discussions of transition mergers caused by other kinds of couplings in Refs. 13, 14, and 35. Panel (b) of Fig. 2 clearly illustrates this behavior. In this panel, the value of bare stiffness disparity is fixed when e increases. For low values of e there are two phase transitions: at lower temperature individual vortices with lower stiffness proliferate while at higher temperature a proliferation of individual vortices of stiffer condensate takes place. However, when e increases, the two lines approach each other and merge at $e \approx 1.3$.

The line merger is a consequence of the fact that at a substantially large electric charge, the bare energy of an individual vortex in a broken $U(1) \times U(1)$ phase is dominated by the neutral mode. Because a proliferation of less energetically expensive individual defects destroys the neutral mode, this eliminates the bare long-range logarithmic interaction between vortices in the stiffer condensate, leading to a dramatic decrease in their bare line tension and thus to their *preemptive* proliferation. On the other hand in a range of parameters a proliferation of composite (1,1) vortices can trigger proliferation of individual vortices again leading to a "preemptive" restoration of the full $U(1) \times U(1)$ symmetry via a single phase transition. When electric charge is increased further, then eventually at a certain point in the interval $e \in (1.75, \ldots, 1.875)$ the (1,1) vortices become much less energetically expensive than other excitations and can proliferate at low temperatures without triggering a proliferation of individual vortices. Then the metallic superfluid phase (II) emerges as discussed in Sec. II B.

C. Order of the phase transition associated with the merged lines

Let us now characterize the phase transition along the merged lines of Figs. 1 and 2. In Ref. 10, using the **j**-current model the transition line from $U(1) \times U(1)$ to fully symmetric state in the case of equal stiffnesses presented in panel (a) of Fig. 2, was found to be a first-order transition. We obtain consistent results in our Villain-model based simulations.

Furthermore in Fig. 3, we report the simulation results associated with the merged line in a case when bare stiffnesses are not equal. We find a first-order transition along the merged line in our case when there is a disparity of the bare phase stiffnesses. This shows that the first-order phase transition in a $U(1) \times U(1)$ noncompact gauge theory is not related to the specific degeneracy of the model with equal stiffnesses $\rho_1 = \rho_2$ but appears to be related to the case when there are several competing or composite topological defects.

V. MONTE CARLO SIMULATION, GENERAL MODEL WITH BOTH GAUGE FIELD AND DISSIPATIONLESS DRAG INTERACTIONS

Next, we present results from Monte Carlo simulations when both drag and gauge-field mediated interactions are included.

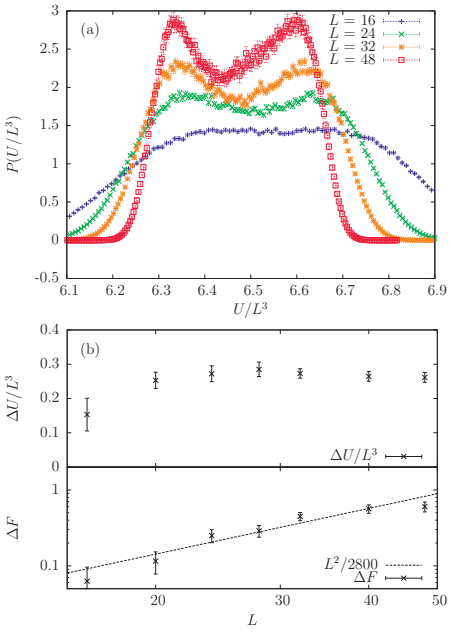

FIG. 3. (Color online) (a) Histograms for the probability distribution of the internal energy per site U/L^3 at $\beta \approx 0.487$ when parameters are $\rho_1 = 1$, $\rho_2 = 1.05$, and $e = 1.5$. This is the merged transition point found in Fig. 1 at $(\rho_2, \beta) = (1.05, 0.487)$ in panel (c). A double-peak structure develops when L increases. (b) Upper panel shows that the finite-size scaling of the latent heat per site $\Delta U/L^3$ approaches a finite value when L increases. This is the distance between the peaks in (a). The lower panel shows the finite-size scaling of the difference in the free energy, $\Delta F = (1/\beta)\ln(P_{\max}/P_{\min})$ taken between the double-peak value $P_{\max}$ and the value of the minimum in between $P_{\min}$ of the histograms in (a). For a first-order phase transition, $\Delta F \sim L^{d-1}$ (Ref. 36). Ferrenberg-Swendsen reweighting was used to obtain histograms with similar height peaks (Ref. 37).

A. Competing gauge field and drag interactions in the case $\rho_1 = \rho_2 = 1$

In Fig. 4, we present results for the case when the bare component stiffnesses are equal $\rho_1 = \rho_2 = \rho = 1$, and the gauge field couplings are equal, $e_1 = e_2 = e$. We vary the inverse temperature β and the bare drag coefficient ρ_d and map out the phase diagram in the $(\beta, \beta\rho_d)$ plane for a number of different values of e. We consider positive ρ_d only. In this specific case, the charged and neutral modes in Eq. (5) are written as

$$F = \frac{1}{2}\left[\frac{\rho - 2\rho_d}{2}(\nabla\theta_1 - \nabla\theta_2)^2 + \frac{\rho}{2}(\nabla\theta_1 + \nabla\theta_2 - 2e\mathbf{A})^2 + (\nabla \times \mathbf{A})^2\right]. \quad (35)$$

Here, we have the interesting situation where drag and gauge-field mediated intercomponent long-range vortex interactions are found to be of opposite signs, see Eq. (18).

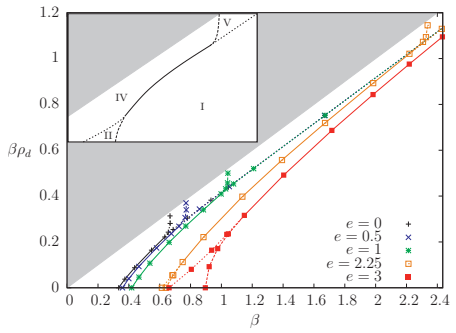

FIG. 4. (Color online) Phase diagram in the $(\beta,\beta\rho_d)$ plane with competing gauge-field and drag interactions. Results are given for five different values of the charge $e_1=e_2=e$. The bare component stiffnesses are equal, $\rho_1=\rho_2=1$, and the system size considered is 32^3. The gray-shaded area is the prohibited region by the stability condition, Eq. (8). Line type corresponds to character of phase transition as in Fig. 1, that is, charged lines are dashed, neutral lines are dotted, and merged transition lines are solid. Except for this, lines are guide to the eyes, only. The inset in the figure shows the schematic structure of the phases in the diagram for all cases with $e>0$. Roman numbers denote phases. Phases I, II, and IV are the same as given in the caption of Fig. 1, whereas V is, similar to phase III in Fig. 1, a phase with spontaneously broken $U(1)$ gauge symmetry, and restored global $U(1)$ symmetry, $m_{\mathbf{A}}\neq 0$, $\Upsilon_{\mu,(1,-1)}=0$. However, in V the broken $U(1)$ gauge symmetry is associated with composite phase sum, whereas in phase III of Fig. 1, it is associated with the phase of the single ordered component. For the given ranges of the phase diagram, II is only found for $e=2.25$ and $e=3$ and V is not found for $e=3$. When $e=0$, all phase transitions are neutral and phase II and V are associated with broken global $U(1)$ symmetry in the phase difference and phase sum, respectively (Ref. 13). The results for $e=0$ are here simulated with a fluctuating gauge field and coincide (as they should) with the equal stiffnesses results in Ref. 13 with no fluctuating gauge field.

Thus, the drag coupling $\rho_d\neq 0$, when significantly strong, favors formation of the $(1,-1)$ composite vortices (via a mechanism similar to that in Ref. 13). On the other hand, the gauge-field coupling favors the formation of (1,1) bound states of individual vortices when e_1 and e_2 are of the same sign. This competition is studied in Fig. 4. Its most striking consequence is that it leads to the existence of four phases: at strong drag there is a superconducting phase where a neutral mode is destroyed by the proliferated $(1,-1)$ vortices (phase V). At strong electric charge there is a superfluid phase with proliferated (1,1) vortices (phase II).

We next consider these phases more closely. The results in Fig. 4 show that the phase V appears when $(1,-1)$ vortices proliferate and thus there is no longer a broken symmetry in the neutral sector of Eq. (35). Note that when we are well above the region of competing topological defects in Fig. 4, then, by neglecting the internal vortex structure, we may approximate the $(1,-1)$ vortices to map onto vortices in a one-component superfluid with stiffness $\rho'=2(\rho-2\rho_d)$,

$$F^{\text{eff}}_{\text{I}\to\text{V}}=(\rho-2\rho_d)(\nabla\theta)^2. \tag{36}$$

This effective limiting model is e independent. Indeed this physics manifests itself in the fact that in Fig. 4, the actual transition is seen to approach asymptotically the reference line $\beta\rho_d=(\beta-\beta_c/2)/2$.

In Sec. IV, the superconducting phase III, which similarly to phase V exhibits charged order and neutral disorder, was created from the fully ordered phase by proliferation of individual vortices when we increased disparity in the bare stiffness of the two components. Here, phase V is created by proliferation of composite vortices and the coupling constant responsible for creating the phase is ρ_d. Consequently, the remaining order is now in the gauge-invariant phase difference of the charged mode, given by second and third terms in Eq. (35). On the other hand, phase III exhibits order in the component with largest bare stiffness. Note also that in the $U(1)\times U(1)$ (phase I) state with equal stiffnesses the (1,0), (0,1) vortices carry half of the magnetic flux quanta.[19] It can be seen from Eq. (35) that in the phase V (1,0), (0,1) vortices become equivalent and no longer have logarithmic divergence of internal energy per unit length due to absence of a neutral mode. That is, they become similar to Abrikosov vortices, but carry only a half quantum of magnetic flux. This phenomenon is related to the fractionalization of superfluid velocity quantum in the metallic superfluid state.[18] From Eq. (35) it also follows that the individual vortices behave as vortices in a one-component superconductor with effective stiffness $\rho'=\rho/2$ and double effective charge $e'=2e$,

$$F^{\text{eff}}_{\text{V}\to\text{IV}}=\frac{\rho}{4}(\nabla\theta-2e\mathbf{A})^2+\frac{(\nabla\times\mathbf{A})^2}{2}. \tag{37}$$

In Fig. 4, the transition from the phase V to the normal phase IV is indeed found to tend asymptotically to a phase transition one would predict from the model, Eq. (37). For this model, the transition line is found to be vertical, in accordance with the drag independent stiffness in Eq. (37). Note that when e increases, the critical temperature of the vortex loop proliferation is decreased and the vertical line moves to the right in Fig. 4.

Next, the phase II may be investigated in a similar way as the phase V above. Phase II appears when (1,1) vortices proliferate. As discussed in Sec. IV, the remaining order is in the neutral sector of Eq. (5) and the transition to the normal state is governed by proliferation of individual vortices that asymptotically behave as a one-component superfluid with effective stiffness $\rho'=(\rho-2\rho_d)/2$,

$$F^{\text{eff}}_{\text{II}\to\text{IV}}=\frac{\rho-2\rho_d}{4}(\nabla\theta)^2. \tag{38}$$

The phase transition of this condensate will follow the line $\beta\rho_d=(\beta-2\beta_c)/2$. Indeed, this is the case for $e=3$ in Fig. 4 away from the region with competing topological defects.

Similarly to Sec. IV we find evidence of a first-order transition when lines are merged and $e>0$, as seen in Fig. 5. When only drag or gauge field is included in a two-component system, first-order transitions may emerge.[10,11,13]

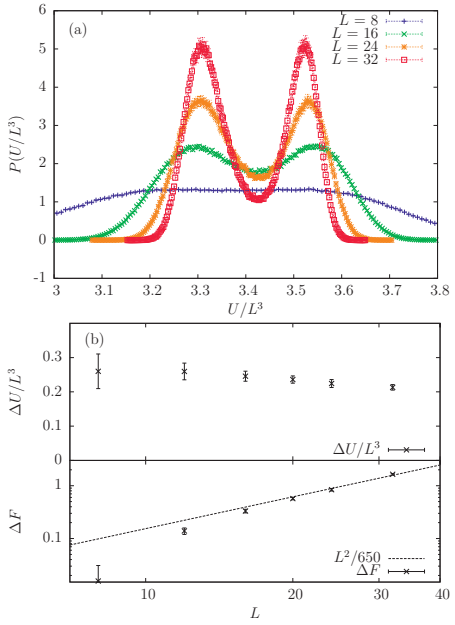

FIG. 5. (Color online) (a) Histograms for the probability distribution of the internal energy per site U/L^3 at the critical point when parameters are $\rho_1=\rho_2=\rho=1$, $e_1=e_2=e=1$, and $\rho_d=0.4$. This is a merged transition point at $(\beta,\beta\rho_d)=(0.948,0.379)$ along the critical line for $e=1$ in Fig. 4. A pronounced double-peak structure is found to develop when L increases. (b) Upper panel shows the finite-size scaling of the latent heat per site $\Delta U/L^3$. This is the distance between the peaks in (a). The lower panel shows the finite-size scaling of the difference in the free energy, $\Delta F=(1/\beta)\ln(P_{\max}/P_{\min})$ taken between the double-peak value $P_{\max}$ and the value of the minimum in between $P_{\min}$ of the histograms in (a). For a first-order phase transition, $\Delta F\sim L^{d-1}$ (Ref. 36). Ferrenberg-Swendsen reweighting was used to obtain histograms with peaks of similar height (Ref. 37).

Our results show that the first-order character of this phase-transition line persists also in the case where both of the interactions are present and competing.

B. Regime where gauge field and drag interactions both favor formation of similar paired phase

In Fig. 6 we present the phase diagram in the case when $\rho_1=\rho_2=\rho=1$ and $e_1=-e_2=e=1$. The separation in neutral and charged modes is now,

$$F=\frac{1}{2}\left[\frac{\rho-2\rho_d}{2}(\nabla\theta_1-\nabla\theta_2-2e\mathbf{A})^2+(\nabla\times\mathbf{A})^2+\frac{\rho}{2}(\nabla\theta_1+\nabla\theta_2)^2\right]. \quad (39)$$

The motivation for investigating this particular case is found in the off-diagonal elements of the matrix in Eq. (18) where the interactions originating with the gauge field will act in unison with the bare drag interactions upon switching the sign of the electric charge in one of the components (in contrast to the situation considered in the previous section).

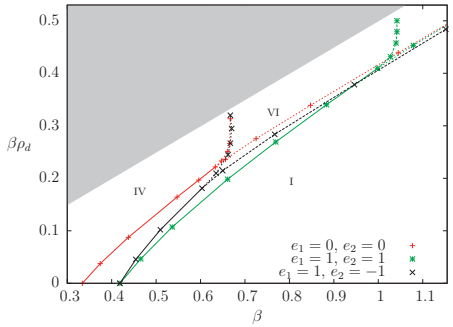

FIG. 6. (Color online) Phase diagram in the $(\beta,\beta\rho_d)$ plane of the general model when $\rho_1=\rho_2=1$ for the case of different charges $e_1=-e_2=1$. These are the black x markers ($\times$) and the line type denotes charged, neutral, and merged critical lines by dashed, dotted, and solid lines as in Figs. 1, 2, and 4. Roman numbers denote the phases of this particular case, $e_1=-e_2=1$. I. Ordered phase with spontaneously broken $U(1)\times U(1)$ symmetry, $m_{\mathbf{A}}\neq 0$, $\Upsilon_{\mu,(1,1)}\neq 0$. IV. Normal phase with fully restored $U(1)\times U(1)$ symmetry, $m_{\mathbf{A}}=0$, $\Upsilon_{\mu,(1,1)}=0$. VI. Spontaneously broken global $U(1)$ symmetry, with restored $U(1)$ gauge symmetry, $m_{\mathbf{A}}=0$, $\Upsilon_{\mu,(1,1)}\neq 0$. For comparison, the results of the two cases $e_1=e_2=0$, 1, from Fig. 4, are presented. The phases for these two cases follow from the inset and caption of Fig. 4. The lines are guide to the eyes. The system size considered is 32^3. The uncertainties in the position of the phase-transition lines are smaller than the marker size and are omitted from the diagram.

Consider the simulation results shown in Fig. 6. For comparison, we include the results when there is no gauge-field coupling, $e_1=e_2=0$, and when gauge-field coupling competes with the drag interaction, $e_1=e_2=1$. First notice that the paired phase which appears when charges are opposite, is the metallic superfluid phase (VI) which now is associated with spontaneously broken global $U(1)$ symmetry in the phase sum (and not the phase difference as in Figs. 1, 2, and 4). Positive drag will favor $(1,-1)$ vortices as before. However, because of the change in sign of one of the charges, the $(1,-1)$ vortices are now associated with the charged sector of Eq. (39). The (1,1) vortices are associated with the neutral mode, and thus the neutral critical point is determined by the onset of the associated helicity modulus $\Upsilon_{\mu,(1,1)}$. The gauge field renders the $(1,-1)$ vortices the topological objects with lowest excitation energy. When they proliferate the superconducting sector is destroyed. Asymptotically, the associated phase-transition line is therefore expected to follow the behavior of a one-component superconductor with $\rho'=2(\rho-2\rho_d)$ and effective charge e,

$$F^{\text{eff}}_{\text{I}\to\text{VI}}=(\rho-2\rho_d)(\nabla\theta-e\mathbf{A})^2+\frac{(\nabla\times\mathbf{A})^2}{2}. \quad (40)$$

The remaining condensate will have superfluidity destroyed via proliferation of individual vortices which asymptotically

can be mapped onto a one-component superfluid with stiffness $\rho' = \rho/2$,

$$F^{\text{eff}}_{\text{VI}\to\text{IV}} = \frac{\rho}{4}(\nabla\theta)^2. \quad (41)$$

This is exactly the same behavior as expected when $e=0$, which is also confirmed by simulations in Fig. 6. Note that there is neither ρ_d nor e dependence of this line.

Figure 6 also shows that when gauge field and drag act in unison it amounts to a small increase in the region of paired phase compared to the case when there is only drag interaction. However when interactions compete there is a stronger effect of the suppression of the corresponding paired phase. Also note that the cases $e_1=-e_2=1$ and $e_1=e_2=1$ coincide when $\rho_d=0$. This is readily inferred from Eq. (1), when $\rho_d=0$, one model can be mapped onto another by change in sign of charges e_j accompanied by a sign change in one of the phases $\nabla\theta_j$.

VI. *N*-COMPONENT CASE

In the case of N-charged components, the $[U(1)]^N$ model can be written as (see Appendix A for notation)

$$F = \sum_{j=1,\ldots,N} \frac{\rho_j}{2}(\nabla\theta_j - e_j\mathbf{A})^2 + \frac{(\nabla\times\mathbf{A})^2}{2} - \sum_{j,k=1,\ldots,N} \frac{\rho_{d,jk}}{2}(\nabla\theta_j - e_j\mathbf{A} - \nabla\theta_k + e_k\mathbf{A})^2. \quad (42)$$

In the N-component case the phase structure becomes more complex than in the two-component case. In the simplest case of different stiffnesses and weak coupling, there can take place a vortex proliferation in individual fields. That reduces the symmetry to the $[U(1)]^{N-1}$. On the other hand, in the case when the gauge-field coupling is dominant there can take place a proliferation of one-flux-quanta composite vortices while individual vortices remain confined. Consider the case of all equal charges. Then, in the N-component model such a vortex has the phase winding $(\Delta\theta_1=2\pi,\Delta\theta_2=2\pi,\ldots,\Delta\theta_N=2\pi)$. When charge is sufficiently large, such a composite object can proliferate while the other kind of (fractional flux) vortices remain confined. The resulting state has broken global symmetries associated with all the combinations of the gauge-invariant phase differences $(\theta_j-\theta_k)$. This is the N-component analog of the metallic superfluid state which has no Meissner effect because of restored symmetry in the charged sector.

On the other hand, by varying the intercomponent drag strength along with the charge strength one can make different topological excitations the energetically cheapest objects (such as, e.g., $(\Delta\theta_1=2\pi M_1,\Delta\theta_2=2\pi M_2,\ldots,\Delta\theta_N=2\pi M_N)$, with any integers $M_N=0,\pm1,\pm2,\ldots$, etc.). This also can be seen from the intervortex interactions derived in Appendix A. Proliferation of such objects reduces broken $[U(1)]^N$ symmetry down to broken symmetries associated with various *weighted* combinations of phases such as $(L_1\theta_1+L_2\theta_2+L_3\theta_3+\cdots)$. Consider, for example, the case where all kinds of "two-vortex" bound states proliferate, i.e., when the drag coupling makes the following objects energetically cheapest to excite, $(\Delta\theta_1=2\pi,\Delta\theta_2=-2\pi,\Delta\theta_3=0,\ldots,\Delta\theta_N=0)$, $(\Delta\theta_1=0,\Delta\theta_2=2\pi,\Delta\theta_3=-2\pi,\Delta\theta_4=0,\ldots,\Delta\theta_N=0),\ldots$, $(\Delta\theta_1=0,\ldots,\Delta\theta_{N-2}=0,\Delta\theta_{N-1}=2\pi,\Delta\theta_N=-2\pi)$. When these kind of topological defects (with two opposite phase windings in different phases) proliferate, the only remaining broken symmetry is associated with the sum of all phases $(\theta_1+\theta_2+\cdots+\theta_N)$ yielding the effective model,

$$\frac{1}{2}\rho_{\text{eff}}[\nabla(\theta_1+\theta_2+\cdots+\theta_N) - Ne\mathbf{A}]^2 + \frac{1}{2}(\nabla\times\mathbf{A})^2, \quad (43)$$

the prefactor N in front of the vector potential $\mathbf{A}$ means that this is a "charge-Ne" superconductor, i.e., in this state only codirected electrical current of all components is dissipationless.

VII. CONCLUSION

We have considered a three dimensional lattice superconductor model in the London limit with two and N individually conserved condensates. These condensates interact with each other by two mechanisms. The first is a dissipationless Andreev-Bashkin drag term representing a current-current interaction. The second is a fluctuating gauge field. Intercomponent Josephson coupling is absent on symmetry grounds. Such models are relevant in a number of physical circumstances ranging from the theories of the quantum ordered states of metallic hydrogen, models of neutron stars, and were earlier suggested as effective models describing valence-bond solid to Neel quantum phase transition in the proposed theories of deconfined quantum criticality.

In the $U(1)\times U(1)$ case when there is no intercomponent drag, $\rho_d=0$, and component charges are equal, $e_1=e_2=e$ and there is a disparity of the bare component stiffnesses, we find that a sufficiently strong coupling to a noncompact gauge field causes a merger of phase-transition lines. This yields a direct transition from broken $U(1)\times U(1)$ to normal state even when the bare component stiffnesses are unequal. When the charge e is increased, the merger occurs for a higher disparity of stiffnesses. However, a further increase in the coupling beyond a certain critical strength results in a new splitting of the transition line. This yields a metallic superfluid phase. The merger of the $U(1)$ transition lines is associated with a competition between different kinds of topological defects where proliferation of one type of vortices triggers a preemptive proliferation of another. The result is a much more complex picture of the behavior of topological defects in the phase transition than in single-component $U(1)$ models. The second splitting is due to the fact that increased coupling to the noncompact gauge field decreases the free energy per unit length of a bound state of topological defects. The bound state in question (a composite vortex) has a topological charge only in the charged sector of the model. This in turn results in increased suppression of the critical stiffness associated with the charged sector of the theory, which eventually undergoes a symmetry-restoring phase transition before the neutral sector.

We find that also when the bare stiffnesses are unequal, the merged phase transition is first order in character. Note

that previously first-order transitions were reported in the $U(1)\times U(1)$ gauge theory with degenerate stiffnesses,[10,11] $U(1)\times U(1)$ models with a compact gauge field, as well as to phase transitions in the SU(2) model with noncompact Abelian gauge field.[14]

In the main part of the paper, we have performed a study of the phase diagram of the generic $U(1)\times U(1)$ lattice London gauge model featuring both gauge field and direct nondissipative drag interactions. We have obtained, through large-scale Monte Carlo simulations, its phase diagram as a function of these two generic coupling constants.

For the case where the bare component stiffnesses and charges are equal, $\rho_1=\rho_2=1$ and $e_1=e_2=e$, we find the formation of two different paired phases as a result of a competition between gauge-field and intercomponent drag couplings. High values of drag produce a composite superconducting phase associated with a broken local $U(1)$ gauge symmetry in the phase sum. There, the theory effectively features a doubled electric charge compared with $U(1)\times U(1)$ phase, cf. Eq. (37). At high values of e, the gauge-field coupling wins over the drag coupling, yielding a paired superfluid phase (the metallic superfluid) associated with the order in the gauge-invariant phase difference. In between these two different phases, there is a region with a direct transition from broken $U(1)\times U(1)$ to normal state, part of which exhibits clear-cut signatures of a first-order transition, cf. the transition line connecting regions II and V in Fig. 4.

For comparison, we reported a quantitative study of the situation where gauge-field mediated intercomponent interactions and intercomponent drag both favor metallic superfluid phase. In the final part of the paper we discussed the physics of states with composite symmetry breakdowns in the N-component London superconductor.

ACKNOWLEDGMENTS

We acknowledge useful discussions with I. B. Sperstad and E. B. Stiansen. E.V.H. thanks NTNU for financial support. E.B. was supported by Knut and Alice Wallenberg Foundation through the Royal Swedish Academy of Sciences, Swedish Research Council and by the National Science Foundation CAREER Award No. DMR-0955902. A.S. was supported by the Norwegian Research Council under Grant No. 167498/V30 (STORFORSK). E.B. and A.S. acknowledge the hospitality of the Aspen Center for Physics, where part of this work was done.

APPENDIX A: VORTEX INTERACTION IN THE N-COMPONENT MODEL

In the case of arbitrary number of components N the action has the form

$$S=\frac{\beta}{2}\int d^3r\{[\nabla\times\mathbf{A}(\mathbf{r})]^2+[\nabla\theta_j(\mathbf{r})-e_j\mathbf{A}(\mathbf{r})]R_{jk}\times[\nabla\theta_k(\mathbf{r})-e_k\mathbf{A}(\mathbf{r})]\}. \tag{A1}$$

The matrix R_{jk} is in general given by

$$R_{jk}=\left(\rho_j-\sum_l\rho_{d,jl}\right)\delta_{jk}+\rho_{d,jk}, \tag{A2}$$

where $\rho_{d,jk}$ is the drag coefficient between components j and k, obviously, $\rho_{d,jk}=\rho_{d,kj}$ and $\rho_{d,jk}=0$ when $j=k$. Following exactly the same procedure as in the case $N=2$, we arrive at the N-component action,

$$S=\frac{\beta}{2}\int d^3q\left[\mathbf{U}_j(\mathbf{q})\left(R_{jk}-\frac{e_le_mR_{lj}R_{mk}}{q^2+m_0^2}\right)\mathbf{U}_k(-\mathbf{q})+\tilde{\mathbf{A}}(\mathbf{q})(q^2+m_0^2)\tilde{\mathbf{A}}(-\mathbf{q})\right], \tag{A3}$$

where the Fourier transform of $\nabla\theta_j(\mathbf{r})$ is denoted by $\mathbf{U}_j(\mathbf{q})$ and

$$m_0^2=e_jR_{jk}e_k. \tag{A4}$$

This expression is seen to reproduce the case $N=2$ given in Eq. (7). The gauge field is integrated out and the dualization now follows the same path as previously, yielding

$$Z=\sum_{\mathbf{m}_1}\cdots\sum_{\mathbf{m}_N}e^{-S},$$

$$S=2\beta\pi^2\int d^3q\mathbf{m}_j(\mathbf{q})V_{jk}(q^2)\mathbf{m}_k(-\mathbf{q}), \tag{A5}$$

where the vortex interactions are given by

$$V_{jk}(q^2)=\frac{1}{q^2}\left(R_{jk}-\frac{e_le_mR_{lj}R_{mk}}{q^2+m_0^2}\right)=\frac{R_{jk}-\frac{e_le_mR_{lj}R_{mk}}{m_0^2}}{q^2}+\frac{\frac{e_le_mR_{lj}R_{mk}}{m_0^2}}{q^2+m_0^2}. \tag{A6}$$

This is seen to be on precisely the same form as Eq. (18) for the case $N=2$. Following Appendix B in Ref. 9, a dualization of the corresponding two-component lattice model in Eq. (21) may be performed to yield the exact same result as in Eqs. (A5) and (A6) where the vortex fields now are defined on the vertices of the Fourier space dual lattice and $q^2\to|\mathbf{Q}_\mathbf{q}|^2$.

APPENDIX B: GAUGE-FIELD CORRELATOR

By adding source term and Fourier transformation of the model in Eq. (A1), the generating functional for deriving the gauge-field correlator reads

$$Z_J=\int\mathcal{D}\theta_1\cdots\int\mathcal{D}\theta_N\int\mathcal{D}\mathbf{A}e^{-S},$$

$$S_J = \frac{\beta}{2}\int d^3q \Bigg\{ \frac{1}{\beta}[\mathbf{J}(\mathbf{q})\mathbf{A}(-\mathbf{q}) + \mathbf{A}(\mathbf{q})\mathbf{J}(-\mathbf{q})] + [\mathbf{U}_j(\mathbf{q}) - e_j\mathbf{A}(\mathbf{q})]R_{jk}[\mathbf{U}_k(-\mathbf{q}) - e_k\mathbf{A}(-\mathbf{q})] + q^2\mathbf{A}(\mathbf{q})\mathbf{A}(-\mathbf{q}) \Bigg\}, \tag{B1}$$

where $\mathbf{J}(\mathbf{q})$ are the electric currents that couples linearly to the gauge field in the source terms. Sum over repeated indices is assumed. We now proceed similar to Sec. II C by completing the squares of the gauge field and integrate out the shifted gauge field $\tilde{\mathbf{A}}(\mathbf{q}) = \mathbf{A}(\mathbf{q}) + [\mathbf{J}(\mathbf{q})/\beta - e_j R_{jk}\mathbf{U}_k(\mathbf{q})]/(q^2 + m_0^2)$ which yields

$$Z_J = \int \mathcal{D}\theta_1 \cdots \int \mathcal{D}\theta_N e^{-S},$$

$$S_J = \frac{\beta}{2}\int d^3q \Bigg\{ -\frac{\mathbf{J}(\mathbf{q})\mathbf{J}(-\mathbf{q})}{\beta^2(q^2 + m_0^2)} + \frac{\mathbf{J}(\mathbf{q})e_j R_{jk}\mathbf{U}_k(-\mathbf{q}) + e_j R_{jk}\mathbf{U}_k(\mathbf{q})\mathbf{J}(-\mathbf{q})}{\beta(q^2 + m_0^2)} + \mathbf{U}_j(\mathbf{q})\left(R_{jk} - \frac{e_l e_m R_{lj}R_{mk}}{q^2 + m_0^2}\right)\mathbf{U}_k(-\mathbf{q}) \Bigg\}. \tag{B2}$$

We now employ the constraint $\nabla \cdot \mathbf{J}(\mathbf{r}) = 0$, i.e., the electrical currents are divergence free, such that components parallel to $\mathbf{q}$ are unphysical. Thus, the physical components of $\mathbf{J}(\mathbf{q})$ in the first term of Eq. (B2) are projected out with the transverse projection operator,

$$P_{T,\mu\nu} = \delta_{\mu\nu} - \frac{q_\mu q_\nu}{q^2}. \tag{B3}$$

As discussed in Sec. II C, we disregard the longitudinal part of $\mathbf{U}_j(\mathbf{q})$ and introduce the Fourier transformed vortex fields by Eq. (16). Thus, the generating functional is written as

$$Z_J = \sum_{\mathbf{m}_1} \cdots \sum_{\mathbf{m}_N} e^{-S_0 - S_1},$$

$$S_0 = 2\beta\pi^2 \int d^3q \mathbf{m}_j(\mathbf{q}) V_{jk}(q^2)\mathbf{m}_k(-\mathbf{q}),$$

$$S_1 = \int d^3q \Bigg\{ \frac{i\pi e_j R_{jk}\varepsilon_{\mu\nu\eta}q_\nu}{q^2(q^2 + m_0^2)}[m_{\eta,k}(\mathbf{q})J_\mu(-\mathbf{q}) - J_\mu(\mathbf{q})m_{\eta,k} \times (-\mathbf{q})] - \frac{J_\mu(\mathbf{q})P_{T,\mu\nu}J_\nu(-\mathbf{q})}{2\beta(q^2 + m_0^2)} \Bigg\}, \tag{B4}$$

where $V_{jk}(q^2)$ is given by Eq. (A6) and $\varepsilon_{\mu\nu\eta}$ is the Levi-Civita symbol. Note that there is an implicit sum over all indices j, k, μ, ν, and η.

The gauge-field correlators are derived the standard way by functional derivation of the currents,

$$\langle A_\mu(\mathbf{q})A_\nu(-\mathbf{q})\rangle = \frac{1}{Z_0}\left.\frac{\delta^2 Z_J}{\delta J_\mu(-\mathbf{q})\delta J_\nu(\mathbf{q})}\right|_{\mathbf{J}=\mathbf{0}} = \left\langle \left.\frac{\delta^2 e^{-S_1}}{\delta J_\mu(-\mathbf{q})\delta J_\nu(\mathbf{q})}\right|_{\mathbf{J}=\mathbf{0}} \right\rangle, \tag{B5}$$

where $Z_0 = Z_J|_{\mathbf{J}=\mathbf{0}} = \Sigma_{\mathbf{m}_1}\cdots\Sigma_{\mathbf{m}_N}e^{-S_0}$ and the brackets denote thermal average with respect to Z_0. The functional derivation is performed by expanding the exponential in series and keep terms of $\mathcal{O}(J^2)$, the only terms that survives both derivation and $\mathbf{J}=\mathbf{0}$, to yield

$$\left.\frac{\delta^2 e^{-S_1}}{\delta J_\mu(-\mathbf{q})\delta J_\nu(\mathbf{q})}\right|_{\mathbf{J}=\mathbf{0}} = \frac{4\pi^2 e_j e_l R_{jk}R_{lm}\varepsilon_{\mu\alpha\beta}\varepsilon_{\nu\gamma\kappa}}{q^4(q^2 + m_0^2)^2} \times q_\alpha q_\gamma m_{\beta,k}(\mathbf{q})m_{\kappa,m}(-\mathbf{q}) + \frac{P_{T,\mu\nu}}{\beta(q^2 + m_0^2)}. \tag{B6}$$

The product $\varepsilon_{\mu\alpha\beta}\varepsilon_{\nu\gamma\kappa}$ is evaluated by the determinant

$$\varepsilon_{\mu\alpha\beta}\varepsilon_{\nu\gamma\kappa} = \begin{vmatrix} \delta_{\mu\nu} & \delta_{\mu\gamma} & \delta_{\mu\kappa} \\ \delta_{\alpha\nu} & \delta_{\alpha\gamma} & \delta_{\alpha\kappa} \\ \delta_{\beta\nu} & \delta_{\beta\gamma} & \delta_{\beta\kappa} \end{vmatrix}, \tag{B7}$$

to yield

$$\langle A_\mu(\mathbf{q})A_\nu(-\mathbf{q})\rangle = \frac{P_{T,\mu\nu}}{\beta(q^2 + m_0^2)} + \frac{4\pi^2 e_j e_l R_{jk}R_{lm}}{q^2(q^2 + m_0^2)^2} \times \langle P_{T,\mu\nu}\mathbf{m}_k(\mathbf{q})\mathbf{m}_m(-\mathbf{q}) - m_{\nu,k}(\mathbf{q})m_{\mu,m} \times (-\mathbf{q})\rangle, \tag{B8}$$

when Eq. (B6) is inserted in Eq. (B5). We now find the gauge-field propagator by letting $\nu \to \mu$ in Eq. (B8) and summing over repeated indices, thus

$$\langle \mathbf{A}(\mathbf{q})\mathbf{A}(-\mathbf{q})\rangle = \frac{4\pi^2 e_j e_l R_{jk}R_{lm}\langle \mathbf{m}_k(\mathbf{q})\mathbf{m}_m(-\mathbf{q})\rangle}{q^2(q^2 + m_0^2)^2} + \frac{2}{\beta(q^2 + m_0^2)}. \tag{B9}$$

The gauge-field correlator of the two-component discrete model in Eq. (21) is found similarly to Appendix C in Ref. 9 and the result is as given in Eq. (B9) with $q^2 \to |\mathbf{Q}_\mathbf{q}|^2$ and vortex fields defined on the vertices of the Fourier space dual lattice.

[1] J. M. Kosterlitz and D. J. Thouless, J. Phys. C **6**, 1181 (1973); J. M. Kosterlitz, *ibid.* **7**, 1046 (1974).
[2] C. Dasgupta and B. I. Halperin, Phys. Rev. Lett. **47**, 1556 (1981).
[3] K. Fossheim and A. Sudbø, *Superconductivity: Physics And Applications* (Wiley, London, 2004); A. K. Nguyen and A. Sudbø, Phys. Rev. B **60**, 15307 (1999).
[4] M. E. Peskin, Ann. Phys. **113**, 122 (1978); P. R. Thomas and M. Stone, Nucl. Phys. B **144**, 513 (1978).
[5] E. Babaev, arXiv:cond-mat/0201547.
[6] A. B. Kuklov and B. V. Svistunov, Phys. Rev. Lett. **90**, 100401 (2003); A. Kuklov, N. Prokof'ev, and B. Svistunov, *ibid.* **92**, 030403 (2004).
[7] E. Babaev, A. Sudbø, and N. W. Ashcroft, Nature (London) **431**, 666 (2004).
[8] E. Smørgrav, E. Babaev, J. Smiseth, and A. Sudbø, Phys. Rev. Lett. **95**, 135301 (2005).
[9] J. Smiseth, E. Smørgrav, E. Babaev, and A. Sudbø, Phys. Rev. B **71**, 214509 (2005).
[10] A. Kuklov, N. Prokof'ev, and B. Svistunov, arXiv:cond-mat/0501052 (unpublished); A. B. Kuklov, N. V. Prokof'ev, B. V. Svistunov, and M. Troyer, Ann. Phys. **321**, 1602 (2006).
[11] S. Kragset, E. Smørgrav, J. Hove, F. S. Nogueira, and A. Sudbø, Phys. Rev. Lett. **97**, 247201 (2006).
[12] O. I. Motrunich and A. Vishwanath, Phys. Rev. B **70**, 075104 (2004).
[13] E. K. Dahl, E. Babaev, S. Kragset, and A. Sudbø, Phys. Rev. B **77**, 144519 (2008).
[14] M. N. Chernodub, E.-M. Ilgenfritz, and A. Schiller, Phys. Rev. B **73**, 100506(R) (2006); M. Bock, M. N. Chernodub, E.-M. Ilgenfritz, and A. Schiller, *ibid.* **76**, 184502 (2007); A. B. Kuklov, M. Matsumoto, N. V. Prokof'ev, B. V. Svistunov, and M. Troyer, Phys. Rev. Lett. **101**, 050405 (2008); F.-J. Jiang, M. Nyfeler, S. Chandrasekharan, and U.-J. Wiese, J. Stat. Mech.: Theory Exp. (2008), P02009. See also the recent work aiming at N-component extension of the compact gauge field model T. Ono, S. Doi, Y. Hori, I. Ichinose, and T. Matsui, Ann. Phys. (N.Y.) **324**, 2453 (2009).
[15] E. Smørgrav, J. Smiseth, E. Babaev, and A. Sudbø, Phys. Rev. Lett. **94**, 096401 (2005).
[16] E. K. Dahl, E. Babaev, and A. Sudbø, Phys. Rev. B **78**, 144510 (2008); Phys. Rev. Lett. **101**, 255301 (2008).
[17] A. F. Andreev and E. P. Bashkin, Sov. Phys. JETP **42**, 164 (1975).
[18] E. Babaev and N. W. Ashcroft, Nat. Phys. **3**, 530 (2007).
[19] E. Babaev, Phys. Rev. Lett. **89**, 067001 (2002).
[20] P. B. Jones, Mon. Not. R. Astron. Soc. **371**, 1327 (2006); E. Babaev, Phys. Rev. Lett. **103**, 231101 (2009).
[21] T. Senthil, A. Vishwanath, L. Balents, S. Sachdev, and M. P. A. Fisher, Science **303**, 1490 (2004).
[22] For a review, see S. Sachdev, Nat. Phys. **4**, 173 (2008).
[23] D. F. Agterberg and H. Tsunetsugu, Nat. Phys. **4**, 639 (2008); D. Podolsky, S. Chandrasekharan, and A. Vishwanath, Phys. Rev. B **80**, 214513 (2009); A. Hu, L. Mathey, I. Danshita, E. Tiesinga, C. J. Williams, and C. W. Clark, Phys. Rev. A **80**, 023619 (2009); E. Berg, E. Fradkin, and S. A. Kivelson, Nat. Phys. **5**, 830 (2009).
[24] V. M. Kaurov, A. B. Kuklov, and A. E. Meyerovich, Phys. Rev. Lett. **95**, 090403 (2005).
[25] E. Babaev, L. D. Faddeev, and A. J. Niemi, Phys. Rev. B **65**, 100512(R) (2002).
[26] Note that in the solutions for fractional flux vortices in the Ginzburg-Landau model, the magnetic field is not exponentially localized. This affects intervortex interactions, see E. Babaev, J. Jaykka, and M. Speight, Phys. Rev. Lett. **103**, 237002 (2009), however, the field delocalization effect diminishes in the short-coherence length limit, considered in the present paper. Hence, in our case the London limit yields a good approximation to intervortex interaction potentials.
[27] J. Villain, J. Phys. (Paris) **36**, 581 (1975).
[28] N. Metropolis, A. W. Rosenbluth, M. N. Rosenbluth, A. H. Teller, and E. Teller, J. Chem. Phys. **21**, 1087 (1953); W. K. Hastings, Biometrika **57**, 97 (1970).
[29] K. Hukushima and K. Nemoto, J. Phys. Soc. Jpn. **65**, 1604 (1996); D. J. Earl and M. W. Deem, Phys. Chem. Chem. Phys. **7**, 3910 (2005).
[30] W. Janke and K. Nather, Phys. Rev. B **48**, 7419 (1993); H. Kleinert, *Gauge Fields in Condensed Matter* (World Scientific, Singapore, 1989), Vol. 1.
[31] K. Hukushima, Phys. Rev. E **60**, 3606 (1999).
[32] A. K. Nguyen and A. Sudbø, Phys. Rev. B **58**, 2802 (1998).
[33] A. K. Nguyen and A. Sudbø, Phys. Rev. B **57**, 3123 (1998).
[34] J. Hove and A. Sudbø, Phys. Rev. Lett. **84**, 3426 (2000); K. Kajantie, M. Laine, T. Neuhaus, A. Rajantie, and K. Rummukainen, Nucl. Phys. B **699**, 632 (2004).
[35] A. Kuklov, N. Prokof'ev, and B. Svistunov, Phys. Rev. Lett. **92**, 050402 (2004).
[36] J. Lee and J. M. Kosterlitz, Phys. Rev. Lett. **65**, 137 (1990); Phys. Rev. B **43**, 3265 (1991).
[37] A. M. Ferrenberg and R. H. Swendsen, Phys. Rev. Lett. **61**, 2635 (1988); **63**, 1195 (1989). The software used to perform the reweighting analysis did not take into account the explicit temperature dependence of the Villain model. However, the temperature interval for which the histogram statistics were obtained was narrow, and we thus expect the error to be negligible, as was checked by comparing reweighted histograms with raw data histograms.

Article II

Screening properties and phase transitions in unconventional plasmas for Ising-type quantum Hall states

Physical Review B **85**, 024520 (2012)

PHYSICAL REVIEW B **85**, 024520 (2012)

Screening properties and phase transitions in unconventional plasmas for Ising-type quantum Hall states

Egil V. Herland,[1] Egor Babaev,[2,3] Parsa Bonderson,[4] Victor Gurarie,[5] Chetan Nayak,[4,6] and Asle Sudbø[1]

[1]*Department of Physics, Norwegian University of Science and Technology, NO-7491 Trondheim, Norway*

[2]*Physics Department, University of Massachusetts, Amherst, Massachusetts 01003, USA*

[3]*Department of Theoretical Physics, The Royal Institute of Technology, SE-10691 Stockholm, Sweden*

[4]*Station Q, Microsoft Research, Santa Barbara, California 93106-6105, USA*

[5]*Department of Physics, CB 390, University of Colorado, Boulder, Colorado 80309, USA*

[6]*Department of Physics, University of California, Santa Barbara, California 93106, USA*

(Received 20 October 2011; published 11 January 2012)

Utilizing large-scale Monte Carlo simulations, we investigate an unconventional two-component classical plasma in two dimensions which controls the behavior of the norms and overlaps of the quantum-mechanical wave functions of Ising-type quantum Hall states. The plasma differs fundamentally from that which is associated with the two-dimensional XY model and Abelian fractional quantum Hall states. We find that this unconventional plasma undergoes a Berezinskii-Kosterlitz-Thouless phase transition from an insulator to a metal. The parameter values corresponding to Ising-type quantum Hall states lie on the metallic side of this transition. This result verifies the required properties of the unconventional plasma used to demonstrate that Ising-type quantum Hall states possess quasiparticles with non-Abelian braiding statistics.

DOI: 10.1103/PhysRevB.85.024520 PACS number(s): 73.43.Cd, 74.20.−z

I. INTRODUCTION

Key properties of physical systems can sometimes be understood by mapping them to seemingly unrelated ones. A powerful example of this was provided by Laughlin, who observed that the squared norm of his $\nu = 1/M$ fractional quantum Hall trial wave function

$$\Psi(z_i) = \prod_{i<j}^{N} (z_i - z_j)^M \, \mathrm{e}^{-\frac{1}{4}\sum_{i=1}^{N} |z_i|^2} \tag{1}$$

(where $z_i = x_i + iy_i$ is a complex coordinate in the two-dimensional plane) could be expressed as the Boltzmann weight of a two-dimensional one-component plasma[1]:

$$\|\Psi(z_i)\|^2 = \int \prod_{i=1}^{N} \mathrm{d}^2 z_i \, |\Psi(z_i)|^2 = \int \prod_{i=1}^{N} \mathrm{d}^2 z_i \, \mathrm{e}^{-\beta V_1(z_i)}, \tag{2}$$

where

$$V_1(z_i) = -Q_1^2 \sum_{i<j}^{N} \ln |z_i - z_j| + \frac{Q_1^2}{4M} \sum_{i=1}^{N} |z_i|^2 \tag{3}$$

and $Q_1^2/T = 2M$. This mapping allows properties such as quasiparticle charge and braiding statistics to be determined by appealing to the known properties of a one-component plasma.

Recently, a similar plasma mapping was established[2] for Ising-type quantum Hall states, such as the Moore-Read (MR),[3] anti-Pfaffian,[4,5] and Bonderson-Slingerland (BS) hierarchy[6] states, which are likely candidates to describe Hall plateaus in the second Landau level, in particular at filling fraction $\nu = 5/2$ (Refs. 7–10). In this case, the mapping is to a two-dimensional (2D) two-component plasma, where the two species of particles, w and z, carry not only different values of charge, but also interact through two different interactions, both of the Coulomb form, so the potential energy is

$$V(z_i; w_a) = V_1(z_i) + V_2(z_i; w_a), \tag{4}$$

$$V_2(z_i; w_a) = -Q_2^2 \sum_{i<j}^{N} \ln |z_i - z_j| - Q_2^2 \sum_{a<b}^{N} \ln |w_a - w_b| + Q_2^2 \sum_{a,i}^{N} \ln |z_i - w_a|, \tag{5}$$

where $Q_2^2/T = 3$. The z particles interact with each other through the first Coulomb-like interaction, $V_1(z_i)$, given in Eq. (3) (and so does not depend on the w_a coordinates). Moreover, the z particles interact with each other and with the w particles through the second Coulomb-like interaction, through which the w particles also interact with each other, according to $V_2(z_i; w_a)$, given in Eq. (5). Note that $V_2(z_i; w_a)$ is the 2D Coulomb potential of the usual two-component plasma (where the two species carry charge Q_2 and $-Q_2$, respectively).

The z particles carry charge Q_1 for the first interaction and charge Q_2 for the second interaction. The w particles carry charge 0 for the first interaction and charge $-Q_2$ for the second interaction. For a plasma with N particles of each species, neutrality is satisfied using a uniform background density of type 1 charge, as in the second term in Eq. (3). This unconventional plasma may be considered as an ordinary neutral two-component gas with positive and negative charges of magnitude Q_2, where the positive charges are given an additional charge of Q_1 that is only felt by the other positive charges and not the negative charges. An illustration of the interactions between the two species in the system is shown in Fig. 1.

We are thus led to consider a class of unconventional plasmas parametrized by Q_1^2/T and Q_2^2/T. As mentioned

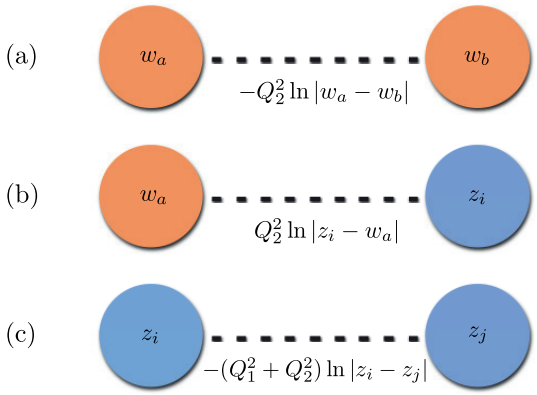

FIG. 1. (Color online) Illustration of interactions between the particles in the 2D system. The w particles only interact by the second Coulomb-like interaction with charge $-Q_2$, whereas the z particles carry charge Q_1 for the first Coulomb-like interaction and Q_2 for the second Coulomb-like interaction. Thus, the intraspecies interaction among the w particles, shown in (a), and the interspecies interaction between w and z particles, shown in (b), are given by Q_2 only, whereas the intraspecies interaction among the z particles, shown in (c), are determined by Q_1 in addition to Q_2. Interactions between the z particles and the neutralizing background are omitted from the figure.

above, for MR Ising-type states with filling $\nu = 1/M$, the relevant values are $Q_1^2/T = 2M$ and $Q_2^2/T = 3$. In this plasma mapping, the z_i particles in the plasma correspond to the electrons in the MR wave functions and the w_a particles correspond to screening operators (fictitious particles). The case $Q_1 = 0$, $Q_2^2/T = 3$ is relevant for the plasma mapping[2] of 2D chiral p-wave superconductors.[11] We note that whenever $Q_1 = 0$, our model is a special case of the well-known 2D two-component plasma of equal and opposite charges.[12–15] The screening properties of multicomponent 2D plasmas with multiple Coulomb interactions of this kind are also important for other physical systems, such as rotating multicomponent Bose-Einstein condensates with interspecies current-current (Andreev-Bashkin) interaction[16,17] and some multicomponent superconducting systems.[18–20] In these systems the screening properties and phase transitions determine superfluid and rotational responses.

In this paper, we fix temperature to $T = 1$ and consider the two most significant values of Q_1, namely, $Q_1 = 0,2$. We investigate the screening and phase transition properties of these plasmas as a function of varying Q_2 by performing a large-scale Monte Carlo simulation. Here a "screening phase" means that the system has a screening length which is finite, and exponentially decaying effective interactions. A system with logarithmic effective interactions is one where screening is defined to be absent. As a first check, we reproduce the well-known result that, for $Q_1 = 0$, there is a Berezinskii-Kosterlitz-Thouless (BKT) phase transition at $Q_2^2 = Q_{2,c}^2 \approx 4$, as expected for a 2D two-component plasma of equal and opposite charges. For $Q_2^2 < Q_{2,c}^2$, the charges are unbound and the plasma screens, but for $Q_2^2 > Q_{2,c}^2$, the charges are bound into dipoles and the interaction is not screened. Thus, for $Q_2^2 = 3$, the value relevant to 2D chiral p-wave superconductors, the plasma screens. For $Q_1 = 2$, we again find a BKT phase transition at $Q_2^2 = Q_{2,c}^2 \approx 4$, with a plasma screening phase for $Q_2^2 < Q_{2,c}^2$. The first Coulomb-like interaction is deep within its screening phase and appears to have a negligibly small effect on the screening of the second interaction. In both cases, the critical values $Q_{2,c}^2$ are obtained by a finite-size scaling fit of the Monte Carlo data to the BKT form. Our findings demonstrate that the unconventional plasma which occurs in the mapping for both a chiral p-wave superconductor and the Ising-type quantum Hall states is clearly in the screening phase (for both types of Coulomb interaction) and hence allows one to discern the non-Abelian braiding properties of these states, as explained in Ref. 2.

The outline of this paper is as follows. In the introductory part of Sec. II, we present the model for the unconventional plasma we will be studying in this paper. In Sec. II A, we connect this to the Ising-type of quantum Hall states. In Sec. II B, we explain its connection to two-component, 2D, Bose-Einstein condensates. In Sec. III A, we present a formulation of the model on a sphere. In Sec. III B, we give details of the Monte Carlo simulations, and in Sec. III C, we present our results for the screening properties, as well as our findings for the character of phase transition between the dielectric nonscreening phase and the metallic screening phase. In Sec. IV, we present our conclusions. Technical details on the derivation of a generalized dielectric constant is given in Appendix A . In Appendix B, we give a derivation of a relevant higher-order response function that we use to characterize the metal-insulator transition. In Appendix C, we present technical details on the finite-size scaling we have used.

II. MODEL

The canonical partition function of the unconventional plasma is written

$$Z = \int \left(\prod_{i=1}^{N} \mathrm{d}^2 z_i\right) \left(\prod_{a=1}^{N} \mathrm{d}^2 w_a\right) \mathrm{e}^{-V}, \tag{6}$$

where the potential energy V is given by the 2D Coulombic interactions

$$\begin{aligned} V = {} & Q_2^2 \sum_{a<b=1}^{N} v_{ww}(|\mathbf{w}_a - \mathbf{w}_b|) \\ & + (Q_1^2 + Q_2^2) \sum_{i<j=1}^{N} v_{zz}(|\mathbf{z}_i - \mathbf{z}_j|) \\ & + Q_2^2 \sum_{a,i=1}^{N} v_{zw}(|\mathbf{z}_i - \mathbf{w}_a|) + V_{z,\mathrm{BG}}. \end{aligned} \tag{7}$$

Similar to the study of the 2D two-component neutral Coulomb gas,[12–15,21] we introduce a short-range hard-core repulsion between all charges in the system. Treating all charges as hard disks with the same diameter d that limits the range of

the hard-core repulsion, the interaction between charges of the same species is

$$v_{zz}(|\mathbf{r}|) = v_{ww}(|\mathbf{r}|) = \begin{cases} \infty, & |\mathbf{r}| \leqslant d, \\ -\ln|\mathbf{r}|, & |\mathbf{r}| > d, \end{cases} \tag{8}$$

and the interaction between charges of different species is

$$v_{zw}(|\mathbf{r}|) = \begin{cases} \infty, & |\mathbf{r}| \leqslant d, \\ \ln|\mathbf{r}|, & |\mathbf{r}| > d. \end{cases} \tag{9}$$

In Eq. (7), $\mathbf{w}_a$ are position vectors for the particles of component w, and $\mathbf{z}_i$ are position vectors for the particles of component z. To ensure neutrality, the term $V_{z,\mathrm{BG}}$ includes the interaction of the Q_1 charges of type 1 for the z particles with a neutralizing background charge density. In Ref. 2, this background is a uniform negatively charged 2D disk with charge density $q_1^{\mathrm{BG}} = -NQ_1/A$, where $N/A = 1/2\pi M$, that yields

$$V_{z,\mathrm{BG}} = \frac{1}{2}\sum_{i=1}^{N}|z_i|^2. \tag{10}$$

The particle-background and the background-background interaction also yields uninteresting constant terms, which are disregarded in Eq. (7).

We note that when $Q_1 = 0$ we have the 2D two-component neutral Coulomb plasma, which is well-studied both analytically and numerically.[12–15,25–30] At low dipole density, this system will undergo a BKT transition, which is a charge-unbinding transition from a low-temperature state where charges of opposite signs form tightly bound dipoles to a high-temperature state in which a finite fraction of charges are not bound in dipoles, but rather form a metallic state. In the low-temperature phase, this Coulomb gas is an insulator and the dielectric constant ϵ (see, for instance, Refs. 26, 31, and 32 and Appendix A for a formal definition of ϵ) is finite. In the high-temperature phase, the existence of free charges yields a conductive gas with an infinite value of ϵ. At the critical temperature T_c, when tightly bound dipoles start to unbind, there is a universal jump in the inverse dielectric constant from a nonzero value in the insulating phase to zero in the metallic phase,

$$\epsilon^{-1} = \begin{cases} 4T_c, & T \to T_c^-, \\ 0, & T \to T_c^+. \end{cases} \tag{11}$$

The screening properties that follow are that the Coulomb gas is able to perfectly screen test charges in the metallic phase when there are free charges in the system, whereas there is no screening in the insulating dielectric phase. In this work, we focus our attention on the low-dipole-density regime, so we do not go into detail on the physics in the 2D two-component neutral Coulomb gas at higher densities. However, we note that when density is increased, the critical point of the BKT transition is shifted toward lower temperatures.[14,15,28,29]

Another well-studied case is when $Q_2 = 0$, for which the model reduces to the 2D one-component plasma (for the z particles only). Early numerical studies of this system found a weak first-order melting transition at $Q_1^2/T \approx 140$ from a state where the charges form a triangular lattice with quasi-long-range translational and long-range orientational order to a fluid plasma state.[33–36] These results were, in a sense, contrasting with the defect-mediated melting theory of Kosterlitz-Thouless-Halperin-Nelson-Young (KTHNY) that predicts melting from a solid to a liquid via two BKT transitions and an intermediate hexatic phase with no translational order and quasi-long-range orientational order.[12,37–39] Other studies of 2D melting point in favor of the KTHNY theory,[40–43] suggesting that the nature of melting transition may depend on details in the interatomic potential or that finite-size effects and lack of equilibration might lead to erroneous conclusions in earlier works. There are also studies that argue for the absence of a phase transition to a low-temperature solid phase in the 2D one-component plasma with repulsive logarithmic interactions because the crystalline state would be unstable to proliferation of screened disclinations for any $T > 0$ (Refs. 44–47).

A. Ising-type quantum Hall states

The unconventional 2D two-component plasma studied here is mapped to inner products of trial wave functions for the MR quantum Hall states using conformal field theory (CFT) methods, as explained in Ref. 2. In particular, this mapping utilizes the Coulomb gas description of CFTs[48,49] together with a procedure for replacing holomorphic-antiholomorphic pairs of contour integrals in screening charge operators for 2D integrals.[2,50]

The MR states' wave functions can be written as a product of correlation functions of fields from the Ising and U(1) CFTs. In particular, the MR ground-state wave function for N electrons is

$$\Psi(z_1,\ldots,z_N) = \mathrm{Pf}\left(\frac{1}{z_i - z_j}\right)\prod_{i<j}^{N}(z_i - z_j)^M\, \mathrm{e}^{-\frac{1}{4}\sum_{i=1}^{N}|z_i|^2}, \tag{12}$$

where the Pfaffian of an antisymmetric matrix A is given by

$$\mathrm{Pf}(A_{i,j}) \equiv \frac{1}{N!!}\sum_{\sigma\in S_N}\mathrm{sgn}(\sigma)\prod_{k=1}^{N/2}A_{\sigma(2k-1),\sigma(2k)}. \tag{13}$$

Here S_N is the symmetric group, σ is one of the permutation elements in S_N, and $\mathrm{sgn}(\sigma)$ is the signature of σ. The $\mathrm{Pf}(\frac{1}{z_i - z_j})$ portion of this wave function is produced from the correlation function of ψ fields in the Ising CFT, while the Laughlin-type portion

$$\prod_{i<j}^{N}(z_i - z_j)^M\, \mathrm{e}^{-\frac{1}{4}\sum_{i=1}^{N}|z_i|^2} \tag{14}$$

is produced from the correlation function of vertex operators in the U(1) CFT.

The Laughlin-type portion of the MR wave functions can be mapped to charges of type 1, similar to Laughlin's plasma mapping. The mentioned CFT methods provide identities such as

$$\left|\mathrm{Pf}\left(\frac{1}{z_i - z_j}\right)\right|^2 = \int\prod_{a=1}^{N}\mathrm{d}^2w_a\prod_{a<b}^{N}|w_a - w_b|^3 \times\prod_{i<j}^{N}|z_i - z_j|^3\prod_{a,i}^{N}|w_a - z_i|^{-3}, \tag{15}$$

which allow the Pfaffian portion of the MR wave functions to be mapped to charges of type 2. This allows one to write the norm of the MR ground-state wave function as the partition function of the unconventional 2D two-component plasma of Eq. (4),

$$\|\Psi(z_1,\ldots,z_N)\|^2 = \int \prod_{i=1}^{N} \mathrm{d}^2 z_i |\Psi(z_1,\ldots,z_N)|^2 = \int \prod_{a=1}^{N} \mathrm{d}^2 w_a \prod_{i=1}^{N} \mathrm{d}^2 z_i \, \mathrm{e}^{-V}, \quad (16)$$

with $Q_1^2 = 2M$ and $Q_2^2 = 3$. More generally, one can also construct a similar, but more complicated mapping between inner products of wave functions of the MR states with quasiparticles, as explained in Ref. 2. In this case, the quasiparticles map to fixed "test" objects in the plasma that carry electric charge of type 1 and can carry both electric and magnetic charges of type 2 (and also changes the number of screening operators, that is, w particles in the plasma, to maintain neutrality). (The charges of types 1 and 2 carried by the quasiparticles are typically some fractions of the charges Q_1 and Q_2 carried by the z particles.)

Strictly speaking, the right-hand side of Eq. (15) is divergent for $Q_2^2 = 3$ (since the integrand diverges as $|w_a - z_i|^{-3}$ as a w particle approaches a z particle). It can be made well-defined (and equal to the left-hand side) by replacing $|w_a - z_i|^{-3}$ with $|w_a - z_i|^{-\alpha}$, evaluating the integrals for $\alpha < 2$ and then analytically continuing α to 3. On the other hand, we regularize the divergences of Eq. (16) in this paper by using a hard-core repulsion that forbids the particles from approaching each other closer than a distance d, that is, replacing V in this expression with that of Eq. (7). It should not matter how we regularize the divergence in Eq. (16) as long as the probability for z particles and w particles to sit right on top of each other has measure zero. As we see in this paper, this is true for $Q_2^2 < Q_{2,\mathrm{c}}^2 \approx 4$, in which case the configurational entropy to be gained by having z particles and w particles separate overcomes the energy gained by having them on top of each other. We refer to this as an "entropic barrier" for putting z particles and w particles on top of each other. In contrast, in Eq. (15), where only the w_i's are integrated over and the z_i coordinates are fixed, regularization by a simple hard-core repulsion does not appear to be a suitable alternative to analytic continuation. In this case, since the z_i coordinates are fixed, the entropic barrier is lower. Equivalently, there are fewer integrals to compensate for the inverse powers. Thus, in Eq. (15), a simple hard-core cutoff will not reproduce the left-hand side, and one must use the analytic continuation procedure described above.

B. Two-component rotating Bose-Einstein condensate in two dimensions

In a rotating frame, a Bose-Einstein condensate in the London limit is described by the uniformly frustrated XY model,

$$H = \frac{\rho}{2} \int \mathrm{d}^2 r \left[\nabla\theta(\mathbf{r}) - \frac{m}{\hbar} \mathbf{\Theta}(\mathbf{r}) \right]^2, \quad (17)$$

where $\rho = \hbar^2 n/m$ for a condensate with mass m, phase θ, density n, and $\mathbf{\Theta}(\mathbf{r}) = \mathbf{\Omega} \times \mathbf{r}$ where $\mathbf{\Omega} = \Omega\hat{z}$ is the angular velocity of the rotation. In 3D, this model is frequently used to describe the melting of vortex-line lattices in extreme type II superconductors and superfluids.[51–54] By a duality transformation, the model in Eq. (17) can be rewritten in terms of vortex fields l to yield[55,56]

$$H = \frac{1}{2} \int \mathrm{d}^2 q [l(\mathbf{q}) - (2\pi)^2 f \delta(\mathbf{q})] \frac{\rho}{q^2} \times [l(-\mathbf{q}) - (2\pi)^2 f \delta(-\mathbf{q})], \quad (18)$$

where $f = 2\Omega/\phi_o$ is the vortex number density and $\phi_0 = 2\pi\hbar/m$ is the fundamental quantum unit of vorticity. This is a one-component 2D classical Coulomb plasma where charges correspond to nonzero values in the vortex field $l(\mathbf{r})$ and the quantity f now plays the role as the neutralizing background number density.

Extending to two components, a model for a rotating two-component Bose-Einstein condensate with a generic Andreev-Bashkin drag interaction[57–59] reads

$$H = \frac{1}{2} \int \mathrm{d}^2 r \left\{ \sum_{i=1,2} m_i n_i \left(\frac{\hbar\nabla\theta_i}{m_i} - \mathbf{\Theta} \right)^2 - \sqrt{m_1 m_2} n_d \left(\frac{\hbar\nabla\theta_1}{m_1} - \frac{\hbar\nabla\theta_2}{m_2} \right)^2 \right\}, \quad (19)$$

where now m, n, and θ is given an index that denotes the component and n_d is the drag density. This model has recently been studied in three dimensions.[16,17] By a duality transformation, we arrive at the following 2D Coulomb plasma:

$$H = \frac{1}{2} \int \mathrm{d}^2 q [l_i(\mathbf{q}) - (2\pi)^2 f_i \delta(\mathbf{q})] \frac{R_{ij}}{q^2} \times [l_j(-\mathbf{q}) - (2\pi)^2 f_j \delta(-\mathbf{q})], \quad (20)$$

where $f_i = 2\Omega/\phi_{0,i}$, $\phi_{0,i} = 2\pi\hbar/m_i$, l_i is the vortex field of component i,

$$R = \hbar^2 \begin{pmatrix} \frac{1}{m_1}\left(n_1 - \sqrt{\frac{m_2}{m_1}} n_d\right) & \frac{1}{\sqrt{m_1 m_2}} n_d \\ \frac{1}{\sqrt{m_1 m_2}} n_d & \frac{1}{m_2}\left(n_2 - \sqrt{\frac{m_1}{m_2}} n_d\right) \end{pmatrix}, \quad (21)$$

and an implicit sum over repeated component indices i, j is assumed. By setting $\hbar = m_i = 1$ such that $f_1 = f_2 = f$, and absorbing a factor $2\pi\beta$ in the density coefficients, we see that the two-component Bose-Einstein condensate in Eq. (19) with $n_1 = 0$, $n_2 = Q_1^2$, and $n_d = -Q_2^2$ corresponds to the unconventional two-component Coulomb plasma in Eq. (7). Thus, the unconventional Coulomb plasma has a counterpart in a two-component Bose-Einstein condensate with a negative nondissipative drag interaction. However, note that in order to preserve a fixed number of charges when going from the plasma description in Eq. (7) to the phase description in Eq. (19), we have to fix the number of vortices to only include rotationally induced vortices. In principle, in the BEC problem, the system can thermally excite vortex-antivortex pairs, but that process can be substantially suppressed by going beyond the phase-only model in Eq. (19) and introducing an additional energy penalty associated with vortex cores.

III. MONTE CARLO SIMULATIONS

A. Considerations for a spherical surface

Computer simulations of Coulomb interactions are generally difficult to perform due to the long-ranged nature of the interaction. Several techniques have been presented to deal with the complications that arise.[60–62] We have performed large-scale Monte Carlo simulations of the system described in Eqs. (6) and (7) on a spherical surface. For other simulations on a spherical surface, see Refs. 14, 34, 43–46, and 63. This may seem like a brute-force approach since the workload of the simulations scales as $\mathcal{O}(N^2)$. However, the benefit is that there are no boundaries, the implementation is relatively easy, and there is no need to constrain the particles to move on a lattice. However, one must also be aware that simulation results may differ due to effects induced by topology. For instance, the triangular crystalline ground state of a 2D one-component plasma will necessarily include a number of dislocations and disclinations on a sphere. These defects are not present in the ground state when the one-component plasma is located on the plane.[45,64]

We consider a sphere with radius R, with origin defined as the center of the sphere such that all particle position vectors $\mathbf{w}_a$ and $\mathbf{z}_i$ are radial vectors with fixed magnitude R in three dimensions. The distance between the particles is measured along the chord[14,63]

$$|\mathbf{r}_i - \mathbf{r}_j| = 2R \sin\left(\frac{\psi_{ij}}{2}\right), \tag{22}$$

where

$$\psi_{ij} = \arccos(\hat{\mathbf{r}}_i \cdot \hat{\mathbf{r}}_j) \tag{23}$$

is the chord angle between the two particles at $\mathbf{r}_i$ and $\mathbf{r}_j$ with unit vectors $\hat{\mathbf{r}}_i$ and $\hat{\mathbf{r}}_j$, respectively. We may now rewrite the model in Eq. (7) on the surface of a unit sphere as

$$V = \frac{1}{2}\Bigg[Q_2^2 \sum_{a<b=1}^{N} \tilde{v}_{ww}(\hat{\mathbf{w}}_a \cdot \hat{\mathbf{w}}_b) + Q_2^2 \sum_{a,i=1}^{N} \tilde{v}_{zw}(\hat{\mathbf{z}}_i \cdot \hat{\mathbf{w}}_a) + \left(Q_1^2 + Q_2^2\right) \sum_{i<j=1}^{N} \tilde{v}_{zz}(\hat{\mathbf{z}}_i \cdot \hat{\mathbf{z}}_j) \Bigg], \tag{24}$$

with interactions given by

$$\tilde{v}_{zz}(\hat{\mathbf{r}}_i \cdot \hat{\mathbf{r}}_j) = \tilde{v}_{ww}(\hat{\mathbf{r}}_i \cdot \hat{\mathbf{r}}_j) = \begin{cases} \infty, & \psi_{ij} \leqslant d/R, \\ -\ln(1 - \hat{\mathbf{r}}_i \cdot \hat{\mathbf{r}}_j), & \psi_{ij} > d/R, \end{cases} \tag{25}$$

and

$$\tilde{v}_{zw}(\hat{\mathbf{r}}_i \cdot \hat{\mathbf{r}}_j) = \begin{cases} \infty, & \psi_{ij} \leqslant d/R, \\ \ln(1 - \hat{\mathbf{r}}_i \cdot \hat{\mathbf{r}}_j), & \psi_{ij} > d/R. \end{cases} \tag{26}$$

Note that the interaction $V_{z,\mathrm{BG}}$ in Eq. (7) between the neutralizing background and the excess charge of type 1 becomes a constant term on the sphere, so we disregard it in Eq. (24).

The dimensionless density of particles on the sphere is given by the packing fraction $\eta = Ns/A$, where $s = A\sin^2(d/4R)$ is the area of a hard disk of diameter d on the sphere of area $A = 4\pi R^2$. In the simulation, we use a unit sphere with $R = 1$.

As explained in Appendix A, in order to account for screening properties when particles interact by two interactions simultaneously, we measure a general inverse dielectric constant, $\epsilon^{-1}_{(a_1,a_2)}$, given by

$$\epsilon^{-1}_{(a_1,a_2)} = a_1^2\epsilon^{-1}_{11} + 2a_1a_2\epsilon^{-1}_{12} + a_2^2\epsilon^{-1}_{22}, \tag{27}$$

where

$$\epsilon^{-1}_{\mu\nu} = \delta_{\mu\nu} - \frac{\pi}{A}\langle \mathbf{M}_\mu \cdot \mathbf{M}_\nu \rangle, \tag{28}$$

is a type-specific inverse dielectric constant, a_1 and a_2 are type-dependent weights for the contributions of the different $\epsilon^{-1}_{\mu\nu}$ (which are determined by the values of both types of charge carried by the test particles for which screening is being measured), and where $\mathbf{M}_1$ and $\mathbf{M}_2$ are the dipole moments for charges of type 1 and type 2, respectively, given by

$$\mathbf{M}_1 = Q_1 R \sum_{i=1}^{N} \hat{\mathbf{z}}_i, \tag{29}$$

$$\mathbf{M}_2 = Q_2 R \left(\sum_{i=1}^{N} \hat{\mathbf{z}}_i - \sum_{a=1}^{N} \hat{\mathbf{w}}_a \right). \tag{30}$$

Note that the type 2 inverse dielectric constant, ϵ^{-1}_{22}, is the same dielectric constant as was used when studying the two-component neutral Coulomb plasma on a spherical surface.[14,63] In addition to measuring the screening properties, the inverse dielectric constant may be used to identify the existence of a BKT transition if it exhibits a universal discontinuous jump at the critical point, according to Eq. (11).

In addition to the inverse dielectric constant, we also measure the fourth-order modulus, γ (Refs. 65 and 66). This quantity may be used to verify a discontinuous jump in the inverse dielectric constant without making any *a priori* assumptions regarding the character of the phase transition. As explained in detail in Appendix B, a negative γ at the phase transition in the thermodynamic limit implies that the inverse dielectric constant jumps to zero discontinuously. As for the inverse dielectric constant, we use a general fourth-order modulus to account for the two interactions,

$$\gamma_{(a_1,a_2)} = \sum_{\mu,\nu,\rho,\sigma=1}^{2} a_\mu a_\nu a_\rho a_\sigma \gamma_{\mu\nu\rho\sigma}, \tag{31}$$

where

$$\gamma_{\mu\nu\rho\sigma} = \left(\frac{\pi}{R^2}\right)^2 [\langle \mathbf{M}_\mu \mathbf{M}_\nu \rangle \langle \mathbf{M}_\rho \mathbf{M}_\sigma \rangle - 3\langle M_{\mu,z} M_{\nu,z} M_{\rho,z} M_{\sigma,z} \rangle]. \tag{32}$$

The explicit derivation of Eqs. (31) and (32) is given in Appendix B .

B. Details of the Monte Carlo simulations

The Monte Carlo updating scheme consists of trial moves for one or two particles at the same time, to a randomly chosen new location on the surface of the sphere. The change in the action Eq. (24) was calculated and the move was accepted or rejected according to the Metropolis-Hastings algorithm.[67,68] The trial moves were performed in three different ways. The

first way was to move a single particle to a new random location uniformly over the total surface. The second way was to move a single particle to a new random location uniformly within some short distance, adjusted to yield a high acceptance rate. The last trial move was to move a nearest-neighbor pair of one z particle and one w particle together, to a random new location uniformly within some short distance, adjusted to yield a high acceptance rate, and with a random new orientation. In order to straightforwardly ensure detailed balance, we additionally required the two particles to mutually be nearest neighbors in both the old and the new configuration. To ensure ergodicity, the pair move must be mixed with a number of single-particle moves. All of these moves were found to be essential in order to have fast thermalization as well as short autocorrelation times for the cases considered here. Pseudorandom numbers were generated by the Mersenne-Twister algorithm[69] and the sampled data were postprocessed using Ferrenberg-Swendsen reweighting techniques.[70,71]

C. Results

Motivated by its relevance to the fractional quantum Hall effect (in particular, the $\nu = 1/2$ MR state), we focus on analyzing the screening properties of this system at $Q_1 = 2$ $(M = 2)^2$. We also perform simulations in the neutral two-component Coulomb gas case at $Q_1 = 0$ $(M = 0)$ in order to provide a check on the numerics, as well as for comparison with the $Q_1 = 2$ case. Furthermore, the system is also studied for a number of values of the packing fraction, η to extract the screening properties in the low-density limit.

For the two cases of Q_1 and the values of Q_2 studied below, the quantities ϵ_{11}^{-1} and ϵ_{12}^{-1} were found to be zero, within statistical uncertainty and except for a small finite-size effect when system size N was small. Thus, we focus on the results for ϵ_{22}^{-1} as this was the only term in Eq. (27) that contributed to the general inverse dielectric constant, $\epsilon_{(a_1,a_2)}^{-1}$. This means that screening properties of particles that interact with charges of both types, are determined by the charges of type 2, only. Note also that when $\epsilon_{11}^{-1} = 0$, the unconventional Coulomb plasma will screen test particles with charge of type 1, only.

In Fig. 2, we plot ϵ_{22}^{-1} in the relevant range of Q_2^2 when the two-component neutral Coulomb gas $(Q_1 = 0)$ is known to have a BKT transition. At small values of Q_2^2, the system is in the screening phase where $\epsilon_{22}^{-1} \approx 0$. The reason for the $\approx$ sign rather than an equal sign is that there is a mainly size-dependent offset from $\epsilon_{22}^{-1} = 0$, because perfect screening is not possible with a small number of charges. For large Q_2^2 there is a phase in which charges of different components form tightly bound dipoles and the Coulomb gas turns into an insulator where $\epsilon_{22}^{-1} \approx 1$. Here there is a mainly density-dependent offset from $\epsilon_{22}^{-1} = 1$ because the polarizability of the system increases with density, since the hard-core diameter d yields a minimum distance between the charges in the dipoles. The plot in Fig. 2 indeed shows that the charge-unbinding transition is dependent on the number of particles in the system, as well as the size of the hard disk charges. When N increases, the onset of a finite value in ϵ_{22}^{-1} moves to higher values of Q_2^2. However, when we reduce η, the value of Q_2^2 at onset of ϵ_{22}^{-1} becomes smaller.

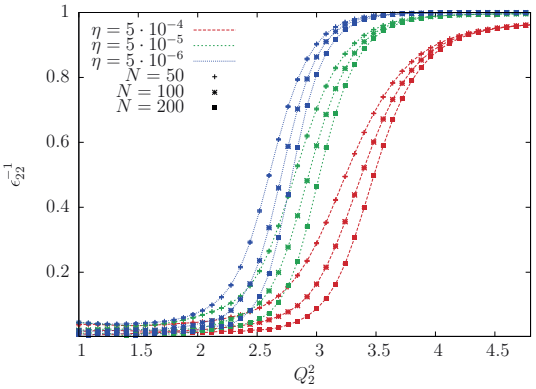

FIG. 2. (Color online) Plot of the inverse dielectric constant ϵ_{22}^{-1} for the model in Eq. (7) with $Q_1 = 0$ and $1 \leqslant Q_2^2 \leqslant 4.8$. Results are presented for three different values of packing fraction η and three different values of system size N.

Thus, this figure illustrates that understanding the behavior in both limits $N \to \infty$ as well as $\eta \to 0$ is not straightforward.

In Fig. 3, results for the same case as in Fig. 2 are presented, but with $Q_1 = 2$. The results for $Q_1 = 0$ and $Q_1 = 2$ are very similar, both qualitatively and quantitatively. Thus, the screening properties with respect to charge of type 2 of the unconventional Coulomb plasma when $Q_1 = 2$ are very similar to the well-studied two-component neutral Coulomb gas.

To get a qualitative picture of the type 2 charge binding of the unconventional plasma, three snapshots of the charge configuration when $Q_1 = 2$, $\eta = 5 \times 10^{-4}$, and $N = 200$ is given in Fig. 4. When $Q_2^2 = 1$, deep into the screening phase of the system (see Fig. 3), most charges are free and only a small fraction of the charges may be said to form closely bound dipoles. At $Q_2^2 = 3$, which is the relevant value for the Ising-type quantum Hall states, the system is closer to the

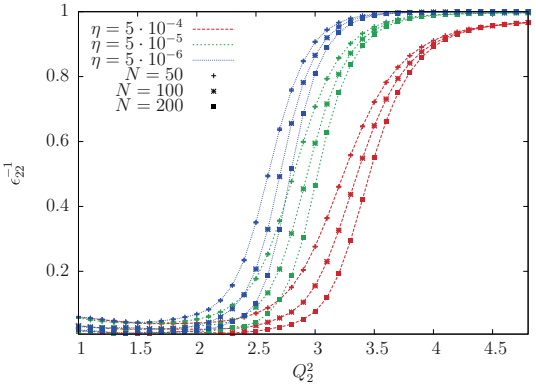

FIG. 3. (Color online) Plot of the inverse dielectric constant ϵ_{22}^{-1} for the model in Eq. (7) with $Q_1 = 2$ and $1 \leqslant Q_2^2 \leqslant 4.8$. Results are presented for three different values of packing fraction η and three different values of system size N.

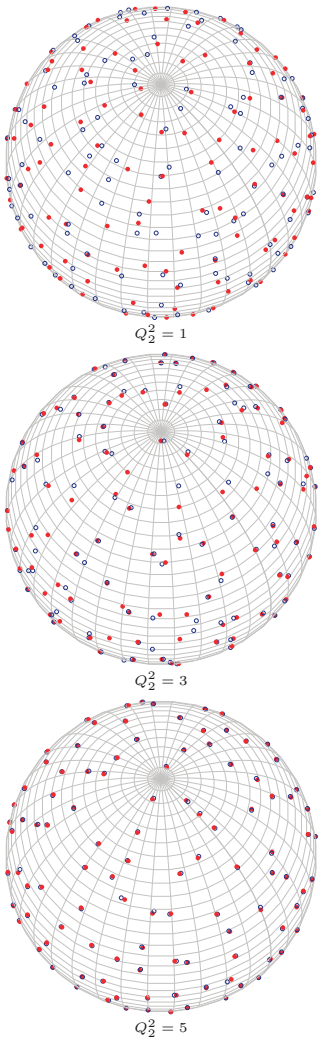

FIG. 4. (Color online) Snapshots of the charge configuration at $Q_2^2 = 1,3,5$ when $Q_1 = 2$, $\eta = 5 \times 10^{-4}$, and $N = 200$. Red markers (solid circles) are w particles, while blue markers (open circles) are z particles. The marker diameters are about 5 times larger than hard disk diameter d.

unbinding transition and a larger fraction (though not all) of the particles are bound in dipoles. At $Q_2^2 = 5$, deep in the type 2 insulating region, all particles form closely bound dipoles and the ability to screen type 2 test charges is lost.

Although it is clear from Figs. 2 and 3 that there is a transition between a screening phase and an insulating phase, it is not easy to spot the transition point in the curves in these figures, which look rather smooth. Therefore, we must make some assumptions about the nature of the transition in order to identify it.

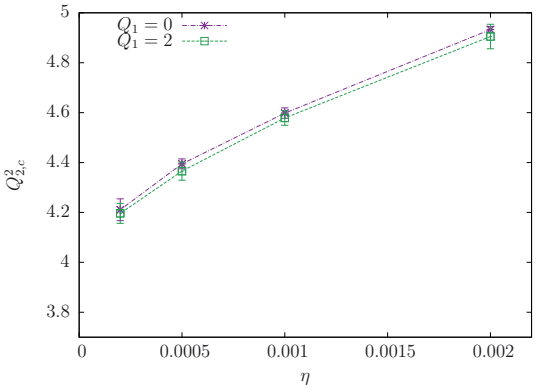

FIG. 5. (Color online) The critical value of Q_2^2 found by curve fitting to Eq. (33) with two free parameters. Results are presented for four values of the packing fraction η and for $Q_1 = 0$ and $Q_1 = 2$. Fourteen system sizes in the range $20 \leqslant N \leqslant 2000$ have been used.

For the case $Q_1 = 0$, where the transition is known to be a BKT transition, it is natural to follow a method that was proposed in Ref. 72. At the BKT critical point, ϵ_{22}^{-1} scales logarithmically with N for large N. It takes the following finite-size scaling form:

$$\epsilon_{22}^{-1}(N) = \epsilon_{22}^{-1}(\infty)\left[1 + \frac{1}{\ln(N) + C}\right], \tag{33}$$

where $\epsilon_{22}^{-1}(\infty)$ is the value of $\epsilon_{22}^{-1}(N)$ when $N \to \infty$ and C is an undetermined constant. Least-squares curve-fitting to Eq. (33) may be performed for various sizes N with C and $\epsilon_{22}^{-1}(\infty)$ as free parameters at fixed values of Q_2^2. The critical point is then estimated as the value of Q_2^2 which exhibits the best fit to Eq. (33). Additionally, for a BKT transition, the value of $\epsilon_{22}^{-1}(\infty)$ obtained at the best fit, must correspond with the universal jump condition, $Q_{2,c}^2 \epsilon_{22}^{-1}(\infty) = 4$ [cf. Eq. (11)]. Details of this procedure are given in Appendix C .

For $Q_1 = 2$, motivated by the similarity between Figs. 2 and 3, we assume that the transition is also a BKT transition. We again look for the Q_2^2 value at which the system best fits Eq. (33). Since we are able to find a value at which there is a very good fit to this form, we conclude that our assumption was justified.

In Fig. 5, we present results for the critical coupling $Q_{2,c}^2$ for four different densities $\eta = 0.0002, 0.0005, 0.001, 0.002$ for $Q_1 = 0$ and $Q_1 = 2$. The results for $Q_1 = 0$ reproduce the main features of the two-component Coulomb gas, namely, that $Q_{2,c}^2 = 4$ when density is low and that $Q_{2,c}^2$ increases when density increases. These results also correspond well with earlier results in Refs. 14 and 15. When $Q_1 = 2$, we find that the behavior of the critical temperature is very similar to the $Q_1 = 0$ case, within statistical uncertainty. In addition, in Fig. 6, results for the corresponding value of the parameter $\epsilon_{22}^{-1}(\infty)$ at the critical point is presented. The values for both $Q_1 = 0$ and $Q_1 = 2$ are close to the universal value of $Q_{2,c}^2 \epsilon_{22}^{-1}(\infty) = 4$ for the BKT transition. Since the results for $Q_1 = 0$ (the standard Coulomb-plasma BKT-transition case) and $Q_1 = 2$ are essentially the same, we suggest that the

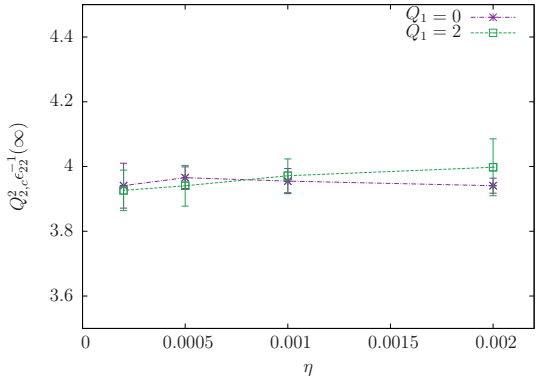

FIG. 6. (Color online) The universal jump value determined by curve fitting to Eq. (33) with two free parameters. Results are presented for four values of the packing fraction η and for $Q_1 = 0$ and $Q_1 = 2$. Fourteen system sizes in the range $20 \leqslant N \leqslant 2000$ have been used.

charge-unbinding transition for the unconventional Coulomb plasma indeed is a BKT transition in the sense that the type 2 inverse dielectric constant ϵ_{22}^{-1} exhibits logarithmic finite-size scaling and a discontinuous jump with a universal value, as predicted by the BKT renormalization equations.

As an additional verification of the discontinuous jump in the BKT transition, we also study the fourth-order modulus $\gamma_{(a_1,a_2)}$, presented in Eqs. (31) and (32). As for the general inverse dielectric constant, we found that the only contributing term in the sum of Eq. (31) is the term with all indices equal to 2, γ_{2222}. Illustrating the typical behavior of this quantity, results for γ_{2222} for a number of sizes when $\eta = 5 \times 10^{-4}$ and $Q_1 = 2$ are presented in Fig. 7. Typically, γ_{2222} exhibits a dip at a value of the coupling that can be associated with the transition. As explained in Appendix B, a negative and finite dip in the limit when $N \to \infty$ signals the discontinuous jump in ϵ_{22}^{-1} that is a characteristic feature of a BKT transition. To this end, the size of the dip in γ_{2222} is plotted as a function

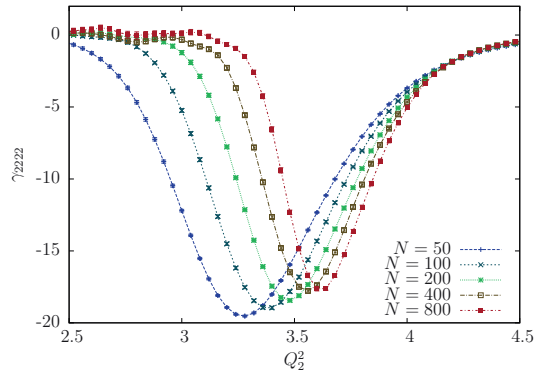

FIG. 7. (Color online) The fourth-order modulus γ_{2222} as a function of coupling Q_2^2 for five different system sizes N, when $Q_1 = 2$ and $\eta = 5 \times 10^{-4}$.

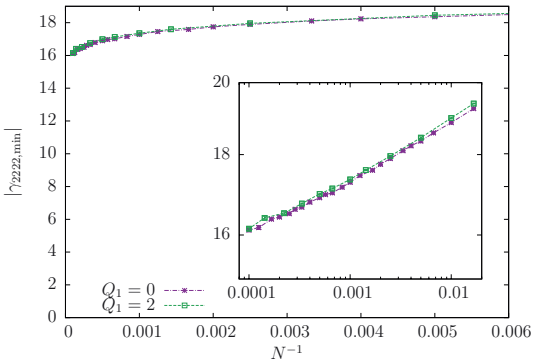

FIG. 8. (Color online) The size of the dip in the fourth-order modulus $|\gamma_{2222,\min}|$ as a function of inverse system size N^{-1}. The packing fraction is $\eta = 5 \times 10^{-4}$, and results for $Q_1 = 0$ and $Q_1 = 2$ are shown. The inset shows the results on a log-log scale. System sizes in the range $60 \leqslant N \leqslant 10\,000$ are used.

of inverse system size N^{-1} in Fig. 8 in the case when $\eta = 5 \times 10^{-4}$. The size of the dip $|\gamma_{2222,\min}|$ decreases when N increases toward the thermodynamic limit. However, assuming power-law dependence of $|\gamma_{2222,\min}|$, the positive curvature in the log-log plot indicates a nonzero value of $|\gamma_{2222,\min}|$ when $N \to \infty$, verifying a discontinuous jump in ϵ_{22}^{-1}, as expected for a BKT transition. Again, we find that the results for $Q_1 = 2$ are very similar to $Q_1 = 0$.

We also associate the coupling value of the minimum in the dip in γ_{2222} with the critical point and the results are shown in Fig. 9 in the case when $\eta = 5 \times 10^{-4}$. Clearly, the position of the dip moves toward higher values of Q_2^2 when the system size increases. However, the evolution toward $N^{-1} = 0$ is too slow to make a sharp determination of Q_2^2 in this limit, as also noted before.[65,66] With this method, we are not able to verify that $Q_{2,c}^2 \approx 4.4$, as was found above in Fig. 5 for this density.

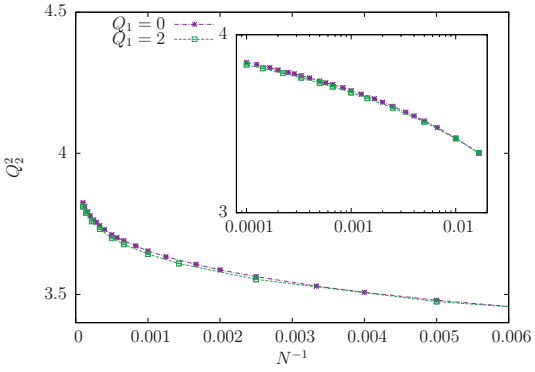

FIG. 9. (Color online) The coupling value at the minimum of the dip in the fourth-order modulus as a function of inverse system size N^{-1}. The packing fraction is $\eta = 5 \times 10^{-4}$, and results for $Q_1 = 0$ and $Q_1 = 2$ are shown. The inset shows the results on a log-log scale. System sizes in the size $60 \leqslant N \leqslant 10\,000$ are used.

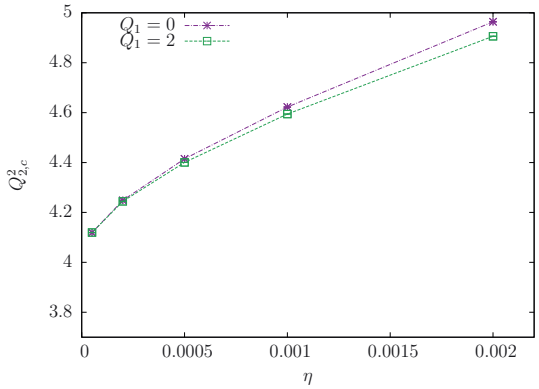

FIG. 10. (Color online) The critical value of Q_2^2 found by curve fitting to Eq. (33) with one free parameter. Results are presented for five values of the packing fraction η and for two values of Q_1.

By assuming a universal value of the discontinuous jump for a BKT transition, we may determine the critical point of the BKT transition using Eq. (33) with only one free parameter as described in Appendix C . The results are given in Fig. 10. The critical values of Q_2^2 are very similar to what was obtained in Fig. 5, but are determined with greater accuracy. For both cases, the critical point appears at higher Q_2^2 when density increases. However, $Q_{2,\mathrm{c}}^2$ is systematically lower at $Q_1 = 2$ compared to $Q_1 = 0$.

For the range of small densities that we have investigated, the Monte Carlo results for the unconventional Coulomb plasma with $Q_1 = 2$ are rather conclusive. This plasma undergoes a charge-unbinding transition that should be regarded as a BKT transition in the sense that the inverse dielectric constant of type 2 exhibits the well-established signatures of a BKT transition. Specifically, there is a density-dependent critical point $Q_{2,\mathrm{c}}^2$ that separates a phase where particles of different species form bound pairs at high values of Q_2^2 from a phase where particles of different species are free at low values of Q_2^2. For test particles carrying type 2 charge, the high-Q_2^2 phase is unscreened, whereas the low-Q_2^2 phase is screened.

The results presented so far show that the behavior when $Q_1 = 0$ and $Q_1 = 2$ are quite similar. However, in the phase with bounded dipoles, when charges of type 2 are not screened, the cases $Q_1 = 0$ and $Q_1 = 2$ behave rather differently. We first consider the case when $Q_1 = 0$. When charges are bound, this system consists of N dipoles that interact by dipole-dipole interactions. Consequently, these dipoles tend to form clusters with increased dipole strength, that is, higher values of the coupling or the density.[15,29] In Fig. 11, a snapshot of a $Q_1 = 0$ configuration with $N = 200$, $Q_2^2 = 7$, and $\eta = 2 \times 10^{-3}$ is shown, where some dipoles are seen to form clusters. In the case when $Q_1 = 2$, the type 2 interactions are effectively reduced to dipole-dipole interactions, similar to the $Q_1 = 0$ case. *However, the logarithmic interactions of type 1 charges remain*. Neglecting the weaker dipole-dipole interactions among dipoles of type two, the dipoles now

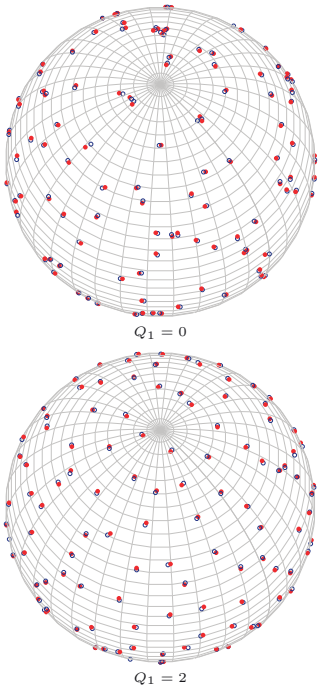

FIG. 11. (Color online) Snapshots of the charge configuration at $Q_1 = 0$ and $Q_1 = 2$ when $Q_2^2 = 7$, $\eta = 2 \times 10^{-3}$, and $N = 200$. Red markers (solid circles) are w particles and blue markers (open circles) are z particles. The marker diameters are about 2.5 times larger than hard disk diameter d.

essentially form elementary constituents with charge Q_1 interacting logarithmically. Effectively, the two-component unconventional plasma is reduced to a one-component plasma where the particles carry charge of type 1 and a (neutral) dipole of type 2. When $Q_1 = 2$ this plasma is in the liquid state; that is, the tightly bound dipoles do not form an ordered state with a broken translational or orientational symmetry. Also, the logarithmic interaction of type 1 charge will prevent the dipoles from forming clusters. A snapshot of the state with bounded dipoles when $Q_1 = 2$ is shown in Fig. 11 and the qualitative difference from the case when $Q_1 = 0$ is clearly seen. Quantitatively, this is seen by the behavior of ϵ_{22}^{-1}, presented in Fig. 12. When $Q_1 = 0$, dipole-dipole interactions at short distances will reduce the fluctuations in the dipole moment resulting in a weakly increasing ϵ_{22}^{-1} inside the bounded phase. On the other hand, when $Q_1 = 2$ the logarithmic interaction of type 1 charge will keep the dipoles at some distance from each other, thus the fluctuations of a dipole are not much restricted by the surrounding dipoles. Moreover, the strength of the dipoles increases with Q_2^2 and a reduction in ϵ_{22}^{-1} follows. The qualitative difference between the cases $Q_1 = 0$ and $Q_1 = 2$ is an effect due to the minimum separation of charges at finite density originating with the hard cores, and it will vanish in the limit $\eta \to 0$.

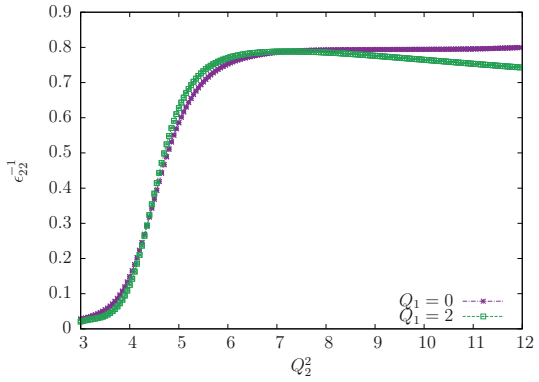

FIG. 12. (Color online) Plot of the type 2 inverse dielectric constant for $Q_1 = 0$ and $Q_1 = 2$ with $N = 100$, $\eta = 5 \times 10^{-3}$ in the range $3 \leqslant Q_2^2 \leqslant 12$.

IV. CONCLUSIONS

We have shown that the unconventional Coulomb plasma analyzed in this paper, where particles can carry two distinct types of Coulombic charge, will screen test particles with charges of both types for the case most relevant for the plasma analogy of Ising-type fractional quantum Hall states, that is, when there is one species of particles that carry type 1 charge $Q_1 = 2$ ($M = 2$) and type 2 charge $Q_2 = \sqrt{3}$ and another species of particles that carry only type 2 charge $-Q_2$. For test particles carrying both types of charge, screening will cease to occur at $Q_2^2 = Q_{2,\mathrm{c}}^2 \approx 4$ in the limit of small density, when $Q_1 = 2$. For higher values of Q_2^2, the system will continue to screen test particles that carry only type 1 charge, but will not be able to screen test particles with type 2 charge.

One striking feature of these results is that $Q_{2,\mathrm{c}}^2$ and the critical behavior at this point hardly seem to depend on Q_1 when density is small. This implies that the role of the type 1 interaction (which corresponds, in quantum Hall wave function language, to the Laughlin-Jastrow factor which accounts for the filling fraction of the system) is simply to maintain the z_i particles in a liquid state. Since its critical point is very far away, the type 1 interaction leads to a weak, smooth dependence on Q_1. The physics in the transition at $Q_{2,\mathrm{c}}^2$ is then dominated by the type 2 interaction. We therefore conjecture that our results hold for all reasonable values of M, not only $M = 0$ and 2, the cases which we have studied here, but also $M = 1$ (which may be relevant to ultracold trapped bosons) and larger values of M, possibly all the way up to or near the critical value $M_{\mathrm{c}} \approx 70$, below which the one-component plasma of Eq. (3) is in the metallic phase.[33–36]

ACKNOWLEDGMENTS

We acknowledge useful discussions with K. Børkje, J. S. Høye, I. B. Sperstad, B. Svistunov, and M. Wallin. E.V.H., E.B., and V.G. thank Nordita for hospitality during the initial stage of this work. E.B., P.B., and A.S. thank the Aspen Center for Physics for hospitality and support under NSF Grant No. 1066293. E.V.H. thanks NTNU for financial support. E.B. was supported by Knut and Alice Wallenberg Foundation through the Royal Swedish Academy of Sciences Fellowship, Swedish Research Council, and by the National Science Foundation CAREER Award No. DMR-0955902. V.G. was supported by NSF Grant No. PHY-0904017. C.N. was supported in part by the DARPA QuEST program. A.S. was supported by the Norwegian Research Council under Grant No. 205591/V30 (FRINAT). The work was also supported through the Norwegian consortium for high-performance computing (NOTUR).

APPENDIX A: GENERALIZING THE INVERSE DIELECTRIC CONSTANT FOR MULTIPLE INTERACTIONS

In the unconventional plasma with two components that interact with two different Coulomb-like interactions, we are free to insert test particles that may interact with different charge strength through both interactions simultaneously. Here we generalize the inverse dielectric constant for such test particles. For consistency, we also perform the derivation on the surface of a sphere by expanding in spherical harmonics. For a similar derivation, but with one interaction only and on a planar geometry, see Refs. 31 and 32.

When an external test charge field is inserted in the system, the free energy in the system will change according to the effective interaction among the test charges,

$$\Delta F[\delta q] = \int \mathrm{d}\Omega \int \mathrm{d}\Omega' \sum_{\mu,\nu} \delta q_\mu(\theta,\phi) U_{\mu\nu}^{\mathrm{eff}}(\hat{\mathbf{r}} \cdot \hat{\mathbf{r}}') \delta q_\nu(\theta',\phi'). \tag{A1}$$

Here the effective interaction between charges of type μ and ν, is assumed to be of the form $U_{\mu\nu}^{\mathrm{eff}} = U_{\mu\nu}^{\mathrm{eff}}(\hat{\mathbf{r}} \cdot \hat{\mathbf{r}}')$, $\delta q_\mu(\theta,\phi)$ is the test charge field for charges of type μ, and the integrations are over the solid angle $\mathrm{d}\Omega$. To correctly model the test particles as carrying charge of different types, we write

$$\delta q_\mu(\theta,\phi) = a_\mu \, \delta q \, \rho(\theta,\phi), \tag{A2}$$

where a_μ is a type-dependent factor that accounts for the relative strength of charges of different types. For instance, the choice $(a_1,a_2) = (Q_1/MQ_2,1) = (\sqrt{2/3M},1)$ describes the test charges corresponding to quasiholes in the MR state, as given in Eq. (125) in Ref. 2, which map to particles in the plasma that carry charge $Q_1/2M = 1/\sqrt{2M}$ of type 1 and charge $Q_2/2 = \sqrt{3}/2$ of type 2. Moreover, in Eq. (A2) δq is a common charge factor for all types such that $a_\mu \, \delta q$ is the total charge of type μ carried by a test particle (which means that $\delta q = \sqrt{3}/2$ in the example above), and $\rho(\theta,\phi)$ is the density field of the test particles.

It is now convenient to expand the interaction and density fields in spherical harmonics. The test particle density field is expanded by

$$\rho(\theta,\phi) = \sum_{l=0}^{\infty} \sum_{m=-l}^{l} \rho_l^m Y_l^m(\theta,\phi), \tag{A3}$$

where

$$Y_l^m(\theta,\phi) = \sqrt{\frac{(2l+1)(l-m)!}{4\pi(l+m)!}} P_l^m(\cos\theta) \, \mathrm{e}^{im\phi}, \tag{A4}$$

and $P_l^m(x)$ are the associated Legendre polynomials. The coefficients are given by

$$\rho_l^m = \int \mathrm{d}\Omega\, \rho(\theta,\phi) Y_l^{m*}(\theta,\phi). \tag{A5}$$

The effective interaction is expanded by using the addition theorem for spherical harmonics,

$$U_{\mu\nu}^{\mathrm{eff}}(\hat{\mathbf{r}}\cdot\hat{\mathbf{r}}') = \sum_{l=0}^{\infty} \frac{4\pi}{2l+1} U_{\mu\nu,l}^{\mathrm{eff}} \sum_{m=-l}^{l} Y_l^{m*}(\theta,\phi) Y_l^m(\theta',\phi'). \tag{A6}$$

Here $U_{\mu\nu,l}^{\mathrm{eff}}$ are the Legendre coefficients of the interaction, given by

$$U_{\mu\nu,l}^{\mathrm{eff}} = \frac{2l+1}{2} \int_0^{\pi} \mathrm{d}\theta\ \sin\theta\, U_{\mu\nu}^{\mathrm{eff}}(\cos\theta) P_l(\cos\theta), \tag{A7}$$

where $P_l(x)$ is the Legendre polynomial of order l. Now Eq. (A1) is written

$$\Delta F[\delta q] = \delta q^2 \sum_{l=0}^{\infty} \frac{4\pi}{2l+1} \sum_{\mu,\nu} a_\mu U_{\mu\nu,l}^{\mathrm{eff}} a_\nu \sum_{m=-l}^{l} \rho_l^{m*} \rho_l^m. \tag{A8}$$

Hence, in the limit when the test charge field is infinitesimal, $\delta q \to 0$, we find that

$$\left.\frac{\partial^2 F[\delta q]}{\partial \delta q^2}\right|_{\delta q=0} = \sum_{l=0}^{\infty} \frac{8\pi}{2l+1} \sum_{\mu,\nu} a_\mu U_{\mu\nu,l}^{\mathrm{eff}} a_\nu \sum_{m=-l}^{l} \rho_l^{m*} \rho_l^m. \tag{A9}$$

This derivative can also be calculated by inspection of the partition function of the system perturbed with the external test charge field. With $F[\delta q] = -\ln Z[\delta q]$ and a potential energy on the form $V[\delta q] = V_0 + V_1[\delta q]$, where V_0 is the potential energy of the unperturbed system and $V_1[\delta q]$ is the contribution due to the test charge field, we find that

$$\left.\frac{\partial^2 F[\delta q]}{\partial \delta q^2}\right|_{\delta q=0} = \left\langle \left.\frac{\partial^2 V_1[\delta q]}{\partial \delta q^2}\right|_{\delta q=0} \right\rangle - \left\langle \left(\left.\frac{\partial V_1[\delta q]}{\partial \delta q}\right|_{\delta q=0} \right)^2 \right\rangle. \tag{A10}$$

Here we have also used that $\partial F[\delta q]/\partial \delta q|_{\delta q=0} = 0$, and the brackets denote statistical average with respect to the unperturbed system. The test charges $\delta q_\mu(\theta,\phi)$ will interact with each other as well as with the charge field $q_\mu(\theta,\phi)$. As for the test charge field, the charge field is expanded according to Eq. (A3) to yield

$$\begin{aligned} V_1[\delta q] &= \int \mathrm{d}\Omega \int \mathrm{d}\Omega' \sum_{\mu} [q_\mu(\theta,\phi) + \delta q_\mu(\theta,\phi)] \\ &\quad \times U(\hat{\mathbf{r}}\cdot\hat{\mathbf{r}}') \delta q_\mu(\theta',\phi') \\ &= \sum_{l=0}^{\infty} \frac{4\pi}{2l+1} U_l \sum_{\mu} a_\mu \sum_{m=-l}^{l} \delta q\, \rho_l^{m*} \left(q_{\mu,l}^m + a_\mu \delta q\, \rho_l^m \right), \end{aligned} \tag{A11}$$

where $U(\hat{\mathbf{r}}\cdot\hat{\mathbf{r}}')$ is the bare interaction, expanded by Eq. (A6) with coefficients U_l. Performing the derivatives in Eq. (A10) yields

$$\begin{aligned} \left.\frac{\partial^2 F[\delta q]}{\partial \delta q^2}\right|_{\delta q=0} &= \sum_{l=0}^{\infty} \frac{8\pi}{2l+1} U_l \sum_{\mu,\nu} a_\mu \delta_{\mu\nu} a_\nu \sum_{m=-l}^{l} \rho_l^{m*} \rho_l^m \\ &\quad - \sum_{l=0}^{\infty} \frac{4\pi}{2l+1} U_l \sum_{l'=0}^{\infty} \frac{4\pi}{2l'+1} U_{l'} \sum_{\mu,\nu} a_\mu a_\nu \\ &\quad \times \sum_{m=-l}^{l} \sum_{m'=-l'}^{l'} \rho_l^{m*} \rho_{l'}^{m'} \langle q_{\mu,l}^m q_{\nu,l'}^{m'*} \rangle. \end{aligned} \tag{A12}$$

We introduce the dielectric function $\epsilon_{\mu\nu,l}$ by

$$U_{\mu\nu,l}^{\mathrm{eff}} = \epsilon_{\mu\nu,l}^{-1} U_l, \tag{A13}$$

and by comparing Eqs. (A9) and (A12), the inverse dielectric function is found to be

$$\begin{aligned} \epsilon_{\mu\nu,l}^{-1} &= \delta_{\mu\nu} - \left(\sum_{m=-l}^{l} \rho_l^{m*} \rho_l^m \right)^{-1} \sum_{l'=0}^{\infty} \frac{2\pi}{2l'+1} U_{l'} \\ &\quad \times \sum_{m=-l}^{l} \sum_{m'=-l'}^{l'} \rho_l^{m*} \rho_{l'}^{m'} \langle q_{\mu,l}^m q_{\nu,l'}^{m'*} \rangle. \end{aligned} \tag{A14}$$

Moreover, since the bare interaction is only dependent on the distance between the charges, $U = U(\hat{\mathbf{r}}\cdot\hat{\mathbf{r}}')$, we have that $\langle q_{\mu,l}^m q_{\nu,l'}^{m'*} \rangle = \langle q_{\mu,l}^m q_{\nu,l'}^{m'*} \rangle \delta_{ll'} \delta_{mm'}$, which yields

$$\begin{aligned} \epsilon_{\mu\nu,l}^{-1} &= \delta_{\mu\nu} - \left(\sum_{m=-l}^{l} \rho_l^{m*} \rho_l^m \right)^{-1} \frac{2\pi}{2l+1} U_l \\ &\quad \times \sum_{m=-l}^{l} \rho_l^{m*} \rho_l^m \langle q_{\mu,l}^m q_{\nu,l}^{m*} \rangle. \end{aligned} \tag{A15}$$

Additionally, the property that the bare interaction is distance dependent, only, yields an interaction U_l that is independent of m. Hence, the correlator $\langle q_{\mu,l}^m q_{\nu,l}^{m*} \rangle$ must be m independent as well, $\langle q_{\mu,l}^m q_{\nu,l}^{m*} \rangle = \langle q_{\mu,l}^0 q_{\nu,l}^0 \rangle$. The dielectric function thus reads

$$\epsilon_{\mu\nu,l}^{-1} = \delta_{\mu\nu} - \frac{2\pi}{2l+1} U_l \langle q_{\mu,l}^0 q_{\nu,l}^0 \rangle. \tag{A16}$$

The dielectric constant $\epsilon_{\mu\nu}$ is now found in the long-wavelength limit of the dielectric function. On a spherical surface, this corresponds to setting $l = 1$ in the dielectric function, that is, $\epsilon_{\mu\nu} = \epsilon_{\mu\nu,1}$. Thus, the dielectric constant is

$$\epsilon_{\mu\nu}^{-1} = \delta_{\mu\nu} - \frac{2\pi}{3} U_1 \langle q_{\mu,1}^0 q_{\nu,1}^0 \rangle. \tag{A17}$$

So far, only a few assumptions are made regarding the bare interaction $U(\hat{\mathbf{r}}\cdot\hat{\mathbf{r}}')$ and the charge field $q_\mu(\theta,\phi)$. To apply Eq. (A17) for the system under consideration in this paper, we invoke $U(\hat{\mathbf{r}}\cdot\hat{\mathbf{r}}') = -\ln(1 - \hat{\mathbf{r}}\cdot\hat{\mathbf{r}}')$ to find $U_1 = 3/2$ by Eq. (A7). Moreover, the charge field is modeled as point charges in a uniform background,

$$q_\mu(\theta,\phi) = q_\mu^{\mathrm{BG}} + \sum_{i=1}^{N} e_{\mu,i} \frac{\delta(\theta-\theta_i)\delta(\phi-\phi_i)}{\sin\theta}, \tag{A18}$$

where $q_\mu^{\mathrm{BG}} = -(\sum_i e_{\mu,i})/(4\pi)$ is the uniform background ensuring charge neutrality for charges of type μ, $e_{\mu,i}$ is the

charge of type μ in particle i, and the sum is over all N particles of the unperturbed system. Now, using Eq. (A5), the actual coefficient of the charge field is found to be

$$q^0_{\mu,1} = \sqrt{\frac{3}{4\pi}}\frac{M_{\mu,z}}{R}, \tag{A19}$$

where $\mathbf{M}_\mu = \sum_{i=1}^N e_{\mu,i}\hat{\mathbf{r}}_i$ is the total dipole moment for charges of type μ. Finally, by inserting these results in Eq. (A17), the inverse dielectric constant is found to be

$$\epsilon^{-1}_{\mu\nu} = \delta_{\mu\nu} - \frac{\pi}{A}\langle \mathbf{M}_\mu \cdot \mathbf{M}_\nu\rangle, \tag{A20}$$

where $\langle M_{\mu,z}M_{\nu,z}\rangle = \langle \mathbf{M}_\mu \cdot \mathbf{M}_\nu\rangle/3$ by assuming isotropy.

When there are test charges with multiple interactions, there are multiple contributions to the change in free energy as seen in Eq. (A1). To account for all contributions to the increase in free energy, we construct a generalized dielectric constant by

$$\epsilon^{-1}_{(a_1,a_2,\ldots)} = \sum_{\mu,\nu} a_\mu \epsilon^{-1}_{\mu\nu} a_\nu. \tag{A21}$$

Notice that even though there is no bare interaction between charges of different type, there may be nonzero cross terms in Eq. (A1), as charges of different type are constrained to be together within the same particle.

APPENDIX B: FOURTH-ORDER FREE ENERGY DERIVATIVE

In Ref. 65 a method of verifying the discontinuous character of the BKT transition was introduced by examining a higher-order term in the free energy expansion in the XY model when the system is perturbed with an infinitesimal phase twist. Similarly, in Ref. 66, the method was applied in a 2D logarithmic plasma. Here we show that the same idea also applies when we perturb a logarithmic Coulomb plasma on a spherical surface with an infinitesimal test charge field with multiple types of Coulomb interactions.

Consider a system with particles interacting with different charges of multiple types, as previously described. We now *choose* to perturb this system with a neutral distribution of test charge of multiple types, which has the form $\delta q_\mu(\theta) = a_\mu \delta q\cos(\theta)$, that is, a similar test particle density field as given in Eq. (A2) but with $\rho^0_1 = \sqrt{4\pi/3}$ being the only nonzero coefficient in the spherical harmonics expansion. This is a convenient choice because it corresponds to the most long-waved nonuniform test charge configuration on the surface of a sphere, and hence, the prefactor of the second-order term in the free energy expansion will be proportional to the inverse dielectric constant, as we see below.

The test charges yield a contribution to the potential energy as given by the $l = 1$ and $m = 0$ term in Eq. (A11),

$$V_1[\delta q] = \frac{4\pi}{3}U_1\sum_\mu a_\mu \delta q\,\rho^0_1\big(q^0_{\mu,1} + a_\mu\delta q\rho^0_1\big). \tag{B1}$$

We now consider how the system responds to the test charges by a Taylor expansion of the free energy in the test charge field around $\delta q = 0$,

$$\Delta F[\delta q] = \left.\frac{\partial F[\delta q]}{\partial \delta q}\right|_{\delta q=0}\delta q + \left.\frac{\partial^2 F[\delta q]}{\partial \delta q^2}\right|_{\delta q=0}\frac{\delta q^2}{2!} + \left.\frac{\partial^3 F[\delta q]}{\partial \delta q^3}\right|_{\delta q=0}\frac{\delta q^3}{3!} + \left.\frac{\partial^4 F[\delta q]}{\partial \delta q^4}\right|_{\delta q=0}\frac{\delta q^4}{4!} + \cdots. \tag{B2}$$

The change in the free energy $\Delta F[\delta q]$ must be invariant to $\delta q_\mu(\theta) \to -\delta q_\mu(\theta)$, and hence, all odd-order derivatives in Eq. (B2) are zero. From Appendix A [see Eqs. (A12), (A17), and (A21)], the second-order free energy derivative is found to be

$$\left.\frac{\partial^2 F[\delta q]}{\partial \delta q^2}\right|_{\delta q=0} = \frac{8\pi}{3}\big(\rho^0_1\big)^2 U_1 \epsilon^{-1}_{(a_1,a_2,\ldots)}. \tag{B3}$$

The fourth-order derivative is

$$\begin{aligned}\left.\frac{\partial^4 F[\delta q]}{\partial \delta q^4}\right|_{\delta q=0} &= 3\left\langle\left(\left.\frac{\partial V_1[\delta q]}{\partial \delta q}\right|_{\delta q=0}\right)^2\right\rangle^2 - \left\langle\left(\left.\frac{\partial V_1[\delta q]}{\partial \delta q}\right|_{\delta q=0}\right)^4\right\rangle \\ &= \left(\frac{4\pi}{3}\rho^0_1 U_1\right)^4 \sum_{\mu,\nu,\rho,\sigma} a_\mu a_\nu a_\rho a_\sigma \\ &\quad\times\big[3\langle q^0_{\mu,1}q^0_{\nu,1}\rangle\langle q^0_{\rho,1}q^0_{\sigma,1}\rangle - \langle q^0_{\mu,1}q^0_{\nu,1}q^0_{\rho,1}q^0_{\sigma,1}\rangle\big].\end{aligned} \tag{B4}$$

where brackets denote a statistical average with respect to the unperturbed action. Inserting Eqs. (B3) and (B4) in Eq. (B2) yields

$$\Delta F[\delta q] = \frac{8\pi}{3}\big(\rho^0_1\big)^2 U_1\left[\epsilon^{-1}_{(a_1,a_2,\ldots)}\frac{\delta q^2}{2!} + \gamma_{(a_1,a_2,\ldots)}\frac{\delta q^4}{4!} + \cdots\right], \tag{B5}$$

where

$$\gamma_{(a_1,a_2,\ldots)} = \sum_{\mu,\nu,\rho,\sigma} a_\mu a_\nu a_\rho a_\sigma \gamma_{\mu\nu\rho\sigma}, \tag{B6}$$

and

$$\gamma_{\mu\nu\rho\sigma} = \left(\frac{4\pi}{3}U_1\right)^3\frac{\big(\rho^0_1\big)^2}{2}\big[3\langle q^0_{\mu,1}q^0_{\nu,1}\rangle\langle q^0_{\rho,1}q^0_{\sigma,1}\rangle - \langle q^0_{\mu,1}q^0_{\nu,1}q^0_{\rho,1}q^0_{\sigma,1}\rangle\big]. \tag{B7}$$

Now, inserting $\rho^0_1 = \sqrt{4\pi/3}$ and assuming the charge field in Eq. (A18) and a logarithmic bare interaction, $U_1 = 3/2$, yields

$$\gamma_{\mu\nu\rho\sigma} = \left(\frac{\pi}{R^2}\right)^2\left[\langle \mathbf{M}_\mu\mathbf{M}_\nu\rangle\langle \mathbf{M}_\rho\mathbf{M}_\sigma\rangle - 3\langle M_{\mu,z}M_{\nu,z}M_{\rho,z}M_{\sigma,z}\rangle\right], \tag{B8}$$

where $\langle M_{\mu,z}M_{\nu,z}\rangle = \langle \mathbf{M}_\mu \cdot \mathbf{M}_\nu\rangle/3$ by assuming isotropy.

A. Stability argument

When $\delta q = 0$, the free energy of the system has a global minimum, and hence the right-hand side of Eq. (B5) must be greater than or equal to zero. Now, if $\gamma_{(a_1,a_2,\ldots)}$ approaches a nonzero negative value at the critical point in the thermodynamical limit, the general inverse dielectric constant must

simultaneously have a nonzero positive value for the ground state to be stable. However, since $\epsilon^{-1}_{(a_1,a_2,\ldots)} = 0$ in the screening phase, it follows that $\epsilon^{-1}_{(a_1,a_2,\ldots)}$ must exhibit a discontinuous jump at the critical point. Hence, investigation of $\gamma_{(a_1,a_2,\ldots)}$ may be used to verify a discontinuity in the inverse dielectric constant, which is a necessary requirement for observing a BKT transition.

APPENDIX C: THE FINITE-SIZE SCALING RELATION

The finite-size scaling relation of the BKT transition has been used throughout this article to verify the universal jump in ϵ^{-1}_{22} and to provide estimates for the critical coupling $Q^2_{2,\mathrm{c}}$. Here some details to the curve fitting procedure and the goodness of fit measure are presented.

1. Two free parameters

Least-squares curve fitting of the Monte Carlo results for ϵ^{-1}_{22} to Eq. (33) may be performed with both $\epsilon^{-1}_{22}(\infty)$ and C as free parameters.[28,30,72,73] If the transition is of the BKT type, a good fit to Eq. (33) should be obtained at the critical point. In addition, when $\epsilon^{-1}_{22}(\infty)$ is free, no *a priori* assumption on the value of the universal jump is made, thus a resulting value of $\epsilon^{-1}_{22}(\infty)$ that corresponds to the universal jump of the BKT transition should be obtained. However, with two free parameters, higher quality of the Monte Carlo statistics is required to single out when they system is closely obeying the behavior of Eq. (33).

We have employed the Marquardt-Levenberg algorithm minimizing χ^2 to the nonlinear fitting function in Eq. (33). Specifically, χ^2 is the sum of squared weighted residuals,

$$\chi^2 = \sum_{i=1}^{n} \left(\frac{\epsilon^{-1}_{22,N_i} - \epsilon^{-1}_{22}(N_i)}{\sigma_{N_i}} \right)^2, \tag{C1}$$

where n is the number of system sizes N_i, ϵ^{-1}_{22,N_i} is the value of the inverse dielectric constant ϵ^{-1}_{22} obtained from the Monte Carlo simulation at system size N_i, and σ_{N_i} is the corresponding error. For a good fit, we expect the weight-normalized residuals, $Y_i = (\epsilon^{-1}_{22,N_i} - \epsilon^{-1}_{22}(N_i))/\sigma_{N_i}$ to be Gaussian-distributed with mean $\mu(Y_i) = 0$ and variance $\sigma^2(Y_i) = 1$. Thus, to measure the goodness of the fit, we use the Anderson-Darling test statistic A^2 for the data set Y_i to arise from a normal distribution with $\mu(Y_i) = 0$ and $\sigma^2(Y_i) = 1$:

$$A^2 = -n - \frac{1}{n} \sum_{i=1}^{n} (2i-1)\{\ln[\Phi(Y_i)] + \ln[\Phi(Y_{n+1-i})]\}, \tag{C2}$$

where $\Phi(Y)$ is the standard normal cumulative distribution function and where the data set Y_i is ordered from low to high values. A smaller value of A^2 essentially means a better fit between the data and the fit function.

To illustrate the method, Monte Carlo results for ϵ^{-1}_{22} at 14 different system sizes and the corresponding curve-fit according to Eq. (33) are given in Fig. 13 for three different values of Q^2_2. Here $\eta = 2 \times 10^{-3}$ and $Q_1 = 0$. Clearly, at $Q^2_2 = 4.933$, the fit between the data and the fit function is better than for the two other cases. Moreover, in Fig. 14 the corresponding results for the goodness of fit parameter as well as the results for the parameter $\epsilon^{-1}_{22}(\infty)$ as a function of Q^2_2 are shown. Indeed, the minimum in A^2 indicates a critical region where the data seem to follow the logarithmic finite size scaling of ϵ^{-1}_{22} given in Eq. (33). Also note that this region coincides with a value of $Q^2_2\epsilon^{-1}_{22}(\infty)$ close to the universal jump value of 4. With the minimum of A^2 as a measure of the critical point and with error estimates obtained by the jackknife method, we find that $Q^2_{2,\mathrm{c}} = 4.933 \pm 0.012$ and that $Q^2_{2,\mathrm{c}}\epsilon^{-1}_{22}(\infty) = 3.941 \pm 0.023$, less than 2% off the universal number. The results in Figs. 5 and 6 are found by repeating this procedure for different values of η and Q_1.

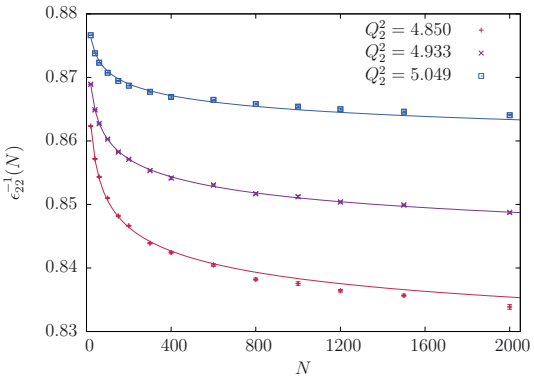

FIG. 13. (Color online) Plot of the size dependence in the inverse dielectric constant $\epsilon^{-1}_{22}(N)$ for 14 different system sizes in the range $20 \leqslant N \leqslant 2000$ at three different values of the coupling Q^2_2. The best fit according to the fit function in Eq. (33) with two free parameters, is given as the corresponding solid line in all three cases. The packing fraction is $\eta = 2 \times 10^{-3}$ and $Q_1 = 0$.

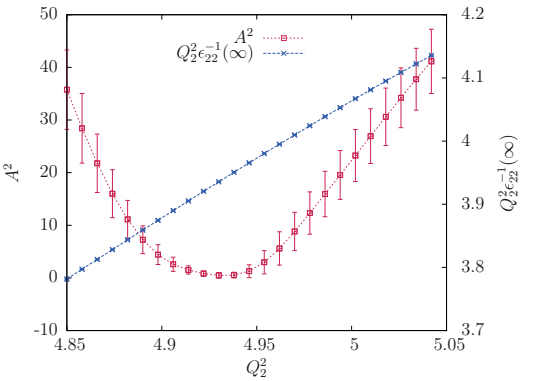

FIG. 14. (Color online) Plot of the goodness of fit parameter A^2 and the corresponding free parameter $\epsilon^{-1}_2(\infty)$ obtained when curve fitting to the critical finite-size relation given in Eq. (33). The results are given as a function of Q^2_2. System sizes N and η and Q_1 are the same as in Fig. 13. Error estimates are obtained by the jackknife method.

2. One free parameter

The procedure described in detail above with two free parameters, may be performed with a fixed value of $\epsilon_{22}^{-1}(\infty) = 4Q_{2,c}^2$ and with C as the only free parameter. If the transition is of the BKT type, a good fit to Eq. (33) should be obtained at the critical point. This is a rather well-used method to determine the critical point of a BKT transition.[29,72,74,75] With only one free parameter, $Q_{2,c}^2$ will be determined with greater accuracy compared to the case when there are two free parameters.

3. Remarks

References 28 and 30 used χ^2 as a goodness-of-fit parameter. We also tried this, and the results for the critical coupling as well as the corresponding parameter $\epsilon_{22}^{-1}(\infty)$ were consistent with A^2 results within statistical uncertainty. However, we found that error estimates were clearly underestimated with χ^2, probably due to overfitting.

The parameter C in the finite-size scaling relation [Eq. (33)] is density dependent.[76] Specifically, C increases when η decreases. Hence, at the critical point, the finite-size scaling slows down when η is lowered. Therefore, larger systems N or better statistics are required to resolve the critical scaling when η is small. In particular, curve fitting to Eq. (33) was also performed for $\eta = 5 \times 10^{-5}$ in addition to the densities presented in Figs. 5 and 6. However, in this case the statistics were not good enough to resolve a clear minimum in A^2. Also note that there are higher-order corrections[76] to Eq. (33) that are not taken into account in this work.

[1] R. B. Laughlin, Phys. Rev. Lett. **50**, 1395 (1983).
[2] P. Bonderson, V. Gurarie, and C. Nayak, Phys. Rev. B **83**, 075303 (2011).
[3] G. Moore and N. Read, Nucl. Phys. B **360**, 362 (1991).
[4] S.-S. Lee, S. Ryu, C. Nayak, and M. P. A. Fisher, Phys. Rev. Lett. **99**, 236807 (2007).
[5] M. Levin, B. I. Halperin, and B. Rosenow, Phys. Rev. Lett. **99**, 236806 (2007).
[6] P. Bonderson and J. K. Slingerland, Phys. Rev. B **78**, 125323 (2008).
[7] R. Willett, J. P. Eisenstein, H. L. Stormer, D. C. Tsui, A. C. Gossard, and J. H. English, Phys. Rev. Lett. **59**, 1776 (1987).
[8] W. Pan, J.-S. Xia, V. Shvarts, D. E. Adams, H. L. Stormer, D. C. Tsui, L. N. Pfeiffer, K. W. Baldwin, and K. W. West, Phys. Rev. Lett. **83**, 3530 (1999).
[9] J. P. Eisenstein, K. B. Cooper, L. N. Pfeiffer, and K. W. West, Phys. Rev. Lett. **88**, 076801 (2002).
[10] J. S. Xia, W. Pan, C. L. Vicente, E. D. Adams, N. S. Sullivan, H. L. Stormer, D. C. Tsui, L. N. Pfeiffer, K. W. Baldwin, and K. W. West, Phys. Rev. Lett. **93**, 176809 (2004).
[11] N. Read and D. Green, Phys. Rev. B **61**, 10267 (2000).
[12] J. M. Kosterlitz and D. J. Thouless, J. Phys. C **6**, 1181 (1973).
[13] J. M. Kosterlitz, J. Phys. C **7**, 1046 (1974).
[14] J. M. Caillol and D. Levesque, Phys. Rev. B **33**, 499 (1986).
[15] G. Orkoulas and A. Z. Panagiotopoulos, J. Chem. Phys. **104**, 7205 (1996).
[16] E. K. Dahl, E. Babaev, and A. Sudbø, Phys. Rev. B **78**, 144510 (2008).
[17] E. K. Dahl, E. Babaev, and A. Sudbø, Phys. Rev. Lett. **101**, 255301 (2008).
[18] J. Smiseth, E. Smørgrav, E. Babaev, and A. Sudbø, Phys. Rev. B **71**, 214509 (2005).
[19] E. V. Herland, E. Babaev, and A. Sudbø, Phys. Rev. B **82**, 134511 (2010).
[20] E. Babaev, Phys. Rev. B **77**, 054512 (2008).
[21] Without the hard-core repulsion, the system will be unstable at high coupling when one charge from each species together will form a pair with infinite negative energy.[22–24]
[22] R. M. May, Phys. Lett. A **25**, 282 (1967).
[23] G. Knorr, Phys. Lett. A **28**, 166 (1968).
[24] E. H. Hauge and P. C. Hemmer, Phys. Norv. **5**, 209 (1971).
[25] V. L. Berezinskii, Sov. Phys. JETP **32**, 493 (1971).
[26] P. Minnhagen, Rev. Mod. Phys **59**, 1001 (1987).
[27] Y. Saito and H. Müller-Krumbhaar, Phys. Rev. B **23**, 308 (1981).
[28] J.-R. Lee and S. Teitel, Phys. Rev. B **46**, 3247 (1992).
[29] J. Lidmar and M. Wallin, Phys. Rev. B **55**, 522 (1997).
[30] P. Gupta and S. Teitel, Phys. Rev. B **55**, 2756 (1997).
[31] P. Olsson, Phys. Rev. B **46**, 14598 (1992).
[32] P. Olsson, Phys. Rev. B **52**, 4511 (1995).
[33] S. W. de Leeuw and J. W. Perram, Physica A **113**, 546 (1982).
[34] J. M. Caillol, D. Levesque, J. J. Weis, and J. P. Hansen, J. Stat. Phys. **28**, 325 (1982).
[35] Ph. Choquard and J. Clerouin, Phys. Rev. Lett. **50**, 2086 (1983).
[36] M. Franz and S. Teitel, Phys. Rev. Lett. **73**, 480 (1994).
[37] B. I. Halperin and D. R. Nelson, Phys. Rev. Lett. **41**, 121 (1978).
[38] D. R. Nelson and B. I. Halperin, Phys. Rev. B **19**, 2457 (1979).
[39] A. P. Young, Phys. Rev. B **19**, 1855 (1979).
[40] K. Chen, T. Kaplan, and M. Mostoller, Phys. Rev. Lett. **74**, 4019 (1995).
[41] J. Dietel and H. Kleinert, Phys. Rev. B **73**, 024113 (2006).
[42] S. I. Lee and S. J. Lee, Phys. Rev. E **78**, 041504 (2008).
[43] A. Pérez-Garrido and M. A. Moore, Phys. Rev. B **58**, 9677 (1998).
[44] J. A. O'Neill and M. A. Moore, Phys. Rev. B **48**, 374 (1993).
[45] M. J. W. Dodgson and M. A. Moore, Phys. Rev. B **55**, 3816 (1997).
[46] M. A. Moore and A. Pérez-Garrido, Phys. Rev. Lett. **82**, 4078 (1999).
[47] P. A. McClarty and M. A. Moore, Phys. Rev. B **75**, 172507 (2007).
[48] V. S. Dotsenko and V. A. Fateev, Nucl. Phys. B **240**, 312 (1984).
[49] G. Felder, Nucl. Phys. B **317**, 215 (1989).
[50] S. D. Mathur, Nucl. Phys. B **369**, 433 (1992).
[51] R. E. Hetzel, A. Sudbø, and D. A. Huse, Phys. Rev. Lett. **69**, 518 (1992).
[52] S. Ryu and D. Stroud, Phys. Rev. B **57**, 14476 (1998).
[53] P. Olsson and S. Teitel, Phys. Rev. B **67**, 144514 (2003).
[54] S. Kragset, E. Babaev, and A. Sudbø, Phys. Rev. Lett. **97**, 170403 (2006).
[55] E. Fradkin, B. A. Huberman, and S. H. Shenker, Phys. Rev. B **18**, 4789 (1978).
[56] T. Chen and S. Teitel, Phys. Rev. B **55**, 15197 (1997).
[57] A. F. Andreev and E. Bashkin, Sov. Phys. JETP **42**, 164 (1975).

[58] A. B. Kuklov and B. V. Svistunov, Phys. Rev. Lett. **90**, 100401 (2003).
[59] A. Kuklov, N. Prokof'ev, and B. Svistunov, Phys. Rev. Lett. **92**, 050402 (2004).
[60] J. W. Perram and S. W. de Leeuw, Physica A **109**, 237 (1981).
[61] L. Greengard and V. Rokhlin, J. Comput. Phys. **73**, 325 (1987).
[62] A. C. Maggs and V. Rossetto, Phys. Rev. Lett. **88**, 196402 (2002).
[63] J. M. Caillol and D. Levesque, J. Chem. Phys. **94**, 597 (1991).
[64] A. Pérez-Garrido, M. J. W. Dodgson, and M. A. Moore, Phys. Rev. B **56**, 3640 (1997).
[65] P. Minnhagen and B. J. Kim, Phys. Rev. B **67**, 172509 (2003).
[66] K. Børkje, S. Kragset, and A. Sudbø, Phys. Rev. B **71**, 085112 (2005).
[67] N. Metropolis, A. W. Rosenbluth, M. N. Rosenbluth, A. H. Teller, and E. Teller, J. Chem. Phys. **21**, 1087 (1953).
[68] W. K. Hastings, Biometrika **57**, 97 (1970).
[69] M. Matsumoto and T. Nishimura, ACM Trans. Model. Comput. Simul. **8**, 3 (1998).
[70] A. M. Ferrenberg and R. H. Swendsen, Phys. Rev. Lett. **61**, 2635 (1988).
[71] A. M. Ferrenberg and R. H. Swendsen, Phys. Rev. Lett. **63**, 1195 (1989).
[72] H. Weber and P. Minnhagen, Phys. Rev. B **37**, 5986 (1988).
[73] P. Minnhagen and H. Weber, Physica B **152**, 50 (1988).
[74] L. Bonnes and S. Wessel, Phys. Rev. Lett. **106**, 185302 (2011).
[75] H. Kuroyanagi, M. Tsukamoto, and M. Tsubota, J. Low Temp. Phys. **162**, 609 (2011).
[76] P. Olsson and P. Minnhagen, Phys. Scr. **43**, 203 (1991).

Article III

Freezing of unconventional two-dimensional plasmas

Preprint

Freezing of unconventional two-dimensional plasmas

Egil V. Herland,[1] Egor Babaev,[2,3] Parsa Bonderson,[4] Victor Gurarie,[5] Chetan Nayak,[4,6] Leo Radzihovsky,[5] and Asle Sudbø[1]

[1] *Department of Physics, Norwegian University of Science and Technology, N-7491 Trondheim, Norway*
[2] *Physics Department, University of Massachusetts, Amherst, Massachusetts 01003, USA*
[3] *Department of Theoretical Physics, The Royal Institute of Technology, 10691 Stockholm, Sweden*
[4] *Station Q, Microsoft Research, Santa Barbara, California 93106-6105, USA*
[5] *Department of Physics, CB 390, University of Colorado, Boulder, Colorado 80309, USA*
[6] *Department of Physics, University of California, Santa Barbara, California 93106, USA*

We study unconventional two-dimensional, two-component classical plasmas on a sphere, with emphasis on detecting signatures of melting transitions. These plasmas, which are relevant to Ising-type quantum Hall states, interact via two different two-dimensional Coulomb interactions. One species of particles in the plasma carries charge of both types (Q_1, Q_2), while the other species carries only charge of the second type $(0, -Q_2)$. We find signatures of a freezing transition at $Q_1^2 \simeq 140$. Here, freezing means that the species with charge of both types will form a Wigner crystal, whereas the species with charge of the second type also shows signatures of being a Wigner crystal, due to the attractive inter-component interaction of the second type. Moreover, there is also a Berezinskii-Kosterlitz-Thouless phase transition at $Q_2^2 \simeq 4$, at which the two species of particles bind to form molecules that are neutral with respect to the second Coulomb interaction. These two transitions appear to be independent of each other, giving a rectangular phase diagram. As a special case, this sheds new light on the freezing transition of two-dimensional one-component plasmas (for which $Q_2 = 0$).

PACS numbers: 73.43.Cd, 74.20.De, 74.25.Uv

I. INTRODUCTION

Multi-component quantum condensates with novel types of inter-component interactions are of considerable interest in contemporary physics. For example, they are relevant to widely disparate systems, including low-dimensional spin-1/2 quantum antiferromagnets[1–3], Bose-Einstein condensates[4–6], multi-component/multi-band superconductors[7–9], and non-Abelian quantum Hall states and topological superconductors[10]. These systems have the remarkable property of possessing a mapping to a classical multi-component plasma system with highly unusual intra- and inter-component interactions. The statistical properties of these associated unconventional plasmas – especially their phase diagrams – have important ramifications for the physics of their corresponding systems[10]. The statistical physics of such systems has only recently begun to be explored. In a previous paper, we investigated the metal-insulator transition in a particular version of such a plasma[11]. In this paper, we will extend these investigations to characterize the melting transition of such a plasma from a Wigner crystal to a liquid.

The canonical partition function of the unconventional two-component plasma that we investigate is given by[10,11]

$$Z = \int \left(\prod_{i=1}^{N} \mathrm{d}^2 z_i \right) \left(\prod_{a=1}^{N} \mathrm{d}^2 w_a \right) \mathrm{e}^{-V}, \qquad (1)$$

where the potential energy

$$\begin{aligned} V = & -Q_2^2 \sum_{a<b=1}^{N} \ln|\mathbf{w}_a - \mathbf{w}_b| + Q_2^2 \sum_{a,i=1}^{N} \ln|\mathbf{z}_i - \mathbf{w}_a| \\ & - (Q_1^2 + Q_2^2) \sum_{i<j=1}^{N} \ln|\mathbf{z}_i - \mathbf{z}_j| + V_{z,\mathrm{BG}} \end{aligned} \qquad (2)$$

describes two species (components) of particles interacting via two different types of two-dimensional (2D) Coulomb interactions, which are logarithmic. Here, the $\mathbf{z}_i$ are coordinate vectors for the N particles of component z, which carry charge Q_1 of the first interaction (type 1) and charge Q_2 of the second interaction (type 2). The $\mathbf{w}_a$ are coordinate vectors for the N particles of component w, which carry no charge of type 1 and charge $-Q_2$ of type 2. The term $V_{z,\mathrm{BG}}$ describes the interaction of the z-particles with a uniform density neutralizing background charge.

This plasma is related[10] to inner products of quantum-mechanical trial wave functions of Ising-type quantum Hall states, such as the Moore-Read Pfaffian[12], anti-Pfaffian[13,14], and Bonderson-Slingerland hierarchy states[15]. For the charge values relevant to these states, the plasma was shown to be in its metallic liquid phase[11], which allows for the calculation of the braiding statistics of quasiparticle excitations of these states[10], confirming their conjectured non-Abelian statistics. This plasma is also related to rotating two-component Bose-Einstein condensates (BECs) in two dimensions[11].

While Ref. 11 focused on the cases $Q_1 = 0, 2$, which are particularly relevant for Ising-type quantum Hall states,

here we will investigate the plasma for large values of Q_1. In the limit in which $Q_2 = 0$, the w-particles do not interact, and the plasma thus reduces to the standard 2D one-component Coulomb plasma (OCP). It is generally believed that, at high values of Q_1, the OCP will be in a 2D solid state in which the charges form a triangular lattice with quasi-long-range translational and long-range orientational order, as found in the simulations in Refs. 16–19. [However, we note that some published studies have claimed that there is no low-temperature (high-Q_1) crystalline state in the OCP, due to the proliferation of screened disclinations[21–24].]

If we assume that the generally-held view is correct (and we present evidence in this paper that it is), so that there is a low-temperature crystalline state, then the melting of this crystal can occur according to either of two possible scenarios. One possibility is the Kosterlitz-Thouless-Halperin-Nelson-Young theory (KTHNY)[25–28], according to which dislocation pairs unbind at a Berezinskii-Kosterlitz-Thouless (BKT) like transition. The system then enters a hexatic phase in which there is no translational order, but there is quasi-long-range orientational order. Then, there is a second BKT transition at which disclination pairs unbind, orientational order is lost, and the system enters an isotropic liquid phase. The other possibility is a first-order melting transition at a lower temperature than the KTHNY-theory predicts[26]. There have been considerable efforts to investigate 2D melting, both experimentally and by numerical simulations. Some studies have found KTHNY transitions while others have found a weakly first-order melting transition[29–36]. It appears that the nature of 2D melting depends on details of the interatomic potential. In the case of logarithmic interactions, most numerical simulations find a first-order transition[16–19].

Before proceeding to a description of our simulations, we must mention that, in principle, there is one other possibility: a Lifshitz transition from the liquid to a striped or "microemulsion" phase and then later to a Wigner crystal, as discussed by Kivelson and Spivak[20]. Such a scenario must be considered when there is a linear coupling between the order parameter and the uniform density (i.e., between the order parameter at wavevector $\mathbf{q}$ and the density at wavevector $-\mathbf{q}$) or, equivalently, when the first derivative of the energy with respect to the density is discontinuous at the transition. However, in our case, the order parameter is the density at nonzero wavevector, so no such linear coupling can occur. Furthermore, the order parameter vanishes on both sides of the transition since the crystalline phase is only quasi-long-range ordered, so there would be no discontinuity even if there were a linear coupling. However, even in systems to which the Kivelson-Spivak[20] argument applies, there are two scenarios, similar to the ones that we consider: a direct first-order phase transition (which is permitted for the case of logarithmic interactions) and a continuous transition via one or more intermediate phases.

II. MODEL AND SIMULATION

The system described in Eqs. (1) and (2) is studied by the means of large-scale Monte Carlo simulations on a sphere of radius R. In this geometry, the distance between two points $\mathbf{r}_1$ and $\mathbf{r}_2$ is taken to be the chord length

$$|\mathbf{r}_1 - \mathbf{r}_2| = \sqrt{2}R\,(1 - \hat{\mathbf{r}}_1 \cdot \hat{\mathbf{r}}_2)^{\frac{1}{2}}, \tag{3}$$

and the term $V_{z,\mathrm{BG}}$ is simply a uniform constant that can be disregarded. Hence, the model in Eq. (2) may be written in the form (up to constant terms)[11,17,37,38]

$$V = \frac{1}{2}\Bigg[Q_2^2 \sum_{a,i=1}^{N} \ln(1 - \hat{\mathbf{z}}_i \cdot \hat{\mathbf{w}}_a) - Q_2^2 \sum_{a<b=1}^{N} \ln(1 - \hat{\mathbf{w}}_a \cdot \hat{\mathbf{w}}_b) - (Q_1^2 + Q_2^2) \sum_{i<j=1}^{N} \ln(1 - \hat{\mathbf{z}}_i \cdot \hat{\mathbf{z}}_j)\Bigg]. \tag{4}$$

Here, $\hat{\mathbf{w}}_a$, $\hat{\mathbf{z}}_i$ are the positions of the particles on the surface of the unit sphere. Details of the derivation, as well as on the technicalities of the Monte Carlo simulations, are presented in Ref. 11. Moreover, to improve sampling at high values of Q_1, we used the parallel tempering algorithm[39,40], where the set of couplings was found by measuring first-passage-times as described in Ref. 41.

In addition to the logarithmic interactions, we regularize the attractive interactions by adding a short-range hard-core repulsion such that particles are not permitted to be closer than particle diameter d. Hence, there is a nonzero dimensionless density $\eta = 2Ns/A$ where $s = \pi d^2/4$ and A is the area of the system.

III. RESULTS FOR THE ONE-COMPONENT PLASMA

Initially, we investigate the unconventional plasma in the OCP limit, where $Q_2 = 0$. This is motivated by the fact that previous studies of OCP on the surface of a sphere are not consistent. In Ref. 17, a freezing transition at $Q_1^2 \simeq 140$ was found by comparing the free energy of the solid and liquid state. However, in Ref. 23, the absence of a finite-temperature crystalline state was claimed and numerical evidence supporting this was provided, essentially by showing that the correlation length for crystalline order was non-divergent, $\xi \propto Q_1$ for all $Q_1^{-1} > 0$.

We measure the azimuthally averaged structure factor modified for a spherical geometry, by[17,23,42]

$$S(q) = 1 + 2\pi n R^2 \int_0^{\pi} \mathrm{d}\theta\,[g(R\theta) - 1] \sin\theta J_0(qR\theta), \tag{5}$$

where n is the number density, R is the radius of the sphere on which the particles live, $g(R\theta)$ is the pair distribution function with θ as the chord angle, $J_0(x)$ is a zeroth order Bessel function, and q is the magnitude of

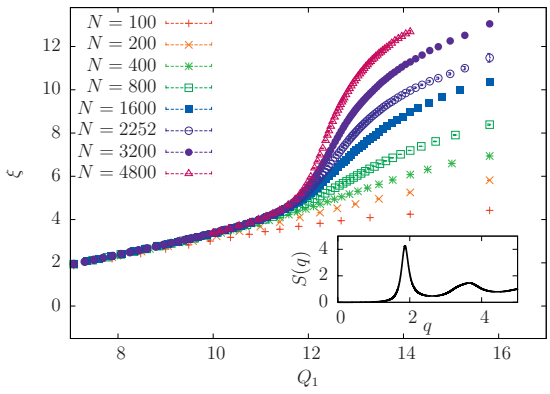

Figure 1: (Color online) Correlation length ξ as a function of Q_1 for 8 different system sizes in the range $100 \leq N \leq 4800$. The inset is a plot of $S(q)$ for the specific case when $N = 3200$ and $Q_1 = \sqrt{120}$.

the Fourier space vector $\mathbf{q}$. The inset of Fig. 1 shows a plot of $S(q)$. We assume that the correlation length ξ is inversely proportional to the width of the first peak in $S(q)$, and may thus be determined by a Lorentzian fit. The procedure is identical to that used in Ref. 23, and the result is given in Fig. 1. For small values of Q_1 our results are similar to Fig. 2 in Ref. 23. However, when $Q_1 \approx 12$, a value that corresponds well with the critical coupling of the freezing transition, we find a kink developing with increasing N, that clearly violates $\xi \propto Q_1$. This kink is not seen in Fig. 2 of Ref. 23. However, we note that the markers of that figure exhibits large scattering and that the authors did not consider larger values of Q_1.

A hallmark of a 2D solid is that translational correlations have a power-law decay, $\langle e^{i\mathbf{G}(\mathbf{r}-\mathbf{r}')}\rangle \sim |\mathbf{r}-\mathbf{r}'|^{-\eta_\mathbf{G}}$, where $\mathbf{G}$ is the reciprocal lattice vector, $\mathbf{r}$, $\mathbf{r}'$ are lattice points in the 2D solid and $\eta_\mathbf{G}$ is a temperature dependent exponent[27,43]. Now, by integrating over the Bragg peak of a 2D solid[44], the finite-size scaling of the first peak in $S(q)$ is given by

$$S(G) \sim L^{1-\eta_\mathbf{G}} \sim N^{(1-\eta_\mathbf{G})/2}. \quad (6)$$

Here, $L \propto N^{1/2}$ is the spatial linear extent of the system. Fig. 2 shows the results for the maximum value of the first peak in $S(q)$ for a wide range of system sizes and for different values of Q_1^2. As for ξ, we find that the peak value also exhibits a kink at $Q_1^2 \approx 140$ that should be associated with an abrupt change in the translational correlations in the plasma. Indeed, when studying the finite-size behavior more closely in the lower panel of Fig. 2, the results show that when $Q_1^2 \leq 130$, $S(G) \sim$ const. when N increases. This is the behavior expected in the liquid phase, with exponentially decaying translational correlations where $S(G) \sim \xi^2$. However, when $Q_1^2 \geq 150$, the results clearly show that there is a positive slope that

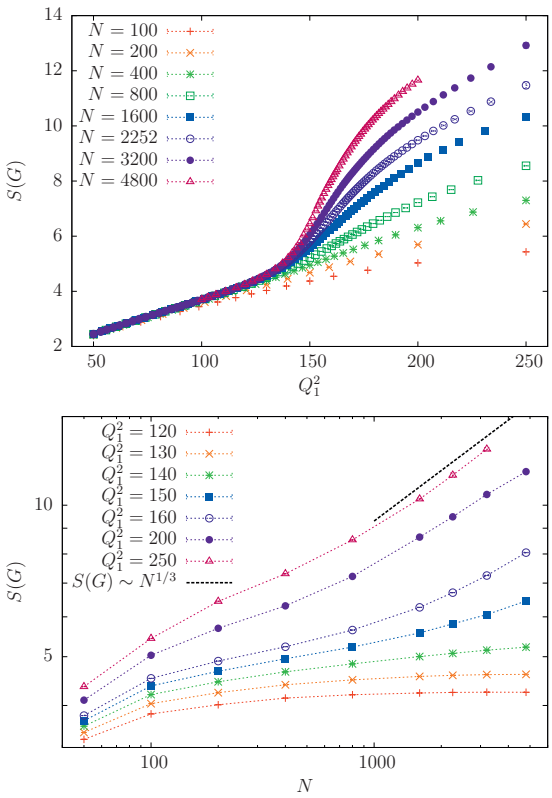

Figure 2: (Color online) Finite-size behavior of the peak value of the structure factor, $S(G)$, as a function of coupling Q_1^2 and size N. The upper panel shows $S(G)$ as a function of Q_1^2 for eight different sizes in the range $100 \leq N \leq 4800$. The lower panel is a log-log plot of $S(G)$ as a function of N for seven fixed values of Q_1^2. The dashed line is a reference line that yields the expected finite-size behavior at the melting point according to KTHNY theory. Lines are guide to the eyes.

develops with increasing N, thus confirming the finite-size behavior of the 2D solid given in Eq. (6). When $Q_1^2 = 140$, it is hard to determine whether the system is in the solid phase or not, suggesting that $Q_1^2 = 140$ is close to the melting point of the OCP. In Fig. 2, note that at this point the height of the first-order peak in $S(q)$, $S(G) \approx 5$, is consistent with the 2D freezing criterion[17,45].

A key prediction of the KTHNY theory is that $\eta_\mathbf{G} \leq 1/3$ in the solid phase, where the limiting value of $1/3$ is reached at the critical point of melting from a triangular lattice to the hexatic phase[19,27]. As a result, in this scenario, $S(G)$ grows more rapidly with N than $N^{1/3}$ for all Q_1^2 greater than the critical value; $S(G)$ grows as $N^{1/3}$ at the transition point; and $S(G)$ saturates in the liquid phase. Meanwhile, if the transition were first-order, the limiting value of $\eta_\mathbf{G}$ would be smaller than

1/3, so that $S(G)$ would grow more rapidly than $N^{1/3}$ at the transition point, i.e., the slowest possible growth of $S(G)$ in the crystalline phase would be faster than $N^{1/3}$. Consequently, we expect the slope of $\ln S(G)$ vs. $\ln N$ to be steeper than 1/3 for all Q_1^2 in the crystalline phase or, by the results above, for all $Q_1^2 > 140$. By determining the slope of $\ln S(G)$ vs. $\ln N$ at $Q_1^2 \approx 140$, we could then determine if the transition is of KTHNY type or is first-order. However, as may be seen in Fig. 2, the slopes of $\ln S(G)$ vs. $\ln N$ in the putative crystalline phase are *not* steeper than 1/3 in our simulations. However, the slopes steepen with increasing N, possibly converging towards the expected behavior in the thermodynamic limit. Therefore, we are unable to determine which type of transition occurs.

However, it is worth emphasizing that, for $Q_1^2 < 140$, $S(G)$ appears to saturate to a finite value, as expected in a liquid, while, for $Q_1^2 > 140$, $S(G)$ does not appear to saturate, as expected in a crystal (although, as noted above, it does not grow as rapidly as expected). Therefore, the lower panel of Fig. 2 is also qualitatively consistent with a crystalline phase of the 2D OCP, which melts at $Q_1^2 \approx 140$. Taken together with Fig. 1 and the upper panel of Fig. 2, this provides clear evidence in support of to earlier studies[16–19]. Consequently, our results contradict the claims made in Ref. 23 for the non-existence of a crystalline phase. The discrepancy may be explained by noting that the authors of Ref. 23 did not consider large enough values of Q_1 and suffer from poor statistics.

IV. RESULTS FOR AN UNCONVENTIONAL TWO-COMPONENT PLASMA

We now turn our attention to the full model in Eq. (2), i.e., when both Q_1 and Q_2 are nonzero. In particular, we would like to investigate how the translational ordering of both w and z particles is affected as we increase the coupling constant in the second interaction-channel, Q_2. As for the OCP, we study translational correlations by measuring the structure factors $S_w(q)$, $S_z(q)$ defined by Eq. (5) with $S(q)$, $g(R\theta) \to S_{w/z}(q)$, $g_{w/z}(R\theta)$. In addition, we also measure the inverse dielectric constant for charges with interaction of type 2, given by

$$\epsilon_{22}^{-1} = 1 - \frac{\pi Q_2^2 R^2}{A} \left\langle \left(\sum_{i=1}^{N} \hat{\mathbf{z}}_i - \sum_{a=1}^{N} \hat{\mathbf{w}}_a \right)^2 \right\rangle . \qquad (7)$$

This quantity measures the screening properties for charges interacting with Q_2, and it signals the charge-unbinding transition when z particles and w particles unbind[11].

In Fig. 3, results are given for the height of the first-order peak in the structure factor for component z and w, for the case when $Q_2^2 = 1$. Apart from the fact that the height of the peak in the structure factor is much larger for the z particles than the w-particles, the size- and Q_1^2-dependence of the peaks are qualitatively very

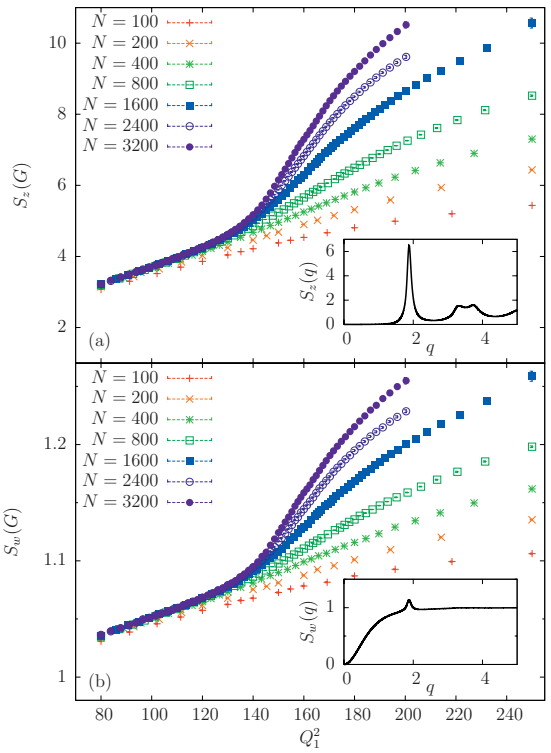

Figure 3: (Color online) Results from the Monte Carlo simulations when $Q_2^2 = 1$ and $\eta = 10^{-3}$. Panel (a) shows the height of the first-order peak in the structure factor for the z particles, $S_z(G)$, as a function of the coupling Q_1^2 for seven different sizes in the range $100 \leq N \leq 3200$. Panel (b) shows the height of the first-order peak in the structure factor for the w particles, $S_w(G)$, as a function of the coupling Q_1^2 for seven different sizes in the range $100 \leq N \leq 3200$. In order to give an impression on how a typical structure factor looks like, the insets of panel (a) and (b) show plots of $S_z(q)$ and $S_w(q)$ for the specific case when $N = 800$, $Q_1^2 = 180$ and $Q_2^2 = 1$.

similar for the two components. In particular, they both exhibit a kink at $Q_1^2 \approx 140$, which should be associated with melting of a 2D solid, similar to the OCP case in the upper panel of Fig. 2. Specifically, when we extract the finite-size behavior in the log-log plots in Fig. 4, we find that both components exhibit $S(G) \sim$ const., consistent with being in the liquid phase, when $Q_1^2 \leq 130$. When $Q_1^2 \geq 150$, the results clearly show that there is a power-law dependence on N, consistent with the finite-size behavior of a 2D solid. These results are consistent with the phase diagram in Fig. 5.

The inverse dielectric constant ϵ_{22}^{-1} is measured to be zero to the left of the red line in Fig. 5. Thus, the w and z particles are in a metallic state regardless of the change in the structural properties when $Q_1^2 \approx 140$. This is

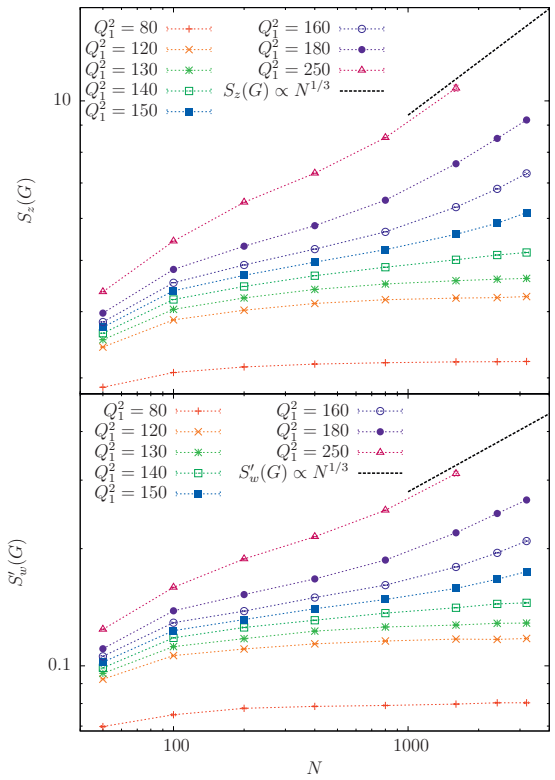

Figure 4: (Color online) Log-log plots of the results in panel (a) and (b) in Fig. 3. Both panels show the height of the first-order peak in the structure factor as a function of size N. In the lower panel, $S'_w(G)$ is the height of the peak of $S_w(G)$ when we have subtracted the regular part in order to properly extract the singular finite-size behavior of $S_w(q)$ in a log-log plot. The solid lines are reference lines that yield the expected finite-size behavior at the melting point according to KTHNY theory. Lines are guide to the eyes.

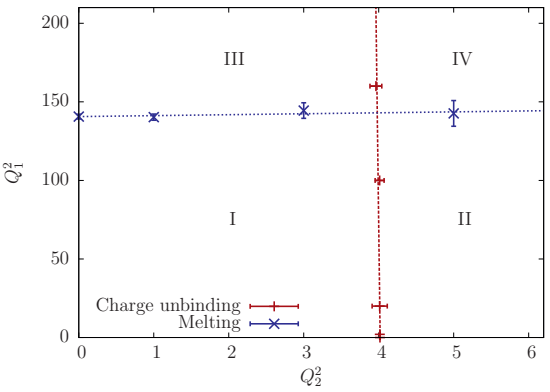

Figure 5: (Color online) The phase diagram as a function of Q_1^2 and Q_2^2. The dashed red line is the charge unbinding transition, at which z and w particles become bound together for at Q_2^2 above this line. The dotted blue line is the melting line of the Wigner crystal. In Phases I and II, the z particles are in a liquid state; in Phases III and IV, the z particles form a Wigner crystal. In Phases I and III, the w and z particles are unbound; in Phases II and IV, they are bound into molecules comprised of one z and one w particle. See the text for details.

most salient with respect to the second type of Coulomb interaction (which has an effective strength that is determined by ϵ_{22}^{-1}). In the liquid phase, it is clear that w and z particles are in a metallic state. In the crystalline phase, there are interstitials and vacancies in the crystal, so that a finite fraction of w and z particles should be considered as unbound particles that are able to screen test particles interacting with charges of type 2, thereby leading to $\epsilon_{22}^{-1} = 0$. At larger values of Q_2^2, there is a transition at which w and z particles are bound into molecules. For Q_2^2 above this transition point, which is at $Q_{2,c}^2 \approx 4$, ϵ_{22}^{-1} has a non-zero value, as found in Ref. 11. Although the w particles are able to screen the type 2 interaction when z particles form a Wigner crystal, their translational correlations exhibit signatures of a 2D solid (as seen in Fig 3), attributed to a higher probability of the w particles to be co-centered with z particles due to the attractive inter-component interactions of type 2. On average, a finite fraction of the w particles should be considered as bound to the z particles, thus adapting to the 2D crystalline structure that is created by the strong repulsive interactions among the z particles, when $Q_1^2 > 140$. The signatures of freezing of the w-particles is thus an effect which is induced by the freezing of the z-particles.

Hence, we can summarize the situation as follows, as depicted in Fig. 5. In Phase I, the w and z particles are unbound and are separately liquid. In Phase II, the w and z particles are bound into molecules that are neutral with respect to the second type of Coulomb interaction, and these molecules form a liquid. In Phase III, the w and z particles are unbound; the z particles form a Wigner crystal while the w particles form a liquid, albeit one with modulated density due to its interaction with the Wigner crystal. In Phase IV, the w and z particles are bound into molecules. and the molecules form a Wigner crystalIn Appendix A, we explain the details of how the transition lines were obtained.

We consider phase III to be a 2D counterpart of the situation that was reported for a three-dimensional system in Ref. 6. In that work, the authors considered a two-component rotating BEC with a negative dissipationless Andreev-Bashkin drag[46]. They found that in this mixture, a situation may arise where the component with the smallest stiffness will be a *modulated vortex liquid*. That is, the soft component breaks translational symmetry while exhibiting an unbroken symmetry in order parameter space. The vortices of the soft component are

likely to be co-centered with the vortices of the stiffest component, and will thus adopt the spatial structure of the latter. As shown in Ref. 11, the MR plasma corresponds to a 2D two-component rotating BEC with negative drag, where the z component is stiffer than the w component when $Q_1^2 > 0$.

V. SUMMARY AND CONCLUSIONS

In summary, we have considered the melting of an unconventional 2D two-component plasma on a sphere with particles interacting in two different channels, which may be viewed as an analogous plasma describing a non-Abelian Ising-type quantum Hall state or a realization of a two-component two-dimensional Bose-Einstein condensate with inter-component non-dissipative drag. In the limiting case where there are no interactions of type 2 ($Q_2 = 0$), the system reverts back to a standard 2D one-component plasma. Both for the one-component plasma and the unconventional two-component plasma, we find that the system freezes on a sphere for large enough interparticle interactions. For the two-component plasma, the w component, which do not have strong intra-component interactions, still shows signatures of being a 2D solid. This is attributed to the attractive inter-component interactions with the particles of the z component that leads to a higher probability of the w particles to be co-centered with z particles. We do not draw firm conclusions on the nature of the melting transition. This is because the results for the translational correlations are not accurate enough to distinguish between a first-order transition and the KTHNY scenario. It is also difficult to examine the possible existence of a hexatic phase as it is hard to measure the quasi-long-range orientational order on the surface of a sphere.

Acknowledgments

We acknowledge useful discussions with J. S. Høye, and I. B. Sperstad. E. B., P. B., C. N. and A. S. thank the Aspen Center for Physics for hospitality and support under the NSF Grant No. 1066293. E. V. H. thanks NTNU for financial support. E. B. was supported by Knut and Alice Wallenberg Foundation through the Royal Swedish Academy of Sciences Fellowship, Swedish Research Council and by the National Science Foundation CAREER Award No. DMR-0955902. V. G. was supported by NSF Grant No. PHY-0904017. C. N. was supported in part by the DARPA QuEST program. A. S. was supported by the Norwegian Research Council under Grant No. 205591/V30 (FRINAT). The work was also supported through the Norwegian consortium for high-performance computing (NOTUR).

Appendix A: Determination of the transition lines

We now discuss the determination of the phase transition lines in Fig. 5 in more detail.

First, consider the line (red in Fig. 5) at which the z and w particles unbind. In this work, we find the critical point of the BKT transition by curve-fitting the inverse dielectric constant to a logarithmic finite-size scaling relation with one free parameter (see Appendix C in Ref. 11). This means that we assume that the transition is a BKT transition as we use the BKT value of the universal jump in the finite-size scaling relation. Thus, it is a slightly less self-consistent approach than what was used in Ref. 11, but still, one can regard this as a verification of the BKT nature, as one should not expect a good fit to the scaling relation if the transition is of a different nature.[47]

The curve-fitting was performed according to the description in Appendix C in Ref. 11 for sizes $N = 70$, 100, 150, 200, 300, and 500, for $Q_1^2 = 20$, 100, and 160 and for densities $\eta = 0.001$, 0.0004, and 0.0001. In Fig. 6, the results for the transition point $Q_{2,\mathrm{c}}^2$ as a function of η and Q_1^2 are given. We have also included the results for $Q_2^2 = 0$ and 2 from Ref. 11. In order to obtain a crude estimate of the transition temperature in the low density limit, we extrapolate to $\eta = 0$ by fitting the results for finite η to a power law $[Q_{2,\mathrm{c}}^2(\eta) = Q_{2,\mathrm{c}}^2 + a\eta^b$, where $Q_{2,\mathrm{c}}^2$, a, and b are free parameters]. The estimates we find are:

$$\begin{array}{lll} Q_{2,\mathrm{c}}^2 = 4.016 \pm 0.002 & \text{for} & Q_1^2 = 0 \\ Q_{2,\mathrm{c}}^2 = 4.015 \pm 0.004 & \text{for} & Q_1^2 = 2 \\ Q_{2,\mathrm{c}}^2 = 4.013 \pm 0.101 & \text{for} & Q_1^2 = 20 \\ Q_{2,\mathrm{c}}^2 = 4.012 \pm 0.060 & \text{for} & Q_1^2 = 100 \\ Q_{2,\mathrm{c}}^2 = 3.963 \pm 0.070 & \text{for} & Q_1^2 = 160 \end{array} \tag{A1}$$

These values are plotted in the phase diagram in Fig. 5, and we take the phase boundary to be the best fit straight line running through them.

We now consider the Wigner crystal melting transition, depicted by the blue line in Fig. 5. This transition is found by measuring the value of Q_1^2 at which $S_z(G)$ attains its maximum second-derivative. (See Fig. 2 and Fig. 3 in the paper for example.) In Fig. 7, we show the estimates of the transition point $Q_{1,\mathrm{c}}^2$ as a function of inverse system size N^{-1} for $Q_2^2 = 0$, 1, 3, and 5. The transition points are estimated by averaging the results for $N \geq 800$, with errors determined by a bootstrap analysis. The estimates we find are:

$$\begin{array}{lll} Q_{1,\mathrm{c}}^2 = 140.6 \pm 1.5 & \text{for} & Q_2^2 = 0 \\ Q_{1,\mathrm{c}}^2 = 140.3 \pm 2.0 & \text{for} & Q_2^2 = 1 \\ Q_{1,\mathrm{c}}^2 = 144.4 \pm 4.9 & \text{for} & Q_2^2 = 3 \\ Q_{1,\mathrm{c}}^2 = 142.6 \pm 8.2 & \text{for} & Q_2^2 = 5 \end{array} \tag{A2}$$

The phase diagram in Fig. 5 is obtained by using these values, and we take the phase boundary to be the best fit straight line running through them.

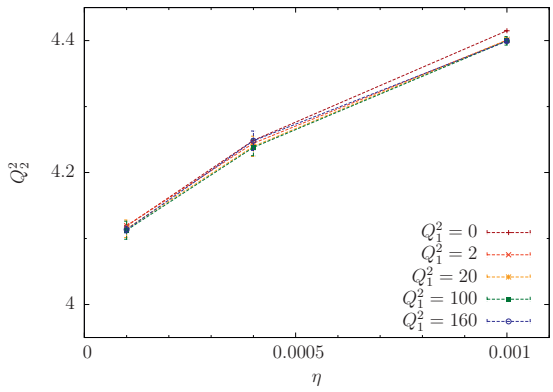

Figure 6: (Color online) The transition point is determined for $\eta \to 0$ by extrapolating the $Q^2_{2,c}$ values obtained for non-zero η, assuming a power-law dependence. Lines are guide to the eyes.

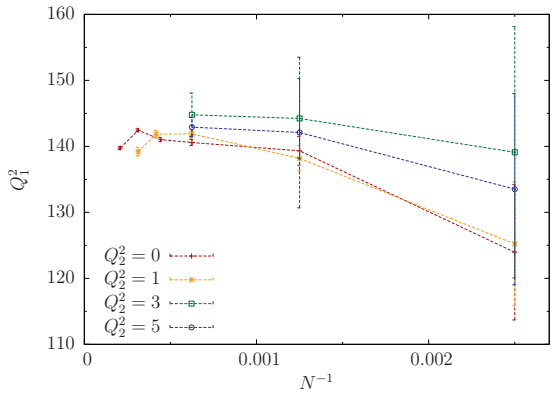

Figure 7: (Color online) The transition point $Q^2_{1,c}$ as a function of system size for $Q_2^2 = 0$, 1, 3, and 5, estimated by the maximum of the second derivative of $S_z(G)$. See text for details. Lines are guide to the eyes.

[1] S. Sachdev and R. Jalabert, Mod. Phys. Lett. B **4**, 1043 (1990).

[2] T. Senthil, A. Vishwanath, L. Balents, S. Sachdev, and M. P. A. Fisher, Science, **303**, 1490 (2004), cond-mat/0311326.

[3] T. Senthil, L. Balents, S. Sachdev, A. Vishwanath, and M. P. A. Fisher, Phys. Rev. B **70**, 144407 (2004), cond-mat/0312617.

[4] E. K. Dahl, E. Babaev, S. Kragset, and A. Sudbø, Phys. Rev. B **77**, 2008), arXiv:0802.2548.

[5] E. K. Dahl, E. Babaev, and A. Sudbø, Phys. Rev. B **78**, 144510 (2008), arXiv:0807.0233.

[6] E. K. Dahl, E. Babaev, and A. Sudbø, Phys. Rev. Lett. **101**, 255301 (2008), arXiv:0810.3833.

[7] E. Babaev, A. Sudbø, and N. W. Ashcroft, Nature, **431**, 666 (2004), cond-mat/0410408.

[8] E. Babaev and N. W. Ashcroft, Nature Physics, **31**, 530 (2007), arXiv:0706.2411.

[9] J. Smiseth, E. Smørgrav, E. Babaev, and A. Sudbø, Phys. Rev. B **71**, 214509 (2005), cond-mat/0411761.

[10] P. Bonderson, V. Gurarie, and C. Nayak, Phys. Rev. B **83**, 075303 (2011), arXiv:1008.5194.

[11] E. V. Herland, E. Babaev, P. Bonderson, V. Gurarie, C. Nayak, and A. Sudbø, Phys. Rev. B **85**, 024520 (2012), arXiv:1111.0135.

[12] G. Moore and N. Read, Nucl. Phys. B **360**, 362 (1991).

[13] S.-S. Lee, S. Ryu, C. Nayak, and M. P. A. Fisher, Phys. Rev. Lett. **99**, 236807 (2007), arXiv:0707.0478.

[14] M. Levin, B. I. Halperin, and B. Rosenow, Phys. Rev. Lett. **99**, 236806 (2007), arXiv:0707.0483.
[15] P. Bonderson and J. K. Slingerland, Phys. Rev. B **78**, 125323 (2008), arXiv:0711.3204.
[16] S. W. de Leeuw and J. W. Perram, Physica A **113**, 546 (1982).
[17] J. M. Caillol, D. Levesque, J. J. Weis, and J. P. Hansen, J. Stat. Phys. **28**, 325 (1982).
[18] Ph. Choquard and J. Clerouin, Phys. Rev. Lett. **50**, 2086 (1983).
[19] M. Franz and S. Teitel, Phys. Rev. Lett. **73**, 480 (1994), cond-mat/9403071.
[20] B. Spivak and S. Kivelson, Ann. Phys. **321**, 2071 (2006).
[21] J. O'Neill and M. A. Moore, Phys. Rev. B **48**, 374 (1993).
[22] M. J. W. Dodgson and M. A. Moore, Phys. Rev. B **55**, 3816 (1997), cond-mat/9512123.
[23] M. A. Moore and A. Pérez-Garrido, Phys. Rev. Lett. **82**, 4078 (1999), cond-mat/9812039.
[24] P. A. McClarty and M. A. Moore, Phys. Rev. B **75**, 172507 (2007), cond-mat/0702282.
[25] J. M. Kosterlitz and D. J. Thouless, J. Phys. C **6**, 1181 (1973).
[26] B. I. Halperin and D. R. Nelson, Phys. Rev. Lett. **41**, 121 (1978).
[27] D. R. Nelson and B. I. Halperin, Phys. Rev. B **19**, 2457 (1979).
[28] A. P. Young, Phys. Rev. B **19**, 1855 (1979).
[29] K. J. Strandburg, Rev. Mod. Phys. **60**, 161 (1988).
[30] K. Chen, T. Kaplan, and M. Mostoller, Phys. Rev. Lett. **74**, 4019 (1995).
[31] J. G. Dash, Rev. Mod. Phys. **71**, 1737 (1999).
[32] K. Zahn, R. Lenke, and G. Maret, Phys. Rev. Lett. **82**, 2721 (1999).
[33] M. A. Bates and D. Frenkel, Phys. Rev. E **61**, 5223 (2000).
[34] J. Dietel and H. Kleinert, Phys. Rev. B **73**, 024113 (2006), cond-mat/0508780.
[35] S. I. Lee and S. J. Lee, Phys. Rev. E **78**, 041504 (2008).
[36] I. Guillamón, H. Suderow, A. Fernández-Pacheco, J. Sesé, R. Córdoba, J. M. De Teresa, M. R. Ibarra, and S. Vieira, Nat. Phys. **5**, 651 (2009), arXiv:0908.2124.
[37] J. M. Caillol and D. Levesque, Phys. Rev. B **33**, 499 (1986).
[38] J. M. Caillol and D. Levesque, J. Chem. Phys. **94**, 597 (1991).
[39] K. Hukushima and K. Nemoto, J. Phys. Soc. Jpn. **65**, 1604 (1996), pcond-mat/9512035.
[40] D. J. Earl and M. W. Deem, Phys. Chem. Chem. Phys. **7**, 3910 (2005).
[41] W. Nadler, J. H. Meinke, and U. H. E. Hansmann, Phys. Rev. E **78**, 061905 (2008).
[42] J. P. Hansen, D. Levesque, and J. J. Weis, Phys. Rev. Lett. **43**, 979 (1979).
[43] Imry, Y. and Gunther, L., Phys. Rev. B **3**, 3939 (1971).
[44] Dutta, P. and Sinha, S. K., Phys. Rev. Lett. **47**, 50 (1981).
[45] Z. Wang, W. Qi, Y. Peng, A. M. Alsayed, Y. Chen, P. Tong, and Y. Han, J. Chem. Phys. **134**, 034506 (2011).
[46] A. F. Andreev and E. Bashkin, Sov. Phys. JETP **42**, 164 (1975).
[47] Using two free parameters, as we did in Ref. 11, is highly demanding in terms of statistical quality. A one-parameter fit requires much less statistics.

Article IV

Monte Carlo simulations of the CP^1 two-component superconductor

Preprint

Monte Carlo simulations of the CP^1 two-component superconductor

Egil V. Herland,[1] Troels A. Bojesen,[1] Egor Babaev,[2,3] and Asle Sudbø[1]

[1] *Department of Physics, Norwegian University of Science and Technology, N-7491 Trondheim, Norway*
[2] *Physics Department, University of Massachusetts, Amherst, Massachusetts 01003, USA*
[3] *Department of Theoretical Physics, The Royal Institute of Technology, 10691 Stockholm, Sweden*

We study the SU(2) symmetric noncompact CP^1 model, with two charged matter fields coupled minimally to a noncompact Abelian gauge field. This model is proposed to exhibit an unusual continuous transition line within the so-called deconfined quantum critical point theory. Earlier Monte Carlo studies of this model have found a weak first-order transition directly between a fully ordered state where the SU(2) is broken, to a fully disordered one. According to earlier studies, the transition line becomes increasingly stronger first-order as a function of coupling up to a bicritical point where the direct transition line splits into two separate transition lines. The intermediate phase is a partially ordered phase in which a global O(3) symmetry is broken, but where the Higgs mass (which is non-zero in the fully ordered state) is zero. The intermediate phase may loosely be described as an SU(2) analogue of a "metallic superfluid". By studying the phase transition at values of the gauge field coupling close to what appears to be a splitting point of the transition line, also considering carefully larger system sizes, we find that the value of the gauge field coupling at which a bicritical point occurs, has been overestimated in previous works. Specifically, we find that the phase transition which in a part of this region can be interpreted as a single first-order line of phase-transitions when studying relatively small system, in actuality reveals itself as two separate phase transitions when studying larger system sizes. This has important ramifications for the determination of the character of the phase-transition line below the bicritical point, describing a direct phase transition from a fully ordered state to a fully disordered state. We also perform a flowgram analysis of the direct transition line with rescaling of the linear system size in order to obtain a data collapse. However, due to large finite-size effects in the data collapse, we are not able to draw firm conclusion on the nature of the transition.

PACS numbers:

I. INTRODUCTION

Over the last decade the concept of deconfined quantum criticality (DQC) has been intensively debated in the scientific community.[1–18] The DQC scenario was suggested to represent phase transitions that do not fit easily into the Landau-Ginzburg-Wilson (LGW) theory.[1,2] In particular, the continuous quantum phase transition from an antiferromagnetic Néel state into a paramagnetic valence-bond solid (VBS) state, does not agree with LGW theory according to which two phases with different broken symmetries are separated by a first-order phase transition.

Most recently, evidence for the DQC scenario was claimed in studies of the so-called J-Q model,[3] which is a Heisenberg model with additional higher-order spin interaction terms. Namely, it was suggested that high-precision Quantum Monte Carlo simulations of this model support a continuous Néel - VBS phase transition in accordance with the DQC scenario.[3–8]

It was proposed that the critical field theory of a continuous Néel - VBS phase transition was the so called noncompact CP^1 model ($NCCP^1$), with two SU(2) symmetric fields coupled to a noncompact U(1) gauge field in three dimensions (3D).[1,2,11] Initial efforts on studying this effective model were focused on the special case where the SU(2) symmetry was broken down to a U(1)×U(1) symmetry, i.e., the easy-plane limit, claiming a continuous phase transition.[11] However, in Ref. 13, Kuklov *et al.* pointed out the existence of paired phases in the U(1)×U(1) easy-plane action (for earlier discussions of paired phases in different U(1)×U(1) systems, see Refs. 12,19–21). The same authors have suggested, by referring to mean-field theory, that at least in the vicinity of a paired state (in the parameter space of the model), the direct phase transition from a symmetric state to a state with broken U(1)×U(1) symmetry, is first-order.[13] Subsequent Monte-Carlo calculations have reported a weakly first-order phase transition.[13,14] Furthermore, by using the so-called flowgram method introduced in Ref. 13, the same authors suggested that the direct phase transition from a symmetric state to a state with broken U(1)×U(1) symmetry, is first-order for any non-zero value of the coupling constant.

For the SU(2) symmetric case, initial simulations were performed in Ref. 11. Here, a direct second order phase transition was suggested, but system sizes were small. In a subsequent paper,[15] an extensive study of the model was performed. In particular, for the direct transition line, they found a second-order phase transition that, at higher couplings to the gauge field, turned into a first-order transition via a tricritical point. Objections to this work were, however, raised in Ref. 16 (see also Ref. 22), where it was argued that the direct transition line is first-order. By using the flowgram method, it was claimed that there is no tricritical point along the direct transition line. Rather, the large-scale behavior at small couplings to the gauge field was claimed to be the same as for

higher couplings where they were able to find a first-order transition by resolving a bimodal distribution in the energy histograms.

The NCCP^1 model is a special case of a charged two-component Ginzburg-Landau model with a constraint on the matter fields, namely $|\psi_1|^2 + |\psi_2|^2 = 1$. The easy-plane limit of the NCCP^1 model was also extensively studied in the context of two-component superconductors with independently conserved condensates.[12,19–21,23–25]

The weakness of the observed first-order phase transition, combined with the necessity of assessing the order of the phase transitions also in the limit of vanishingly small coupling strength, renders this problem computationally extremely demanding. In this work, we therefore examine the phase diagram of the NCCP^1 model at substantially larger systems sizes than what has been done in the earlier works (Refs. 15 and 16). The new physics which we find by performing the computations on larger systems, concerns a narrow range of parameters where there is a paired phase sandwiched between the symmetric and fully broken state. We find that at small system sizes, these two phase transitions give signatures of a single first-order phase transition. Correspondingly, we find that the bicritical point has been overestimated in earlier works. Although we find bimodal distributions and signatures of first-order transitions at smaller couplings along the direct transition line, the above mentioned effect raises the question of whether considering larger system sizes would transform signatures of a first-order transition into two separate phase transitions from a fully symmetric phase to fully symmetry-broken state via an intermediate partially ordered state. This raises the possibility that the NCCP^1 model exhibits a completely ordered and disordered state that always is separated by an intermediate paired phase. We cannot prove or rule out this scenario. However, we provide an upper estimate for a bicritical point which could shift further for larger system sizes.

II. MODEL

The continuum NCCP^1 model is written as

$$Z = \int \mathcal{D}\mathbf{\Psi}\, \mathcal{D}\mathbf{\Psi}^\dagger\, \mathcal{D}\mathbf{A}\ \mathrm{e}^{-\beta H}, \tag{1}$$

$$H = \frac{1}{2}\int \mathrm{d}^3\mathbf{x}\left\{ |[\boldsymbol{\nabla} - \mathrm{i}e\mathbf{A}(\mathbf{x})]\,\mathbf{\Psi}(\mathbf{x})|^2 + [\boldsymbol{\nabla}\times\mathbf{A}(\mathbf{x})]^2 \right\}, \tag{2}$$

where β is the inverse temperature and $\mathbf{\Psi}^\dagger(\mathbf{x}) = (\psi_1^*(\mathbf{x}), \psi_2^*(\mathbf{x}))$ are two complex fields that are coupled to a noncompact gauge field $\mathbf{A}(\mathbf{x})$ with charge e. The fields $\psi_c(\mathbf{x})$, $c \in \{1,2\}$, obey the CP^1 constraint, $|\mathbf{\Psi}(\mathbf{x})| = 1$.

The model can be mapped onto a nonlinear O(3) σ model coupled to massive vector fields.[23] By introducing the fields,

$$\mathbf{C}(\mathbf{x}) = \frac{\mathrm{i}}{2}\sum_c [\psi_c(\mathbf{x})\nabla\psi_c^*(\mathbf{x}) - \psi_c^*(\mathbf{x})\nabla\psi_c(\mathbf{x})] - e\mathbf{A}(\mathbf{x}), \tag{3}$$

$$\mathbf{n}(\mathbf{x}) = \mathbf{\Psi}^\dagger(\mathbf{x})\boldsymbol{\sigma}\mathbf{\Psi}(\mathbf{x}), \tag{4}$$

where the components of $\boldsymbol{\sigma}$ are the Pauli matrices, the NCCP^1 model (1) can be rewritten as[23]

$$\begin{aligned} H =& \frac{1}{8}[\nabla\cdot\mathbf{n}(\mathbf{x})]^2 + \frac{1}{2}\left[\mathbf{C}(\mathbf{x})\right]^2 \\ &+ \frac{1}{2e^2}\Bigg\{ \epsilon_{\mu\nu\lambda}\Big[\partial_\nu C_\lambda(\mathbf{x}) \\ &- \frac{1}{4}\mathbf{n}(\mathbf{x})\cdot\partial_\nu\mathbf{n}(\mathbf{x})\times\partial_\lambda\mathbf{n}(\mathbf{x})\Big]\Bigg\}^2, \end{aligned} \tag{5}$$

where sum over repeated indices is assumed. The model represents an O(3) nonlinear σ model coupled to a massive vector field $\mathbf{C}(\mathbf{x})$. The latter represents a charged mode, and its mass is the inverse magnetic field penetration length. The model can undergo a Higgs transition without restoring any broken global symmetries. In that case, the remaining broken global symmetry is O(3). If one introduces an easy-plane anisotropy for the vector field $\mathbf{n}(\mathbf{x})$, this would break the symmetry of the model to U(1)×U(1), and the separation of variables yields a neutral and a charged mode, the physics of which was intensively studied in connection with superconductors.[12,19–21,23–25] However, there is one substantial difference in the case of an SU(2) symmetry. The charged and neutral sectors are coupled through the last term in Eq. (5). Another difference compared to the U(1)×U(1) case is that in two dimensions, stable singly quantized vortex lines do not exist in a type-II SU(2) model (the same applies to vortex lines in three dimensions).[26] On the other hand, a type-I SU(2) model has energetically stable counterparts of singly quantized vortices. Since composite vortices are topological excitations which lead to the occurrence of paired states in U(1)×U(1) systems, this aspect makes the phase diagram of SU(2) theory an especially interesting problem to study.

In the Monte Carlo simulations, we employ a lattice realization of this model on a cubic lattice with size L^3 and with lattice constant $a = 1$. The fields $\psi_c(\mathbf{x})$ are then defined on the vertices $\mathbf{r} \in \{i\hat{\mathbf{x}} + j\hat{\mathbf{y}} + k\hat{\mathbf{z}} | i,j,k \in \{1,\ldots,L\}\}$ of the lattice, $\psi_c(\mathbf{x}) \to \psi_{c,\mathbf{r}}$. For the first term in (2), we rescale the gauge field by e^{-1} and invoke the gauge invariant lattice difference,

$$\left[\frac{\partial}{\partial x_\mu} - \mathrm{i}eA_\mu(\mathbf{x})\right]\psi_c(\mathbf{x}) \to \psi_{c,\mathbf{r}+\hat{\boldsymbol{\mu}}}\,\mathrm{e}^{-\mathrm{i}A_{\mu,\mathbf{r}}} - \psi_{c,\mathbf{r}}, \tag{6}$$

where $\mu \in \{x,y,z\}$ and $\mathbf{r} + \hat{\boldsymbol{\mu}}$ denotes the nearest-neighbor lattice point to vertex $\mathbf{r}$ in the μ-direction. The

gauge field $A_{\mu,\mathbf{r}}$ lives on the $(\mathbf{r}, \mathbf{r}+\hat{\boldsymbol{\mu}})$ links of the lattice. For the Maxwell term we get

$$[\boldsymbol{\nabla} \times \mathbf{A}(\mathbf{x})]_\mu \to e^{-1} \sum_{\nu,\lambda} \epsilon_{\mu\nu\lambda} \Delta_\nu A_{\lambda,\mathbf{r}}, \tag{7}$$

where Δ_ν is the forward finite difference operator, $\Delta_\nu A_{\lambda,\mathbf{r}} \equiv A_{\lambda,\mathbf{r}+\hat{\boldsymbol{\nu}}} - A_{\lambda,\mathbf{r}}$, and $\epsilon_{\mu\nu\lambda}$ is the Levi-Civita symbol. In addition, by invoking the CP[1] constraint and discarding constant factors in the partition function Z, we obtain the following lattice realization of the NCCP[1] model:

$$Z = \int \mathcal{D}\mathbf{A} \int_0^1 \mathcal{D}u \int_0^{2\pi} \mathcal{D}\theta_1 \int_0^{2\pi} \mathcal{D}\theta_2 \ \mathrm{e}^{-\beta H}, \tag{8}$$

$$\begin{aligned} H = \sum_{\mathbf{r},\mu} \Big[& - \sqrt{u_{\mathbf{r}}} \sqrt{u_{\mathbf{r}+\hat{\boldsymbol{\mu}}}} \cos\left(\Delta_\mu \theta_{1,\mathbf{r}} - A_{\mu,\mathbf{r}}\right) \\ & - \sqrt{1-u_{\mathbf{r}}} \sqrt{1-u_{\mathbf{r}+\hat{\boldsymbol{\mu}}}} \cos\left(\Delta_\mu \theta_{2,\mathbf{r}} - A_{\mu,\mathbf{r}}\right) \\ & + \frac{1}{2e^2} \left(\sum_{\nu,\lambda} \epsilon_{\mu\nu\lambda} \Delta_\nu A_{\lambda,\mathbf{r}} \right)^2 \Big], \end{aligned}$$

where $u_{\mathbf{r}} = |\psi_{1,\mathbf{r}}|^2 = 1 - |\psi_{2,\mathbf{r}}|^2$ and where $|\psi_{c,\mathbf{r}}|$ is the amplitude and $\theta_{c,\mathbf{r}}$ is the phase of the complex fields $\psi_{c,\mathbf{r}}$.

III. DETAILS OF THE MONTE CARLO SIMULATIONS

The Monte Carlo simulations are performed on a cubic lattice with periodic boundary conditions in all directions and with size L^3 where $L \in \{8, \ldots, 96\}$. For most of the simulations, the parallel tempering (PT) algorithm was employed.[27–29] To be specific, we fix the coupling e and simulate a number of replicas (typically from 8 to 32 depending on the system size L and the range of β values) in parallel at different values of β. A Monte Carlo sweep consists of systematically traversing all lattice points with local trial moves of all six field variables by the Metropolis-Hastings algorithm.[30,31] For $u_{\mathbf{r}}$, the proposed new values are found randomly within the interval $[0, 1]$, and for $\theta_{c,\mathbf{r}}$, the proposed new values are found randomly within the interval $[0, 2\pi\rangle$. For the non-compact gauge field, the proposed new values are found within some limited increment (typically $\pi/4$) from the old values. There is no gauge fixing involved in the simulations. In addition to these local trial moves, the Monte Carlo sweep also includes a PT trial move of swapping replicas at neighboring β values.

All replicas are initially thermalized from a randomly disordered or an ordered start configuration. Then, initial runs are performed in order to produce an optimal distribution of couplings for the simulation. In some cases, we found the set of couplings by measuring first-passage-times as described by Nadler *et al.* in Ref. 32. In this approach, the optimal set of couplings maximizes the flow of replicas in parameter space, essentially by shifting coupling values towards the bottlenecks.[33] However, in cases with no severe bottleneck, we also used the method proposed in Ref. 34. Here, the optimal set of couplings is found by demanding that the acceptance rates for swapping neighboring replicas are equal for all couplings. Irrespective of how the set of couplings was found, we always made sure that replicas were able to traverse parameter space sufficiently many times during production runs. The measurements were postprocessed by multiple histogram reweighting.[35] Random numbers were generated by the Mersenne-Twister algorithm.[36] Errors were determined by the jackknife method.[37]

A. Monte-Carlo approach

As mentioned in the introduction, the NCCP[1] model is a difficult model on which to perform Monte Carlo computations. In Ref. 16, the NCCP[1] model was mapped to a so-called J-current model, which allows simulations based on the worm algorithm.[38,39] (For the sake of completeness, and since they, to our knowledge, did not publish the details of their mapping, we present the derivation of this mapping in appendix A.) We tried this approach as well, but found it more demanding to work with when considering lattice sizes above $L \sim 40$, due to the presence of long-range interactions. Our choice was thus in the end to perform computations on the model in the original NCCP[1] formulation, using the PT algorithm with which it is easy to grid-parallelize the lattice.

IV. OBSERVABLES AND FINITE-SIZE SCALING

Perhaps the most familiar quantity that is used to explore phase transitions, is the specific heat C_v. The specific heat is given by the second moment of the action,

$$C_v = \frac{\beta^2}{L^3} \left\langle \left(H - \langle H \rangle\right)^2 \right\rangle, \tag{9}$$

where brackets $\langle \ldots \rangle$ denote statistical averages. In most cases, C_v exhibits a well-defined peak at the phase transition. For a continuous phase transition the correlation length diverges with critical exponent ν as $\xi \sim |t|^{-\nu}$, with $t = (\beta - \beta_c)/\beta$ being the deviation from the critical coupling β_c. The critical exponent α is defined by the singular part of C_v, given by $C_v \sim |t|^{-\alpha}$. Then, in a limited system of size L^3, the finite-size scaling (FSS) of the specific heat is given by

$$C_v \sim C_0 + C_1 L^{\alpha/\nu}, \tag{10}$$

where C_0 and C_1 are non-universal coefficients. For a first order transition, with two coexisting phases and no diverging correlation length, there is no true critical behavior at the phase transition. Still, first-order transitions exhibit well-behaved FSS with effective exponents,

$\alpha = 1$ and $\nu = 1/3$.[40,41] Hence, the peak of the specific heat scales as

$$C_v \sim L^3, \tag{11}$$

for a first-order transition. Distinguishing between continuous and first-order transitions is an important task in this work. For that purpose, FSS of the specific heat peak will play an important role.

We also investigate the third moment of the action given by[42,43]

$$M_3 = \frac{\beta^3}{L^3}\left\langle (H - \langle H\rangle)^3 \right\rangle. \tag{12}$$

In the vicinity of the critical point, this quantity typically features a minimum point and a maximum point [see for instance the inset in panel (b) of Fig. 2]. The difference in the M_3 value of these two extrema scales as

$$(\Delta M_3)_{\text{height}} \sim L^{(1+\alpha)/\nu}, \tag{13}$$

and the difference in the coupling values scales as

$$(\Delta M_3)_{\text{width}} \sim L^{-1/\nu}, \tag{14}$$

for a continuous phase transition. For a first-order transition, the FSS is

$$(\Delta M_3)_{\text{height}} \sim L^6, \tag{15}$$

and

$$(\Delta M_3)_{\text{width}} \sim L^{-3}. \tag{16}$$

As was mentioned above, one may construct a gauge neutral field $\mathbf{n_r}$,[23] given by

$$\mathbf{n_r} = \mathbf{\Psi}^*_{\mathbf{r}} \boldsymbol{\sigma} \mathbf{\Psi}_{\mathbf{r}}, \tag{17}$$

where the components of $\boldsymbol{\sigma}$ are the Pauli matrices. Correspondingly, we may associate a magnetization,

$$\mathbf{M} = \sum_{\mathbf{r}} \mathbf{n_r}. \tag{18}$$

The order parameter $\langle m\rangle$, where $\mathbf{m} = \mathbf{M}/L^3$, signals the onset of order in the O(3) gauge neutral vector field $\mathbf{n_r}$, and the critical point of this transition can be accurately determined by a proper analysis of the finite-size crossings of the associated Binder cumulant,[44–46]

$$U_4 = \frac{5}{2} - \frac{3\langle M^4\rangle}{2\langle M^2\rangle^2}. \tag{19}$$

The finite-size crossings of the Binder cumulant are known to converge rapidly towards the critical coupling β_c. Hence, β_c can be accurately determined by a simple extrapolation of the finite-size crossings to the thermodynamic limit or by invoking scaling forms that account for finite-size corrections.[46,47]

A number of quantities related to magnetization may be used to extract critical exponents from the Monte Carlo simulations. The magnetic susceptibility, given by

$$\chi = L^3 \beta \left\langle m^2 \right\rangle, \tag{20}$$

when $\beta < \beta_c$, scales as $\chi \sim L^{2-\eta}$ at $\beta = \beta_c$. Hence, we may determine the anomalous scaling dimension η by FSS of χ measurements obtained at β_c.

The exponent ν can, alternatively, be determined by calculating the logarithmic derivative of the second power of the magnetization,[48]

$$\frac{\partial}{\partial\beta} \ln \left\langle m^2 \right\rangle = \frac{\left\langle m^2 H \right\rangle}{\left\langle m^2 \right\rangle} - \langle H \rangle. \tag{21}$$

The FSS of this quantity is $\frac{\partial}{\partial\beta} \ln \left\langle m^2 \right\rangle \sim L^{1/\nu}$. Since the logarithmic derivative exhibits a peak that is associated with the critical point, it is possible to extract ν by measuring the logarithmic derivative at the pseudocritical point, without an accurate determination of β_c.

Similar to Ref. 15, we find the critical point of the Higgs transition by measuring the dual stiffness

$$\rho^{\mu\mu}_{\text{dual}}(\mathbf{q}) = \left\langle \frac{\left| \sum_{\mathbf{r},\nu,\lambda} \epsilon_{\mu\nu\lambda} \Delta_\nu A_{\lambda,\mathbf{r}}\, \mathrm{e}^{\mathrm{i}\mathbf{q}\mathbf{r}} \right|^2}{(2\pi)^2 L^3} \right\rangle, \tag{22}$$

which is the Fourier space correlator of the magnetic field. This order parameter for the Higgs transition is dual in the sense that it is finite in the high-temperature phase and zero in the low-temperature phase. As explained in Ref. 15, this quantity is measured at the smallest available wavevector $\mathbf{q} \neq \mathbf{0}$. We chose to measure ρ^{zz}_{dual} at $\mathbf{q}_{\text{min}} = (2\pi/L, 0, 0)$. At the critical point, the quantity $L\rho^{\mu\mu}_{\text{dual}}(\mathbf{q}_{\text{min}})$ is universal, such that the finite-size crossings of $L\rho^{\mu\mu}_{\text{dual}}(\mathbf{q}_{\text{min}})$ can be used to estimate the critical point of the Higgs transition. In addition, measuring the coupling derivate of $L\rho^{\mu\mu}_{\text{dual}}(\mathbf{q}_{\text{min}})$ can be used to estimate the correlation length exponent ν as

$$\frac{\partial}{\partial\beta} L\rho^{\mu\mu}_{\text{dual}}(\mathbf{q}_{\text{min}}) \sim L^{1/\nu}, \tag{23}$$

at the critical point.

V. NUMERICAL RESULTS

A. Outline of the phase diagram

The phase diagram of the NCCP[1] model is presented in Fig. 1. For small values of β, there is a normal phase that can be recognized by a disordered gauge neutral vector field $\mathbf{n_r}$ and a massless gauge field. Hence, $\langle m\rangle = 0$ and $\rho^{\mu\mu}_{\text{dual}}(\mathbf{q}) \neq 0$ in this phase. For large values of e and higher values of β, there is a transition into a phase that we label the O(3) phase. Here, the vector field $\mathbf{n_r}$ is ordered (the O(3) symmetry is spontaneously broken), $\langle m\rangle \neq 0$, whereas the gauge field remains massless,

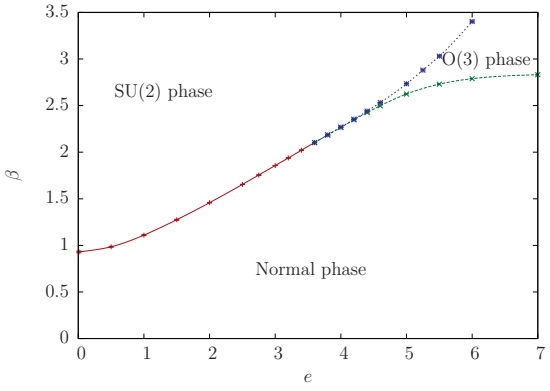

Figure 1: (Color online) Phase diagram of the NCCP[1] model. SU(2) phase: Fully ordered phase where the O(3) symmetry is spontaneously broken, $\langle m\rangle \neq 0$, and the gauge field is massive, $\rho^{\mu\mu}_{\rm dual}(\mathbf{q}) = 0$. O(3) phase: O(3) symmetry is spontaneously broken, $\langle m\rangle \neq 0$, but the gauge field is massless, $\rho^{\mu\mu}_{\rm dual}(\mathbf{q}) \neq 0$. Normal phase: O(3) symmetry is restored, $\langle m\rangle = 0$, and the gauge field is massless, $\rho^{\mu\mu}_{\rm dual}(\mathbf{q}) \neq 0$. The direct transition line from the SU(2) phase to the normal phase is denoted by +-markers and a solid red line. The Higgs transition line between the SU(2) phase and the O(3) phase is denoted by $*$-markers and a dotted blue line. The transition line between the O(3) phase and the normal phase is denoted by $\times$-markers and a dashed green line. Lines are guide to the eyes.

$\rho^{\mu\mu}_{\rm dual}(\mathbf{q}) \neq 0$. In the case of U(1) × U(1) symmetric superconductors, this phase is sometimes denoted a *metallic superfluid* or a *paired phase*, with long-range order in the gauge neutral linear combination of the phases, but not in the individual ones.[12,13,19–21,25,49] From the O(3) phase, by reducing the value of e, one enters an ordered phase that we label the SU(2) phase. Going into this phase, the gauge field dynamically acquires a Higgs mass and the system becomes a two-component superconductor. Note that the Higgs transition is related to a local U(1) symmetry, and indeed, is not associated with spontaneous symmetry breaking.[50] (this aspect should be kept in mind where we for brevity refer to the ordered state as "broken SU(2)" or "fully broken state" to distinguish it from a paired state). The SU(2) phase is recognized by measuring $\langle m\rangle \neq 0$ and $\rho^{\mu\mu}_{\rm dual}(\mathbf{q}) = 0$. At small values of e, the SU(2) phase may also be entered directly from the normal phase. The nature of the phase transition along this direct transition line is very important and intensively debated due to the relevance for the DQC scenario. We will return to this line in Secs. V B and V C, but first, we will detail results for the two separate transition lines.

1. O(3) line

In Refs. 16,51, the existence of an intermediate paired phase, separating a fully ordered state from a fully disordered one, was shown in the SU(2)-symmetric theory. As immediately follows from the nonlinear σ model mapping presented above, the transition line between the normal phase and the O(3) phase could be a continuous transition in the O(3) universality class, at least in the limit far from the bicritical point. As a step towards validating the numerics, we have considered this for the case $e = 6.0$, and the FSS results are given in Fig. 2. A log-log plot of the FSS of the peak height in $\frac{\partial}{\partial\beta}\ln\langle m^2\rangle$ is given in panel (a), and the measured peak heights fall on a straight line for $L \geq 20$. The best fit to the form $\frac{\partial}{\partial\beta}\ln\langle m^2\rangle \sim L^{1/\nu}$ yields $\nu = 0.715 \pm 0.004$. In panel (b), we also measure $(\Delta M_3)_{\rm height}$, and this quantity exhibits negligible finite-size corrections to scaling at least for $L \geq 10$. The best fit according to Eq. (13) yields $\alpha = -0.117 \pm 0.011$, where the value of ν obtained above was used. We should mention that in this case, it was found that ν was most precisely determined by measuring the peak height in $\frac{\partial}{\partial\beta}\ln\langle m^2\rangle$ rather than measuring $(\Delta M_3)_{\rm width}$. This follows since the maximum peak in M_3 is not very sharp [see the inset of panel (b)], and hence, the errors in $(\Delta M_3)_{\rm width}$ were large. In order to determine η, the FSS of the magnetic susceptibility χ is given in panel (c). Here, χ is measured at the critical coupling $\beta_{\rm c} = 2.7894 \pm 0.0003$, which was determined by curvefitting the Binder crossings of L and $L/2$ to a fit function that accounted for power-law finite-size corrections. The best fit of $\chi(L)$ was determined for sizes $L \in \{12, \ldots, 64\}$ to yield $\eta = 0.024 \pm 0.014$. All the calculated exponents above correspond well with the exponents of the O(3) universality class.[52,53]

2. Inverted U(1) line

Investigations were also performed along the transition line between the O(3) phase and the SU(2) phase. To check the universality class of this line, FSS results of $\partial/\partial\beta[L\rho^{zz}_{\rm dual}(\mathbf{q}_{\rm min})]$, obtained at the critical point with $e = 5.0$, is given in Fig. 3. First, the critical coupling was determined to be $\beta_{\rm c} = 2.7347 \pm 0.0005$, by considering the crossings of $L\rho^{zz}_{\rm dual}(\mathbf{q}_{\rm min})$ [see the inset of Fig. 3]. Then, the correlation length exponent was estimated to be $\nu = 0.664 \pm 0.039$. This value is consistent with interpreting this line as an inverted 3Dxy transition line.[54]

B. The region of the bicritical point

By utilizing the flowgram method, the authors of Ref. 16 argue that the true nature of the direct phase transition can most easily be revealed at large coupling to the gauge field, just below the bicritical point above which

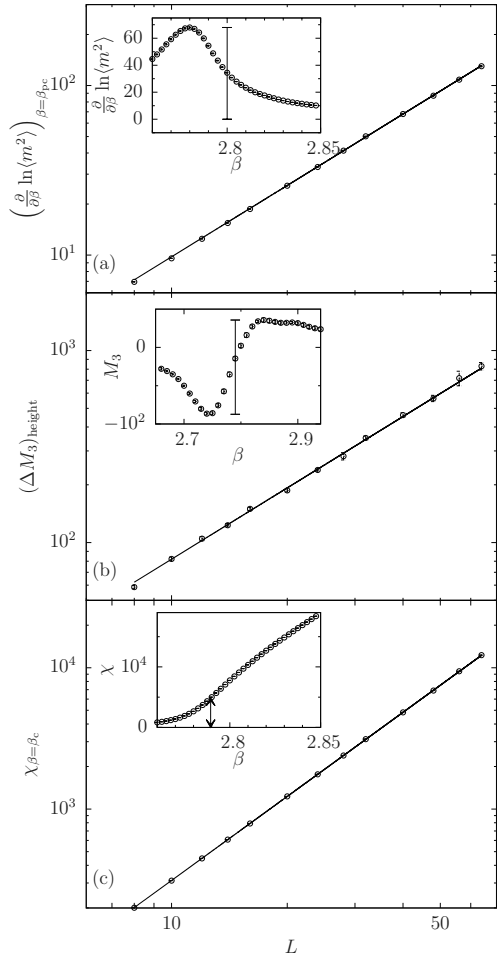

Figure 2: FSS results for the transition between the normal phase and the O(3) phase when $e = 6.0$. 13 system sizes $L \in \{8, \ldots, 64\}$ are used. In all panels, the solid straight line is the best fit obtained for a fit function on the form aL^b with two free parameters a and b. Panel (a): Log-log plot of the maximum in the logarithmic derivative of the second power of the magnetization $(\partial/\partial\beta \ln\langle m^2\rangle)_{\beta=\beta_{\rm pc}}$ [see Eq. (21)] as a function of L. The best fit is obtained for sizes $L \in \{20, \ldots, 64\}$. The inset shows the measure of $(\partial/\partial\beta \ln\langle m^2\rangle)_{\beta=\beta_{\rm pc}}$ in the case when $L = 40$. Panel (b): Log-log plot of the third moment height difference $(\Delta M_3)_{\rm height}$ as a function of L. The best fit is obtained for sizes $L \in \{10, \ldots, 64\}$. The inset shows the measure $(\Delta M_3)_{\rm height}$ in the case when $L = 14$. Panel (c): Log-log plot of the magnetic susceptibility measured at the critical coupling $\chi_{\beta=\beta_{\rm c}}$ as a function of L. The best fit is obtained for sizes $L \in \{12, \ldots, 64\}$. The inset shows measuring $\chi_{\beta=\beta_{\rm c}}$ in the case when $L = 40$, and the arrowheads indicate that χ is measured at the same fixed coupling $\beta_{\rm c}$ for all sizes.

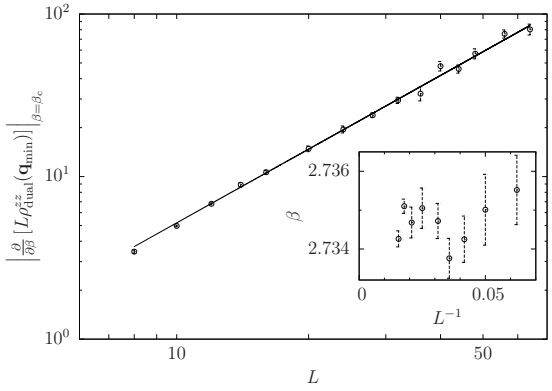

Figure 3: Log-log plot of $\frac{\partial}{\partial\beta} L\rho^{zz}_{\rm dual}(\mathbf{q}_{\rm min})$ measured at the critical point $\beta_{\rm c}$, as a function of system size L. The charge is $e = 5.0$. Measurements are performed for 15 different system sizes $L \in \{8, \ldots, 64\}$. The derivative was found by calculating the differences of $\rho^{zz}_{\rm dual}(\mathbf{q}_{\rm min})$. The solid straight line is the best fit obtained with a fit function on the form aL^b where a and b are two free parameters. The inset shows the $L\rho^{zz}_{\rm dual}(\mathbf{q}_{\rm min})$ crossings for systems L and $L/2$ as a function of L^{-1}. These crossings were used to estimate the critical point, $\beta_{\rm c} = 2.7347 \pm 0.0005$. Errors in determining $\beta_{\rm c}$ are taken into account by also considering the sensitivity of ν with respect to β when estimating the uncertainty in the exponent.

the paired phase is sandwiched in between the normal phase and the ordered SU(2) phase. It is thus important to be able to determine the bicritical point accurately. For this purpose, we will focus on the region slightly *above* the bicritical point and establish when two separate phase transitions are clearly resolved. In this way, we can determine an upper limit of the bicritical point.

1. *Monte Carlo results for $e = 4.2$. Signatures of splitting*

In order to discern two separate but close-lying phase transitions, we need to establish signatures that can be taken as evidence for splitting. To this end, results are presented for the case when $e = 4.2$, where we find unambiguous evidence for two separate phase transitions. Note that this was found to be a single first-order transition in Ref. 16 ($e = 4.2$ corresponds to $g \approx 1.88$ in the units of Ref. 16 whereas the bicritical point is found at $g \approx 2.0$ in that work). As we will see, going to larger system sizes leads to a different conclusion as finite-size effects will disguise the true nature of separate transitions and make them appear as one.

In Fig. 4, results are presented for four different observables obtained at 12 different system sizes, $L \in \{8, \ldots, 56\}$, in a coupling range covering both phase transitions. In panel (a), results for the specific heat are given. When system sizes are small, it is only possible to resolve one peak in the specific heat. However, when

$L = 40$, it is possible to resolve a bump to the left of the peak. The bump, which corresponds to the O(3) ordering phase transition, becomes more pronounced when L increases. This behavior suggests that there are two transitions instead of one. Moreover, in the inset of panel (a) we study the scaling of the peak in a log-log scale. When L is small, there is a rather steep and slightly increasing slope. However, at higher values of L there is a definite change in the slope towards smaller values, corresponding to a sudden slowing down in the growth of the peak. This behavior should clearly be associated with resolving separate transitions with increasing L.

In panel (b) of Fig. 4, results for the third moment of the action are presented. When system sizes are small, it is only possible to resolve a characteristic form corresponding to a single phase transition. However, at $L \geq 40$, a secondary form is developing to the left of the original form, resolving the O(3) ordering transition. When studying the scaling of the quantities $(\Delta M_3)_{\text{height}}$ and $(\Delta M_3)_{\text{width}}$ in the insets of the panel, it is clear that they both exhibit slope changes associated with resolving both transitions.[60]

The Binder cumulant is given in panel (c) of Fig. 4, and its crossings are given in the inset of the panel. By considering the crossings with largest L, we find that the critical point of the O(3) ordering transition is $\beta_{\text{c}} = 2.347 \pm 0.001$, a value that corresponds well with the leftmost transition point in panel (a) and (b). Note that there is a non-monotonic behavior in the coupling values of the Binder crossings. Hence, by studying small systems only, one might be misled to overestimate the critical point of the phase transition.

In panel (d) of Fig. 4, we show results for the quantity $L\rho^{zz}_{\text{dual}}(\mathbf{q}_{\text{min}})$, and the corresponding crossings are given in the inset. We estimate the critical point of the Higgs transition to be $\beta_{\text{c}} = 2.353 \pm 0.001$ by a crude extrapolation to the thermodynamic limit. Hence, the critical point of the Higgs transition is significantly different from the critical point of the O(3) ordering transition.

The results in Fig. 4 show that it is of utmost importance to simulate large systems in regions where there might be multiple phase transitions. If we discard data points for $L > 20$, the crossings in panel (c) and (d) seem to converge to the same coupling, and in panel (a) and (b), we would only resolve a single phase transition with rather strong thermal signatures. More formally, since the size of the critical region scales as $\sim L^{-1/\nu}$, there is some limiting size $L_{\text{lim}} = \max\{\xi_1, \xi_2\}$, where $\xi_i \sim |(\beta_{\text{c},1} - \beta_{\text{c},2})/\beta_{\text{c},i}|^{-\nu_i}$ is the correlation length associated with transition i when the deviation from the critical coupling equals the coupling difference between the two transitions. If system sizes are smaller than L_{lim}, the critical point of one phase transition will be inside the critical region of the other and/or vice versa. However, when L is larger than L_{lim}, one should be able to resolve two phase transition as the two critical regions will not interfere. When one or both transitions are first-order, the picture is somewhat different, but the main

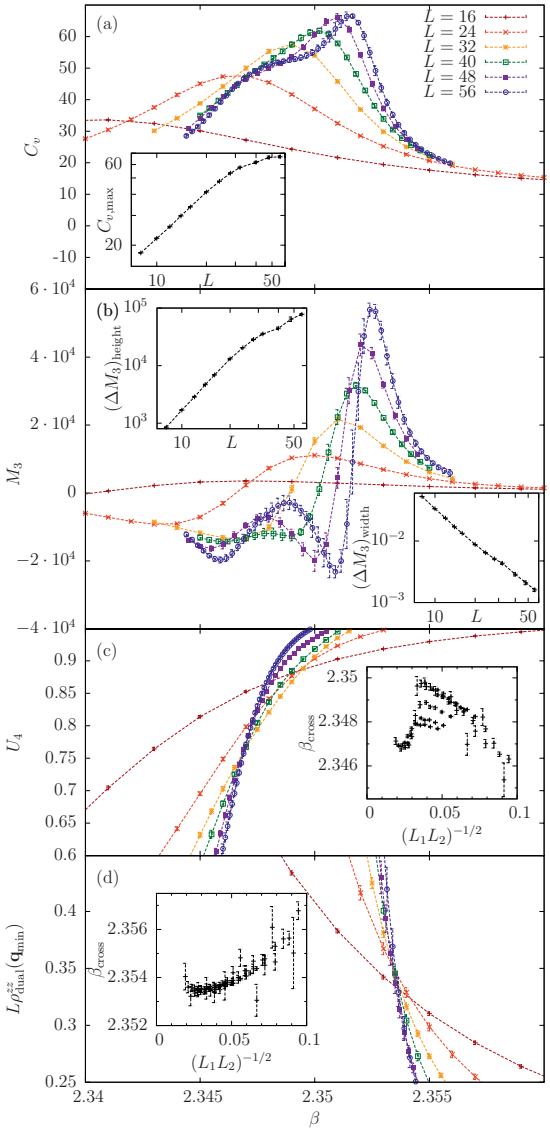

Figure 4: (Color online) Monte Carlo results for four different quantities and 12 different system sizes obtained for a coupling range covering two separate, but close-lying phase transitions. The gauge field coupling $e = 4.2$. For clarity, the panels only show results for $L \in \{16, 24, 32, 40, 48, 56\}$, but insets include all 12 sizes, $L \in \{8, \ldots, 56\}$. Panel (a) shows results for the specific heat C_v, and the inset shows the scaling of the peak $C_{v,\text{max}}$ in a log-log scale. Panel (b) shows the results for the third moment of the action M_3, and the insets show the scaling of $(\Delta M_3)_{\text{height}}$ and $(\Delta M_3)_{\text{width}}$ in a log-log scale. Panel (c) shows the Binder cumulant U_4, and the inset shows the coupling β_{cross} where the Binder curves cross as a function of $(L_1 L_2)^{-1/2}$ where L_1 and L_2 are the two actual sizes. Panel (d) shows the quantity $L\rho^{zz}_{\text{dual}}(\mathbf{q}_{\text{min}})$ and the inset shows the coupling where the curves cross. Lines are guide to the eyes.

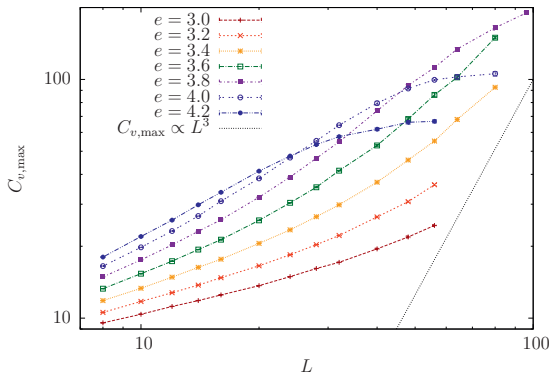

Figure 5: (Color online) Log-log plot of the value of the specific heat peak $C_{v,\max}$ as a function of system size L for seven different values of $e \in \{3.0, \ldots, 4.2\}$. The dotted line corresponds to the slope expected for a first-order transition, according to Eq. (11). Lines are guide to the eyes.

point remains that large systems are needed to resolve phase transitions that are close.

2. *Monte Carlo results for* $e \in \{3.0, \ldots, 4.6\}$

We now turn our attention to the region with $e < 4.2$ to look for the signatures that we have established above. Fig. 5 shows the FSS of the peak in the heat capacity for $e \in \{3.0, \ldots, 4.2\}$. The results show that there is a definite change in the slope of the scaling of $C_{v,\max}$, also for $e = 4.0$ and 3.8. Note that this signature of splitting appears at higher L when e is reduced, corresponding to the coupling difference between the two transitions being smaller. The slope of the dotted line in Fig. 5 is the slope of a first-order transition [see Eq. (11)]. For all values of e in Fig. 5, we find that for small and intermediate L the slope is steep and increasing, and one might be tempted to conclude that they all are first-order transitions. However, the change towards a smaller slope, that we find for large L and $e \in \{3.8, 4.0, 4.2\}$, is clearly inconsistent with a first-order phase transition.

In Fig. 6, we show the FSS of $(\Delta M_3)_{\text{height}}$ and $(\Delta M_3)_{\text{width}}$. Observe that the same signatures of splitting appears for $e \in \{3.8, 4.0\}$ as found for $e = 4.2$ above, namely that the slope of $(\Delta M_3)_{\text{height}}$ changes to a smaller value and the slope of $(\Delta M_3)_{\text{width}}$ changes to a higher value. This is again inconsistent with the scaling of a first-order transition. For a first-order transition the slopes should converge towards the scaling for first-order transitions, given in Eqs. (15) and (16) (see Ref. 14 for an example).

To determine the critical points of the O(3) ordering transition and the Higgs transition, the finite size crossings of U_4 and $L\rho^{zz}_{\text{dual}}(\mathbf{q}_{\min})$ are given in Fig. 7 for eight different values of $e \in \{3.2, \ldots, 4.6\}$. For

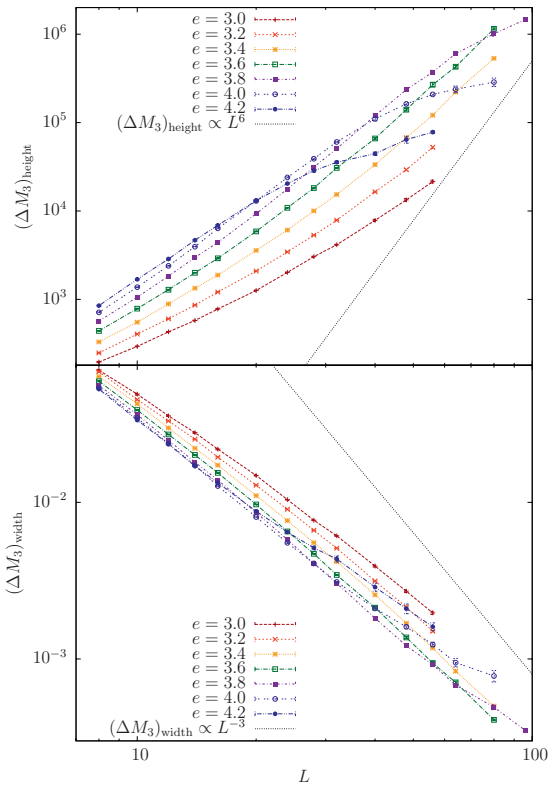

Figure 6: (Color online) Log-log plot of the FSS of the height (upper panel) and the width (lower panel) of the third moment of the action, for seven different values of $e \in \{3.0, \ldots, 4.2\}$. The dotted lines correspond to the slope expected for a first-order transition, according to Eqs. (15) and (16). Lines are guide to the eyes.

$e \in \{4.0, \ldots, 4.6\}$, the U_4 crossings and the $L\rho^{zz}_{\text{dual}}(\mathbf{q}_{\min})$ crossings clearly extrapolates to different couplings as expected for two separate transitions. Also note the corresponding non-monotonic behavior for the Binder crossings. When the coupling difference between the two phase transitions decreases, larger systems are needed to resolve this feature. For the sizes available, the crossings seem to converge to the same coupling value for $e \in \{3.2, \ldots, 3.8\}$.

Based on the results in Figs. 5, 6 and 7, it should be clear that there are two separate transitions when $e \geq 4.0$. Also, based on the scaling curves in Figs. 5, 6 it is also reasonable to conclude that $e = 3.8$ is above the bicritical point, but that sizes are slightly too small to observe the non-monotonic behavior for the Binder crossings in Fig. 7. We thus estimate that the bicritical point must be below $e = 3.8$. Clearly, the system sizes we are able to reach are too small to conclusively determine if there are separate transitions for $e \leq 3.8$.

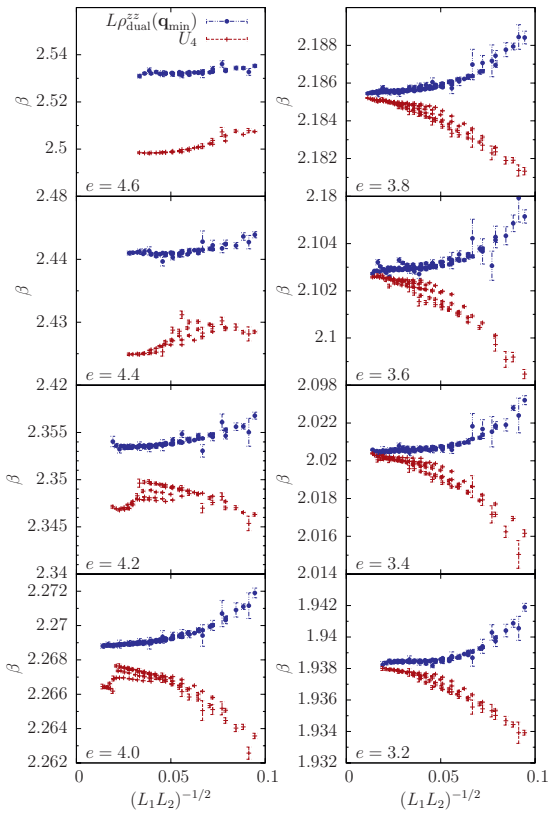

Figure 7: (Color online) Plots of the finite size crossings of the Binder cumulant U_4 [Eq. (19)], and the $L\rho^{zz}_{\rm dual}(\mathbf{q}_{\rm min})$ for eight different values of $e \in \{3.2, \ldots, 4.6\}$. The x-values are given by $(L_1L_2)^{-1/2}$ where L_1 and L_2 are the two sizes that form the crossing.

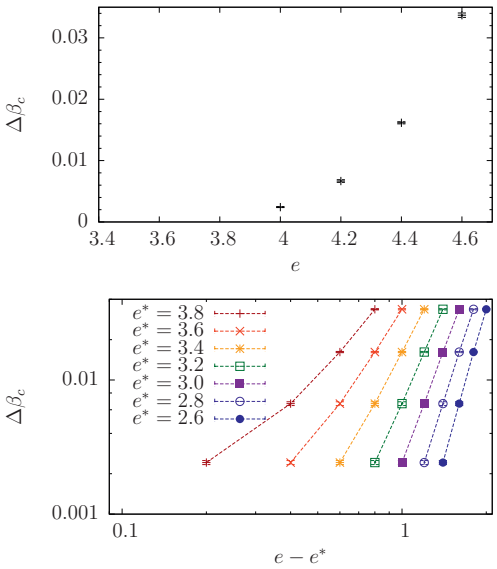

Figure 8: (Color online) Plot of the difference in the critical coupling between the Higgs transition and the O(3) ordering transition, $\Delta\beta_c$. $\Delta\beta_c$ is determined by calculating the difference between the $L\rho^{zz}_{\rm dual}(\mathbf{q}_{\rm min})$ crossing and the U_4 crossing, and averaging over four of these differences with largest value of $(L_1L_2)^{1/2}$ (i.e., the four leftmost data points from the panels in Fig. 7). We only include results for $e \geq 4.0$ where the non-monotonic behavior of the Binder crossings can be resolved. Upper panel: $\Delta\beta_c$ as a function of e. Lower panel: Log-log plot of $\Delta\beta_c$ as a function of $e - e^*$ where e^* is given in the key. Positive curvature suggests that $e^* > e_{\rm bc}$, negative curvature suggests that $e^* < e_{bc}$ and a straight line suggests that $e^* \approx e_{\rm bc}$. Lines are guide to the eyes.

However, as a crude approach to determine the bicritical point $e_{\rm bc}$, in Fig. 8, we show results for the coupling difference between the two phase transitions $\Delta\beta_{\rm c}$ as a function of coupling e. To estimate when $\Delta\beta_{\rm c} \to 0$, in the lower panel, we show $\Delta\beta_{\rm c}$ as a function of $e - e^*$ on a log-log scale where e^* is some trial value as labeled in the key of the figure. If $e^* \approx e_{\rm bc}$, a straight line should be expected. A positive curvature suggests that $e^* > e_{\rm bc}$ and a negative curvature suggests that $e^* < e_{\rm bc}$. Since there is a clear positive curvature both for $e = 3.8$ and $e = 3.6$, this suggests that $e_{\rm bc} < 3.6$. However, we should mention that the results given in the lower panel of Fig. 8 essentially is an extrapolation of the difference $\Delta\beta_{\rm c}$ (which also in an extrapolation) in the upper panel to find the point $e_{\rm bc}$ where $\Delta\beta_{\rm c} = 0$. Hence, simulations of even larger systems are needed to determine the exact position of $e_{\rm bc}$ with higher certainty.

Our estimates for the bicritical point is clearly different compared with the results in Refs. 15 and 16. Our *upper* limit of $e_{\rm bc} < 3.8$ corresponds to $\mathcal{K}_{\rm bc} > 0.151$ in Ref. 15, which means that a part of the line that was interpreted as a direct first order transition in that work, in fact is two separate transitions. Moreover, the upper limit of $e_{\rm bc} < 3.8$ corresponds to $g_{\rm bc} < 1.65$ in Ref. 16 where the bicritical point was estimated to $g \approx 2.0$.

3. *First-order signals*

Although we are led to a different conclusion than Refs. 15 and 16 at least for $e \geq 3.8$, we find some of the same thermal signatures. As mentioned above (see Figs. 5 and 6), when systems are too small to resolve two phase transitions, the Monte Carlo results show that the growth of $C_{v,\rm max}$ and $(\Delta M_3)_{\rm height}$ is fast, almost as fast as one would expect for a first-order transition. Also when investigating the energy distributions for $e \in \{3.4, 3.6, 3.8, 4.0\}$ in Fig. 9, we find that the histograms are broad, and for $e \in \{3.4, 3.6, 3.8\}$ a very weak bimodal structure can be seen for a few of the sizes.

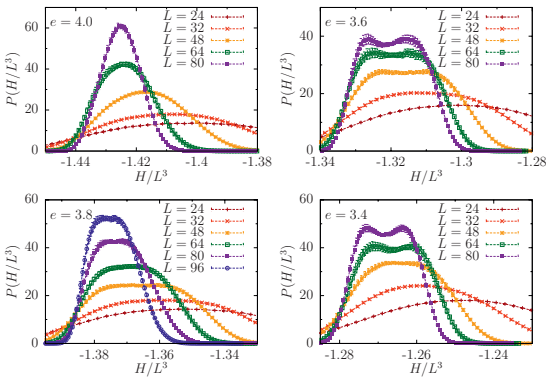

Figure 9: (Color online) Histograms of the probability distribution of the energy per site H/L^3, for $e \in \{3.4, 3.6, 3.8, 4.0\}$. In every case the flattest (or most bimodal) energy histograms were found by reweighting in the vicinity of the pseudocritical coupling corresponding to the peak of the specific heat, $C_{v,\max}$.

However, for the system sizes available, the bimodal signatures are too weak to determine if the appropriate scaling for first-order transition is obeyed.[55,56] Also note that for $e \in \{3.8, 4.0\}$, the width of the histograms decreases and the bimodal structure disappears when L increases. This is not consistent with being a single first-order transition.

Combining the results in Figs. 5, 6 and 9, it seems that for couplings slightly above the bicritical point, there are strong thermal signatures in terms of broad energy distributions and rapidly increasing peaks in the specific heat and the third moment of the action. However, when system sizes are larger, we can explicitly see signatures of splitting for $e \geq 3.8$. We cannot exclude the possibility that this may also be the case for some of the couplings with $e < 3.8$. Indeed, the crude extrapolation in Fig. 8 suggests that $e = 3.6$ also is above the bicritical point. If so, we should expect to see signatures of splitting for system sizes larger than available in this work. On the other hand, the strong thermal signatures we find for $e < 3.8$ can also be consistent with a weak first-order transition. In that case, we should expect to see that proper first-order scaling is obeyed for larger system sizes.

In this work, we find that the strongest first-order-like signatures were found at $e = 3.4$ and $e = 3.6$. Previous works on smaller systems did not resolve bimodal structure at these couplings. For $e < 3.4$, we did not find any bimodal structure in the energy histograms. Thus to assess the nature of the phase transitions at these couplings we have to resort to flowgram method.

C. Flowgram

In Ref. 13, the flowgram method was proposed as a useful tool to distinguish between a weak first-order and a continuous phase transition. In Fig. 10, we show results of a flowgram analysis of the quantity $L\rho^{zz}_{\rm dual}(\mathbf{q}_{\rm min})$ along the O(3) ordering transition line. Specifically, the quantity $L\rho^{zz}_{\rm dual}(\mathbf{q}_{\rm min})$ is measured at the critical point. For this analysis, the critical point is defined to be at the coupling where the Binder cumulant $U_4 = 0.775$. Hence, with this definition of the critical point, we will follow the O(3) ordering transition line. As mentioned above, $L\rho^{zz}_{\rm dual}(\mathbf{q}_{\rm min})$ is a universal quantity for a continuous Higgs transition, whereas it will diverge $\sim L$ for a first-order transition. In Fig. 10 we clearly see such diverging behavior when $e \geq 3.8$ and the FSS is consistent with $L\rho^{zz}_{\rm dual}(\mathbf{q}_{\rm min}) \sim L$. In Refs. 15 and 22, this was interpreted as a first-order transition. However, we would like to stress that a diverging $L\rho^{zz}_{\rm dual}(\mathbf{q}_{\rm min})$ also is consistent with being above the bicritical point, when following the transition line of the O(3) ordering transition. Hence, the results in Fig. 10 correspond well with there being two closely separated phase transition for these values of e, as was found in Figs. 4-8 above.

For $e \in \{3.4, 3.6\}$, the flowgram analysis also suggest that $L\rho^{zz}_{\rm dual}(\mathbf{q}_{\rm min})$ diverges, but the FSS is weaker than $\sim L$ for the sizes available. This can be consistent with being above the bicritical point, but it can also be consistent with a first-order transition. For $e \in \{3.0, 3.2\}$, it is hard to draw conclusions on the large-scale behavior of the flowgram in Fig. 10. For $e = 2.0$ and $e = 2.5$ the lines seem to converge slowly to a fixed value, at least for the system sizes available. This is consistent with Ref. 15, namely that for these couplings the phase transition is continuous.

By rescaling the linear system size $L \to C(g)L$, where $g = e^2/(4\beta)$ and where $C(g)$ is a scaling function, the authors of Ref. 22 were able to collapse the curves in the flowgram onto the same master curve. The collapse implies that the large-scale behavior is identical for all couplings for which the curve collapses onto the master curve. To this end, in Fig. 11 are the results if the flowgram data in Fig. 10 when rescaled with the scaling function $C(g) = 8.2876g + 0.3689[\exp(3.8127g) - 1]$.[61] When observed with a coarse-grained view, the flowgram curves seem to collapse onto the same master curve, at least for $e \leq 3.6$. However, a close inspection reveals that there are large deviations for small systems.

We find it hard to draw firm conclusions based on Fig. 11. Clearly, there is an adequate collapse for $e \leq 3.6$ and for large systems. This would lead to the conclusion that all $e \in [0.5, 3.6]$ have the same large-scale behavior. However, we are concerned about the deviations that are found for $e > 1.5$ and sizes $L \lesssim 20$. These points are impossible to collapse without destroying the good collapse that is obtained for large systems. Hence, even larger systems are needed to be certain that the collapse is good. If so, additional data points for larger systems should fall

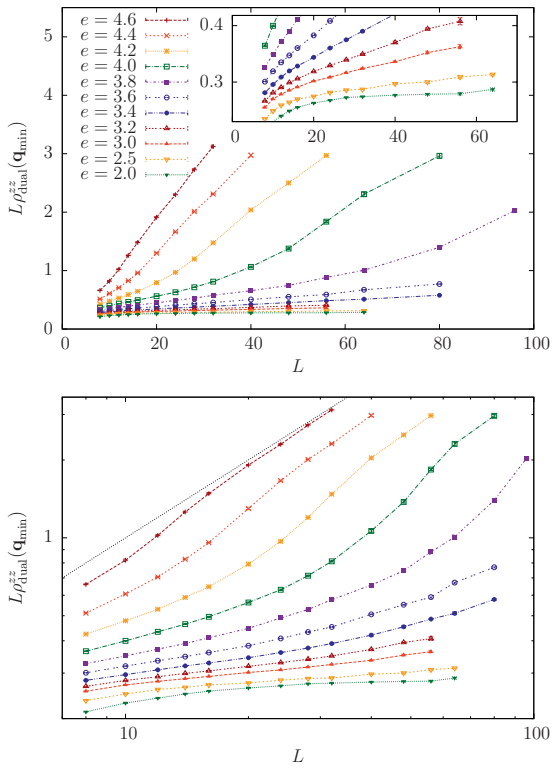

Figure 10: (Color online) Flowgram of $L\rho^{zz}_{\rm dual}(\mathbf{q}_{\rm min})$ along the O(3) ordering transition line. In this analysis, the critical point is fixed by $U_4 = 0.775$. Then $L\rho^{zz}_{\rm dual}(\mathbf{q}_{\rm min})$ is measured at this point and plotted as a function of system size L. The results are given for 11 different values of $e \in \{2.0, \ldots, 4.6\}$. The upper panel shows results on a normal scale and the inset zooms in on the results for $e \in \{2.0, \ldots, 3.2\}$. The lower panel shows the results on a log-log scale and the dotted line correspond to FSS $\propto L$. Lines are guide to the eyes.

on the master curve without making significant changes in $C(g)$. On the other hand, if additional data points means that systematic changes has to be made in $C(g)$ in order to obtain a good collapse for large systems, and with more data points that do not fall on the master curve for small systems, one should be careful to draw conclusions. In that case, there may be a tricritical point within this region.

D. Results for $e < 2.0$

For $e < 2.0$ we obtain FSS curves (not shown here) qualitatively similar to the results for $e \leq 3.6$ in Figs. 5 and 6. I.e., for the system sizes available, the curves have not converged to a proper straight line in a log-log plot, so we have not performed a FSS analysis to extract critical

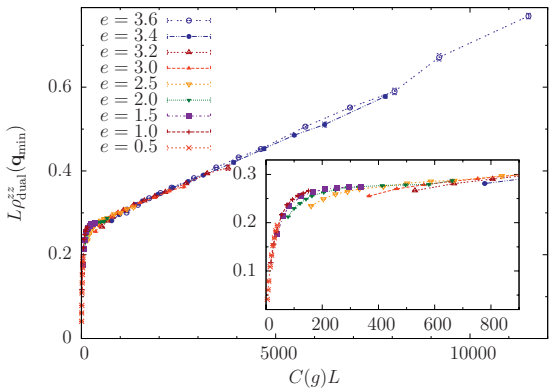

Figure 11: (Color online) Rescaled flowgram of the data in Fig. 10. For clarity, we have removed the curves for $e > 3.6$. These curves did clearly not collapse onto the master curve. On the other side, we have included curves for $e \in \{0.5, 1.0, 1.5\}$. The system size L is rescaled by $L \to C(g)L$ where $C(g) = 8.2876g + 0.3689[\exp(3.8127g) - 1]$ with $g = e^2/(4\beta)$. The inset zooms in on the lower left corner of the diagram. Lines are guide to the eyes.

exponents. In this sense, we do not have evidence for a continuous transitions along this direct transition line. On the other hand, we note that in this context such large finite-size effects are not necessarily inconsistent with a continuous transition.[6]

VI. SUMMARY AND DISCUSSION

In Sec. V B, we have performed a thorough investigation of the region around the bicritical point. We have established that certain signatures should be taken as direct evidence of two separate phase transition. Here, these signatures are i) distinct changes in the FSS slope of the specific heat and the third moment of the action that are inconsistent with first-order scaling, and ii) the crossings of the Binder cumulant and $L\rho^{zz}_{\rm dual}(\mathbf{q}_{\rm min})$ extrapolates to different values in the thermodynamic limit. We also observe that when the two transitions approach each other, larger systems are needed to resolve these signatures. For the system sizes we are able to reach, all of these signatures can conclusively be observed for $e \geq 4.0$. In addition, we also observe distinct changes in the FSS slopes for $e = 3.8$. Hence, the bicritical point must be below $e = 3.8$. We also note that the crude extrapolation in Fig. 8 suggests that the bicritical point may even be below $e = 3.6$. However, we believe that larger systems must be studied before drawing firm conclusions for these values of e. We would also like to emphasize that for values of $e \geq 3.8$ that conclusively show two closely separated transitions at large sizes, one can, at smaller sizes, observe strong thermal signatures, similar to what one would expect for a weak first-order transition. This

may explain why the observed transition in a part of this region previously has been interpreted as weakly first-order.

Similar to earlier investigations,[15,16,57] there are strong thermal signatures in this region that indicate the existence of first-order transitions. In particular, we observe strong FSS of the specific heat and the third moment of the action for all e values in the region of the bicritical point. Also, we observe broad energy histograms for these values of e, and for $e \in \{3.4, 3.6, 3.8\}$ there are a few histograms that are slightly bimodal. There is a strong mean-field argument suggesting that there must be a first-order transition along the Higgs transition line in the vicinity of the bicritical point.[13,58] Hence, the most obvious interpretation of the first-order signatures here is that there is a first-order transition line for these values of e. On the other hand, for slightly larger values of the coupling, $e \geq 3.8$, we find that the same strong signatures weaken at large systems, and for $e \geq 4.0$ we can explicitly observe two separate transitions. Since it is clear that larger systems are needed to observe signatures of splitting when e is reduced, we cannot exclude the possibility that the strong thermal signatures that we observe for $e < 3.8$ are finite-size artifacts similar to those we observe for $e \geq 3.8$. To conclusively determine the existence of a first-order transition for $e < 3.8$, larger systems should be considered in order to reveal that proper first-order scaling is well obeyed in energy histograms and scaling plots.

As for the DQC scenario, we are not able to draw firm conclusions. Our results are consistent with those of Ref. 16 in that we observe an adequate flowgram collapse that connects the region of small couplings with a region where signatures of first-order transitions are found. However, we also observe that there are large finite-size effects in the data collapse and that proper FSS is yet to be observed for the first-order transition. We thus cannot exclude the possibility that there is a tricritical point along the direct transition line, below which there is a continuous transition with large finite size effects. This appears to require systems sizes that are currently beyond our reach.

Acknowledgments

We acknowledge useful discussions with A. Kuklov, N. V. Prokof'ev, B. V. Svistunov and I. B. Sperstad. E. V. H. and T. A. B. thank NTNU for financial support. E. B., and A. S. thank the Aspen Center for Physics for hospitality and support under the NSF grant #1066293. The work was also supported through the Norwegian consortium for high-performance computing (NOTUR).

Appendix A: Mapping the NCCP^1 model to a J-current model

We start with the lattice formulation of the NCCP^1 model,

$$Z = \prod_{c,\mathbf{r}} \int \mathrm{d}\psi_{c,\mathbf{r}}\, \mathrm{d}\psi^*_{c,\mathbf{r}} \prod_{\mu,\mathbf{r}} \int \mathrm{d}A_{\mu,\mathbf{r}}\ \mathrm{e}^{-S}, \tag{A1}$$

$$S = S_t + S_g, \tag{A2}$$

$$S_t \equiv -t \sum_{c,\mu,\mathbf{r}} \psi_{c,\mathbf{r}} \psi^*_{c,\mathbf{r}+\hat{\boldsymbol{\mu}}}\, \mathrm{e}^{\mathrm{i}A_{\mu,\mathbf{r}}} + \text{c.c.}, \tag{A3}$$

$$S_g \equiv \frac{1}{8g} \sum_{\mu,\mathbf{r}} \left(\sum_{\nu,\lambda} \epsilon_{\mu\nu\lambda} \Delta_\nu A_{\lambda,\mathbf{r}} \right)^2, \tag{A4}$$

$$|\psi_{1,\mathbf{r}}|^2 + |\psi_{2,\mathbf{r}}|^2 = 1 \quad \forall \mathbf{r}, \tag{A5}$$

where we have introduced $t \equiv \beta/2$ and $g \equiv e^2/(4\beta)$ – the same coupling constants as in Ref. 16. Writing the complex fields on polar form,

$$\psi_{c,\mathbf{r}} = \rho_{c,\mathbf{r}}\, \mathrm{e}^{\mathrm{i}\theta_{c,\mathbf{r}}}, \tag{A6}$$

$$\int \mathrm{d}\psi_{c,\mathbf{r}}\, \mathrm{d}\psi^*_{c,\mathbf{r}} = \int_0^{2\pi} \mathrm{d}\theta_{c,\mathbf{r}} \int_0^\infty \rho_{c,\mathbf{r}}\, \mathrm{d}\rho_{c,\mathbf{r}}, \tag{A7}$$

we note that the constraint (A5) becomes

$$\rho_{1,\mathbf{r}}{}^2 + \rho_{2,\mathbf{r}}{}^2 = 1, \quad \forall \mathbf{r}, \tag{A8}$$

which describes the unit circle in the first quadrant of the $\rho_{1,\mathbf{r}}\rho_{2,\mathbf{r}}$-plane (since $\rho_{c,\mathbf{r}} \geq 0$). This means that we can incorporate the constraint directly into the integral by introducing the new field ϕ,

$$\rho_{1,\mathbf{r}} = \cos\phi_{\mathbf{r}}, \quad \rho_{2,\mathbf{r}} = \sin\phi_{\mathbf{r}} \tag{A9}$$

$$\prod_c \int_0^\infty \rho_{c,\mathbf{r}}\, \mathrm{d}\rho_{c,\mathbf{r}} \bigg|_{\sum_c \rho_{c,\mathbf{r}}{}^2 = 1} = \int_0^{\frac{\pi}{2}} \cos\phi_{\mathbf{r}} \sin\phi_{\mathbf{r}}\, \mathrm{d}\phi_{\mathbf{r}}, \tag{A10}$$

such that (A1), (A3) and (A5) can be replaced by

$$Z = \prod_{\mathbf{r}} \int_0^{2\pi} \mathrm{d}\theta_{1,\mathbf{r}}\, \mathrm{d}\theta_{2,\mathbf{r}} \int_0^{\frac{\pi}{2}} \cos\phi_{\mathbf{r}} \sin\phi_{\mathbf{r}}\, \mathrm{d}\phi_{\mathbf{r}} \prod_{\mu,\mathbf{r}} \int \mathrm{d}A_{\mu,\mathbf{r}}\ \mathrm{e}^{-S}, \tag{A11}$$

$$S_t = -t \sum_{\mu,\mathbf{r}} \Big[\cos\phi_{\mathbf{r}} \cos\phi_{\mathbf{r}+\hat{\boldsymbol{\mu}}} \left(\mathrm{e}^{\mathrm{i}(\theta_{1,\mathbf{r}} - \theta_{1,\mathbf{r}+\hat{\boldsymbol{\mu}}} + A_{\mu,\mathbf{r}})} + \text{c.c.} \right) + \sin\phi_{\mathbf{r}} \sin\phi_{\mathbf{r}+\hat{\boldsymbol{\mu}}} \left(\mathrm{e}^{\mathrm{i}(\theta_{2,\mathbf{r}} - \theta_{2,\mathbf{r}+\hat{\boldsymbol{\mu}}} + A_{\mu,\mathbf{r}})} + \text{c.c.} \right) \Big]. \tag{A12}$$

Next, we focus on the the θ-dependent part of the integrand, namely $\exp(-S_t)$, aiming at replacing this field with a J-current field. First we symmetrize (A12): Assuming periodic boundary conditions and using that

$$A_{\mu,\mathbf{r}-\hat{\boldsymbol{\mu}}} = -A_{-\mu,\mathbf{r}}, \tag{A13}$$

we get

$$S_t = -\frac{t}{2}\sum_{\kappa,\mathbf{r}}\Big[\cos\phi_{\mathbf{r}}\cos\phi_{\mathbf{r}+\hat{\boldsymbol{\kappa}}}\left(\mathrm{e}^{\mathrm{i}(\theta_{1,\mathbf{r}}-\theta_{1,\mathbf{r}+\hat{\boldsymbol{\kappa}}}+A_{\kappa,\mathbf{r}})}+\mathrm{c.c.}\right) + \sin\phi_{\mathbf{r}}\sin\phi_{\mathbf{r}+\hat{\boldsymbol{\kappa}}}\left(\mathrm{e}^{\mathrm{i}(\theta_{2,\mathbf{r}}-\theta_{2,\mathbf{r}+\hat{\boldsymbol{\kappa}}}+A_{\kappa,\mathbf{r}})}+\mathrm{c.c.}\right)\Big], \quad \text{(A14)}$$

where κ runs over negative as well as positive lattice directions, $\kappa \in \{\pm x, \pm y, \pm z\}$. Then we split $\exp(-S_t)$ into its individual factors and Taylor expand each of them:

$$\begin{aligned}\mathrm{e}^{-S_t} = \prod_{\kappa,\mathbf{r}}\sum_{\substack{k_{1,\kappa,\mathbf{r}}=0\\ l_{1,\kappa,\mathbf{r}}=0}}^{\infty}\sum_{\substack{k_{2,\kappa,\mathbf{r}}=0\\ l_{2,\kappa,\mathbf{r}}=0}}^{\infty} &\Bigg[\frac{\left(\frac{t}{2}\cos\phi_{\mathbf{r}}\cos\phi_{\mathbf{r}+\hat{\boldsymbol{\kappa}}}\right)^{k_{1,\kappa,\mathbf{r}}+l_{1,\kappa,\mathbf{r}}}}{k_{1,\kappa,\mathbf{r}}!l_{1,\kappa,\mathbf{r}}!}\times \\ &\frac{\left(\frac{t}{2}\sin\phi_{\mathbf{r}}\sin\phi_{\mathbf{r}+\hat{\boldsymbol{\kappa}}}\right)^{k_{2,\kappa,\mathbf{r}}+l_{2,\kappa,\mathbf{r}}}}{k_{2,\kappa,\mathbf{r}}!l_{2,\kappa,\mathbf{r}}!}\times \\ &\mathrm{e}^{\mathrm{i}(k_{1,\kappa,\mathbf{r}}-l_{1,\kappa,\mathbf{r}})(\theta_{1,\mathbf{r}}-\theta_{1,\mathbf{r}+\hat{\boldsymbol{\kappa}}}+A_{\kappa,\mathbf{r}})}\times \\ &\mathrm{e}^{\mathrm{i}(k_{2,\kappa,\mathbf{r}}-l_{2,\kappa,\mathbf{r}})(\theta_{2,\mathbf{r}}-\theta_{2,\mathbf{r}+\hat{\boldsymbol{\kappa}}}+A_{\kappa,\mathbf{r}})}\Bigg]\end{aligned} \quad \text{(A15)}$$

The factors of the product over the lattice and directions in (A15) may be rearranged such that all the terms containing $\theta_{c,\mathbf{r}}$ are collected into one,

$$\mathrm{e}^{-S_t} = \sum_{\{k,l\}}\prod_{c,\mathbf{r}}\mathrm{e}^{\mathrm{i}\theta_{c,\mathbf{r}}\sum_\kappa(k_{c,\kappa,\mathbf{r}}-l_{c,\kappa,\mathbf{r}}-k_{c,\kappa,\mathbf{r}-\hat{\boldsymbol{\kappa}}}+l_{c,\kappa,\mathbf{r}-\hat{\boldsymbol{\kappa}}})} \times (\text{Everything else}). \quad \text{(A16)}$$

Here $\{k,l\}$ denotes the set of all possible Taylor expansion index field configurations. Inserting this in the partition function (A11), the θ-integrals may now be performed. The result is Dirac delta functions (up to an irrelevant scaling factor, which we ignore) at each lattice point, revealing the ("J-current") constraint

$$\sum_\kappa k_{c,\kappa,\mathbf{r}} - l_{c,\kappa,\mathbf{r}} - k_{c,\kappa,\mathbf{r}-\hat{\boldsymbol{\kappa}}} + l_{c,\kappa,\mathbf{r}-\hat{\boldsymbol{\kappa}}} = 0, \quad \forall c,\mathbf{r}. \quad \text{(A17)}$$

It is convenient to introduce the non-negative bond subcurrents

$$J_{c,\kappa,\mathbf{r}} \equiv k_{c,\kappa,\mathbf{r}} + l_{c,-\kappa,\mathbf{r}+\hat{\boldsymbol{\kappa}}} \in \mathbb{N}_0, \quad \text{(A18)}$$

as well as the total bond currents

$$I_{c,\kappa,\mathbf{r}} \equiv J_{c,\kappa,\mathbf{r}} - J_{c,-\kappa,\mathbf{r}+\hat{\boldsymbol{\kappa}}} \in \mathbb{Z}. \quad \text{(A19)}$$

Reordering the sum, the constraint (A17) then simplifies to

$$\sum_\kappa I_{c,\kappa,\mathbf{r}} = 0, \quad \forall c,\mathbf{r}; \quad \text{(A20)}$$

the current conservation in each component at each lattice site.

Getting rid of the θ-field we turn our attention to the ϕ-field. The terms containing $\phi_{\mathbf{r}}$ for a given $\mathbf{r}$ are on the form

$$\begin{aligned}\int_0^{\frac{\pi}{2}}\mathrm{d}\phi_{\mathbf{r}}\cos^{1+2\mathcal{N}_{1,\mathbf{r}}}\phi_{\mathbf{r}}\sin^{1+2\mathcal{N}_{2,\mathbf{r}}}\phi_{\mathbf{r}}\times(\text{Everything else}) \\ = \frac{\mathcal{N}_{1,\mathbf{r}}!\mathcal{N}_{2,\mathbf{r}}!}{2\left(\mathcal{N}_{1,\mathbf{r}}+\mathcal{N}_{2,\mathbf{r}}+1\right)}\times(\text{Everything else}),\end{aligned} \quad \text{(A21)}$$

where, using (A18),(A19) and (A20),

$$\begin{aligned}\mathcal{N}_{c,\mathbf{r}} &\equiv \frac{1}{2}\sum_\kappa k_{c,\kappa,\mathbf{r}} + l_{c,\kappa,\mathbf{r}} + k_{c,\kappa,\mathbf{r}-\hat{\boldsymbol{\kappa}}} + l_{c,\kappa,\mathbf{r}-\hat{\boldsymbol{\kappa}}} \\ &= \frac{1}{2}\sum_\kappa J_{c,\kappa,\mathbf{r}} + J_{c,-\kappa,\mathbf{r}+\hat{\boldsymbol{\kappa}}} \\ &= \sum_\kappa J_{c,\kappa,\mathbf{r}} \in \mathbb{N}_0.\end{aligned} \quad \text{(A22)}$$

The Taylor expansion (A15) contains an index field dependent factor as well,

$$\sum_{\{k,l\}}\prod_{c,\kappa,\mathbf{r}}\frac{\left(\frac{t}{2}\right)^{k_{c,\kappa,\mathbf{r}}+l_{c,\kappa,\mathbf{r}}}}{k_{c,\kappa,\mathbf{r}}!l_{c,\kappa,\mathbf{r}}!}, \quad \text{(A23)}$$

which we want to write as a function of the J-subcurrent field instead. It is easy to see that

$$\prod_{c,\kappa,\mathbf{r}}\left(\frac{t}{2}\right)^{k_{c,\kappa,\mathbf{r}}+l_{c,\kappa,\mathbf{r}}} = \prod_{c,\kappa,\mathbf{r}}\left(\frac{t}{2}\right)^{J_{c,\kappa,\mathbf{r}}} \quad \text{(A24)}$$

by reordering the terms in the product. Using the definition (A18), as well as some standard combinatorial results, we may rewrite the denominator part of (A23) as

$$\begin{aligned}\sum_{\{k,l\}}\prod_{c,\kappa,\mathbf{r}}\frac{1}{k_{c,\kappa,\mathbf{r}}!l_{c,\kappa,\mathbf{r}}!} &= \sum_{\{J\}}\prod_{c,\kappa,\mathbf{r}}\sum_{k_{c,\kappa,\mathbf{r}}=0}^{J_{c,\kappa,\mathbf{r}}}\frac{1}{k_{c,\kappa,\mathbf{r}}!(J_{c,\kappa,\mathbf{r}}-k_{c,\kappa,\mathbf{r}})!} \\ &= \sum_{\{J\}}\prod_{c,\kappa,\mathbf{r}}\frac{1}{J_{c,\kappa,\mathbf{r}}!}\sum_{k_{c,\kappa,\mathbf{r}}=0}^{J_{c,\kappa,\mathbf{r}}}\binom{J_{c,\kappa,\mathbf{r}}}{k_{c,\kappa,\mathbf{r}}} \\ &= \sum_{\{J\}}\prod_{c,\kappa,\mathbf{r}}\frac{2^{J_{c,\kappa,\mathbf{r}}}}{J_{c,\kappa,\mathbf{r}}!},\end{aligned} \quad \text{(A25)}$$

where $\{J\}$ denotes the set of all possible subcurrent configurations. (There is no problem in summing k away, as it is an independent variable, and all other terms in the partition function are exclusively J-dependent – as we will see in a moment.) Inserting (A24) and (A25) into (A23) gives

$$\sum_{\{J\}}\prod_{c,\kappa,\mathbf{r}}\frac{t^{J_{c,\kappa,\mathbf{r}}}}{J_{c,\kappa,\mathbf{r}}!}, \quad \text{(A26)}$$

which is what we desired.

Lastly, we want to integrate out the gauge field. The gauge field dependent factors of (A15) are on the form

$$\exp\left[\mathrm{i}\sum_{c,\kappa,\mathbf{r}} A_{\kappa,\mathbf{r}}\left(k_{c,\kappa,\mathbf{r}} - l_{c,\kappa,\mathbf{r}}\right)\right] = \exp\left[\mathrm{i}\sum_{c,\mu,\mathbf{r}} A_{\mu,\mathbf{r}} I_{c,\mu,\mathbf{r}}\right]. \tag{A27}$$

Note that the summation is over *only positive* directions on the RHS. (The RHS is found by expanding and reordering the sum in the exponent on the LHS and applying the identity (A13) and the bond current definition (A19).) Combining (A27) with $\exp(-S_g)$, the total gauge field contribution to the partition function reads (up to an irrelevant scaling factor)

$$\begin{aligned}\prod_{\mu,\mathbf{r}}\int \mathrm{d}A_{\mathbf{r}}\ \exp\sum_{\mu,\mathbf{r}}\Bigg[&\mathrm{i}A_{\mu,\mathbf{r}}\left(I_{1,\mu,\mathbf{r}} + I_{2,\mu,\mathbf{r}}\right)\\ &-(8g)^{-1}\left(\sum_{\nu,\lambda}\epsilon_{\mu\nu\lambda}\Delta_\nu A_{\lambda,\mathbf{r}}\right)^2\Bigg]\\ &\propto \exp\left(-\frac{g}{2}\sum_{\substack{c,c',\\ \mu,\mathbf{r},\mathbf{r}'}} I_{c,\mu,\mathbf{r}} V_{\mathbf{r},\mathbf{r}'} I_{c',\mu,\mathbf{r}'}\right),\end{aligned} \tag{A28}$$

where we have applied the Coulomb gauge $\Delta_\mu A_{\mu,\mathbf{r}} = 0$. $V_{\mathbf{r},\mathbf{r}'}$ is a long range potential given by by the inverse Fourier transform

$$V_{\mathbf{r},\mathbf{r}'} \equiv \mathcal{F}^{-1}\left\{\left[\sum_\mu \sin^2\left(\frac{q_\mu}{2}\right)\right]^{-1}\right\}(\mathbf{r}-\mathbf{r}'), \tag{A29}$$

where q_μ is the μ component of the Fourier space wave vector $\mathbf{q}$.

Combining everything, (A20), (A21), (A26), and (A28), leaving out trivial scaling factors, we end up with

$$Z = \sum_{\{J|\sum_\kappa I_\kappa = 0\}}\left[\prod_{c,\kappa,\mathbf{r}}\frac{t^{J_{c,\kappa,\mathbf{r}}}}{J_{c,\kappa,\mathbf{r}}!}\right]\left[\prod_{\mathbf{r}}\frac{\mathcal{N}_{1,\mathbf{r}}!\mathcal{N}_{2,\mathbf{r}}!}{(\mathcal{N}_{1,\mathbf{r}}+\mathcal{N}_{2,\mathbf{r}}+1)}\right]\exp\left(-\frac{g}{2}\sum_{\substack{c,c',\\ \mu,\mathbf{r},\mathbf{r}'}} I_{c,\mu,\mathbf{r}} V_{\mathbf{r},\mathbf{r}'} I_{c',\mu,\mathbf{r}'}\right), \tag{A30}$$

which is a J-current formulation of the NCCP[1] model.

[1] T. Senthil, A. Vishwanath, L. Balents, S. Sachdev, and M. P. A. Fisher, Science **303**, 1490 (2004), arXiv:cond-mat/0311326v1 [cond-mat.str-el].

[2] T. Senthil, L. Balents, S. Sachdev, A. Vishwanath, and M. P. A. Fisher, Phys. Rev. B **70**, 144407 (2004), arXiv:cond-mat/0312617v1 [cond-mat.str-el].

[3] A. W. Sandvik, Phys. Rev. Lett. **98**, 227202 (2007), arXiv:cond-mat/0611343v3 [cond-mat.str-el].

[4] R. G. Melko and R. K. Kaul, Phys. Rev. Lett. **100**, 017203 (2008), arXiv:0707.2961v2 [cond-mat.str-el].

[5] J. Lou, A. W. Sandvik, and N. Kawashima, Phys. Rev. B **80**, 180414 (2009), arXiv:0908.0740v1 [cond-mat.str-el].

[6] A. W. Sandvik, Phys. Rev. Lett. **104**, 177201 (2010), arXiv:1001.4296v2 [cond-mat.str-el].

[7] A. Banerjee, K. Damle, and F. Alet, Phys. Rev. B **82**, 155139 (2010), arXiv:1002.1375v1 [cond-mat.str-el].

[8] R. K. Kaul and A. W. Sandvik, Phys. Rev. Lett. **108**, 137201 (2012), arXiv:1110.4130v1 [cond-mat.str-el].

[9] F.-J. Jiang, M. Nyfeler, S. Chandrasekharan, and U.-J. Wiese, J. Stat. Mech.: Theory Exp. **2008**, P02009 (2008), arXiv:0710.3926v1 [cond-mat.str-el].

[10] L. Isaev, G. Ortiz, and J. Dukelsky, Journal of Physics: Condensed Matter **22**, 016006 (2010), arXiv:0903.1630v2 [cond-mat.str-el].

[11] O. I. Motrunich and A. Vishwanath, Phys. Rev. B **70**, 075104 (2004), arXiv:cond-mat/0311222v2 [cond-mat.str-el].

[12] J. Smiseth, E. Smørgrav, E. Babaev, and A. Sudbø, Phys. Rev. B **71**, 214509 (2005), arXiv:cond-mat/0411761v2 [cond-mat.supr-con].

[13] A. Kuklov, N. Prokof'ev, B. Svistunov, and M. Troyer, Annals of Physics **321**, 1602 (2006), arXiv:cond-mat/0602466v1 [cond-mat.str-el].

[14] S. Kragset, E. Smørgrav, J. Hove, F. S. Nogueira, and A. Sudbø, Phys. Rev. Lett. **97**, 247201 (2006), arXiv:cond-mat/0609336v3 [cond-mat.str-el].

[15] O. I. Motrunich and A. Vishwanath (2008), arXiv:0805.1494v1 [cond-mat.stat-mech].

[16] A. B. Kuklov, M. Matsumoto, N. V. Prokof'ev, B. V. Svistunov, and M. Troyer, Phys. Rev. Lett. **101**, 050405 (2008), arXiv:0805.4334v1 [cond-mat.stat-mech].
[17] F. S. Nogueira, S. Kragset, and A. Sudbø, Phys. Rev. B **76**, 220403 (2007), arXiv:0708.3633v2 [cond-mat.str-el].
[18] R. K. Kaul and R. G. Melko, Phys. Rev. B **78**, 014417 (2008), arXiv:0804.2279v1 [cond-mat.str-el].
[19] E. Babaev, Nucl. Phys. B **686**, 397 (2004), arXiv:cond-mat/0201547v7 [cond-mat.supr-con].
[20] Babaev Egor, Sudbo Asle, and Ashcroft N. W., Nature **431**, 666 (2004), arXiv:cond-mat/0410408v1 [cond-mat.supr-con].
[21] E. Smørgrav, E. Babaev, J. Smiseth, and A. Sudbø, Phys. Rev. Lett. **95**, 135301 (2005), arXiv:cond-mat/0508286v1 [cond-mat.supr-con].
[22] A. B. Kuklov, M. Matsumoto, N. V. Prokof'ev, B. V. Svistunov, and M. Troyer (2008), arXiv:0805.2578v1 [cond-mat.stat-mech].
[23] E. Babaev, L. D. Faddeev, and A. J. Niemi, Phys. Rev. B **65**, 100512 (2002), arXiv:cond-mat/0106152v3 [cond-mat.supr-con].
[24] J. Smiseth, E. Smørgrav, and A. Sudbø, Phys. Rev. Lett. **93**, 077002 (2004), arXiv:cond-mat/0403417v4 [cond-mat.supr-con].
[25] E. V. Herland, E. Babaev, and A. Sudbø, Phys. Rev. B **82**, 134511 (2010), arXiv:1006.3311v1 [cond-mat.supr-con].
[26] A. Achúcarro and T. Vachaspati, Physics Reports **327**, 347 (2000).
[27] K. Hukushima and K. Nemoto, J. Phys. Soc. Jpn. **65**, 1604 (1996), arXiv:cond-mat/9512035v1.
[28] D. J. Earl and M. W. Deem, Phys. Chem. Chem. Phys. **7**, 3910 (2005), arXiv:physics/0508111v2 [physics.comp-ph].
[29] H. G. Katzgraber (2011), arXiv:0905.1629v3 [cond-mat.stat-mech].
[30] N. Metropolis, A. W. Rosenbluth, M. N. Rosenbluth, A. H. Teller, and E. Teller, J. Chem. Phys. **21**, 1087 (1953).
[31] W. K. Hastings, Biometrika **57**, 97 (1970).
[32] W. Nadler, J. H. Meinke, and U. H. E. Hansmann, Phys. Rev. E **78**, 061905 (2008).
[33] H. G. Katzgraber, S. Trebst, D. A. Huse, and M. Troyer, J. Stat. Mech.: Theory Exp. **2006**, P03018 (2006), arXiv:cond-mat/0602085v3 [cond-mat.other].
[34] K. Hukushima, Phys. Rev. E **60**, 3606 (1999), arXiv:cond-mat/9903391v1 [cond-mat.dis-nn].
[35] A. M. Ferrenberg and R. H. Swendsen, Phys. Rev. Lett. **63**, 1195 (1989).
[36] M. Matsumoto and T. Nishimura, ACM Trans. Model. Comput. Simul. **8**, 3 (1998).
[37] B. A. Berg, Comput. Phys. Commun. **69**, 7 (1992).
[38] N. Prokof'ev, B. Svistunov, and I. Tupitsyn, Physics Letters A **238**, 253 (1998).
[39] N. Prokof'ev and B. Svistunov, Phys. Rev. Lett. **87**, 160601 (2001), arXiv:cond-mat/0103146.
[40] M. E. Fisher and A. N. Berker, Phys. Rev. B **26**, 2507 (1982).
[41] J. L. Cardy and P. Nightingale, Phys. Rev. B **27**, 4256 (1983).
[42] A. Sudbø, E. Smørgrav, J. Smiseth, F. S. Nogueira, and J. Hove, Phys. Rev. Lett. **89**, 226403 (2002), arXiv:cond-mat/0207501v2 [cond-mat.str-el].
[43] J. Smiseth, E. Smørgrav, F. S. Nogueira, J. Hove, and A. Sudbø, Phys. Rev. B **67**, 205104 (2003), arXiv:cond-mat/0301297v2 [cond-mat.str-el].
[44] K. Binder, Phys. Rev. Lett. **47**, 693 (1981).
[45] K. Binder, Z. Phys. B **43**, 119 (1981).
[46] A. W. Sandvik, AIP Conference Proceedings **1297**, 135 (2010), arXiv:1101.3281v1 [cond-mat.str-el].
[47] K. S. D. Beach, L. Wang, and A. W. Sandvik, arXiv:cond-mat/0505194v1 [cond-mat.stat-mech].
[48] A. M. Ferrenberg and D. P. Landau, Phys. Rev. B **44**, 5081 (1991).
[49] E. Babaev, A. Sudbø, and N. W. Ashcroft, Phys. Rev. Lett. **95**, 105301 (2005), arXiv:cond-mat/0507605v1 [cond-mat.supr-con].
[50] S. Elitzur, Phys. Rev. D **12**, 3978 (1975).
[51] A. Kuklov (2007), at the Nordita Quantum Fluids workshop, Stockholm, URL `http://www.nordita.org/~qf2007/kuklov.pdf`.
[52] C. Holm and W. Janke, Phys. Rev. B **48**, 936 (1993).
[53] M. Campostrini, M. Hasenbusch, A. Pelissetto, P. Rossi, and E. Vicari, Phys. Rev. B **65**, 144520 (2002), arXiv:cond-mat/0110336v2 [cond-mat.stat-mech].
[54] M. Campostrini, M. Hasenbusch, A. Pelissetto, P. Rossi, and E. Vicari, Phys. Rev. B **63**, 214503 (2001), arXiv:cond-mat/0010360v1 [cond-mat.stat-mech].
[55] J. Lee and J. M. Kosterlitz, Phys. Rev. Lett. **65**, 137 (1990).
[56] J. Lee and J. M. Kosterlitz, Phys. Rev. B **43**, 3265 (1991).
[57] A. B. Kuklov, M. Matsumoto, N. V. Prokof'ev, B. V. Svistunov, and M. Troyer, Bull. Am. Phys. Soc. **53**, S12.00006 (2008).
[58] A. Kuklov, N. Prokof'ev, and B. Svistunov, Phys. Rev. Lett. **92**, 050402 (2004), arXiv:cond-mat/0306662v2 [cond-mat.soft].
[59] B. Svistunov and N. Prokof'ev (2012), private communication.
[60] When L is large, such that there are two clearly separate transitions, $(\Delta M_3)_{\rm height}$ and $(\Delta M_3)_{\rm width}$ are determined by the two extrema of the most prominent transition in the M_3 plot, which is the Higgs transition.
[61] This is not the same scaling function as suggested in Ref. 22. In that work the system sizes were smaller than in this work. Because of finite-size effects, the best scaling function may change slightly when larger systems are included. In this context, the best scaling function will be when the largest systems fall on the same master curve.[59]